

Interactive Segmentation of 3D Medical Images with Implicit Surfaces

THÈSE N° 5247 (2011)

PRÉSENTÉE LE 22 DÉCEMBRE 2011

À LA FACULTÉ DES SCIENCES ET TECHNIQUES DE L'INGÉNIEUR
LABORATOIRE DE TRAITEMENT DES SIGNAUX 5
PROGRAMME DOCTORAL EN GÉNIE ÉLECTRIQUE

ÉCOLE POLYTECHNIQUE FÉDÉRALE DE LAUSANNE

POUR L'OBTENTION DU GRADE DE DOCTEUR ÈS SCIENCES

PAR

Benoit MORY

acceptée sur proposition du jury:

Prof. F. Rachidi-Haeri, président du jury
Prof. J.-Ph. Thiran, directeur de thèse
Dr R. Ardon, rapporteur
Prof. P. Vandergheynst, rapporteur
Prof. A. J. Yezzi, rapporteur



ÉCOLE POLYTECHNIQUE
FÉDÉRALE DE LAUSANNE

Suisse
2011

A Maïa et nos filles, Carla et Léonor.

Remerciements

Je tiens tout d'abord à remercier chaleureusement le Professeur Jean-Philippe Thiran qui a accepté de diriger cette thèse et m'a encouragé sans relâche en dépit de l'éloignement géographique.

Je souhaite également remercier très sincèrement les directeurs successifs du laboratoire Medisys, Jean Pergrale puis Nicolas Villain, pour m'avoir accordé confiance et liberté tout au long de ces années. Jean se rappelle peut-être de notre premier entretien, il y a bientôt dix ans, au cours duquel j'avais exprimé pour la première fois mon souhait de réaliser un doctorat. Je remercie également Shérif Makram-Ebeid d'avoir été à l'origine du projet de collaboration entre Medisys et l'EPFL ainsi que pour ses critiques bienveillantes.

J'adresse de vifs remerciements au président du jury, le Professeur Farad Rachidi-Haeri, ainsi qu'au Professeur Pierre Vanderghyest qui me fit l'honneur d'être rapporteur de cette thèse.

Je suis infiniment reconnaissant au Professeur Anthony J. Yezzi, également rapporteur, d'avoir été une si grande source d'inspiration lors d'échanges réguliers à l'origine de nombreuses nouvelles idées. Sincere and grateful thanks, Tony.

Je ne sais comment remercier suffisamment Roberto Ardon tant il a contribué et partagé, dès le départ, chacune des idées développées dans ce manuscrit, ainsi que bien d'autres pistes qui n'ont pu être décrites ici. Roberto, j'espère tout simplement avoir la chance de continuer à travailler à tes côtés pendant encore quelques belles années.

Je remercie également Xavier Bresson, qui finissait son doctorat à l'EPFL quand je commençais et a participé par ses conseils avisés et ses travaux antérieurs à la direction donnée aux premiers chapitres de ce manuscrit.

Je tiens à souligner que cette étude trouve sa raison d'être dans l'environnement stimulant des multiples projets d'applications cliniques innovantes développées au sein du laboratoire Medisys. Ainsi, au moment de terminer cette thèse, j'ai une pensée toute particulière pour tous ceux avec qui j'ai eu le privilège de travailler durant ces dernières années; en particulier pour Oudom, mon relecteur préféré qui prit une grande part dans l'élaboration de cette thèse, dans le fond comme dans la forme. Mes pensées très amicales vont également à Emmanuel qui est bien plus que notre référence en matière d'implémentation efficace, ainsi qu'aux illustres Olivier, Antoine, Raoul, Cécile, Mathieu, Franck, Javier, Jean-Michel, Laurence, Cybèle, Maxim, David, Raphaël, Guillaume et les autres.

Je remercie également les anciens stagiaires qui ont contribué par leurs travaux au développement des méthodes présentées ici, en particulier Khaoula, Marc et Thierry.

Enfin, je comprends maintenant pourquoi chaque doctorant termine ses remerciements par un sentiment de gratitude infinie envers ses amis et les membres de sa famille; leur soutien s'avère indispensable, en particulier quand la fin semble interminable.

Ainsi, je pense aujourd'hui à mes amis de toujours, Fred, Nico, Greg, François mais aussi à tous les autres; à mon père, souvent trop loin mais toujours présent; à ma mère à qui je dois tout, même mon goût pour la recherche; à mes soeurs Nathalie et Marie-Sophie qui m'ont toujours accompagné; à mes très chères grand-mères Liliane et Berthou; à Mati, qui fut souvent d'une aide très précieuse.

Pour finir, mes plus profonds sentiments vont à celles qui ont supporté quotidiennement, avec amour, mes épisodes de surmenages et autres sauts d'humeur. Maïa, je tiens à te dire merci du fond du coeur, celui qui t'appartient. Carla, ma grande fille, merci pour ta patience, je te promets d'être maintenant plus disponible que jamais. Ma petite Léonor, je retiendrai que j'écris ces dernières lignes à l'heure où tu prononces de si jolis premiers mots.

Abstract

To cope with a variety of clinical applications, research in medical image processing has led to a large spectrum of segmentation techniques that extract anatomical structures from volumetric data acquired with 3D imaging modalities. Despite continuing advances in mathematical models for automatic segmentation, many medical practitioners still rely on 2D manual delineation, due to the lack of intuitive semi-automatic tools in 3D.

In this thesis, we propose a methodology and associated numerical schemes enabling the development of 3D image segmentation tools that are reliable, fast and interactive. These properties are key factors for clinical acceptance.

Our approach derives from the framework of *variational methods*: segmentation is obtained by solving an optimization problem that translates the expected properties of target objects in mathematical terms. Such variational methods involve three essential components that constitute our main research axes: an *objective criterion*, a *shape representation* and an optional *set of constraints*.

As objective criterion, we propose a unified formulation that extends existing homogeneity measures in order to model the spatial variations of statistical properties that are frequently encountered in medical images, without compromising efficiency.

Within this formulation, we explore several shape representations based on *implicit surfaces* with the objective to cover a broad range of typical anatomical structures. Firstly, to model tubular shapes in vascular imaging, we introduce *convolution surfaces* in the variational context of image segmentation. Secondly, compact shapes such as lesions are described with a new representation that generalizes *Radial Basis Functions* with non-Euclidean distances, which enables the design of basis functions that naturally align with salient image features. Finally, we estimate geometric *non-rigid deformations* of prior templates to recover structures that have a predictable shape such as whole organs.

Interactivity is ensured by restricting admissible solutions with additional constraints. Translating user input into constraints on the sign of the implicit representation at prescribed points in the image leads us to consider *inequality-constrained optimization*.

Keywords: image segmentation, medical imaging, implicit surfaces, interactive segmentation, vascular segmentation, variational methods, inequality constraints, convex optimization, non-Euclidean radial basis functions, non-rigid deformation.

Version Abrégée

Afin de répondre aux multiples besoins des applications cliniques, la recherche en traitement d'images médicales a permis le développement d'une large palette de techniques de segmentation capables d'extraire des structures anatomiques à partir de données volumiques acquises dans des modalités d'imagerie 3D. Pourtant, en dépit de progrès constants dans la modélisation mathématique du problème de la segmentation automatique, de nombreux praticiens hospitaliers ont toujours recours au contourage manuel de structures d'intérêt en 2D, car les outils semi-automatiques intuitifs sont encore rares en 3D.

Dans cette thèse, nous proposons un cadre méthodologique et des schémas numériques adaptés qui permettent le développement d'outils fiables, rapides et interactifs pour la segmentation d'images volumiques. Ces propriétés sont essentielles pour l'acceptation clinique.

Notre approche s'inscrit dans le cadre des méthodes variationnelles: la segmentation est obtenue grâce à la résolution d'un problème d'optimisation qui traduit en termes mathématiques les propriétés attendues des objets cibles. Ces méthodes variationnelles reposent sur trois ingrédients qui constituent nos principaux axes de recherche: un *critère objectif*, une *représentation des formes* et, de manière optionnelle, un *ensemble de contraintes*.

Nous proposons comme critère objectif une formulation unifiée qui étend les critères d'homogénéité existants afin de prendre en compte de manière efficace les variations spatiales des propriétés statistiques fréquemment rencontrées dans les images médicales.

Dans ce cadre, nous explorons plusieurs représentations des formes à l'aide de *surfaces implicites* pour couvrir une variété importante de structures anatomiques. Tout d'abord, afin de modéliser les formes tubulaires en imagerie vasculaire, nous introduisons les *surfaces de convolution* dans le contexte variationnel de la segmentation. Ensuite, les objets compacts comme les tumeurs sont décrits à l'aide d'une nouvelle représentation qui généralise les *fonctions de base radiale* au cas des distances non-Euclidiennes. Les fonctions de base ainsi créées ont une forme qui épouse naturellement les contours de l'image. Enfin, nous estimons la *transformation géométrique non-rigide* de formes à priori pour extraire des structures dont la forme est caractéristique, comme par exemple des organes complets.

L'interactivité est assurée de manière générique en réduisant les solutions admissibles grâce à des contraintes additionnelles. Le fait d'exprimer l'intervention de l'utilisateur comme des contraintes ponctuelles sur le signe de la représentation implicite des objets nous amène à considérer le cadre de l'*optimisation sous contraintes d'inégalités*.

Mots-clés: segmentation d'images, imagerie médicale, surfaces implicites, segmentation interactive, segmentation vasculaire, méthodes variationnelles, contraintes d'inégalité, optimisation convexe, fonctions de base radiale non-Euclidiennes, déformation non-rigide.

Contents

Abstract	v
Version Abrégée	vii
Notations	5
List of Figures	7
1 Introduction	1
1.1 Context and Objectives	1
1.2 Implicit Surfaces	3
1.3 Variational Image Segmentation	4
1.4 Contributions	5
2 A Short Survey on Image Segmentation Techniques	9
2.1 Low-level Classification	10
2.1.1 Thresholding	10
2.1.2 Classifiers	10
2.1.3 Clustering	11
2.2 Regions as Connected Sets	12
2.2.1 Region Growing	12
2.2.2 Markov Random Fields	12
2.2.3 Graph-Partitioning	13
2.3 Deformable Models	14
2.3.1 Parametric Active Contours	15
2.3.2 Geometric Active Contours	17
2.4 Region-Based Variational Approaches	22
2.4.1 Optimal Piecewise-Smooth Approximation	22
2.4.2 Region Competition	23
2.4.3 Active Contours Without Edges	25
2.4.4 Non-Parametric Models with Information Theory	30
2.5 Conclusion	34

3	Convex Framework for Two-Phase Image Segmentation	35
3.1	Introduction	36
3.2	General Variational Formulation	36
3.2.1	Gaussian Distributions	39
3.2.2	Non-Parametric Distributions	40
3.2.3	Local Gaussian Distributions	42
3.2.4	Local Non-Parametric Distributions	45
3.2.5	Maximum-Flux Criterion	46
3.3	Convex Relaxation with a Membership Function	48
3.3.1	Functions of Bounded Variations	48
3.3.2	General Convex Extension	49
3.3.3	Fast Minimization Scheme	50
3.3.4	The Piecewise-Constant Case	54
3.4	Unsupervised Fuzzy Region Competition	57
3.4.1	Non-Parametric Distributions	57
3.4.2	The Piecewise-Smooth Case	62
3.4.3	Local Non-Parametric Distributions	66
3.5	Conclusion	70
4	Tubular Constraints and Implicit Convolution Surfaces	73
4.1	Introduction	74
4.2	Piecewise-Smooth Fuzzy Region Competition	75
4.2.1	Contrast constraint	76
4.2.2	Local Volume constraint	76
4.2.3	Minimization Scheme	79
4.2.4	Extraction of liver veins in CTA	80
4.3	Implicit Convolution Surfaces	82
4.3.1	Generalized Cylinder Implicit Representation	82
4.3.2	Problem Formulation	83
4.3.3	Minimization Scheme	85
4.3.4	Inferior Vena Cava Segmentation	87
4.4	Conclusion	91
5	Interactive Segmentation with Non-Euclidean Radial Basis Functions	93
5.1	Introduction	94
5.2	Segmentation with Radial Basis Functions	95
5.3	Proposed Algorithm	96
5.3.1	Switching to Non-Euclidean Distances	96
5.3.2	Interactions as Linear Inequality Constraints	100
5.3.3	Minimization Scheme with Active Sets	102
5.4	3D Interactive Application Workflow	104
5.5	Conclusion	106

6	Non-Rigid Implicit Template Deformation with User Constraints	111
6.1	Introduction	112
6.2	Region-Based Implicit Template Deformation	113
6.3	Proposed Algorithm	114
6.3.1	Interactions as Non-Linear Inequalities	115
6.3.2	Algebraic Definition Of Shapes	116
6.3.3	Transformation Model	118
6.3.4	Augmented Lagrangian Minimization Scheme	119
6.4	Experiments and Validation	122
6.4.1	Applications Without User Interactions	123
6.4.2	Applications With User Interactions	126
6.5	Conclusion	130
7	Conclusion	131
7.1	Unified Variational Formulation	131
7.2	Diversity of Representations	132
A	Proof of Proposition 1	135
B	Generalized Scaling Property of δ	137
C	Centerline and Scales Derivatives	139
	Curriculum Vitae	147
	Bibliography	151

Notations

n	image dimension, $n = 2$ for 2D images, $n = 3$ for 3D volumes.
Ω	image domain, an open subset of \mathbb{R}^n , $\Omega \subset \mathbb{R}^n$.
d	number of image components (channels), e.g. $d = 3$ for color images.
I	an image, an integrable function $I : \Omega \mapsto \mathbb{R}^d$.
\mathbf{x}	a point in the image domain, $\mathbf{x} \in \Omega$.
\mathbf{y}	another point in the image domain, $\mathbf{y} \in \Omega$.
Ω_i	closed subset of Ω , $\Omega_i \subset \Omega$, region number i .
Ω_1	closed subset of Ω , $\Omega_1 \subset \Omega$, referred to as the "foreground" region.
$ \Omega_i $	measure of the continuous set Ω_i , s.t. $ \Omega_i = \int_{\Omega_i} d\mathbf{x}$
$\text{Per}(\Omega_i)$	perimeter of Ω_i , i.e. a measure of its boundary.
Γ	region boundary, a closed curve or surface, such that $\Gamma = \partial\Omega_1$.
\mathbf{n}	outward pointing unit normal field of the boundary Γ .
∇	gradient operator in \mathbb{R}^n .
$\nabla \cdot$	divergence operator in \mathbb{R}^n .
Δ	Laplacian operator in \mathbb{R}^n , such that $\Delta = \nabla \cdot (\nabla)$.
p_i	a non-parametric distribution of intensity in the region i
H	Heaviside step function
δ	Dirac distribution
Φ	implicit function, positive in the foreground.
u	a membership function to the foreground.
\circ	functional composition, i.e. $f \circ g(\mathbf{x}) = f(g(\mathbf{x}))$
$*$	convolution, i.e. $[f * g](\mathbf{x}) = \int_{\Omega} f(\mathbf{x})g(\mathbf{x} - \mathbf{y})d\mathbf{y}$
W_{σ}	n-dimensional Gaussian functions of scale σ
K_{ϵ}	1-dimensional Gaussian of scale ϵ

List of Figures

1.1	Implicit Representations of a contour in 2D	4
1.2	All proposed algorithms in a preview example in CT	7
2.1	Geometric Heat Equation in 2D: smoothing property and shrinking to a point.	18
2.2	Geometric Heat Equation in 2D: level-set implementation.	20
2.3	Geometric/Geodesic active contours in 2D with a level-set representation .	21
2.4	Active Contours Without Edges	26
2.5	Approximations H_ϵ and δ_ϵ for various values of ϵ	27
2.6	Active Contours Without Edges - issues with intensity variations	28
2.7	Piecewise-smooth simultaneous segmentation and noise removal	29
2.8	Probability density function using Parzen windows in the discrete case . . .	31
2.9	Segmentation with entropy and non-parametric distributions - multiple modes.	32
2.10	Segmentation with non-parametric distributions - identical means & variances.	33
3.1	Partitioning of the image domain Ω in two regions Ω_1 and Ω_2	37
3.2	<i>Fuzzy Region Competition</i> , supervised segmentation of the zebra image . . .	52
3.3	Global geometric flux-maximization with $r = -\Delta I_\sigma$, breast lesion	53
3.4	Fuzzy Region Competition, piecewise-constant model, ultrasound breast lesion	55
3.5	Fuzzy Region Competition, piecewise-constant model, X-Ray aneurysm . .	56
3.6	Synthetic image segmentation with non-parametric distributions	58
3.7	Fuzzy Region Competition with a non-parametric probability distribution .	59
3.8	Color images: the global non-parametric model in the multivariate case. . .	60
3.9	Color images: the global non-parametric model in the multivariate case (2).	61
3.10	Fuzzy Region Competition with a piecewise-smooth model	63
3.11	An example of piecewise-smooth segmentation of a natural image in 2D . .	64
3.12	Piecewise-smooth segmentation of a liver veins in 3D CT angiography . . .	65
3.13	Local non-parametric distributions on the cameraman image.	67
3.14	Hierarchical segmentation of a 3D CT volume of the lungs.	69
4.1	Inconsistent piecewise-smooth foreground/background decisions.	76
4.2	Evolution for various constraint settings and initial conditions.	77
4.3	Piecewise-smooth vessels on a 2D synthetic image.	80

4.4	Fuzzy Region Competition with constraints in 3D liver CTA	81
4.5	Analytical implicit representation of a vessel in 2D.	82
4.6	Using convolution surfaces for visualization of complex vascular structures .	83
4.7	Joint regularization of scale variations and centerline length, fixed end-points.	84
4.8	Illustration of the centerline evolution by gradient descent	86
4.9	2D joint centerline and vessel boundary extraction on a 2D ultrasound image.	86
4.10	3D evolution of a medial convolution surface on synthetic data	87
4.11	2D joint centerline and vessel boundary extraction on a 2D X-Ray angiography.	88
4.12	Sagittal/axial views of a contrast-enhanced liver CT scan	89
4.13	Front and side views of IVC + liver veins segmentation in CT.	90
4.14	Segmentation of the Inferior Vena CavaVC in 2 CT volumes	91
5.1	An implicit contour with Euclidean RBFs	96
5.2	Switching to non-Euclidean distances	98
5.3	An implicit contour with Non-Euclidean RBFs	99
5.4	Non-Euclidean kernels increase segmentation accuracy	101
5.5	Principles of Active Sets Algorithm	103
5.6	Approximation $\delta_\epsilon(\Phi_\lambda)$ for $\epsilon = 0.01, 0.05$ and 0.15	104
5.7	One-Click” initialization, segmentation of a brain volume in CT.	106
5.8	2D interactive segmentation of the Left Ventricle in a Cardiac CT slice . .	107
5.9	General-purpose 3D interactive segmentation tool - cardiac CT	108
5.10	General-purpose 3D interactive segmentation tool - kidneys	109
6.1	Implicit template deformation	114
6.2	User constraints as inside/outside labeled points	115
6.3	Image and shape referentials in \mathbb{R}^2	117
6.4	Transformation decomposition into pose and deformation	118
6.5	Gradient computation with coarse-to-fine distance warping and convolutions	122
6.6	Segmentation of 3 cardiac ultrasound images in short axis view	123
6.7	3D kidney segmentation for two different patients in CT and US.	124
6.8	Myocardium segmentation for 3 different patients in 3D US and cardiac CT.	125
6.9	Cardiac chambers segmentation in 3D US and cardiac CT	126
6.10	Interactive Liver segmentation in MRI for preoperative resection planning. .	127
6.11	Interactive carotid segmentation in 3DUS for atherosclerosis assessment . .	128
6.12	3D Contrast-Enhanced Ultrasound (CEUS) image of a kidney	128
6.13	Interactive Segmentation Evaluation in Contrast-Enhanced Ultrasound . . .	129

1

Introduction

1.1 Context and Objectives

In the last 30 years, digital diagnostic imaging has become pervasive in all aspects of medicine. Among other modalities, Magnetic Resonance Imaging, X-ray Computerized Tomography and Ultrasound provide effective and non-invasive means for mapping the anatomy of a patient in 3D. With the ever-increasing number and size of digital medical images acquired daily in hospitals, advanced image processing is already an essential tool in oncology, cardiology, neurology and many other clinical application areas. In particular, image *segmentation* algorithms that delineate anatomical structures of interest are a key component to assist and automate radiological tasks in a timely fashion.

In the computer vision community, segmentation is usually defined as the process of separating an image into constituent regions in a way that mimics the human visual system, which is closely related to perceptual grouping and clustering [81]. In the context of medical imaging, segmentation has an even broader meaning that encompasses a variety of computer-assisted tasks, with extremely diverse motivations. The same term can refer for instance to the automatic contouring of organs, the extraction of their vascular structures (inner and outer vessel walls) or to the classification of healthy vs abnormal/necrotic/malignant tissues. In the current practice, clinical usages of the outcome of segmentation algorithms include volume measurements, visualization and rendering, follow-up and registration of an anatomical structure over time or across different modalities, therapy planning, image-guided interventions or surgical simulations. Imaging artifacts that may significantly affect the performance of algorithms are as diverse as the applications, stemming from noise, partial volume effect or motion during acquisitions.

To cope with a considerable variety of clinical needs in terms of application requirements, research in medical image processing has led to a large spectrum of 3D segmentation methods, ranging from surface reconstruction of manual slice-by-slice contouring to fully-automatic techniques that incorporate prior knowledge on the shape and appearance of the target anatomical structures. Within this spectrum, the more automation is expected from a segmentation algorithm, the more specificity, sophistication and computational complexity are usually involved. However, reality is that any image segmentation algorithm is inevitably prone to errors, which makes acceptance of such fully-automatic tools in clinical routine a true challenge. In the timely context of repeated examinations, it is unreasonable to expect a radiologist to rely on an algorithm that occasionally fails after having processed the image for one minute.

Despite continuing advances in segmentation methodology and mathematical models, many applications still rely on manual delineation, due partly to insufficient reliability of automatic tools, partly to the lack of easy-to-use semi-automatic methods. In this respect, the remaining bottlenecks for clinical acceptance of image segmentation algorithms in 3D are reliability, efficiency and interactivity. These three properties are the essential motivations behind the work presented in this manuscript.

Reproducibility is often mentioned as a key factor in favor of automatic methods. However, reproducibility should sometimes be balanced to satisfy medical practitioners who also considerably value control and supervision on the final result. Semi-automatic segmentation techniques that incorporate knowledge from an expert are the best candidates to combine efficiency, accuracy and repeatability while offering better confidence and avoiding the risk of complete failures.

In this perspective, *interactivity* should be envisaged more thoroughly than a post-processing correction step, as a means to design techniques that place the radiologist's expertise at the core of the segmentation process. Not only does this require appropriate computational algorithms, but also intuitive user interfaces, in particular for 3D data. The challenges of these new application workflows are only briefly addressed in this work, although they are probably equally important for clinical applicability.

Our objective is to develop computational approaches to 3D interactive medical image segmentation that are broadly useful. In order to fulfill a large spectrum of application requirements, we believe that there exists a need for both diversity and unification. While general paradigms are important for software re-usability, rapid algorithm prototyping and interoperability, only the multiplicity of techniques inside a unified formulation can achieve broad utility. Our approach derives from the mathematical framework of *variational image segmentation* with *implicit surfaces*, principles of which are briefly reminded hereunder.

1.2 Implicit Surfaces

Implicit surfaces, also called *isosurfaces* or *equipotential* surfaces, refer to a widely used representation of 3D surfaces for scientific visualization of medical, material or atmospheric data, surface reconstruction from unorganized point sets as well as image segmentation. An implicit surface Γ is defined by a continuous scalar-valued *field function* Φ over the domain Ω , through its *zero-set*, the locus of points at which the function equals zero:

$$\Gamma = \{\mathbf{x} \in \Omega, \Phi(\mathbf{x}) = 0\} = \Phi^{-1}(0) \quad (1.1)$$

An implicit surface Γ can be recovered from its scalar field Φ for instance using the *Marching Cubes* algorithm [111], which results in a triangular mesh.

With polynomial expressions, algebraics such as spheres, quadrics and ellipsoids are common building blocks to design simple implicit surfaces. There is also a number of well-established methods to create scalar fields by analytically expressing the value of $\Phi(\mathbf{x})$ at every point in space as a function of some underlying geometric primitives. For instance, using points as primitives, blobby models such as *meta-balls* [20] and *soft objects* [182] are popular in computer graphics. They are specific examples of the Radial Basis Functions framework, in which the field function Φ is built as a linear combination of translated and scaled versions of a radially-symmetric non-negative kernel φ centered around N points \mathbf{x}_i :

$$\Phi(\mathbf{x}) = \sum_{i=1}^N \lambda_i \varphi \left(\frac{\|\mathbf{x} - \mathbf{x}_i\|}{\sigma_i} \right) \quad (1.2)$$

where λ_i , \mathbf{x}_i and σ_i for $i \in \{1..N\}$ are the free parameters of the representation illustrated in the 2D case in Figure 1.1. We refer the reader to the book of Bloomenthal [21] for generalizations to other primitives such as lines, arcs or planes to create implicit representations usually referred to as *convolution surfaces*. An implicit function can also be represented as a sampled volume on a regular grid as in the level-set framework for image segmentation [133]. In this case, the field does not have an analytical expression but is defined as a solution of a partial differential equation.

From the implicit function theorem, it can be shown that if 0 is a regular value of a continuous function $\Phi : \mathbb{R}^3 \rightarrow \mathbb{R}$, the implicit surface $\{\Phi(\mathbf{x}) = 0\}$ is a two-dimensional manifold [32]. Moreover, the Jordan-Brouwer separation theorem states that such a manifold separates space into the surface itself and two connected open sets: an infinite *outside* and a finite *inside* [79]. Therefore, an implicit function is a suitable representation of a partitioning of an image into two phases.

Implicit surfaces have a number of other desirable properties in the context of 3D image segmentation. Smooth scalar field functions guarantee a continuous and smoothly changing surface that is readily usable for differential calculus. In particular, differential quantities such as unit normals and curvature can be directly and accurately computed from the field function. Another useful attribute is that implicit surfaces easily allow objects of arbitrary topology to blend together by simply summing their implicit representations. Furthermore, interactive segmentation may benefit from the property that implicit surfaces directly incorporate information of whether a given point lies inside or outside of the surface.

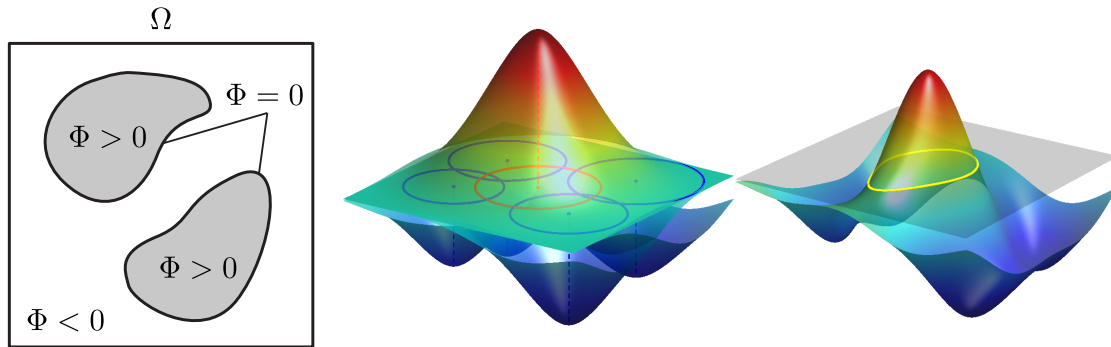


Figure 1.1 — Left: implicit representation of a contour in 2D defined by $\{\Phi = 0\}$ where $\Phi : \Omega \rightarrow \mathbb{R}$ is a 2D function - Right: an implicit contour obtained with Radial Basis Functions as in Eq. (1.2). 5 basis functions shown in the middle with positive (red) and negative (blue) weights λ_i create a scalar field function by linear blending; a corresponding implicit contour $\{\Phi = 0\}$ (yellow).

1.3 Variational Image Segmentation

Since the pioneer work of Roberts et al. on pose estimation using least squares fitting [145], almost all fundamental areas of image processing such as object recognition, restoration and registration adopt a variational perspective and cast their mathematical formulation as an optimization problem.

Classically, segmentation consists in partitioning an image into non-overlapping constituent regions that are *homogeneous* with respect to some prescribed characteristic attributes, often called *features*, such as intensity, color or texture. With the multiplicity of possible image cues, the success of segmentation algorithms is highly dependent on the specification of which coherent attributes are relevant for a given application.

Casting segmentation into an optimization problem, the solution is explicitly defined as an optimum of an objective function that precisely defines what properties are expected of a meaningful partitioning. Focusing on the case of only two regions that correspond to the target anatomical structure (inside) and its surrounding tissues (outside), we can formulate the segmentation problem as:

$$\min_{\Phi \in \mathcal{S}} F(\Phi, I) \quad (1.3)$$

where I is the original image, Φ is a mathematical representation of the inside region and \mathcal{S} is a set of admissible solutions. The objective criterion F encodes suitable homogeneity measures that discriminate objects from each others. In probabilistic methods, minimization of F is equivalent to maximizing a *likelihood* or a *posteriori probability*.

In this work, we only consider the case of *continuous* representations, from which implicit surfaces Φ are a special type, as opposed to *discrete* representations such as graphs [23, 25, 76, 148, 158]. Since both the image I and the scalar field Φ are functions, the criterion F is a *functional*, usually minimized by numerical schemes derived from calculus of variations [123, 154, 165] or shape gradients [54, 55].

1.4 Contributions

Within the general formulation (1.3), specific choices for F , Φ and \mathcal{S} are simultaneously explored in this work on algorithms for interactive segmentation of 3D medical images with implicit surfaces.

First, we propose a unified functional F that extends standard homogeneity measures to model spatial variations of statistical tissue properties without compromising efficiency.

Then, in this formulation, we explore a number of novel complementary representations Φ to cover a diversity of object descriptions, ranging from very general *membership functions* to vessel-specific *implicit generalized cylinders*. Targeting rather spherical shapes such as lesions, we also develop a new surface representation based on a generalization of *Radial Basis Functions* with non-Euclidean distances. For other anatomical structures that follow a known predictable shape, Φ is designed as a *geometrically-deformed template* for model-based segmentation. Dedicated numerical schemes to minimize F are associated to each representation Φ .

Finally, interactivity is ensured in a generic fashion by restricting the set \mathcal{S} of admissible solutions with additional *constraints*. Translating user input into constraints on the sign of the implicit function Φ at prescribed points in the image leads us to consider inequality-constrained optimization algorithms.

Our main contributions can be summarized as follows:

- A unified variational formulation generalizing statistical criteria derived from the *Region Competition* algorithm [189] to localized, non-parametric homogeneity measures that can be efficiently computed. In the case of a standard geometric constraint, problem is solved with convex relaxation, which gives a new interpretation of global minimizers of Active Contours [26, 130] with a membership function.
- A robust method for joint centerline extraction and vessel segmentation with a tubular representation based on smooth implicit convolution surfaces. To our knowledge, this representation has already been proposed for rendering complex vascular structures [132] but was never used in the context of variational image segmentation.
- The introduction of a non-Euclidean, image-dependent distance in conventional Radial Basis Functions [73] for interactive segmentation. This new representation creates feature-aligned kernels and yields more accurate results with much fewer control points than its Euclidean counterpart, leading to a small number of variables to optimize.
- A fast algorithm for live, interactive and model-based segmentation. The method recovers a geometric transformation of an implicit shape by jointly optimizing a global alignment and a smooth non-rigid deformation field. User input is translated into non-linear inequality constraints that are solved with an Augmented Lagrangian approach.

As a preview example on a computerized tomography angiography image, Figure 1.2 shows the diversity and complementarity of implicit representations. In the same variational formulation, each anatomical structure is extracted using one of the proposed representations and a dedicated numerical scheme. Each algorithm runs in a few seconds. This illustration sums up the outline of the manuscript.

Chapter 2 is devoted to a brief survey of image segmentation techniques. The main principles of well-established methods such as graph-partitioning, deformable models, geometric curve evolution and level-set representations are exposed. Region-based variational approaches such as the Region Competition algorithm [189], the Mumford-Shah functional [126] or the Active Contours Without Edges [39] are discussed more thoroughly.

The liver venous tree, rendered in yellow in Figure 1.2, is automatically extracted as an optimal solution of the general convex optimization framework presented in chapter 3. We enumerate a wide spectrum of statistical region descriptions, ranging from globally-Gaussian to locally non-parametric distributions. In particular, locally-Gaussian models are shown to constitute a fast alternative to piecewise-smooth approaches and enable to capture spatial variations of radio-opaque contrast product concentration in angiography.

The aorta (green) and the Inferior Vena Cava (blue) are modeled as generalized cylinders and implicitly represented with a smooth convolution surface around a medial curve. Within the unified region-based formulation, we develop in chapter 4 all necessary components to perform a joint optimization of the vessel centerline curve and the corresponding scales, defined along the curve.

The four lesions (in red) inside the liver are delineated with the interactive segmentation method presented in chapter 5. A new surface representation is defined as a linear combination of non-Euclidean basis functions that naturally align with the image features. Interactivity is enabled by casting user-given labels as linear inequality constraints that are solved using a variant of the Active Sets method.

Using the non-rigid deformation technique described in chapter 6, the liver and both kidneys are obtained by considering the unknown implicit function to be a geometric transformation of a prior shape. This formulation is consistent with the algebraic definition of *shapes* proposed in [184]. The joint optimization of a global *pose* and a local *deformation*, subject to a set of non-linear inequality constraints derived from user interactions, is performed by an Augmented Lagrangian approach.

Note that the CT liver image does not relate to a clinical application evaluation and only serves to illustrate the spectrum of possible shapes considered in this work. Focusing on a broadly-useful methodology and algorithms, we show numerous other examples in ultrasound and magnetic resonance or even on photographic images.

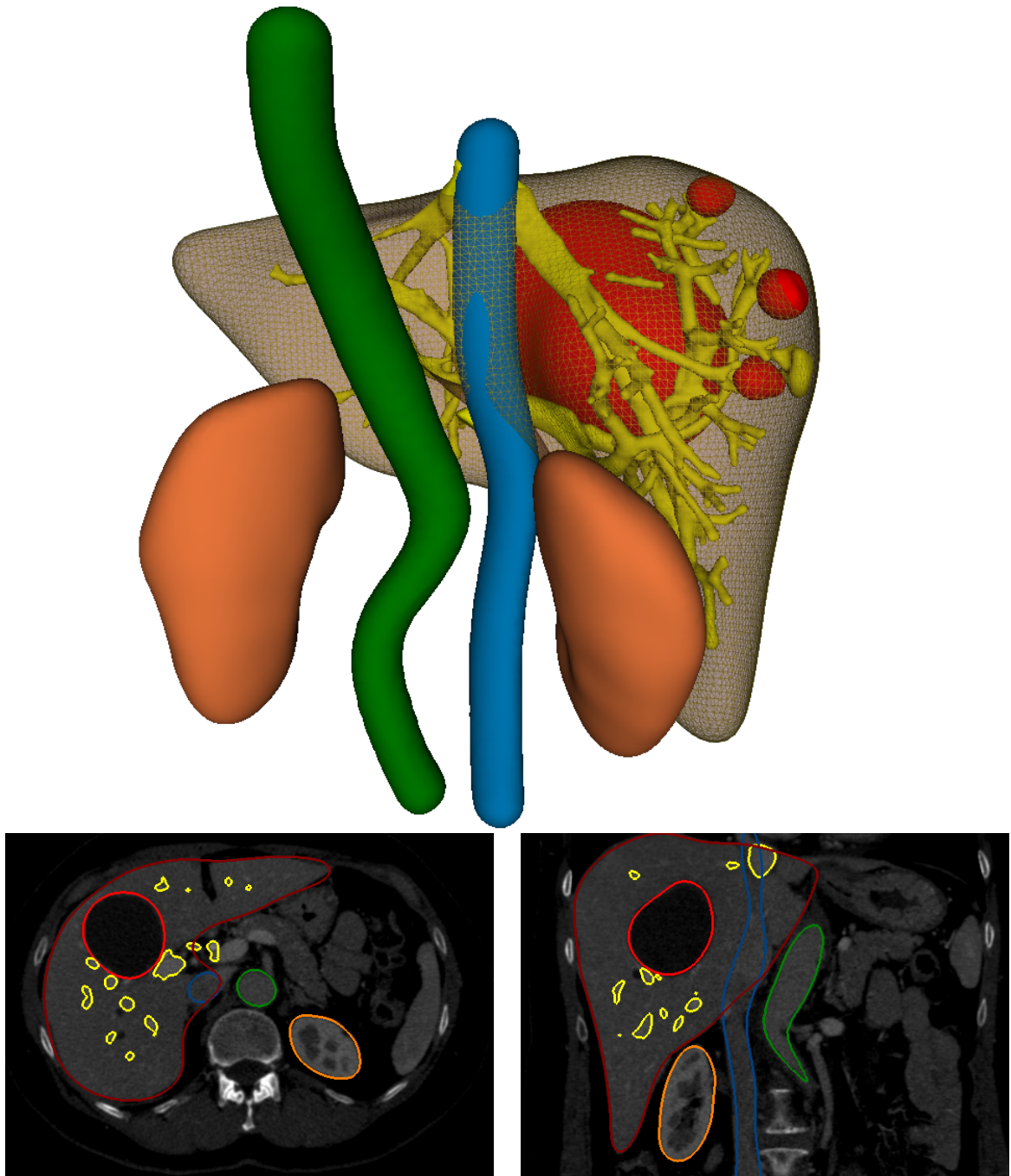


Figure 1.2 — All proposed algorithms in a preview example on a Computerized Tomography image of the liver. Anatomical structures shown in surface rendering illustrate the diversity of representations obtained with implicit surfaces. Liver and kidneys are obtained through a geometrical transformation of a predefined template by a smooth deformation field (see Chapter 6). The hepatic lesions (in red) are semi-automatically segmented with non-Euclidean Radial Basis Functions (see Chapter 5). The hepatic and portal veins (in yellow) are the result of a convex optimization scheme on a membership function (see Chapter 3). The Inferior Vena Cava (in green) and the aorta (in blue) are implicit representations of generalized cylinders, known as convolution surfaces (see Chapter 4).

A Short Survey on Image Segmentation Techniques

2

This chapter presents a short survey on techniques that were developed in the past for image segmentation. As a fundamental problem in machine vision, medical imaging and pattern recognition, segmentation is one of the most active research fields in image processing and has already led to a considerably large number of approaches. Even restricted to the context of medical imaging, the spectrum is so large in terms of techniques and applications that this survey is by no means intended to be exhaustive.

Consequently, the objective is first to provide the reader with a brief general overview on some popular families of methods, then to progressively study in more details the influential works that are most related to ours. In particular, we highlight the advantages and limitations of a number of existing region-based algorithms that fit in the general variational framework adopted in chapter 3. In this regard, this chapter can be viewed as an introduction to the unified formulation from which all algorithms presented in this manuscript are derived.

This chapter is divided into four parts. In section 2.1, we briefly introduce some low-level classification algorithms such as thresholding, clustering and machine-learning techniques to group pixels in their feature space, regardless of their spatial relationships. Then, section 2.2 presents the basics of discrete frameworks for region-based segmentation that further make use of *contextual* information like the region-growing algorithm, Markov Random Fields and graph-theoretic methods. In the continuous setting, fundamental principles of deformable models are given in section 2.3 with parametric active contours, geometric curve evolution theory and level-set numerical schemes. The last section 2.4 is more specifically focused on existing powerful *region-based* variational formulations originating from the Mumford-Shah image model and the Region Competition algorithm, and their current limitations regarding fast 3D interactive segmentation.

2.1 Low-level Classification

Low-level classification methods for image segmentation assign a class label or a membership value to each pixel of the image without implying any type of spatial consistency. Their efficiency is their key advantage for 3D medical applications and they are often used as a coarse pre-segmentation step to find an initial guess for more advanced algorithms. Often, the total number of classes to search for is assumed known based on prior knowledge of the considered anatomical structure (e.g. white matter/gray matter/bone) or estimated using automatic techniques such as Minimum Description Length.

2.1.1 Thresholding

Thresholding is the oldest, simplest, fastest, yet sometimes effective algorithm for obtaining a pixel-wise classification from images in which the target structure exhibits well contrasted intensities, or any other measurable feature. Classification is achieved by grouping all pixels that have a value greater than a reference, the *threshold*, into one class, and all other pixels into another class. Multiple thresholds can of course be used to obtain more than two classes or to better characterize a single class. In medical applications, variations on classical thresholding are still often resorted to, usually in a locally-adaptive fashion to make the process less sensitive to noise and intensity inhomogeneities.

2.1.2 Classifiers

Pattern recognition classifiers for low-level image segmentation consist in the supervised process of labeling each pixel of an image based solely on the analysis of its feature space (e.g. the range of possible intensity values), according to a prior learning of labels performed manually on some training data. In its simplest form, the *nearest neighbor* classifier, this corresponds to assigning each pixel to the same class as the one associated with the training sample having the closest feature value. The main advantage stems from the flexibility to specialize classifiers to a target application, by choosing a set of discriminant features. The features can be vector-valued, usually automatically extracted from the image such as multiple responses to filters at different scales and orientations to represent texture properties. In general, difficulties arise with the crucial definition of proper metrics in the feature space and the dimensioning of a representative, unbiased training dataset. Moreover, spatial relationships between pixels are not easily modeled in an efficient way.

Various assumptions on the statistical structure of the feature space can be made, with a crucial impact on classification performance. For instance, The Maximum Likelihood classifier assumes that all measurements are independent and identically distributed (i.i.d.) and generated from a mixture of probability distributions, usually Gaussian. In contrast, the k-Nearest Neighbor classifier does not assume any specific structure and classifies each pixel according to a majority of label votes within the k-closest examples of the training set.

Many other non-linear statistical methods can be borrowed from the machine learning literature to translate classification of image pixels into an inference problem. Analysis of the underlying structure of a training dataset can be performed with Kernel Density Estimation (KDE), Artificial Neural Networks, Support Vector Machines [178], as well as boosting techniques such as AdaBoost [70] or Probabilistic Boosting Tree [173].

2.1.3 Clustering

Clustering can be thought of as the *unsupervised* counterpart of classifiers, with the aim to uncover natural classes, called *clusters*, from the available image directly, without using any prior learning from a training set. In most clustering algorithms, the learning phase is replaced by an iterative process that alternates between an assignment stage, in which each and every sample is associated with a given class, and a characterization stage in which the descriptive properties of each class are estimated.

The simplest clustering algorithm is the K-Means that characterizes a given class by an average of the feature values over all its samples and assigns each sample to the class with the closest centroid. When the number of classes is not known in advance, ISODATA (Iterative Self-Organizing Data Analysis Techniques) is a possible alternative to extend standard K-Means by including splitting and merging criteria at each iteration. The Fuzzy C-means algorithm [61] is a generalized and relaxed version that allows the membership to each class and the average operations to be fuzzy. The Fuzzy C-means provides soft segmentations and usually produces better results on low-resolution medical images in the case of partial volume effects, since each voxel measurement might originate from more than one tissue.

The Expectation-Maximization (EM) algorithm applies the same principles in a Bayesian framework with the underlying assumption that the data follows a Gaussian mixture model. It iterates between the computation of the posterior probability that each sample belongs to a given class and the maximum likelihood estimation of all statistical parameters for each class, typically the mean, the covariance and the mixing weights of the mixture model. The EM algorithm is theoretically superior to the standard k-means in the sense that it is capable of recovering clusters of arbitrary ellipsoidal shapes in the feature space, at the price of an increased sensitivity to initial cluster guesses.

All above-mentioned clustering methods rely implicitly or explicitly on a parametric form of the probability distribution of feature samples, such as the Gaussian Mixture Model (GMM) in the EM algorithm. A more general-purpose non-parametric procedure is the Mean-Shift [47] that has become popular for image segmentation for its ability to recover an unknown number of arbitrary-shaped clusters. The key idea is to jointly perform classification and estimate the salient *modes* of the probability density function. This algorithm relies on the estimation of the gradient of the density to iteratively move each cluster centroid towards the closest prominent mode, in a hill-climbing fashion.

2.2 Regions as Connected Sets

Contrary to the aforementioned approaches that perform pixel grouping in the feature space only, methods that consider regions as spatially-connected sets make use of contextual information as an essential key to achieve a proper segmentation of the image. We review in this section a non-exhaustive list of discrete techniques such as region growing, Markov random fields and graph-partitioning.

2.2.1 Region Growing

Region growing [2, 28] is a popular technique for isolating a region of the image that is connected to a given pixel, called the *seed point*, based on some predefined homogeneity criterion. These criteria are mostly based on intensity or texture properties but can also incorporate information from the edges in the image. Region growing is sensitive to noise, heavily depends on the initial seed placement and is prone to leakages in places where the boundaries between the objects are weak or blurry. Moreover, constraints on spatial connectivity and boundary smoothness cannot be easily enforced; as a result, the segmentation may include holes and highly irregular boundaries. Often combined with other pre- and post-processing operations such as feature extraction or morphological cleaning, Region Growing algorithms are primarily adapted for isolating small-sized, simple-shaped, homogeneous anatomical structures and can easily be applied in 3D. Split-and-merge algorithms are interesting variants of Region Growing that extract multiple regions at once without the need for seed points [117, 139], using a recursive splitting and merging strategy according to both homogeneity and inhomogeneity criteria.

2.2.2 Markov Random Fields

The theory of Random Fields is an highly versatile paradigm to model spatial relationships between random variables that lie on a lattice structure such as the discrete grid of an image. Local interactions are described through a probabilistic setting in which random variable realizations at adjacent sites have a higher probability to be the same than if the sites are further apart. Several kinds of random fields exist, among which the Markov random field (MRF), Gibbs random field (GRF), conditional random field (CRF) and Gaussian random field.

Originally developed in the context of statistical mechanics [74], Markov Random Fields have been used for a wide spectrum of image processing problems including segmentation, restoration, texture synthesis, surface reconstruction and motion estimation [109]. For segmentation applications, the random variables are typically composed of an *observable* intensity value and an unknown, *hidden* label assignment. The Markovian property implies that the probability distribution of a variable at a given site is conditioned by (and only by) the configuration of a predefined set of surrounding neighborhoods, called *cliques*. Prior conditional probabilities can be set in order to enforce contextual coherence and smoothness constraints by associating costs for various configurations of adjacent labels, referred to as

clique potentials. Maximum A Posteriori (MAP) inference can eventually provide unknown labels, given the observed image and the local interaction penalties. In the general case, this Bayesian formulation, called MAP-MRF labeling, is computationally intractable and leads either to sub-optimal solutions or to slow algorithms such as simulated annealing. However, if certain conditions are fulfilled, for instance for binary labels or sub-modular (e.g. additive) adjacency costs, the MAP estimation process can be cast as a minimization problem that can be efficiently solved with *Graph Cuts* [99] or with Belief Propagation [64]. This intricate link between Markov Random Fields and the combinatorial methods involved in Graph Theory has renewed the interest of the image processing community regarding MRFs in the last ten years, in particular for image segmentation [17, 23, 25].

2.2.3 Graph-Partitioning

Graph-based segmentation techniques are built on the representation of the image in terms of a undirected, weighted graph containing a set of vertices V and a set of edges E ,

$$G = (V, E). \quad (2.1)$$

Each node $v_i \in V$ corresponds to a pixel in the image and each edge $e_i = \{v_j, v_k\} \in E$ connects pairs of neighboring pixels, with a non-negative weight that is typically some measure of the dissimilarity between the two pixels connected by that edge. It is possible to transform and simplify such a graph into a tree, not necessarily unique, called a Minimum Spanning Tree (MST), which is a minimum-weight, cycle-free (i.e. tree) subset of the graph's edges such that all nodes are connected. The early works in graph-theoretic approaches to segmentation and clustering [174, 187] used fixed or adaptive thresholds to *cut* some edges with the largest weights in the MST, in order to split the graph into pieces, each subgraph corresponding to a different cluster/region.

A cut is a partition of the graph into two disjoint sets of vertices, or equivalently, the set of edges whose removal induces the splitting. Finding closed contours composed of strong edges as optimal cuts is the principle of several segmentation algorithms that mainly differ in the definition of the optimized quality measure. Since standard minimal cuts, minimizing the sum of the edge weights, tend to create small, isolated regions [181], several variants have been proposed to alleviate this bias and obtain more balanced partitions, such as the Normalized Cuts [158] or Isoperimetric Partitioning [77].

Graph-Cuts correspond to a specific sub-field of graph-partitioning algorithms in which the optimization is made efficient by the min-cut/max-flow equivalence [66]. The idea is to interpret the graph as a network in which the edge weights are capacities, and maximize the flow between two specific nodes called *source* and *sink*. For the segmentation of an image in two regions, source and sink are usually additional nodes associated to the foreground and background labels, respectively. Both region nodes are connected to each pixel with an additional edge whose weight reflects the pixel's affinity with the label, given its intensity value. This approach has been successfully applied to interactive segmentation in [25, 148]. User-marked seeds provide an estimate of foreground/background intensity distributions

and are linked to either the source or the sink with infinite *unbreakable* weights, which guarantees their inclusion in the corresponding region once the optimal cut of the augmented graph is found. In 2D, instant feedback in interactive applications has been achieved by using dynamic versions [23]. The principle is to re-run the optimization algorithm much faster after slight modifications of the graph, when new seeds have been added by the user.

The usefulness of Graph-Cuts for image processing goes beyond the field of interactive segmentation, as a generic computational framework for globally optimizing energy functionals in a discrete setting [99], or to use the underlying discrete topology to approximate any continuous Riemannian metric space [24]. Recent works towards unified algorithms investigate their connection with other segmentation techniques, such as the Random Walkers [76, 159] and Watersheds [49].

Although now a well-recognized framework for interactive segmentation of 2D images, Graph-Partitioning techniques are still not so pervasive for segmenting volumetric data, in particular because of their inherent difficulty to handle very large datasets for which the graph can grow in a memory-prohibitive fashion. A solution would be to either reduce the discrete first-order neighborhood from the standard 26-connectivity to the simplest 6-connectivity (ignoring all diagonal interactions), or to work at a lower resolution. In both cases, this would reveal one of the main drawbacks of graph-based algorithms, the appearance of blockiness artifacts on the resulting cut surface, known as metrication errors. These artifacts are more severe in 3D than in 2D and are clearly visible when weak boundaries are present. The surface has a directional bias to be perfectly straight and aligned with one of the lattice axes. This is for instance discussed and illustrated in [8], where a continuous formulation of the maximum flow problem is studied to overcome metrication artifacts, at the cost of an increased computational complexity that is incompatible with 3D interactive applications.

2.3 Deformable Models

Deformable models are one of the most vigorously researched and published technique in the field of computer-assisted medical image analysis. They have been widely recognized as a major breakthrough for their ability to not only segment, but also match and track anatomical structures over time. The main strength of deformable models is their ability to exploit both the image data itself and some strong a priori knowledge about the characteristics of the shape of the target structure, which goes beyond the simple assumptions that objects correspond to regions that are connected homogeneous sets.

There are a number of literature reviews on deformable models, and we refer in particular to the work of McInerney and Terzopoulos [119] for their early use in medical applications and to the survey by Montagnat et al. [122] for the mathematical foundations of discrete and continuous deformable surfaces in 3D. The book *Active Vision*, by Blake and Yuille [18], also provides extensive background information on these techniques. Ever since, researchers have continued to explore potential improvements towards better shape representations with the rapid expansion of implicit representations and *level-sets*, towards better robustness with

advanced statistical analysis of shapes and image features, towards more efficient numerical algorithms. In this section, we will briefly draw a non-exhaustive list of influential works in those directions by reviewing some related segmentation models that are not restricted to medical imaging.

2.3.1 Parametric Active Contours

The popularity of deformable models is largely due to the seminal paper *Snakes: Active Contours* by Kass et al. [92], originally proposed as a dynamic evolution of a curve towards strong edges of the image and soon extended to the case of 3D surfaces by Terzopoulos et al. [167]. Such active contours are examples of the general technique of matching deformable models to image data by means of energy minimization, which was also suggested by Blake and Zisserman in [19].

In [92], the evolution equation for the parameterized planar curve $\mathcal{C} : [0, 1] \rightarrow \mathbb{R}^2$ is driven by the minimization of the following, physically-motivated, energy functional¹:

$$F_{[92]}(\mathcal{C}) = \alpha \int_0^1 \left\| \frac{\partial \mathcal{C}}{\partial p} \right\|^2 dp + \beta \int_0^1 \left\| \frac{\partial^2 \mathcal{C}}{\partial p^2} \right\|^2 dp + \int_0^1 P(\mathcal{C}(p)) dp \quad (2.2)$$

in which α, β are positive weights balancing the model terms to obtain the desired behavior. The first term is an elastic membrane energy that constraints the stretching, the second term is a thin-plate energy that limits the bending. Those two terms are generally referred to as an *internal* energy since they relate to the intrinsic physical properties of the curve, modeled as a string. The last term is a line integral along the curve of an *external* potential, designed to attract the curve in the lowest values of the field P . In practice, the scalar field $P : \mathbb{R}^2 \rightarrow \mathbb{R}$ is derived from the image and should take smaller values in places where the object boundaries are more likely. For instance one can choose a decreasing function of the image gradient, such as:

$$P = -\lambda \|\nabla I_\sigma\|^2 \quad (2.3)$$

where λ is a normalizing positive constant and I_σ is the image smoothed with a Gaussian kernel of scale σ . Calculus of variations on the curve \mathcal{C} yields the Euler-Lagrange equation, the necessary condition that the curve \mathcal{C} must satisfy to be a local minimizer of the functional $F_{[92]}$,

$$\alpha \frac{\partial^2 \mathcal{C}}{\partial p^2} - \beta \frac{\partial^4 \mathcal{C}}{\partial p^4} - \nabla P(\mathcal{C}) = 0 \quad (2.4)$$

To find a solution of the above equation, an artificial variable t is usually introduced. Starting from an initial curve \mathcal{C}_0 at $t = 0$, the evolution equation

$$\frac{\partial \mathcal{C}}{\partial t} = \alpha \frac{\partial^2 \mathcal{C}}{\partial p^2} - \beta \frac{\partial^4 \mathcal{C}}{\partial p^4} - \nabla P(\mathcal{C}) \quad (2.5)$$

¹In this manuscript, we use the following convention to avoid multiple use of the letter F for various functional definitions: $F_{[X]}$ corresponds to the functional defined in the reference paper [X]

is followed until a steady state is reached, the left-hand side of (2.5) vanishes, hence a local minimizer of (2.2) is found. It is essentially a gradient-descent algorithm. In [92], a numerical scheme based on finite differences is used to discretize the fourth-order equation (2.5).

The Active Contours can be extended to 3D for segmenting volumetric data in the field of medical imaging [119]. For instance, Cohen et al. in [43] proposed a finite element scheme for the evolution equation of a parameterized surface. Bardinet et al. [12, 13] have used superquadrics with global shape parameters and local deformations. Delingette [56] advocated the use of discrete simplex meshes whose geometry is particularly adapted to the implementation of smoothness constraints in 3D. As we will see in section 2.3.2, the level-set framework proposed by Osher and Sethian [133] defines implicit representations that readily extend all principles to 3D and beyond.

Although the key idea of moving an energy-minimizing curve/surface towards image features had a remarkable influence on the design of new segmentation algorithms in the last two decades, the original formulation is not without limitations. Two main practical shortcomings were soon recognized and addressed by several researchers: (a) the paramount influence of the initial conditions on the segmentation result and (b) the dependence on an arbitrary parameterization of the curve/surface.

Functional (2.2) is non-convex, due to the external potential and the irregular landscape created by the image gradients. As such, it possibly admits a huge number of local minima, and as many valid segmentation results. In this respect, the example potential (2.3) is particularly problematic, since it is only effective in the immediate vicinity of the step edges, with a capture range of the order of the smoothing scale σ . Consequently, a curve initialized far from the desired result would inevitably be attracted by other salient features, or get stuck in flat areas. Increasing the capture range using a larger scale σ would not be acceptable since this would significantly dislocate the edges.

This motivated the use of an external *ballon* force, proposed by Cohen et al. in [46], designed to systematically push/shrink the curve in the absence of features. This is obtained by adding in the evolution equation a constant term along the normal direction, or equivalently by adding in the energy a maximizing/minimizing term proportional to the area enclosed by the curve. However, this requires to initialize the process with a curve lying completely inside/outside the target object, and may introduce a bias in the final boundary location.

An alternative solution to increase the capture range is to compute a linear *diffusion* of the gradients of an edge map, in order to spread the forces in the flat areas. This new force field, called Gradient Vector Flow and proposed by Xu and Prince in [183], cannot be written as a negative gradient of a potential function, hence the evolution equation is formulated directly from a force balance condition rather than a variational formulation.

Reducing the sensitivity to initial conditions can also be obtained by replacing the gradient-descent algorithm by a global optimization strategy such as Dynamic Programming, which was proposed by Amini et al. in [6] for 2D spline curves, with no straightforward extension to 3D.

One of the most effective way of reducing the limited capture range of active contours is to add region-based forces which rely on a *global* quality measure of the produced segmentation, contrary to *local* features derived from image gradients [147, 189]. These region-based strategies are at the core of our work and are reviewed in more details in section 2.4.

Ever since, the search for global minimizers in variational formulations of deformable models has continued in the image segmentation community. In chapter 3, we will review in more details some recent developments in this area, in particular the works of Nikolova et al. [130] and Bresson et al. [26] on convex relaxation techniques that have influenced the convex formulation of region-based segmentation with a membership function that we present in section 3.3.2.

2.3.2 Geometric Active Contours

In addition to a potentially large number of local minimizers, the original variational formulation of snakes and their early variants are often criticized for their dependence on an arbitrary parameterization of the curve, e.g. $p \in [0, 1]$ in (2.2). This is the main motivation behind *geometric* active contours that are based on mathematical foundations of curve evolution theory.

Geometric Curve Evolution

According to differential geometry, intrinsic properties of a curve (e.g. length, normal, curvature) are invariant under reparameterization, which means that they do not depend on the speed at which the curve is traversed. Hence, it is natural to require energy functionals for image segmentation to be also independent on the curve parameterization. Let $\mathcal{C}(p, t) : [0, 1] \times \mathbb{R}^+$ denote a family of planar closed curves where p is a given parameterization and t a time variable. Geometric evolution equations of \mathcal{C} are of the form

$$\frac{\partial \mathcal{C}}{\partial t} = \mathcal{F}(\mathcal{C})\mathcal{N} \quad (2.6)$$

where \mathcal{N} the inward unit normal to the curve and the speed function $\mathcal{F}(\mathcal{C})$ depends only on differential invariants of \mathcal{C} such as its curvature or torsion. Note that the general form of geometric evolution equations has only a normal component since a tangential component would only affect the *parameterization* of the curve, not its *geometry*. In the field of computer vision, one of the most thoroughly studied type of geometric evolution is the *Euclidean curve shortening flow*, also called the *geometric heat equation*:

$$\frac{\partial \mathcal{C}}{\partial t} = \kappa \mathcal{N} \quad (2.7)$$

where κ is the curvature. This equation is the evolution of \mathcal{C} that yields the fastest decrease of the Euclidean length of the curve, since (2.7) is the gradient flow of the length functional $L(\mathcal{C})$:

$$L(\mathcal{C}) = \int_0^1 \left\| \frac{\partial \mathcal{C}}{\partial p} \right\| dp \quad (2.8)$$

The geometric heat equation also has a smoothing behaviour on the initial closed curve. It gradually removes small-scale features, without developing any singularity or new extrema, and eventually shrinks to a point [72], as illustrated in Fig. 2.1. Considering t as a scale variable, this creates a scale-space representation for planar curves similarly to linear scale-spaces defined for images based on the heat equation [110]. This evolution flow for 2D curves has an equivalent for hyper-surfaces, with slightly different properties, called the *mean curvature flow*, where κ in (2.7) becomes the mean curvature of the surface.

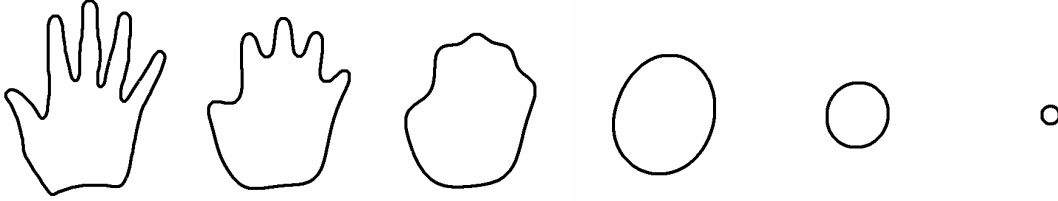


Figure 2.1 — Geometric Heat Equation in 2D: Following (2.7) has a smoothing effect on the curve that eventually shrinks to a point.

Geodesic Active Contours

The smoothing property obtained by minimizing the Euclidean length already suggests to replace the two regularization terms in the original active contours model (2.2) by the length functional to avoid the fourth-order term in (2.5). Kichenassamy et al. [93, 94], Caselles et al. [34] and Shah et al. [157] independently proposed a new variational model that goes one step further and simplifies (2.2) to a single term that encompasses both the internal regularization of the curve and the external image features. The idea is to minimize the following modified length:

$$L_g(C) = \int_0^1 g(C) \left\| \frac{\partial C}{\partial p} \right\| dp \quad (2.9)$$

where $g : \mathbb{R}^2 \rightarrow \mathbb{R}$ is typically a positive decreasing function of the image gradient or any other detector required to be small where object boundaries are expected. Functional L_g generalizes the Euclidean definition of length to a *weighted* length that takes into account image characteristics. This turns boundary extraction into the problem of finding a geodesic curve (a path with minimal length) in a Riemannian space. Taking the first variation of L_g , it can be shown that a geodesic curve is obtained by the following geometric flow:

$$\frac{\partial C}{\partial t} = g\kappa\mathcal{N} - \langle \nabla g, \mathcal{N} \rangle \mathcal{N} \quad (2.10)$$

(2.10) is the curve evolution equation referred to as Geometric/Geodesic Active Contours ([94]/[34]). The first term regularizes (and shrinks) the curve by curvature flow with an increased effect away from salient features, while the second term attracts the curve towards the bottom of a potential well created by the function g . A typical choice for g is the

following gradient-based potential:

$$g = \frac{1}{1 + \|\nabla I_\sigma\|^2} \quad (2.11)$$

In the specific case of open curves with fixed end-points, the Fast Marching algorithm [133] enables to find a global minimum of L_g in (2.9), as shown by Cohen and Kimmel in [45]. In an earlier work, Fua and Leclerc have studied the minimization of a normalized version L_g/L for open curves with free end-points [71] for the purpose of edge detection.

Level-Set Representation

Since their introduction in computational fluid dynamics by Osher and Sethian [133] and in the image processing community by Casseles et al. [33] and Malladi et al. [113], the *level-set* framework is the reference numerical implementation of geometric flows for closed curves and surfaces such as (2.6). In a general setting, let $\Gamma(t) : \mathbb{R}^+ \rightarrow \mathbb{R}^n$ be a smooth family of $n - 1$ dimensional closed hyper-surfaces evolving in the direction of their normal \mathcal{N} with the image-dependent speed function F , such that

$$\frac{\partial \Gamma}{\partial t} = \mathcal{F} \mathcal{N} \quad (2.12)$$

The level-set methodology is a numerical implementation of the above equation that relies on the definition of an auxiliary real-valued embedding function $\Phi(\mathbf{x}, t) : \mathbb{R}^n \times \mathbb{R}^+ \rightarrow \mathbb{R}$, required to be Lipschitz-continuous. The implicit representation Φ is constructed so that Γ corresponds to the zero-crossings of Φ at all times:

$$\forall t, \quad \Gamma(t) = \{\mathbf{x} \in \mathbb{R}^n, \Phi(\mathbf{x}, t) = 0\} \quad (2.13)$$

or, equivalently:

$$\forall t, \quad \Phi(\Gamma(t), t) = 0 \quad (2.14)$$

To satisfy the above equation for $t = 0$, let the initial $\Phi(\mathbf{x}, 0)$ be a function that takes negative values inside the region enclosed by the closed surface $\Gamma(0)$ and positive values outside. Then, the inward unit-normal of Γ (and of every other level-set) is given by

$$\mathcal{N} = -\frac{\nabla \Phi}{\|\nabla \Phi\|} \quad (2.15)$$

.

Differentiating (2.14) with respect to t yields the evolution equation for Φ such that its 0-level coincides at all times with the geometric flow (2.12):

$$\frac{\partial \Phi}{\partial t} = \mathcal{F} \|\nabla \Phi\| \quad (2.16)$$

Unlike *Lagrangian* approaches for evolution equations of parameterized curves and surfaces, level-set formulations are purely geometric, valid in any dimension, and readily handle changes of topology such as splitting and merging of the interface. This last property can

be very valuable for segmentation applications in medical imaging in order to capture objects of complex topology such as 3D vascular structures. This *Eulerian* specification of the flow field also yields easier numerical implementations on a fixed Cartesian grid and avoids polygonal meshes issues like self-intersections and degeneracy of the polygons. Differential quantities of the propagating front can also be directly obtained from the embedding function. In particular, the mean curvature κ is given by:

$$\kappa = \nabla \cdot \left(\frac{\nabla \Phi}{\|\nabla \Phi\|} \right) \quad (2.17)$$

Thus, the level-set version of the curvature flow (2.7), illustrated in Fig. 2.2 is:

$$\frac{\partial \Phi}{\partial t} = \|\nabla \Phi\| \nabla \cdot \left(\frac{\nabla \Phi}{\|\nabla \Phi\|} \right) \quad (2.18)$$

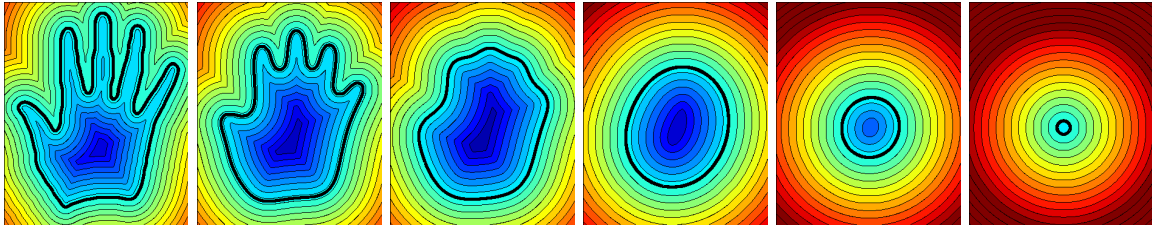


Figure 2.2 — Geometric Heat Equation in 2D, with an implicit representation of the contour. Level-Set implementation using (2.18) with periodic re-distancing.

Similarly, the Geometric Active Contours model described by (2.10) can be realized by the following level-set version to handle changes of topology, as illustrated in Fig. 2.3:

$$\frac{\partial \Phi}{\partial t} = g \nabla \cdot \left(\frac{\nabla \Phi}{\|\nabla \Phi\|} \right) \|\nabla \Phi\| + \langle \nabla g, \nabla \Phi \rangle \quad (2.19)$$

In the examples shown in Fig. 2.2 and Fig. 2.3, the initial embedding function $\Phi(\mathbf{x}, 0)$ is the signed distance function to $\Gamma(0)$, an obvious candidate chosen in most applications of level-set techniques since this function is easy to compute and smooth in the vicinity of the curve. To avoid numerical stability issues due the tendency of the level-sets of Φ to get close to each other near the object boundaries, causing $\|\nabla \Phi\|$ to become increasingly large, the standard trick of re-initializing of the function Φ to the signed distance function of its 0-level is performed periodically.

We have briefly exposed the principles and theoretical advantages of level-set techniques to model the evolution of curves or higher-dimensional manifolds towards image features. This constitutes the beginnings of the popularity of implicit representations in image segmentation. In this respect, this is related to our work on implicit surfaces. Among all aforementioned advantages, the ease of description and manipulation of surfaces in 3D is probably the most prominent to handle volumetric data in medical imaging. However, level-set implementations, as they were first exposed, suffer from a relatively high computational complexity, hence are unable to cope with requirements of 3D interactive applications.

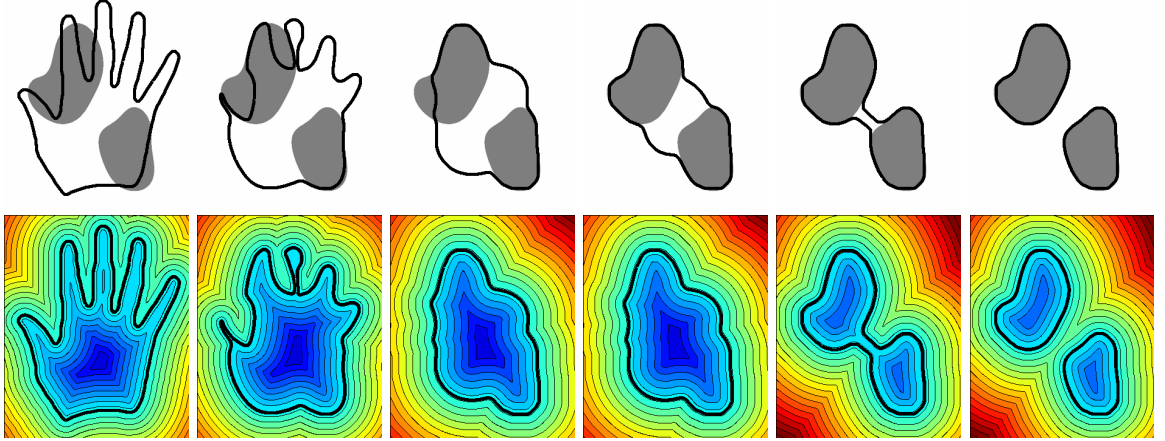


Figure 2.3 — Geometric/Geodesic active contours in 2D with a level-set representation and periodic re-distancing. First row: geometric flow of Eq. (2.10) where g is given by (2.11) and I is the background image composed of two binary objects. Second row: the curve \mathcal{C} is embedded in a level-set representation Φ , resulting in the flow (2.19). Observe that the initial curve \mathcal{C}_0 (left) is able to split to capture two separate objects (right)

There exists an extensive literature on improving the efficiency of numerical solvers for the underlying partial differential equations, such as the Additive Operator Splitting scheme described by Goldenberg et al. in [75] and references therein. Other improvements consist in reducing the number of nodes of the Cartesian grid on which computations are performed, taking advantage of the fact that only the neighborhood of the evolving interface matters. This is the rationale behind the narrow-band method of Adalsteinsson and Sethian [1], the hierarchical octree representation proposed by Strain et al. [163] as well as the use of coarser grid decompositions with B-Splines [14, 15] or Radial Basis Functions [73]. Nonetheless, level-set implementations of geometric flows still remain intrinsically slow due to the way the smoothness of the solution is enforced. They require solving nonlinear parabolic partial differential equations on a possibly large time domain, from the initial position until the actual object boundary is reached. The parabolic nature is due to the mean curvature term and imposes a stringent restriction on the time step to ensure stability. Using curvature to control the regularity of the solution is theoretically sound for many applications in computational physics. For segmentation applications in medical imaging, regularity is needed to cope with noisy acquisitions and to model the smooth nature of anatomical structures boundaries. In this case, the use of curvature terms is certainly not the only possible choice and is questionable from a practical perspective. As we will see, all the algorithms that we have developed in this work are also iterative schemes derived from variational formulations using implicit representations in 3D, but none relies on the computation of the surface curvature.

Another intrinsic limitation to all previously-described deformable models is their *edge-based* strategy, since they aim at finding an optimal curve or surface that best fits local features such as image gradients. Unfortunately, good performance is only achieved when

they are properly initialized and the target structure is well-contrasted everywhere . In the following section, we will review variational formulations derived from global quality measures, usually justified from a probabilistic perspective, which leads to *region-based* rather than edge-based cost functionals. Nonetheless, local edge information can also be included. Hence, the resulting formulations are more general, while keeping the same local fitting accuracy. Although gradient-descent optimization schemes are still employed, the respective functionals have less local minima so that segmentation results tend to be more robust to imaging noise and initial conditions. This key advantage is the main practical motivation for the general framework that will be followed throughout this manuscript and presented in details in Chapter 3.

2.4 Region-Based Variational Approaches

Region-based deformable models constitute a slight change of perspective compared to previous edge-based formulations. Rather than considering the evolving curve/surface *in itself*, it is comprehended as the *boundary* of a region, the set of pixels that it encloses. The goal is to take into account in the evolution equation global information on the image features that lie inside and outside this region. Obviously, this perspective is only meaningful for closed surfaces.

2.4.1 Optimal Piecewise-Smooth Approximation

Noteworthy, the pioneering works in this direction are not in the area of deformable models. In a spatially-discrete setting, Region Growing [2, 28], Split-And-Merge [139] and Markov Random Fields are the first region-based approaches. In a spatially-continuous setting, seminal works include the Minimum Description Length (MDL) proposed by Leclerc [103] and the Graduated-Non-Convexity optimization of the weak membrane model, by Blake and Zisserman [19]. The Mumford-Shah piecewise-smooth image approximation model [126] has a major influence in most subsequent segmentation algorithms that rely on region-wise features. This inverse problem, originally developed for the purpose of restoration, involves the recovery of a noise-free, piecewise-smooth image f from a degraded version, the measured image I , with the following functional:

$$F_{[126]}(f, \Gamma) = \mu L(\Gamma) + \lambda \int_{\Omega} (I - f)^2 + \nu \int_{\Omega - \Gamma} \|\nabla f\|^2 \quad (2.20)$$

where Γ is the set of discontinuities of f and $L(\Gamma)$ is the length of this set, chosen as a geometric constraint. The second term is a quadratic elastic energy that tightly links f to the original image I and the third term enforces the smoothness of f almost everywhere except at the discontinuities that shall be preserved. Even though the study of the general Mumford-Shah variational problem is particularly involved and still an active research topic, minimization algorithms exist (see for instance [3, 123, 143] and references therein). However, they are both non-trivial and of little practical use for segmentation applications in medical imaging, in particular because the set of discontinuities Γ is not in general a set

of closed curves. Nevertheless, several simplifications and approximations can be studied. For instance, in the limiting case $\nu \rightarrow \infty$, $\|\nabla f\|$ has to vanish, leaving only constant values for the function f , which yields the following simplified functional, often referred to as the piecewise-constant *cartoon* limit

$$\hat{F}_{[126]}(\{c_i\}, \Gamma) = \mu L(\Gamma) + \lambda \sum_i \int_{\Omega_i} (I - c_i)^2 \quad (2.21)$$

where Γ is now the set of curves delineating the boundaries of closed and disjoint regions $\Omega_i \subset \Omega$ and the c_i 's are the constant values of f in each Ω_i . The values c_i can be easily shown to correspond to the average intensity of I in each region. Numerous efforts have been directed towards turning this simplified functional, also studied by Blake and Zisserman [19], into a variational model for segmentation in both the discrete [23] and continuous [39] settings. Besides its influence for many algorithms, the cartoon model, also referred to as the *minimal partition problem*, remains of limited application scope since images that can be accurately described by constant values in each region are extremely rare in practice.

2.4.2 Region Competition

Although region-based criteria already appear in the works by Cohen et al. [44], Ronfard [147] and Chakraborty et al. [35] for image segmentation in two regions with curve evolution schemes, a remarkable unification effort is proposed by Zhu and Yuille in the description of their *Region Competition* algorithm [189]. They identified many relations between the variational models derived from the Mumford-Shah approximation, the Minimum Description Length principles [103] and the heuristic procedures behind algorithms such as Region Growing. Inspired by Maximum a Posteriori approaches from Markov Random Fields [74], they proposed to extend the cartoon limit (2.21) by replacing the constant values in each region by a more general parametric form of intensity distributions, in a Bayesian framework. Assuming the image intensities are independent and identically distributed (i.i.d.) in each region i , let $P(I(\mathbf{x})|\boldsymbol{\alpha}_i)$ be the posterior probability that point \mathbf{x} belongs to region i given its intensity $I(\mathbf{x})$ and the parameters of the distribution described by the vector $\boldsymbol{\alpha}_i$. The authors in [189] propose the following variational formulation for segmentation into an unknown number of disjoint regions:

$$F_{[189]}(\{\Omega_i\}, \{\boldsymbol{\alpha}_i\}) = \sum_i \left(\lambda + \frac{\mu}{2} \int_{\partial\Omega_i} ds - \int_{\Omega_i} \log P(I(\mathbf{x})|\boldsymbol{\alpha}_i) d\mathbf{x} \right) \quad (2.22)$$

where $\mu > 0$ balances the geometric smoothness prior which corresponds to the length of the boundary curves and $\lambda > 0$ is a code length to describe a region Ω_i that only serves as MDL criterion for the merging stage of the algorithm. In the case of a fixed number of regions, λ can be set to 0. If P is chosen to be a Gaussian probability distribution of known variance, $F_{[189]}$ eventually reduces to the cartoon limit (2.21). In this simplified case, the unknown parameters $\boldsymbol{\alpha}_i$ correspond to the average values c_i in each region in (2.21).

The optimization can be done by following an alternate scheme for the unknown variables Ω_i and α_i . In a first stage, regions Ω_i are fixed, optimal parameters α_i in each region are estimated by Maximum a Posteriori. This is particularly easy in the Gaussian case but the principle applies to any other parametric probability distribution. In a second stage, parameters α_i are fixed and boundaries move according to gradient-descent equations obtained from functional derivatives of $F_{[189]}$. After transformation of the region integrals in (2.22) into boundary integrals using Green-Riemann theorem and calculation of the corresponding Euler-Lagrange equations, the authors show in [189] that any point \mathbf{y} lying on one of the region boundaries $\partial\Omega_i$ should move according to:

$$\frac{d\mathbf{y}}{dt} = \sum_{k \in Q(\mathbf{y})} \left\{ -\frac{\mu}{2} \kappa_k \mathbf{n}_k + \log P(I(\mathbf{y}) | \alpha_k) \mathbf{n}_k \right\} \quad (2.23)$$

$Q(\mathbf{y})$ corresponds to the set of k such that \mathbf{y} lies on $\partial\Omega_k$, to account for multiple junction points, and \mathbf{n}_k and κ_k are respectively the outward unit normal and the curvature of $\partial\Omega_k$ at point \mathbf{y} . Considering a point \mathbf{y} that belongs to exactly two boundary curves, for instance at the interface between region 1 and region 2, since the normals and curvature are the same with opposite signs, $\kappa_1 \mathbf{n}_1 = \kappa_2 \mathbf{n}_2$ and (2.23) simplifies to:

$$\frac{d\mathbf{y}}{dt} = -\mu \kappa_1 \mathbf{n}_1 + \log \frac{P(I(\mathbf{y}) | \alpha_1)}{P(I(\mathbf{y}) | \alpha_2)} \mathbf{n}_1 \quad (2.24)$$

The first smoothing term corresponds exactly to the Euclidean curve shortening flow¹ (2.7) while the second one determines the motion of \mathbf{y} according a likelihood ratio test: if $I(\mathbf{y})$ fits better to the distribution of Ω_1 than to that of Ω_2 , $P(I(\mathbf{y}) | \alpha_1) > P(I(\mathbf{y}) | \alpha_2)$ and the curve will move so that Ω_1 embraces \mathbf{y} . This algorithm is called *Region Competition* since the intuition behind (2.24) is that adjacent regions *compete* for ownership of pixels along their boundaries [189].

This Region Competition algorithm, in particular the probabilistic formulation of region-wise terms and their inclusion in boundary evolution schemes, has inspired many authors and paved the way for a vast number of subsequent algorithmic improvements and generalizations [31, 39, 59, 83–85, 89, 134, 135, 137, 153], including the ones presented in this manuscript. In [52], Cremers et al. give a broad overview of statistical approaches in level-set segmentation that include color, motion and shape as additional features to simple pixel intensity.

Zhu and Yuille use a Lagrangian numerical implementation (2.24), despite the advantages of Eulerian versions with the level-set technique already discussed in section 2.3.2. Moreover, they mention the possible inclusion of additional edge-based terms, without further details. Jehan-Besson et al propose in [89] an alternative Eulerian minimization scheme using mathematical tools from shape optimization of Delfour and Zolesio [54, 55]. In the *Geodesic Active Regions* [137], Paragios and Deriche propose to substitute the length constraint with the geodesic length L_g (2.9) to complement the region competition framework

¹the negative sign is the consequence of an opposite (here outward) convention for the unit normal

with both an edge-based term and a multi-phase level-set technique [153, 188]. The important conceptual difference with what follows is that the implicit representation is only used as a numerical implementation of a boundary evolution derived from a region-based functional.

In the following section, we describe an alternative approach, proposed by Chan and Vese [39], in which the implicit representation is directly expressed in the functional itself, as the optimization variable. We emphasize this difference since we adopt a similar perspective for designing the algorithms presented in chapter 4, 5 and 6.

2.4.3 Active Contours Without Edges

In [39], Chan and Vese propose a numerical algorithm to solve a simplified version of the minimal partition problem (2.21). They assume the image $I : \Omega \rightarrow \mathbb{R}$ is composed of only two regions that can be approximated by constant values c_1 and c_2 , without clearly-defined edges. Let $\Omega_1 \subset \Omega$ be the foreground region, $\Omega_2 = \Omega \setminus \Omega_1$ the background region, and $\text{Per}(\Omega_1)$ the perimeter of their common boundary. Then, the minimal partition problem can be re-written as the minimization of:

$$F_{[39]}(\Omega_1, c_1, c_2) = \mu \text{Per}(\Omega_1) + \lambda \int_{\Omega_1} (I(\mathbf{x}) - c_1)^2 d\mathbf{x} + \lambda \int_{\Omega \setminus \Omega_1} (I(\mathbf{x}) - c_2)^2 d\mathbf{x} \quad (2.25)$$

Their key idea is to use an implicit representation $\Phi : \Omega \rightarrow \mathbb{R}$, not as a mean to describe the evolving boundary as in previous level-set techniques, but as a representation of the foreground region Ω_1 . With the *Heaviside* step function $H : \mathbb{R} \rightarrow \{0, 1\}$ defined by

$$H(a) = \begin{cases} 1 & \text{if } a \geq 0 \\ 0 & \text{otherwise,} \end{cases} \quad (2.26)$$

the characteristic function of the foreground set Ω_1 is equal to $H(\Phi(\mathbf{x}))$. By means of the Dirac distribution $\delta(a) = H'(a)$, where the derivative is defined in the sense of distributions, the perimeter of the boundary of Ω_1 is given by [39]:

$$\text{Per}(\Omega_1) = \int_{\Omega} \|\nabla H(\Phi)\| = \int_{\Omega} \delta(\Phi) \|\nabla \Phi\| \quad (2.27)$$

Consequently, minimizing (2.25) is equivalent to minimizing:

$$F_{[39]}(\Phi, c_1, c_2) = \mu \int_{\Omega} \delta(\Phi) \|\nabla \Phi\| + \lambda \int_{\Omega} H(\Phi)(I - c_1)^2 + \lambda \int_{\Omega} H(-\Phi)(I - c_2)^2 \quad (2.28)$$

The new unknown variable is the function Φ , and the three integrals are now defined over the whole fixed domain Ω , which will eventually simplify the computation of the functional derivatives with respect to Φ . Since H is not differentiable in the usual sense, a smooth approximation H_ϵ is introduced in [39], and we will come back later to the important implications of this choice. Given this approximation, the gradient-descent equation for Φ , directly derived from the first variation of the functional (2.28), is:

$$\frac{\partial \Phi}{\partial t} = \delta_\epsilon(\Phi) \left[\mu \nabla \cdot \left(\frac{\nabla \Phi}{\|\nabla \Phi\|} \right) - \lambda (I - c_1)^2 + \lambda (I - c_2)^2 \right] \quad (2.29)$$

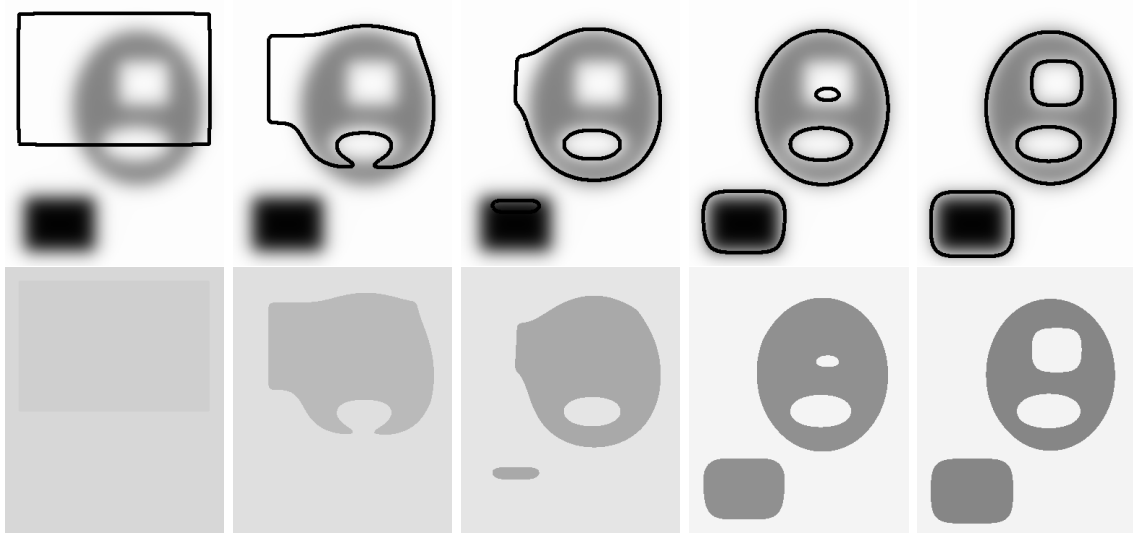


Figure 2.4 — Active Contours Without Edges - Experiment on a 2D image with blurry object boundaries, following evolution given by (2.29). First row: evolution of the contour $\{\Phi = 0\}$. Second row: evolution of the underlying optimal piecewise-constant approximation $\hat{I} = H(\Phi)c_1 + H(-\Phi)c_2$ where optimal c_1 and c_2 are given by (2.30). Observe that the contour automatically undergoes topology changes, not only by split/merge mechanisms, but also by *spontaneously* creating new regions or holes.

At regular time intervals, this evolution of Φ should be interlaced with an estimation of the other unknown variables, the scalar values c_1 and c_2 . They are obtained by setting the derivatives of $F_{[39]}$ with respect to c_1 and c_2 to 0, which yields:

$$c_1 = \frac{\int_{\Omega} H(\Phi)I}{\int_{\Omega} H(\Phi)} \quad \text{and} \quad c_2 = \frac{\int_{\Omega} H(-\Phi)I}{\int_{\Omega} H(-\Phi)} \quad (2.30)$$

In Fig. 2.4, the *Active Contours Without Edges* [39] algorithm is illustrated on an image composed of two synthetic objects with blurred edges. Observe that the contour automatically undergoes changes of topology, not only by splitting or merging, but also by *spontaneously* creating new regions and holes, which enables the detection of inner structures as well as objects that lie completely outside the initial contour. In theory, this should not be possible for boundary evolution algorithms, even with a level-set representation, since this behavior does not correspond to a continuous evolution of a curve. This is a side effect of the substitution of the smooth approximation H_{ϵ} for H that significantly alleviates the sensitivity of the method to initial conditions. As discussed in the original paper [39], this effect relates to the tendency to obtain a global minimizer, even though $F_{[39]}$ is non-convex. Indeed, the precise choice of the regularization H_{ϵ} of H is a crucial ingredient of the algorithm. While any approximation H_{ϵ} satisfying $\lim_{\epsilon \rightarrow +\infty} H_{\epsilon} = H$ would be a valid choice to compute the functional derivatives, Chan and Vese suggest the use of the following C^{∞}

non-compactly supported approximation (see Fig. 2.5):

$$H_\epsilon(a) = \frac{1}{2} \left(1 + \frac{2}{\pi} \arctan \left(\frac{a}{\epsilon} \right) \right) \quad \Rightarrow \quad \delta_\epsilon(a) = \frac{\epsilon}{2(\epsilon^2 + a^2)} \quad (2.31)$$

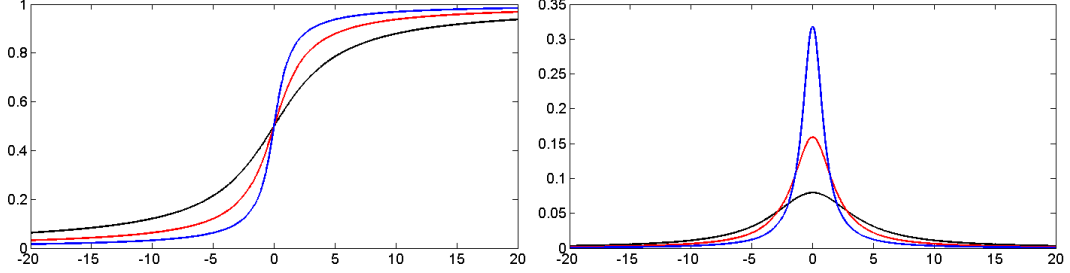


Figure 2.5 — Approximations H_ϵ and δ_ϵ , for various values of ϵ , using the non-compact smooth approximation (2.31), with $\epsilon = 4$ (black), $\epsilon = 2$ (red) and $\epsilon = 1$ (blue)

Since the approximation is non-compact, the data term is non-zero away from the current boundary, with a capture range that depends on the value of ϵ , as shown in Fig 2.5. Although large values of ϵ enable the creation of holes and new regions, it is not an intrinsic feature of the variational problem (2.28) itself, but rather a side consequence of the chosen approximation for H , which means that other choices would lead to different results. How this relates to the global minimization of the minimal partition problem is best explained in a later work by Nikolova et al. [130]. It is shown that $\delta_\epsilon(\Phi)$ can be removed from the gradient-descent evolution (2.29) without affecting the stationary solution, since $\forall a \in \mathbb{R}, \delta_\epsilon(a) > 0$, which yields:

$$\frac{\partial \Phi}{\partial t} = \mu \nabla \cdot \left(\frac{\nabla \Phi}{\|\nabla \Phi\|} \right) - \lambda r \quad \text{with} \quad r = (I - c_1)^2 - (I - c_2)^2 \quad (2.32)$$

In turn, (2.32) is the gradient-descent equation of the following functional [130]:

$$F_{[130]}(\Phi) = \mu \int_{\Omega} \|\nabla \Phi\| + \lambda \int_{\Omega} \Phi r \quad (2.33)$$

The key observation is that $F_{[130]}$ in (2.32) is *convex* with respect to Φ . Hence, the choice of a non-compact approximation H_ϵ is equivalent in practice to changing the original non-convex functional into a convex one, which explains the propensity of the algorithm for providing globally-minimizing solutions regardless of initial conditions. More details on the associated convex problem are discussed in Chapter 3. A convex formulation is developed that relates to $F_{[130]}$, with a new interpretation of Φ as a membership function. We will also discuss how convexity has both practical advantages and shortcomings. In particular, global minimizers tend to include many disconnected objects in the image, which is not always a desired feature.

Extension to Piecewise-Smooth Images

As already mentioned, the piecewise-constant hypothesis is too unrealistic for medical images and fails to provide accurate segmentations in most cases. A first possible generalization is that of Zhu and Yuille [189], substituting the single constant value in each region with a global probability distribution. This has the advantage of covering the non-Gaussian case, but does not handle the case of spatial variations of tissue properties within a single object. Even closer to reality is to assume that objects have *smoothly-varying* properties in space, with jumps across their boundaries, as in the *full* Mumford-Shah functional, with $\nu < +\infty$ in (2.20). Modeling these variations can be crucial for vessel segmentation in angiography, due to the non-constant concentration of contrast agent in blood after injection, as discussed in Chapter 4. The bias field corrupting Magnetic Resonance images is another example source of low-frequency spatial variations in intensity that need to be modeled.

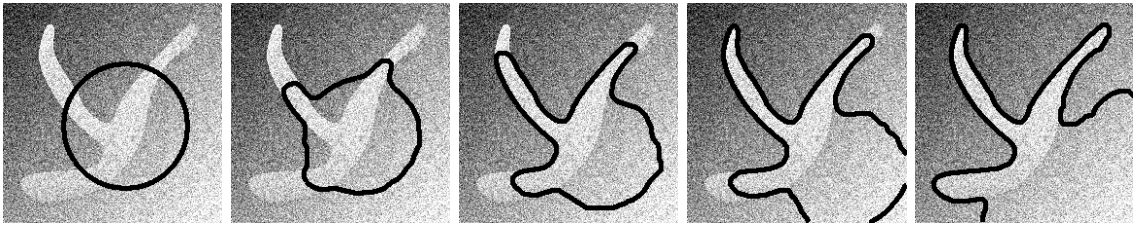


Figure 2.6 — Piecewise-constant model fails to capture spatial variations in intensity. Experiment on a synthetic image with linear ramp as background and a smoothly-varying foreground, following (2.29). The Evolution of $\{\Phi = 0\}$ in this case illustrates the need for modeling smoothly-varying intensities, as in Fig. 2.7

In order to generalize previous models to *piecewise-smooth* images, Vese and Chan [177] and Tsai et al. [172] propose two similar algorithms, with slightly different numerical schemes, in an attempt to solve the Mumford-Shah functional with curve evolution techniques and the level-set method. In [44], Cohen et al. already develop a related idea to extract a lake of approximately constant intensity from its surrounding landscape that shows spatially-varying intensity values. In the following, we focus on the formulation for two regions, although the case of multiple regions, with possible triple junctions, is also discussed in [177] and [172].

The extension to piecewise-smooth images involves the substitution of the constant values c_1 and c_2 with two unknown C^1 functions, namely $s_1 : \Omega_1 \rightarrow \mathbb{R}$ and $s_2 : \Omega_2 \rightarrow \mathbb{R}$, defined in each region Ω_1 and Ω_2 . With an implicit representation Φ , $\Omega_1 = \{\mathbf{x} \in \Omega, \Phi(\mathbf{x}) \geq 0\}$ and $\Omega_2 = \{\mathbf{x} \in \Omega, \Phi(\mathbf{x}) < 0\}$, so that the new functional reads [177]:

$$\begin{aligned}
 F_{[177]}(\Phi, s_1, s_2) = & \mu \int_{\Omega} \|\nabla H(\Phi)\| + \lambda \left(\int_{\Omega} H(\Phi)(I - s_1)^2 + \int_{\Omega} H(-\Phi)(I - s_2)^2 \right) \\
 & + \nu \left(\int_{\Omega} H(\Phi) \|\nabla s_1\|^2 + \int_{\Omega} H(-\Phi) \|\nabla s_2\|^2 \right)
 \end{aligned} \tag{2.34}$$

The regularity of the functions s_i is enforced by the last two terms, penalizing the square

norm of their gradient with a *scale* parameter $\nu > 0$. Following the same methodology as in the previous section with a smooth approximation H_ϵ , the first variation with respect to Φ yields the gradient-descent equation:

$$\frac{\partial \Phi}{\partial t} = \delta_\epsilon(\Phi) \left[\mu \nabla \cdot \left(\frac{\nabla \Phi}{\|\nabla \Phi\|} \right) + \lambda ((I - s_2)^2 - (I - s_1)^2) + \nu (\|\nabla s_2\|^2 - \|\nabla s_1\|^2) \right] \quad (2.35)$$

The evolution equation (2.35) should be interlaced with an estimation of the smooth approximations s_i . The Euler-Lagrange equation of $F_{[177]}$ shows that they are solutions of a Poisson equation, with Neumann boundary conditions [172, 177]:

$$\begin{aligned} \nu \Delta s_i &= \lambda (s_i - I) & \text{in } \Omega_i \\ \frac{\partial s_i}{\partial \mathbf{n}} &= 0 & \text{on } \partial \Omega_i \cup \partial \Omega \end{aligned} \quad (2.36)$$

where $\partial/\partial \mathbf{n}$ denotes the derivative in the normal direction \mathbf{n} at the boundary. This equation can be solved by conjugate-gradient iterative solvers [126] and has the effect of selectively smoothing the image by a diffusion process restricted to the domain Ω_i . As shown in Fig. 2.7, the coupled partial differential equations (2.35) and (2.36) simultaneously realize both image segmentation and edge-preserving smoothing.

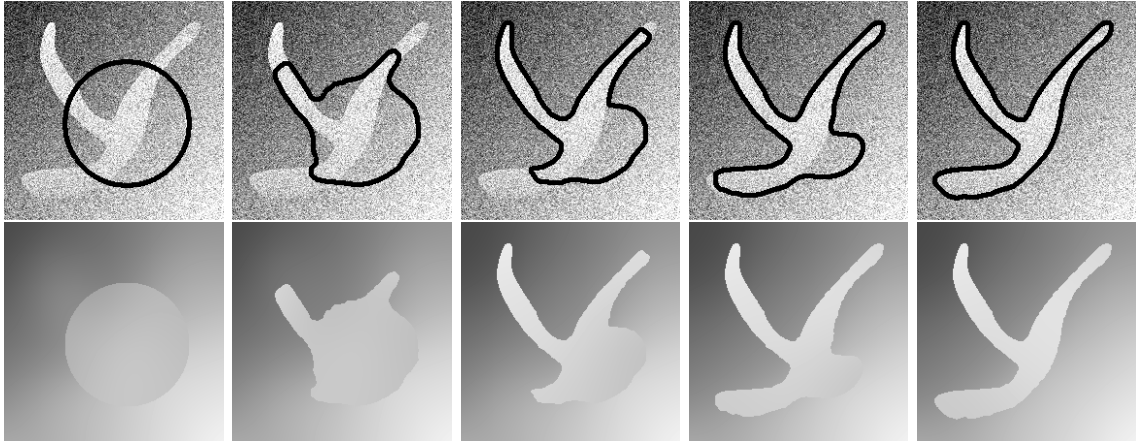


Figure 2.7 — Simultaneous segmentation and noise removal with piecewise-smooth model, with recovery of spatial intensity variations. Experiment on a synthetic image with linear ramp as background and a smoothly-varying foreground, following (2.35). First row: evolution of $\{\Phi = 0\}$. Second row: optimal piecewise-smooth approximation $\hat{I} = H(\Phi)s_1 + H(-\Phi)s_2$.

A first practical difficulty arises in the evolution of Φ , where terms in $\|\nabla s_i\|$ in (2.35) appear multiplied by $\delta_\epsilon(\Phi)$. As already discussed, $\delta_\epsilon(\Phi)$ is non-zero everywhere in Ω , since the support of δ_ϵ is non-compact. Even with a compact-support approximation such that $\delta_\epsilon(\Phi)$ is confined in a narrow band around the zero-crossings of Φ , knowledge of s_1 and s_2 is still needed *on both sides* of the boundary, while their definition domain is theoretically restricted to one or the other, as solutions of (2.36). In [177], the authors propose a numerical fix through a heuristic extension, solving the Laplace equation $\Delta s_i = 0$ with

prescribed boundary conditions, but this is not justified from the variational formulation $F_{[177]}$. In contrast, we develop in Chapter 3 a method that gives similar results but relies on approximations s_i that are defined over the whole domain Ω .

The second major practical limitation of such piecewise-smooth approaches with coupled partial differential equations is their computational complexity: the estimation of both functions s_1 and s_2 should be performed *at each step* because the boundary conditions move accordingly to the evolution of the interface. Combined with the time step restrictions induced by the curvature term in (2.35), the computational complexity becomes prohibitively expensive and, to our knowledge, this method has never been applied to volumetric datasets for this reason. On the contrary, the piecewise-smooth formulation that we develop in Chapter 3 does not have this limitation. Instead of being solutions of diffusion equations such as (2.36) that require iterative solvers, the optimal approximation functions s_i have a simple closed-form expression, which allows much faster evaluations and 3D implementations.

2.4.4 Non-Parametric Models with Information Theory

Using Bayesian principles, the *Region Competition* algorithm [189] and subsequent efforts along the same line [30, 40, 52, 89, 137] have in common to derive a statistical criterion from the maximization of the posterior probability of the segmentation, given the observed image. Such methods make strong assumptions about the probability distribution of features in each region in the form of *parametric* models, so that only a small set of statistical parameters (such as mean and variance) are optimized. The choice of a specific model, often Gaussian or mixtures of Gaussian, restricts the applicability to the limited set of images that satisfy the underlying assumptions. Deviations from the expected model can significantly degrade the result of the segmentation.

To overcome this limitation, *non-parametric* statistical boundary evolution algorithms have emerged for segmentation and tracking [83, 85, 90, 95]. Using intensity distributions [95], multivariate texture features [9] or motion information [84], these methods follow a common methodology. An objective criterion is derived from information-theoretic measures such as the entropy of the region distributions. In all cases, the *Parzen window* estimation is used as an analytical expression of unknown probability distributions in order to calculate derivatives.

Recall that Parzen window method [138], also referred to as *kernel density estimation*, is a standard tool to estimate a smooth probability distribution in a non-parametric fashion. Its principle is illustrated in Fig. 2.8 in the discrete case.

In the continuous case, the analytical expression of the estimated density in a region $\Omega_i \subset \Omega$ of a scalar image $I : \Omega \rightarrow \mathbb{R}$ reads :

$$p_i(a) = \frac{1}{|\Omega_i|} \int_{\Omega_i} K(I(\mathbf{x}) - a) d\mathbf{x} \quad (2.37)$$

where the kernel K , typically Gaussian, satisfies:

$$\forall a \in \mathbb{R}, \quad K(a) > 0 \quad \text{and} \quad \int_{\mathbb{R}} K(a) da = 1 \quad (2.38)$$

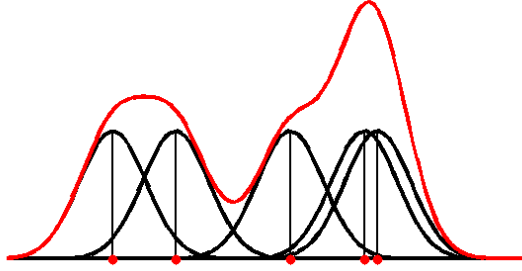


Figure 2.8 — Estimation of a probability density function using Parzen windows in the discrete case: The red dots corresponds to N realizations of a discrete random variables $\{x_i\}$. Each x_i is associated to a kernel $K(x_i - a)$, here Gaussian, shown in black. The estimated probability distribution is $p(a) = \frac{1}{N} \sum_i K(x_i - a)$

Using kernel density estimation, non-parametric segmentation algorithms do not make any assumption on the underlying probability distribution. Therefore, they are suitable for intensity distributions with multiple modes. Such distributions are encountered in practice for objects composed of multiple tissues where each tissue is roughly homogeneous, as illustrated on a synthetic image in Fig. 2.9. In particular, the background region of anatomical structures often falls in this category, since target objects are usually surrounded by several organs.

Region-based segmentation algorithms using non-parametric density estimation differ in the choice of an objective criterion derived from information theory, in particular based on Shannon's entropy. The underpinning assumption is that a region may be characterized by the average quantity of information conveyed by its intensity values. Intuitively, the entropy of a region provides a measure of uncertainty and statistical inhomogeneity. The extension of Shannon's entropy to continuous variables is often referred to as the *differential entropy*:

$$h(p) = - \int_{\mathbb{R}} p(a) \log p(a) da \quad (2.39)$$

In [83], Herbulot et al. propose to minimize the sum of foreground and background entropies $h(p_1) + h(p_2)$, with p_i expressed as in (2.37) to make the dependence of the criterion on the segmentation explicit. In [95], Kim et al. choose to maximize the mutual information between the original image and a label map, taking one discrete value in each region. It can be shown to be equivalent to the minimization of [84, 95]:

$$\begin{aligned} F_{[95]}(\Omega_1) &= \mu \text{Per}(\Omega_1) - \lambda \sum_{i=1}^2 \int_{\Omega_i} \log p_i(I(\mathbf{x})) d\mathbf{x} \\ &= \mu \text{Per}(\Omega_1) - \lambda \sum_{i=1}^2 \int_{\Omega_1} \log \left(\frac{1}{|\Omega_i|} \int_{\Omega_i} K(I(\mathbf{x}) - I(\mathbf{y})) d\mathbf{y} \right) d\mathbf{x} \end{aligned} \quad (2.40)$$

where the boundary perimeter is again the geometric constraint that regularizes the solution. With an implicit representation Φ , positive in the foreground region, the gradient-descent evolution of (2.40) is:

$$\begin{aligned} \frac{\partial \Phi}{\partial t}(\mathbf{x}) &= \delta_\epsilon(\Phi) \left(\mu \nabla \cdot \frac{\nabla \Phi}{\|\nabla \Phi\|} - \log \frac{p_1(I(\mathbf{x}))}{p_2(I(\mathbf{x}))} \right) \\ &+ \delta_\epsilon(\Phi) \left(\frac{1}{|\Omega_2|} \int_{\Omega_2} \frac{K(I(\mathbf{y}) - I(\mathbf{x}))}{p_2(I(\mathbf{y}))} d\mathbf{y} - \frac{1}{|\Omega_1|} \int_{\Omega_1} \frac{K(I(\mathbf{y}) - I(\mathbf{x}))}{p_1(I(\mathbf{y}))} d\mathbf{y} \right) \end{aligned} \quad (2.41)$$

In Fig.2.9, we show the evolution (2.41) on a synthetic image in which object and background are composed of several inner structures. In such a case, non-parametric estimation enables to capture multiple modes in the intensity distributions. In Fig.2.10, the regions are generated by two intensity distributions of exact same mean and variance, which makes the foreground object invisible to the eye. Nevertheless, the algorithm is able to recover the correct segmentation by exploiting higher-order statistical moments of the distributions.

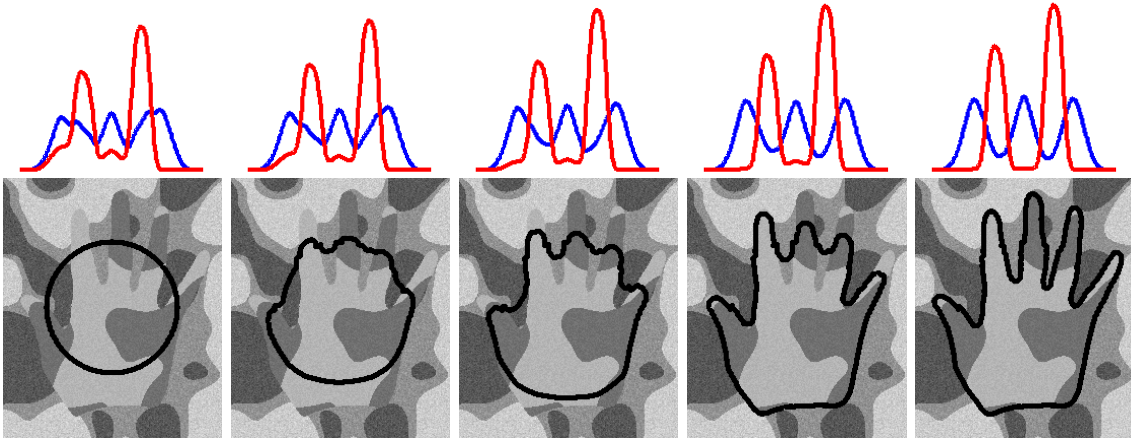


Figure 2.9 — Segmentation with entropy and non-parametric distributions - the case of multiple modes. The first row shows the evolution of the inside (red) and outside (blue) probability distributions during the evolution of the segmentation given in the second row: Starting from an initial circle (black), the curve evolves following (2.41) towards the boundaries of a synthetically-generated hand composed of several intensity modes.

Interestingly, the functional $F_{[95]}$ in (2.40) is almost identical to the region competition functional with the only difference that the parametric density function $P(I|\alpha_i)$ is replaced by a non-parametric estimate $p_i(I)$. Consequently, the likelihood ratio test $\log(p_1/p_2)$ is still present in the evolution (2.41). The conceptual difference is revealed by the last two terms, reflecting the changes in the density function induced by the movement of the boundary. These coupling terms are a consequence of introducing the analytical expression of the density estimate directly in the functional, rather than considering it as an unknown variable that is periodically re-estimated. Therefore, (2.41) can be viewed as a *true* gradient-descent in contrast to the *coordinate-wise* descent of region competition. However, since the evolution of the boundary is usually much faster than the changes in intensity distributions,

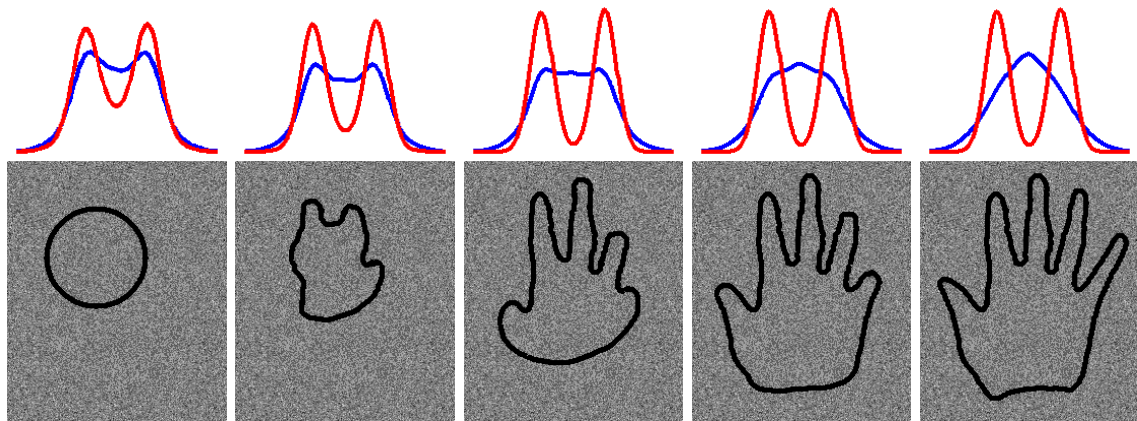


Figure 2.10 — Segmentation with entropy and non-parametric distributions - the case of identical means and variances. The first row shows the evolution of the inside (red) and outside (blue) probability distributions during the evolution of the segmentation given in the second row: In this case, the inside and outside regions of the same hand as in Fig. 2.9 are generated by two intensity distributions of exact same mean and variance. Although the foreground is virtually invisible, (2.41) enables the recovery of the correct boundaries by exploiting higher-order statistical moments of the distributions.

it is questionable from a practical perspective whether the coupling terms are worth the significant complexity overhead. We come back to this discussion in the next chapter and provide other justifications in favor of the *decoupling* strategy that consists in neglecting the last two terms in (2.41). We also develop a generalization to model possible spatial variations of intensity distribution within a single region, in a similar way than piecewise-smooth approximations generalize the constant case.

To conclude this section on non-parametric models with information theory, let us mention other possible measures of segmentation quality. The previous algorithm aims at maximizing the mutual information between each region and its corresponding label. An alternative criterion is to minimize the mutual information between foreground and background regions, which is equivalent to maximizing their relative entropy, also known as the *Kullback-Leibler* divergence, as proposed by Houhou et al in [87]. Along the same line, other definitions of distances between probability distributions can be maximized, such as the *Bhattacharyya* [120] or the *Wasserstein* distance. The latter depends on *cumulative* distributions to better exploit the relative contrast between regions, as proposed by Chan et al. in [37]. Spatially-localized extensions are also considered in [129].

2.5 Conclusion

In the last section of this survey, we exposed the variational principles of region-based segmentation with a set of reference methods. As a conclusion, let us summarize some key features that shall be retained in the design of computational algorithms for 3D interactive medical image segmentation.

First, region *homogeneity* as a measure of segmentation quality appears to be a simple and flexible paradigm that applies to a variety of image features and application areas. Except for simple cases, homogeneity should be regarded in a wider sense than a simple dispersion around an average value and include information on the whole distribution of image values inside a given region. In this respect, non-parametric kernel density estimation is a particularly versatile tool since no assumption on the underlying region distribution is made.

Secondly, piecewise-smooth image approximations offer the significant advantage of taking into account spatial intensity variations that may occur inside a single object. This is an important property for many applications in medical imaging that can not rely on the hypothesis that the anatomical structure follows a single generative model, in particular for vessel segmentation. Unfortunately, the existing techniques are seldom used in 3D due to their prohibitive computational complexity.

Finally, implicit representations are a powerful description of 3D objects of arbitrarily-complex shapes with for instance several constituent components or inner holes. They can be used within numerical implementations of surface evolution schemes, as in the level-set framework, or directly considered to be the unknown variable in the minimization criterion. To regularize the set of possible solutions, a geometric constraint is most often included. Unfortunately, this induces a motion by curvature terms that has intrinsic limitations in terms of numerical stability.

Convex Framework for Two-Phase Image Segmentation

3

In this chapter, we develop a generic framework for segmentation of images in two regions (foreground/background) together with a collection of specific, application-dependent settings. The variational formulation is derived from a number of existing unsupervised region-based techniques, such as Zhu and Yuille’s *Region Competition* [189] or Chan and Vese’s *Active Contours Without Edges* [40]. However, we extend the standard collection of available region homogeneity measures with *localized* versions that do not rely on the usual assumption that probability distributions of features are space-invariant in each region. These local extensions are designed so that the computational complexity is kept to a minimum. In particular, the use of local intensity averages as descriptive features yields qualitatively similar results than *piecewise-smooth* approaches derived from the *Mumford-Shah* functional [126], only used in 2D, with 3D computing times that are compatible with clinical usage.

The regularity of the optimal segmentation is usually ensured through a geometric constraint on the perimeter of the boundary. In this case, we show that the problem can be re-formulated in a convex way by generalizing the global minimizers of active contours [26, 39]. We give an intuitive interpretation of the convex relaxation process through the use of a *membership* function as optimization variable, which allows to update the region statistics in a consistent way throughout the minimization process. As Bresson et al. in [26], we borrow a fast optimization scheme from total variation theory and design an algorithm that provides globally-minimizing solutions in the supervised case. In the unsupervised case, we illustrate by several examples using global and local region statistics in 2D and 3D that the result of the minimization algorithm is in practice weakly dependent on initial conditions.

3.1 Introduction

This chapter is divided into three parts. Section 3.2 is a reminder on the fundamental principles of variational region-based image segmentation. After a description of standard measures of intensity homogeneity, we also propose two novel classification errors that are specifically designed to efficiently account for space-varying statistical analysis. In section 3.3, a computational algorithm is developed that relies on a geometric constraint to regularize the set of possible solutions. This algorithm, which we called *Fuzzy Region Competition*, has a number of desirable properties such as convexity and numerical stability. Moreover, the optimization scheme works with any intensity homogeneity measure. In terms of 3D surface representation, which is an important focus of this work, a membership function describes the foreground region. Finally, we illustrate in section 3.4 on a number of practical segmentation examples the versatility of the approach combined with global and local features statistics.

3.2 General Variational Formulation

This first part starts with a unified formulation of a variational problem on which many image segmentation algorithms, in particular region-based level-set methods exposed in the previous chapter, are derived. Besides an introduction of the main notations, it is also an opportunity to present the methodology and underpinning principles that will be followed throughout the whole manuscript.

From sections 3.2.1 to 3.2.5, we compile a list of possible segmentation quality measures that can be plugged in the general framework for specific applications, depending on the expected appearance of target objects in terms of image features. We start from classical *global* measures, assuming constant statistical properties in each region. Then, we develop new extensions to model *local*, space-varying properties as well. Additional edge-based criteria are also possible in the same framework, by maximizing the *flux* of the image gradient through the region boundary.

For the purpose of this work, the objective of a unified formulation with a catalog of compatible objective criteria is that all region models will be readily available for each and every algorithm to support concrete illustrative examples.

Minimization Problem

Let the original image $I : \Omega \rightarrow \mathbb{R}$ be a n -dimensional, square-integrable function defined on a bounded domain $\Omega \subset \mathbb{R}^n$. For the sake of simplicity, we assume that I takes values on the real line, although the extension to vectorial images is often natural and examples will be shown on multi-channel color images.

A region $\Omega_i \subset \Omega$, where i is a region index, is considered to be a subset of the image domain that can be characterized by a set of descriptive parameters, denoted $\alpha_i \in \mathcal{A}$. In the simplest case, α_i is a finite-dimensional vector of real values. For instance, if each region is assumed to follow a Gaussian distribution of image intensities, α_i denotes the mean and

variance of this distribution and $\mathcal{A} = \mathbb{R}^2$. As we will see, α_i can also correspond to a function such as a smooth approximation or a probability distribution, in which case \mathcal{A} is a functional space.

In order to define an objective criterion that quantifies the quality of a segmentation, we assume that there exists, for each region Ω_i , a function r_i that at each point $\mathbf{x} \in \Omega$ associates a scalar value that measures the classification error of $\mathbf{x} \in \Omega_i$, according to the descriptive parameters α_i . This error function depends on the image I and often takes the following form:

$$r_i : \Omega \times \mathcal{A} \rightarrow \mathbb{R} \quad \text{with} \quad r_i(\mathbf{x}, \alpha_i) = f(I(\mathbf{x}), \alpha_i) \quad (3.1)$$

For instance, if a region is described only by its average intensity value c_i , the set of parameters is $\mathcal{A} = \mathbb{R}$ and a natural choice is $r_i(\mathbf{x}, c_i) = (I(\mathbf{x}) - c_i)^2$. In all cases, the classification error E_i associated to the whole region Ω_i is obtained by integrating the point-wise error,

$$E_i(\Omega_i, \alpha_i) = \int_{\Omega_i} r_i(\mathbf{x}, \alpha_i) d\mathbf{x} \quad (3.2)$$

A partitioning of the image into M disjoint regions is obtained by a set of regions $\{\Omega_i\}_{i=1\dots M}$ that satisfies:

$$\forall i \neq j, \Omega_i \cap \Omega_j = \emptyset \quad \text{and} \quad \bigcup_{i=1}^M \Omega_i = \Omega \quad (3.3)$$

Consequently, the total classification error E that should be minimized to obtain an optimal partitioning is:

$$E = \sum_{i=1}^M E_i(\Omega_i, \alpha_i) = \sum_{i=1}^M \int_{\Omega_i} r_i(\mathbf{x}, \alpha_i) d\mathbf{x} \quad (3.4)$$

Focusing on the case of only two regions, a segmentation is defined by a foreground Ω_1 while the background corresponds to everything else $\Omega_2 = \Omega \setminus \Omega_1$. Note that the foreground region is not necessarily a connected set and might contain several *objects*, as illustrated in Fig. 3.1.

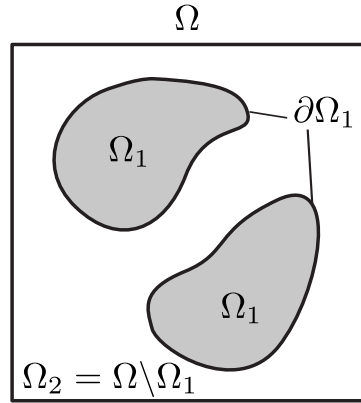


Figure 3.1 — Partitioning of the image domain Ω in two regions Ω_1 and $\Omega_2 = \Omega \setminus \Omega_1$

In order to impose geometric constraints on admissible partitions, the classification error (3.4) shall be regularized by adding a penalization term, denoted here $\mathcal{R}(\Omega_1)$. For instance, in many active contour algorithms, the regularization term corresponds to the perimeter of the foreground, $\mathcal{R}(\Omega_1) = \text{Per}(\Omega_1)$. Therefore, with the above assumptions, a general formulation of the minimization problem for segmentation of an image into two disjoint regions reads:

$$\min_{\Omega_1, \alpha_1, \alpha_2} \left\{ F(\Omega_1, \alpha_1, \alpha_2) = \mathcal{R}(\Omega_1) + \lambda \int_{\Omega_1} r_1(\mathbf{x}, \alpha_1) d\mathbf{x} + \lambda \int_{\Omega \setminus \Omega_1} r_2(\mathbf{x}, \alpha_2) d\mathbf{x} \right\} \quad (3.5)$$

where λ balances the classification error relatively to the regularization constraint. This minimization problem involves three variables: the foreground region Ω_1 and two sets of descriptive parameters α_1 and α_2 , one for each region. If α_1 and α_2 are known a priori, the process of obtaining an optimal partition by minimizing $F(\Omega_1)$ is referred to as a *supervised* segmentation algorithm. On the contrary, if α_1 and α_2 are unknown and should also be recovered by minimizing $F(\Omega_1, \alpha_1, \alpha_2)$, the process is said to be *unsupervised*. In the latter case, we follow the common methodology of a two-stage iterative procedure, summarized in Algorithm 1 below:

Algorithm 1: General minimization scheme in the *unsupervised* case

Set iteration $j = 0$, choose initial Ω_1^0

repeat

(A) Ω_1^j fixed, minimize (3.5) w.r.t. α and update parameters α^j ,

(B) α^j fixed, minimize (3.5) w.r.t Ω_1 and update segmentation Ω_1^{j+1} .

until *convergence*

Step **(B)** depends on how the foreground region is represented, which is the key differentiating factor between segmentation methods that follow the general form (3.5). In the next chapters, we study a number of implicit surface representations and associated computational algorithms that are applicable in a variety of 3D applications in medical imaging. Since α_1 and α_2 are fixed, Step **(B)** also corresponds to the supervised case. In this case, it is convenient to re-arrange the terms of F in (3.5) as:

$$\begin{aligned} F(\Omega_1) &= \mathcal{R}(\Omega_1) + \lambda \int_{\Omega_1} r_1(\mathbf{x}, \alpha_1) d\mathbf{x} + \lambda \int_{\Omega \setminus \Omega_1} r_2(\mathbf{x}, \alpha_2) d\mathbf{x} \\ &= \mathcal{R}(\Omega_1) + \lambda \int_{\Omega_1} (r_1(\mathbf{x}, \alpha_1) - r_2(\mathbf{x}, \alpha_2)) d\mathbf{x} + \lambda \int_{\Omega} r_2(\mathbf{x}, \alpha_2) d\mathbf{x} \end{aligned} \quad (3.6)$$

Since the last term is an integral over the whole domain Ω , it does not play any role in the minimization with respect to the segmentation Ω_1 . Thus, **(B)** is equivalent to

$$\min_{\Omega_1} \left\{ \mathcal{R}(\Omega_1) + \int_{\Omega_1} r(\mathbf{x}) d\mathbf{x} \right\} \quad \text{with} \quad r(\mathbf{x}) = \lambda (r_1(\mathbf{x}, \alpha_1) - r_2(\mathbf{x}, \alpha_2)) \quad (3.7)$$

Function r in (3.7) will be referred to as the *competition function* since it drives the solution towards the object(s) of interest as a result of the competition between inside and outside

intensity models. r can be interpreted as a signed likelihood test where a negative value indicates the propensity of pixel \mathbf{x} to be part of the foreground. Indeed, in absence of regularization, $\mathcal{R}(\Omega_1) = 0$ and the solutions of (3.7) are simply obtained by thresholding:

$$\Omega_1^* = \{\mathbf{x} \in \Omega, r(\mathbf{x}) \leq 0\} \quad (3.8)$$

In the next sections, we study Step **(A)** for a list of global and local statistical region models and give update formula for the periodic re-estimation of their parameters. This step only depends on the choice of r_i and α_i and applies to every algorithm, regardless of how the foreground is represented. In all cases, it involves the minimization of:

$$E_i(\alpha_i) = \int_{\Omega_i} r_i(\mathbf{x}, \alpha_i) d\mathbf{x} \quad (3.9)$$

3.2.1 Gaussian Distributions

Following Zhu and Yuille's Region Competition [189] principle of maximizing a log-likelihood criterion and assuming a parametric probability distribution $P(\cdot|\alpha_i)$, the total classification error associated to a region Ω_i can be defined as:

$$E_i(\alpha_i) = - \int_{\Omega_i} \log P(I(\mathbf{x})|\alpha_i) d\mathbf{x} \quad (3.10)$$

which corresponds in the general framework of the previous section to the choice:

$$r_i(\mathbf{x}, \alpha_i) = -\log P(I(\mathbf{x})|\alpha_i) \quad (3.11)$$

If we further assume P to be a Gaussian distribution, this yields the setting:

$$\begin{cases} \alpha_i = \{c_i, \sigma_i\} \\ r_i(\mathbf{x}, c_i, \sigma_i) = \frac{1}{2\sigma_i^2} (I(\mathbf{x}) - c_i)^2 + \log(\sigma_i) \end{cases} \quad (3.12)$$

and the classification error becomes:

$$E_i(c_i, \alpha_i) = \frac{1}{2\sigma_i^2} \int_{\Omega_i} (I(\mathbf{x}) - c_i)^2 d\mathbf{x} + |\Omega_i| \log(\sigma_i) \quad (3.13)$$

In order to find the update formula at Step **(A)** of Algorithm 1, we set the derivatives of E_i with respect to c_i and σ_i to 0:

$$\begin{aligned} \frac{\partial E_i}{\partial c_i} = 0 & \Leftrightarrow \frac{1}{\sigma_i^2} \int_{\Omega_i} (I(\mathbf{x}) - c_i) d\mathbf{x} = 0 \\ & \Rightarrow c_i^* = \frac{1}{|\Omega_i|} \int_{\Omega_i} I(\mathbf{x}) d\mathbf{x} \end{aligned} \quad (3.14)$$

and

$$\begin{aligned} \frac{\partial E_i}{\partial \sigma_i} = 0 & \Leftrightarrow -\frac{1}{\sigma_i^3} \int_{\Omega_i} (I(\mathbf{x}) - c_i)^2 d\mathbf{x} + \frac{|\Omega_i|}{\sigma_i} = 0 \\ & \Rightarrow \sigma_i^* = \sqrt{\frac{1}{|\Omega_i|} \int_{\Omega_i} (I(\mathbf{x}) - c_i)^2 d\mathbf{x}} \end{aligned} \quad (3.15)$$

This gives the well-known result for a maximum-likelihood estimator of parameters of a Gaussian distribution: the optimal c_i and σ_i are simply the mean and the standard deviation inside the region. Note that if σ is known in advance, for instance by relying on noise estimation techniques prior to segmentation, the Gaussian case simplifies to the cartoon limit of the Mumford-Shah functional for piecewise-constant images.

Similar maximum-likelihood principles apply to other non-Gaussian parametric families of intensity distributions. For instance, Bernard et al. exploited the nature of radio-frequency signals to segment echo-cardiographic images with a Rayleigh distribution [16]. Elagouni et al. have also used a similar prior for pathological myocardial tissues in Late Enhancement Magnetic Resonance images [63].

3.2.2 Non-Parametric Distributions

When reliable a priori information about the expected distributions is available, parametric models perform remarkably well. Unfortunately, the choice of a specific model inevitably limits its applicability to a restricted class of images. Moreover, if parametric distributions can, in some cases, describe the inside region of an homogeneous anatomical structure, it is rarely the case for its background, usually composed of various surrounding organs that create more complex arbitrary intensity distributions. In this section, we develop a non-parametric formulation and consider the probability density function itself to be the unknown region parameter.

It seems natural to substitute the parametric form discussed in the previous section with an estimate of the true probability density, approximated with kernel density estimation. However, to ensure that the resulting optimization process converges, the following question arises: is it justified from a variational perspective to alternate between non-parametric density estimation and segmentation in the two-stage approach? In other words, does an update of the probability distribution using Parzen windows decrease the overall objective criterion? To verify this assumption, let us consider the following setting:

$$\begin{cases} \alpha_i = \{p_i\} \\ r_i(\mathbf{x}, p_i) = -\log p_i(I(\mathbf{x})) \end{cases} \quad (3.16)$$

where the region parameter $p_i : \mathbb{R} \rightarrow \mathbb{R}$ is now a function. To go further, additional constraints are necessary to ensure that p_i is a valid probability distribution:

$$\int_{\mathbb{R}} p_i(a) da = 1 \quad \text{and} \quad \forall a \in \mathbb{R}, p_i(a) > 0, \quad (3.17)$$

With the above assumptions, the constrained minimization problem to solve at each update Step **(A)** of the general unsupervised segmentation algorithm is:

$$\begin{aligned} \min_{p_i \in L^1(\mathbb{R})} \quad & \left\{ E_i(p_i) = - \int_{\Omega_i} \log p_i(I(\mathbf{x})) d\mathbf{x} \right\} \\ \text{subject to} \quad & \int_{\mathbb{R}} p_i(a) da = 1 \end{aligned} \quad (3.18)$$

To find a minimizer under the constraint that function p_i sums to 1, we should study the critical points of the Lagrangian

$$\mathcal{L}(p_i, \mu_i) = E_i(p_i) + \mu_i \left(\int_{\mathbb{R}^d} p_i(a) da - 1 \right) \quad (3.19)$$

where $\mu_i \in \mathbb{R}$ is a Lagrange multiplier. A necessary condition for p_i^* to be a minimizer of \mathcal{L} is that the directional derivative of \mathcal{L} in the direction η vanishes for all η . Thus a minimizer of (3.18) should satisfy:

$$\begin{cases} \left. \frac{\partial \mathcal{L}(p_i + t\eta)}{\partial t} \right|_{t=0} = 0, & \forall \eta \\ \frac{\partial \mathcal{L}}{\partial \mu_i} = 0 \end{cases} \quad (3.20)$$

By the convolution property of the Dirac distribution, the following holds:

$$\begin{aligned} E_i(p_i) = - \int_{\Omega_i} \log p_i(I(\mathbf{x})) d\mathbf{x} &= - \int_{\Omega_i} \left(\int_{\mathbb{R}} \log p_i(a) \delta(I(\mathbf{x}) - a) da \right) d\mathbf{x} \\ &\approx - \int_{\Omega_i} \left(\int_{\mathbb{R}} \log p_i(a) K_\epsilon(I(\mathbf{x}) - a) da \right) d\mathbf{x} \end{aligned} \quad (3.21)$$

where K_ϵ is chosen so that the approximation becomes exact when $\epsilon \rightarrow 0$, which is in particular true for a Gaussian of scale ϵ . With this approximation, switching the order of integration yields:

$$E_i(p_i) = - \int_{\mathbb{R}} \log p_i(a) \left(\int_{\Omega_i} K_\epsilon(I(\mathbf{x}) - a) d\mathbf{x} \right) da \quad (3.22)$$

Under this form, the directional derivative of \mathcal{L} is much easier to calculate:

$$\begin{aligned} \left. \frac{\partial \mathcal{L}(p_i + t\eta)}{\partial t} \right|_{t=0} &= - \int_{\mathbb{R}} \frac{\eta(a)}{p_i(a)} \int_{\Omega_i} K_\epsilon(I(\mathbf{x}) - a) d\mathbf{x} da + \mu_i \int_{\mathbb{R}} \eta(a) da \\ &= \int_{\mathbb{R}} \eta(a) \left(- \frac{1}{p_i(a)} \int_{\Omega_i} K_\epsilon(I(\mathbf{x}) - a) d\mathbf{x} + \mu_i \right) da \end{aligned} \quad (3.23)$$

Since the right-hand side should vanish for any function η , the integrand must be equal to 0 for all $a \in \mathbb{R}$ and the necessary condition becomes:

$$p_i^*(a) = \frac{1}{\mu_i} \int_{\Omega_i} K_\epsilon(I(\mathbf{x}) - a) d\mathbf{x} \quad (3.24)$$

Finally, satisfying the second condition in (3.20) implies:

$$\int_{\mathbb{R}} p_i^*(a) da = \frac{1}{\mu_i} \int_{\Omega_i} \left(\int_{\mathbb{R}} K_\epsilon(I(\mathbf{x}) - a) da \right) d\mathbf{x} = 1 \Rightarrow \mu_i = \int_{\Omega_i} d\mathbf{x} \quad (3.25)$$

Thus, the optimal p_i^* is a function that takes the form of a continuous version of the Parzen window estimate of the density within the region Ω_i , with an estimation kernel K_ϵ :

$$p_i^*(a) = \frac{1}{|\Omega_i|} \int_{\Omega_i} K_\epsilon(I(\mathbf{x}) - a) d\mathbf{x} \quad (3.26)$$

Note that the second constraint in (3.17), $\forall a, p_i(a) > 0$, is automatically satisfied. In the case of a negative log-likelihood term, we have formally checked that the update procedure of p_i with (3.26) in Step **(A)** using kernel density estimation is consistent with the minimization criterion. Without any assumption on a parametric form of the probability density, this estimation offers more flexibility for representing complex, unknown intensity distributions. As discussed in section 2.4.4, non-parametric models have been used for region-based segmentation with information theory [9, 83–85, 90, 95, 120, 129]. In the latter techniques, additional computationally-expensive terms are involved to account for the coupling between the segmentation and the probability density function. Ignoring the coupling and considering p_i as an unknown function, we have shown that non-parametric models are also valid in more conventional region-based strategies and two-stage minimization approaches such as the general framework (3.5).

Besides its simplicity, the alternate minimization scheme has additional advantages. First, Step **(B)** can be relaxed to a convex problem, which provides global minimizers. This will be shown in section 3.3. Second, it is possible to develop a simple extension of this model to account for spatial variations of probability distributions, leading to a very general setting with local and non-parametric distributions. In the next section, we explain the principle of this localization in the Gaussian case, then develop a full extension to the general case in section 3.2.4.

3.2.3 Local Gaussian Distributions

Most segmentation techniques that describe each region with a global intensity distribution suffer from several practical limitations regarding discrimination power and reproducibility. In medical images, it is seldom possible to discriminate between foreground and background with a single probability density for each region. Typical difficulties include the cases of cluttered, heterogeneous backgrounds and low-frequency artifacts such as diffusion of contrast product in tissues or bias fields in MRI. Reproducibility is also hindered by the fact that simple operations like cropping the image to a region of interest around the target structure affect the estimation of the background distribution and lead to significant changes on the final result.

The aforementioned limitations could be significantly reduced if the distributions were defined locally and allowed to vary in space. We shall first develop such a localized extension for the piecewise-constant case, assuming Gaussian distributions of known and equal variance for all regions. This yields a formulation that bears similarities with piecewise-smooth models, with a much lower complexity.

The key idea to achieve a space-varying extension of a global region-based criterion is to introduce in the functional a sliding window in order to localize the classification error. For the piecewise-constant case, the following global classification error is associated to a region Ω_i :

$$E_i(c_i) = \int_{\Omega_i} (I(\mathbf{x}) - c_i)^2 d\mathbf{x} \quad (3.27)$$

Now, let us consider the same classification error *locally*, in a neighborhood of point $\mathbf{y} \in \Omega$. A local measure $e_i(\mathbf{y})$ of the classification error can be obtained with a symmetric and positive window function $W : \Omega \mapsto \mathbb{R}^{+*}$, such that $W(\mathbf{z}) \rightarrow 0$ when $\|\mathbf{z}\| \rightarrow +\infty$:

$$e_i(\mathbf{y}) = \int_{\Omega_i} W(\mathbf{x} - \mathbf{y}) (I(\mathbf{x}) - s_i(\mathbf{y}))^2 d\mathbf{x} \quad (3.28)$$

Due to the dependence on the location \mathbf{y} where the error is estimated, the previously constant approximation c_i is now allowed to vary in space and becomes a square-integrable function $s_i : \Omega \rightarrow \mathbb{R}$. The total classification error associated to the region Ω_i is obtained by integrating the localized error $e_i(\mathbf{y})$ in the whole domain Ω :

$$\begin{aligned} E_i(s_i) &= \int_{\Omega} e_i(\mathbf{y}) d\mathbf{y} \\ &= \int_{\Omega} \left(\int_{\Omega_i} W(\mathbf{x} - \mathbf{y}) (I(\mathbf{x}) - s_i(\mathbf{y}))^2 d\mathbf{x} \right) d\mathbf{y} \end{aligned} \quad (3.29)$$

Switching the order of integration reveals the point-wise error function $r_i(\mathbf{x}, s_i)$

$$E_i(s_i) = \int_{\Omega_i} \underbrace{\left(\int_{\Omega} W(\mathbf{x} - \mathbf{y}) (I(\mathbf{x}) - s_i(\mathbf{y}))^2 d\mathbf{y} \right)}_{r_i(\mathbf{x}, s_i)} d\mathbf{x} \quad (3.30)$$

and the corresponding setting in the general framework (3.5):

$$\begin{cases} \boldsymbol{\alpha}_i = \{s_i\} \\ r_i(\mathbf{x}, s_i) = \int_{\Omega} W(\mathbf{x} - \mathbf{y}) (I(\mathbf{x}) - s_i(\mathbf{y}))^2 d\mathbf{y} \end{cases} \quad (3.31)$$

In section 3.3, we will show several examples of segmentations produced using this localized model with the two-stage iterative minimization scheme. Here, we focus on Step **(A)** of the algorithm and study how local average functions s_i should be updated when the region Ω_i is considered fixed. The optimal s_i^* should satisfy the following condition, with E_i given by (3.30):

$$\left. \frac{\partial E_i(s_i^* + t\eta)}{\partial t} \right|_{t=0} = 0, \quad \forall \eta \quad (3.32)$$

The functional derivative of $E_i(s_i)$ in the direction η is:

$$\begin{aligned} \left. \frac{\partial E_i(s_i + t\eta)}{\partial t} \right|_{t=0} &= 2 \int_{\Omega_i} \left(\int_{\Omega} \eta(\mathbf{y}) W(\mathbf{x} - \mathbf{y}) (I(\mathbf{x}) - s_i(\mathbf{y})) d\mathbf{y} \right) d\mathbf{x} \\ &= 2 \int_{\Omega} \eta(\mathbf{y}) \left(\int_{\Omega_i} W(\mathbf{x} - \mathbf{y}) (I(\mathbf{x}) - s_i(\mathbf{y})) d\mathbf{x} \right) d\mathbf{y} \end{aligned} \quad (3.33)$$

Since the above expression should vanish for every perturbation η , the integrand inside the parenthesis must be equal to 0 for all $\mathbf{y} \in \Omega$. Thus, the optimal s_i^* must satisfy:

$$\int_{\Omega_i} W(\mathbf{x} - \mathbf{y}) (I(\mathbf{x}) - s_i^*(\mathbf{y})) d\mathbf{x} = 0 \quad (3.34)$$

If Ω_i is non-empty and W is strictly positive, this yields:

$$\forall \mathbf{y} \in \Omega, \quad s_i^*(\mathbf{y}) = \frac{\int_{\Omega_i} W(\mathbf{x} - \mathbf{y}) I(\mathbf{x}) d\mathbf{x}}{\int_{\Omega_i} W(\mathbf{x} - \mathbf{y}) d\mathbf{x}} \quad (3.35)$$

Since W is symmetric, $W(\mathbf{x} - \mathbf{y}) = W(\mathbf{y} - \mathbf{x})$ the above expression is a *normalized convolution*, involving the characteristic function χ_i of the set Ω_i :

$$s_i^* = \frac{W * [\chi_i I]}{W * \chi_i} \quad \text{with} \quad \chi_i(\mathbf{x}) = \begin{cases} 1 & \text{if } \mathbf{x} \in \Omega_i \\ 0 & \text{otherwise} \end{cases} \quad (3.36)$$

The theory of normalized convolution, introduced by Knutsson and Westin in [97], is a simple and useful extension of convolution that accounts for uncertain or missing image samples. In this formulation, normalized convolutions naturally appear from the optimality conditions to produce local intensity averages inside a region.

Since no smoothing occurs across the boundary of Ω_i in (3.36), s_i can be interpreted as a smooth approximation of the image restricted to the region Ω_i . It is in analogy with optimal approximations obtained with piecewise-smooth formulations derived from the full Mumford-Shah functional [172, 177]. Even though no constraint on the derivatives of s_i is explicitly minimized, the resulting functions are as regular as the window W . Moreover, since W is positive everywhere, the denominator of (3.36) does not vanish. Consequently, the approximation is defined everywhere and extrapolates intensity information of a single region over the entire image domain. This property is an important difference with the piecewise-smooth segmentation models in [172] and [177] that confine the definition of s_i in the region Ω_i only.

Another advantage is that the approximations are obtained by closed-form analytical expressions involving only two convolutions instead of an iterative process to solve a partial differential equation. As a result, 3D applications can be envisaged without compromising efficiency. Furthermore, if W is chosen to be a Gaussian function, having all desired properties (positivity, symmetry), convolutions can be approximated by recursive linear filtering [57, 185] with an algorithmic cost that does not depend on the spatial scale.

Let us mention that similar ideas of localizing a piecewise-constant minimal partition with efficient convolution-based approximations have been independently and simultaneously proposed by several authors, including Piovanio et al. [140], Brox et al. [29, 31], Li et al. [107] and our work, described in [125]. Lankton et al. have describe in [102] a slightly different approach in which localized criteria are defined only around the boundary, not in the whole domain. They also extend the localization principle to histogram separation based on the Bhattacharyya distance [120]. Along the same line, we develop in the next section a generalization of the localized piecewise-constant model, assuming space-varying Gaussian probabilities, to the case of non-parametric distributions.

3.2.4 Local Non-Parametric Distributions

Recall that the global classification error of a region Ω_i described by a non-parametric probability distribution is:

$$E_i(p_i) = - \int_{\Omega_i} \log p_i(I(\mathbf{x})) d\mathbf{x} \quad (3.37)$$

where no assumption is made on p_i other than $\int_{\mathbb{R}} p_i(a) da = 1$. Exactly as in the previous section, we shall consider the same error locally, within a window W around $\mathbf{y} \in \Omega$:

$$e_i(\mathbf{y}) = - \int_{\Omega_i} W(\mathbf{x} - \mathbf{y}) \log p_i(\mathbf{y}, I(\mathbf{x})) d\mathbf{x} \quad (3.38)$$

To avoid multiplication of symbol definitions, we adopt the same notation p_i , although it is important to note that $p_i : \Omega \times \mathbb{R} \rightarrow \mathbb{R}$ becomes a function of both space and intensity. Again, the global classification error is obtained by integrating $e_i(\mathbf{y})$ in the whole domain Ω , yielding:

$$E_i(p_i) = \int_{\Omega} e_i(\mathbf{y}) d\mathbf{y} = - \int_{\Omega_i} \underbrace{\left(\int_{\Omega} W(\mathbf{x} - \mathbf{y}) \log p_i(\mathbf{y}, I(\mathbf{x})) d\mathbf{y} \right)}_{r_i(\mathbf{x}, p_i)} d\mathbf{x} \quad (3.39)$$

Thus, the new setting in the general formulation (3.5) becomes:

$$\begin{cases} \boldsymbol{\alpha}_i = \{p_i\} \\ r_i(\mathbf{x}, p_i) = - \int_{\Omega} W(\mathbf{x} - \mathbf{y}) \log p_i(\mathbf{y}, I(\mathbf{x})) d\mathbf{y} \end{cases} \quad (3.40)$$

with the additional constraint that p_i must be a valid probability density at each point in space, such that:

$$\forall \mathbf{y} \in \Omega, \quad \int_{\mathbb{R}} p_i(\mathbf{y}, a) da = 1 \quad (3.41)$$

Combining calculus of variations from section 3.2.2 and section 3.2.3, it can be shown that the optimal p_i^* that minimizes (3.39) under the constraint (3.41) is given by:

$$p_i^*(\mathbf{y}, a) = \frac{\int_{\Omega_i} W(\mathbf{x} - \mathbf{y}) K_{\epsilon}(I(\mathbf{x}) - a) d\mathbf{x}}{\int_{\Omega_i} W(\mathbf{x} - \mathbf{y}) d\mathbf{x}} \quad (3.42)$$

This expression is the formula for the parameter update step of the alternate minimization algorithm. It is a generalization of normalized convolution to local, space-varying Parzen window estimates. This is the most general description of a region that we consider in this work. This generalization is consistent with all previously-mentioned models in the following sense: in the limiting case of W reducing to a constant value, (3.42) amounts to computing p_i with standard kernel density estimation (3.26). Likewise, if p_i is assumed to be a Gaussian distribution, (3.42) boils down to the piecewise-smooth model with normalized

convolution (3.36). Finally, if W is constant and p_i is assumed Gaussian, everything reduces to the piecewise-constant model with a single average value as region descriptor. This property enables all these models to be used in combination so that one can select different criteria in background and foreground regions of the image for specific target applications.

3.2.5 Maximum-Flux Criterion

In this section, we complete the list of compatible models that can be plugged in the general framework with an edge-based criterion, a useful complement to the previously-mentioned region homogeneity measures. A practical motivation of such a combination is that region-based terms are usually more robust and less sensitive to initial conditions while the edge-based terms increase segmentation accuracy.

In [176], Vasilevskiy and Siddiqi propose to segment contrasted objects such as vessels in angiography by maximizing the flux of the image gradient through the region boundary. This flux is obtained as a boundary integral of the scalar product between ∇I and the outward-pointing unit normal \mathbf{n} to the surface:

$$\mathbf{F}(\Omega_i) = \int_{\partial\Omega_i} \langle \nabla I_\sigma, \mathbf{n} \rangle d\mathbf{s} \quad (3.43)$$

where I_σ is a smoothed version of the image to ensure differentiability before computing the image derivatives. Intuitively, maximizing $\mathbf{F}(\Omega_i)$ not only attracts the boundary of Ω_i in areas where the norm of the gradient is high, but also tends to snap and align the surface normals with the gradient in order to maximize the scalar product $\langle \nabla I_\sigma, \mathbf{n} \rangle$.

The boundary integral $\mathbf{F}(\Omega_i)$ can be easily transformed into a region integral with the divergence theorem that states that the outward flux of any differentiable vector field $\mathbf{v} : \Omega \mapsto \mathbb{R}^n$ through a closed surface is equal to the volume integral of the divergence of \mathbf{v} within the enclosed region:

$$\int_{\partial\Omega_i} \langle \mathbf{v}, \mathbf{n} \rangle d\mathbf{s} = \int_{\Omega_i} \nabla \cdot (\mathbf{v}) d\mathbf{x} \quad (3.44)$$

Using (3.44) with $\mathbf{v} = \nabla I_\sigma$, the flux-maximizing criterion can be expressed as:

$$\begin{aligned} \mathbf{F}(\Omega_i) &= \int_{\partial\Omega_i} \langle \nabla I_\sigma, \mathbf{n} \rangle d\mathbf{s} = \int_{\Omega_i} \nabla \cdot (\nabla I_\sigma(\mathbf{x})) d\mathbf{x} \\ &= \int_{\Omega_i} \Delta I_\sigma(\mathbf{x}) d\mathbf{x} \end{aligned} \quad (3.45)$$

where Δ is the Laplacian operator. Thus, maximizing the image gradient flux through a boundary has a tight relationship with the use of Laplacian zero-crossings in the context of edge detection, as studied by Kimmel et al. in [96]. This corresponds to the following setting for $r_i(\mathbf{x}, \boldsymbol{\alpha}_i)$ in the general framework:

$$\begin{cases} \alpha_i = \{\emptyset\} \\ r_1(\mathbf{x}) = \pm \Delta I_\sigma(\mathbf{x}) \\ r_2(\mathbf{x}) = 0 \end{cases} \quad (3.46)$$

	Classification error function $r_i(\mathbf{x}, \boldsymbol{\alpha}_i)$	Update of parameters $\boldsymbol{\alpha}_i$
Piecewise-Constant	$r_i = (I(\mathbf{x}) - c_i)^2$	$c_i = \text{mean}$
Gaussian	$r_i = \frac{1}{2\sigma_i^2} (I(\mathbf{x}) - c_i)^2 + \log(\sigma_i)$	$(c_i, \sigma_i^2) = (\text{mean}, \text{var})$
Non-Parametric	$r_i = -\log(p_i(I(\mathbf{x})))$	$p_i = \text{Parzen PDF}$
Piecewise-Smooth	$r_i = \int_{\Omega} W(\mathbf{x} - \mathbf{y})(I(\mathbf{x}) - s_i(\mathbf{y}))^2 d\mathbf{y}$	$s_i = \text{Norm. Conv.}$
Local Non-Parametric	$r_i = -\int_{\Omega} W(\mathbf{x} - \mathbf{y}) \log p_i(I(\mathbf{x}), \mathbf{y}) d\mathbf{y}$	$p_i = \text{Local PDF}$
Gradient Flux	$r_1 = \pm \Delta I(\mathbf{x}) \quad r_2 = 0$	N/A

Table 3.1 — Catalog of global/local region statistics and flux maximization. This table provides summary information of the region models that can be used with all the algorithms developed in this manuscript, in a supervised or unsupervised fashion. Depending on the target anatomical structure, one model can be chosen from this list, optionally with different settings for the foreground ($i = 1$) and the background regions ($i = 2$). The novel piecewise-smooth and local non-parametric models are contributions of this work and rely on normalized convolution to model spatial variation of statistical properties with a much lower computational cost than existing approaches with Partial Differential Equations.

The sign of ΔI_{σ} must be chosen in advance to perform either minimization or maximization of \mathbf{F} , which depends on the expected contrast of the target structure. For instance, segmentation of a dark object on a brighter background implies the choice of $r_1 = -\Delta I_{\sigma}$ for the foreground and $r_2 = 0$.

This concludes the list of intensity models that will be used in all experiments and illustrations for the unsupervised region-based segmentation algorithms developed in the following chapters. Table 3.2.5 provides a summary of these criteria and the associated expression of $r_i(\mathbf{x}, \boldsymbol{\alpha}_i)$, including two new models that are specifically designed to efficiently account for spatial variations of statistical properties.

In the next section, we propose an algorithm that specializes the general framework in the case of a geometric constraint on the perimeter of the foreground region, which is a standard regularization choice since the seminal works on geometric active contours [34, 94] and the Mumford-Shah model [126]. This leads to a convex minimization with respect to the partition variable, using a membership function u to represent the foreground region. Illustrations of all previously-mentioned region intensity models will show the versatility of this framework to deal with various imaging conditions.

3.3 Convex Relaxation with a Membership Function

Using the perimeter of the foreground as a geometric constraint $\mathcal{R}(\Omega_1) = \text{Per}(\partial\Omega_1)$, the general formulation (3.5) becomes the following minimization problem:

$$\min_{\Omega_1, \alpha_1, \alpha_2} \left\{ F_0(\Omega_1, \alpha_1, \alpha_2) = \text{Per}(\partial\Omega_1) + \lambda \int_{\Omega_1} r_1(\mathbf{x}, \alpha_1) d\mathbf{x} + \lambda \int_{\Omega \setminus \Omega_1} r_2(\mathbf{x}, \alpha_2) d\mathbf{x} \right\} \quad (3.47)$$

where λ balances the classification error relatively to the geometric constraint.

Deriving a computational algorithm to solve (3.47) requires first to choose a representation of the foreground region with a suitable function space to allow for calculus of variations. For their ability to deal with discontinuities, functions of bounded variations are particularly adapted to study a geometric functional such as (3.47).

3.3.1 Functions of Bounded Variations

A function $u : \Omega \rightarrow \mathbb{R}$ is said to be of *bounded variation* if its *total variation* is finite. If u is differentiable, its total variation is the integral over the domain Ω of the norm of its gradient:

$$TV(u, \Omega) = \int_{\Omega} \|\nabla u\| \quad (3.48)$$

If the function u is integrable but not differentiable, its total variation can still be measured by:

$$TV(u, \Omega) = \int_{\Omega} |Du| := \sup \left\{ \int_{\Omega} u(\mathbf{x}) \nabla \cdot \varphi(\mathbf{x}) d\mathbf{x} : \varphi \in C_c^1(\Omega, \mathbb{R}^n), \forall \mathbf{x} \|\varphi(\mathbf{x})\| \leq 1 \right\} \quad (3.49)$$

where $C_c^1(\Omega, \mathbb{R}^n)$ is the set of continuously-differentiable vectorial functions of compact support. With this definition, the space of functions of bounded variations is usually denoted $BV(\Omega)$ and defined by:

$$BV(\Omega) = \left\{ u \in L^1(\Omega), \int_{\Omega} |Du| < +\infty \right\} \quad (3.50)$$

This space is crucial in order to represent discontinuous functions of bounded variations such as a binary characteristic function of a set $\Omega_i \subset \Omega$ defined by:

$$\chi_i(\mathbf{x}) = \begin{cases} 1 & \text{if } \mathbf{x} \in \Omega_i \\ 0 & \text{otherwise} \end{cases} \quad (3.51)$$

By construction, χ_i is not differentiable in the usual sense at the boundary $\partial\Omega_i$ but is a valid function of $BV(\Omega)$ if Ω_i is of finite perimeter with piecewise-regular boundaries [4]. Since a characteristic function mathematically characterizes a region Ω_i as a subset of the image domain Ω , $BV(\Omega)$ is a suitable space to perform calculus of variations in segmentation algorithms and in many other application areas in image processing such as restoration [3, 149]. Moreover, a useful geometric interpretation of $BV(\Omega)$ is obtained with the definition of the perimeter of $\partial\Omega_i$, given as:

$$\text{Per}(\partial\Omega_i) = TV(\chi_i, \Omega) = \int_{\Omega} |D\chi_i| \quad (3.52)$$

3.3.2 General Convex Extension

The crux of the extension is that the minimization problem (3.47) can be solved by considering a closely related problem that is convex with respect to the *partition* variable. Recall that an optimization problem is convex if it involves both a convex function *and* a convex set of admissible solutions. In this respect, (3.47) is not convex since the set of sub-domains $\Omega_i \subset \Omega$ is not convex. Nonetheless, it can be expressed as an optimization problem in the set of characteristic functions (still non-convex), so that it also reads

$$\min_{\chi, \alpha_1, \alpha_2} \left\{ \int_{\Omega} |D\chi(\mathbf{x})| d\mathbf{x} + \lambda \int_{\Omega} \chi(\mathbf{x}) r_1(\mathbf{x}, \alpha_1) d\mathbf{x} + \lambda \int_{\Omega} (1 - \chi(\mathbf{x})) r_2(\mathbf{x}, \alpha_2) d\mathbf{x} \right\} \quad (3.53)$$

Under this form, we propose to extend (3.47) into a problem that is convex in its *partition* variable, replacing the characteristic function χ by a fuzzy membership function u belonging to a convex set. A suitable choice for this set is the space of functions of bounded variations taking values in the interval $[0, 1]$, noted hereafter $BV_{[0,1]}(\Omega)$. In principle, this extension bears some similarities with relaxation techniques in linear programming, which consist in substituting a function constrained to only take discrete values $\{0, 1\}$ with one that takes intermediate real values in the interval $[0, 1]$. In this context, the relaxation leads to a new formulation of the segmentation problem, which we call *Fuzzy Region Competition* in [125]:

$$u \in BV_{[0,1]}, \alpha_1, \alpha_2 \left\{ \underbrace{\int_{\Omega} |Du| + \lambda \int_{\Omega} u(\mathbf{x}) r_1(\mathbf{x}, \alpha_1) d\mathbf{x} + \lambda \int_{\Omega} (1 - u(\mathbf{x})) r_2(\mathbf{x}, \alpha_2) d\mathbf{x}}_{F_1(u, \alpha_1, \alpha_2)} \right\} \quad (3.54)$$

The relaxed problem (3.54) is convex with respect to u , hence its solutions globally minimize F_1 and can be found with fast algorithms from convex optimization theory [62]. Note that (3.54) is convex, but it is not *strictly* convex. Consequently its solution is not necessarily unique. However, convexity implies that all solutions form a convex set and correspond to equal values of F .

Furthermore, the key property is that the solutions of the relaxed problem (3.54) allow to find solutions of the original problem (3.47) by a thresholding operation, which is formalized in Proposition 1 below.

Proposition 1 *Fixing α_1 and α_2 , if $u^* \in BV_{[0,1]}(\Omega)$ is a global minimizer of F_1 then for almost every $t \in [0, 1]$, the characteristic function $\chi_u^*(\mathbf{x}, t)$ defined in $\Omega \times [0, 1]$ by*

$$\chi_u^*(\mathbf{x}, t) = \begin{cases} 1 & \text{if } u^*(\mathbf{x}) > t \\ 0 & \text{otherwise} \end{cases} \quad (3.55)$$

is also a global minimizer of F_1 . In addition, the set $\Omega_t = \{\mathbf{x} \in \Omega, u^(\mathbf{x}) > t\}$ is a global minimizer of F_0 .*

A proof of Proposition 1 is given in Annex A. Proposition 1 reveals that the set of solutions of Problem (3.54), expressed with a membership function, is *stable under thresholding*: any binary function obtained by thresholding an optimal membership function is still a solution of (3.54). In addition, such thresholded binary solution corresponds to the characteristic function of a set that is a global minimizer of the original problem (3.47).

In practice, the membership function u converges in most cases to a binary function during the minimization of F_1 . In this case, all thresholds $t \in [0, 1]$ are equivalent and the solution of both the relaxed problem and the original one is unique. However, there exist 'pathological' cases for which several minimizers of F_1 , not necessarily binary, could solve the non strictly convex problem (3.54). Those cases do not contradict Proposition 1, neither do they easily show up numerically.

3.3.3 Fast Minimization Scheme

We can now develop a general optimization strategy to solve every two-phase segmentation problem that can be expressed through the general formulation (3.47), choosing any of the models from the list provided in section 3.2. In the *unsupervised* setting, F_1 can be minimized iteratively by alternating the following two steps:

Algorithm 2: Alternate minimization Scheme with a membership function u

Set $j = 0$, choose initial u^0

repeat

(A) u^j fixed, minimize (3.54) w.r.t. α and update parameters α^j ,

(B) α^j fixed, minimize (3.54) w.r.t u and update membership u^{j+1} .

until steady state of u^* is found

Choose any t to threshold membership, $\Omega_1^* = \{\mathbf{x} \in \Omega, u^*(\mathbf{x}) > t\}$

Step **(A)** depends on the specific choice of error functions such as the region models listed in section 3.2, relying on global or local statistics. As we will see in various examples, the update formula for the optimal region parameters are similar to the expressions developed in section 3.2.1 to 3.2.4, with a slight difference: They are obtained using the fuzzy membership function u instead of a domain integral with a characteristic function.

Step **(B)**, can be realized by applying a generic minimization scheme for the variable u , following the strategy proposed by Bresson et al. in [26]: Fixing the region parameters, minimizing F_1 with respect to u in $BV_{[0,1]}$ is equivalent to minimizing

$$\int_{\Omega} |Du| + \int_{\Omega} ur \quad (3.56)$$

in BV under the constraint $0 \leq u \leq 1$, where $r(\mathbf{x}) = \lambda(r_1(\mathbf{x}, \alpha_1) - r_2(\alpha_2, \mathbf{x}))$ is the competition function. Based on [130], this *constrained* problem has the same set of minimizers than the *unconstrained* problem of minimizing

$$\int_{\Omega} |Du| + \int_{\Omega} ur + \beta \nu(u), \quad (3.57)$$

with the exact penalty term $\nu(\xi) = \max(0, |2\xi - 1| - 1)$ and $\beta > \frac{1}{2} \|r\|_\infty$. Even though the minimization of (3.57) can be numerically performed using a gradient-descent scheme based on the *Euler-Lagrange* equation, as in [130] no advantage would be taken of convexity. We thus choose to follow [26] and exploit the fast duality projection algorithm of *Chambolle* [36]. To that end, we add an auxiliary variable v and consider the following weak approximation:

$$\min_{(u,v) \in BV} \left\{ \int_{\Omega} |Du| + \frac{1}{2\theta} \int_{\Omega} (u - v)^2 + \int_{\Omega} rv + \beta \nu(v) \right\}, \quad (3.58)$$

where θ is chosen to be small enough so that the two components of any minimizing couple (u^*, v^*) are almost identical with respect to the L^2 norm. Note that this approximation is still component-wise convex in u and v . Again, the problem is minimized by a two-stage alternate iterative scheme. u being fixed, the optimal v is directly solved point-wise [26]:

$$v = \max(\min(u - \theta r, 1), 0) \quad (3.59)$$

This update formula should be interpreted in terms of the competition function r . Recall that negative values of r indicate a propensity of a given pixel to be included in the foreground region, which corresponds to a membership value of 1. Thus, (3.59) reflects this propensity with a linear update at a speed proportional to θ . When full membership is attained, $v = 1$ or $v = 0$, the function saturates. For large values of θ , this corresponds to thresholding r at 0, without imposing any regularity. The geometric regularization is obtained by the coupling between u and v in a second inner loop: v being fixed, we should find the function u that minimizes the first two terms of (3.58):

$$\int_{\Omega} |Du| + \frac{1}{2\theta} \int_{\Omega} (u - v)^2 \quad (3.60)$$

which is a convex $TV + L^2$ problem, also known as the Rudin-Osher-Fatemi model for image restoration with a total variation regularizer [149]. The convex functional (3.60) can be minimized with a fast duality projection algorithm proposed by Chambolle in [36]. Thus, Chambolle's total variation algorithm can be applied for the minimization of (3.58) with respect to u . This algorithm consists in computing the restored function u from the noisy image v with [36]:

$$u = v - \theta \nabla \cdot \mathbf{p} \quad (3.61)$$

where the vector field \mathbf{p} is computed using a fixed point algorithm, iterating on $n \geq 0$

$$\tau > 0, \quad \mathbf{p}^0 = 0, \quad \mathbf{p}^{n+1} = \frac{\mathbf{p}^n + \tau \nabla(\nabla \cdot (\mathbf{p}^n) - v/\theta)}{1 + \tau \|\nabla(\nabla \cdot (\mathbf{p}^n) - v/\theta)\|} \quad (3.62)$$

In practice, this algorithm is numerically very stable. Even though there is a geometric constraint on the perimeter of the region, the algorithm does not explicitly require the computation of the curvature of u , contrary to Euclidean length shortening flows and most level-set algorithms. In fact, it does not rely on any derivative of u since the evolving function, in $BV(\Omega)$, is not assumed to be differentiable. Thus, the numerical scheme is consistent with Proposition 1 that expects convergence of u to a binary function.

Decoupling u and v has a relaxation effect on the regularization and a positive impact on the overall convergence. Nonetheless, choosing an unreasonably large value of θ is counterproductive since it diminishes regularization almost completely. In all experiments, a decoupling parameter value of $\theta = 0.01$ is used.

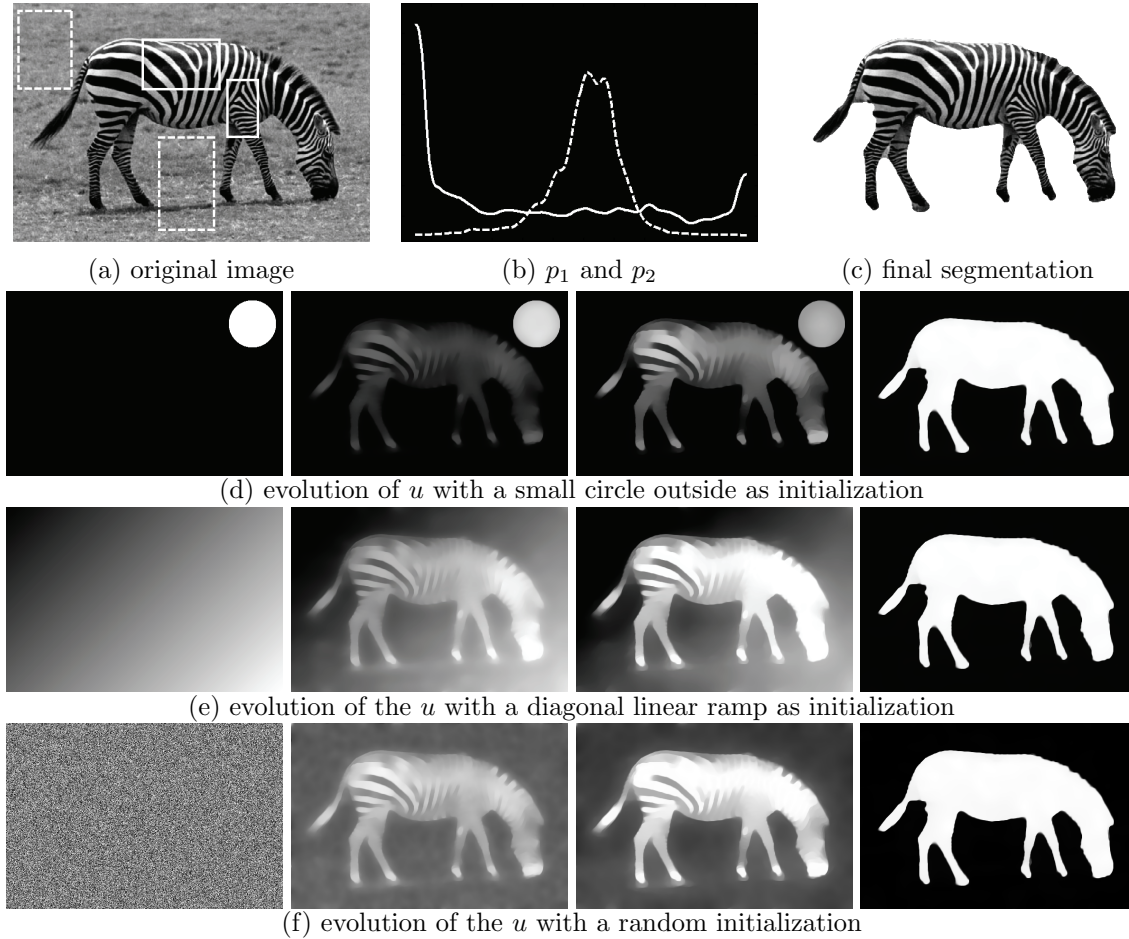


Figure 3.2 — *Fuzzy Region Competition*, supervised segmentation of the zebra image: (a) original image and patches used to estimate the background (dashed) and foreground (solid) histograms p_1 and p_2 given in (b). (c) Final segmentation. (d-f) 3 different initializations, intermediary states (step 10-20) and final partition function u (step 300). In all cases, $\lambda = 0.1$ and $\theta = 0.01$

In Figure 3.2, we show an immediate application of the generic minimization scheme in a *supervised* segmentation experiment on the *zebra* image. The competition function $r = r_1 - r_2$ is built *a priori*, using a non-parametric negative log-likelihood model. Probability distributions $p_i(I)$ are estimated from foreground/background user-defined patches in the image and are kept fixed during evolution, such that $r = \log(p_2/p_1)$. We observe that this supervised method gives always the same binary partition function, regardless of initial conditions, even with an initial random initialization.

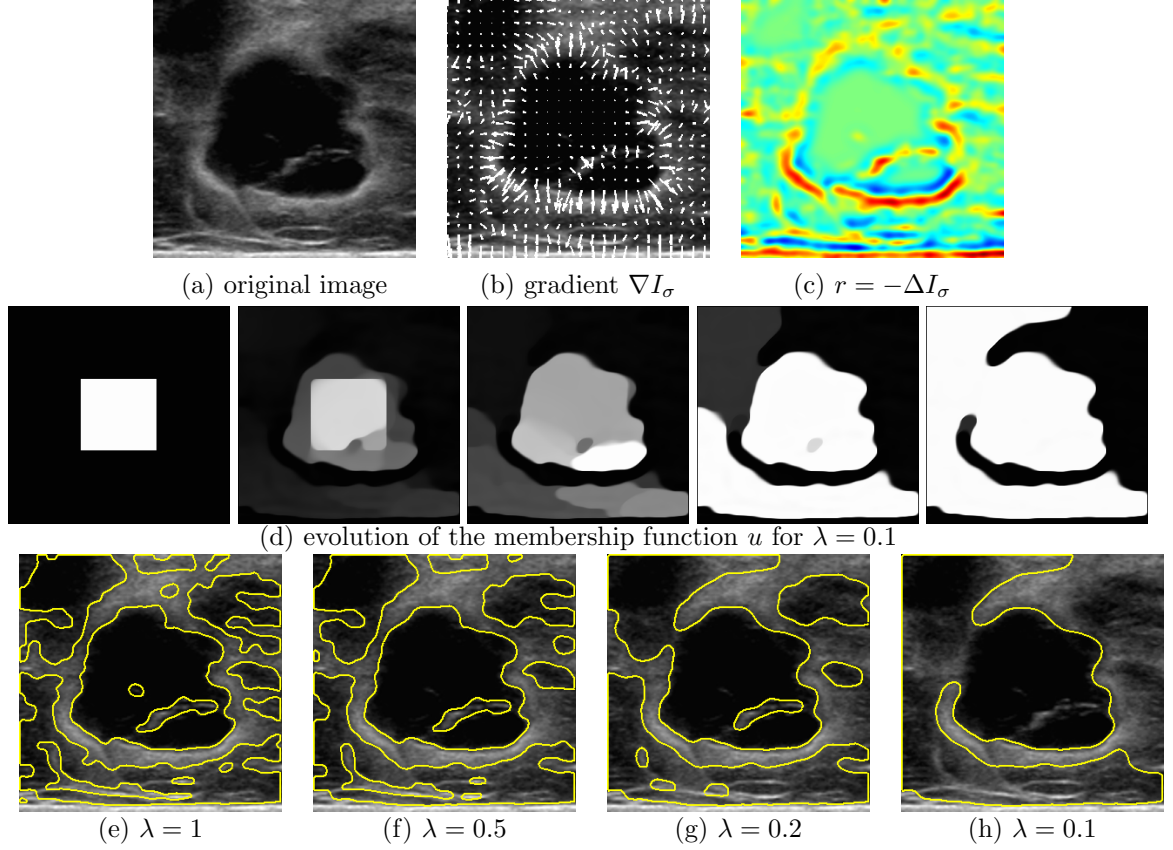


Figure 3.3 — 2D Ultrasound image of a breast lesion. Global geometric flux-maximization with $r = -\Delta I_\sigma$. The resulting segmentation *globally maximizes the image gradient flux through the boundary*, subject to a geometric constraint. Results are shown for decreasing values of λ to show the effect of the length-shortening constraint. In all cases, $\theta = 0.01$

Figure 3.3 illustrates another supervised example, using the gradient flux as a minimization criterion, as detailed in section 3.2.5. The test image is a 2D ultrasound acquisition of a breast lesion. The competition function is in this case $r = -\Delta I_\sigma$, fixed throughout the minimization process. Using Proposition 1, the segmenting curve Γ^* global maximizes the image gradient flux through the boundary, subject to a geometric constraint:

$$\Gamma^* = \min \left\{ \text{Per}(\Gamma) - \lambda \int_{\Gamma} \langle \nabla I_\sigma, \mathbf{n} \rangle \right\} \quad (3.63)$$

The influence of the geometric constraint is shown by comparing the result for different values of the free parameter λ in Fig.3.3. Besides smoothing, lower values of λ also tend to fuse connected components in order to decrease to overall perimeter of the boundary.

In general, flux-maximization provides good accuracy of the boundary localization. However, without additional intensity homogeneity criterion, it is prone to severe leakages in areas where the contrast tends to fade. Consequently, gradient flux should most often be combined with other region-based criteria.

We can now consider *unsupervised* examples, using classification errors $r_i(\mathbf{x}, \boldsymbol{\alpha}_i)$ developed in the general case from section 3.2.1 to 3.2.4. In the following, we show that the new relaxed formulation with a membership function has a consequence on the periodic update formula for the region parameters $\boldsymbol{\alpha}_i$. They should now be estimated in a fuzzy way at Step **(A)** of the two-stage iterative process.

3.3.4 The Piecewise-Constant Case

In [130], Nikolova et al. propose to solve the minimization involved in Chan and Vese's *Active Contours Without Edges* [40] by considering an auxiliary convex problem. They show that if c_1 and c_2 are fixed and u^* is a solution of

$$\min_{u \in BV_{[0,1]}(\Omega)} \left\{ F_{[130]}(u) = \int_{\Omega} |Du| + \lambda \int_{\Omega} u ((I - c_1)^2 - (I - c_2)^2) \right\}, \quad (3.64)$$

then the set $\Omega_t = \{\mathbf{x} \in \Omega, u^*(\mathbf{x}) > t\}$ is for almost every $t \in [0, 1]$ a minimizer of the minimal variance functional:

$$F_{[40]}(\Omega_1) = \text{Per}(\partial\Omega_1) + \lambda \int_{\Omega_1} (I - c_1)^2 + \lambda \int_{\Omega \setminus \Omega_1} (I - c_2)^2 \quad (3.65)$$

This result inspired the general formulation of section 3.3.2, and also guides the first unsupervised segmentation algorithm. Solving the *Active Contours Without Edges* model corresponds to choosing $r_i(c_i) = \lambda (I - c_i)^2$, $\boldsymbol{\alpha}_i = \{c_i\}$ in the general formulation (3.54), such that the problem becomes

$$\min_{\substack{u \in BV_{[0,1]} \\ (c_1, c_2) \in \mathbb{R}^2}} \left\{ F_c(u, c_1, c_2) = \int_{\Omega} |Du| + \lambda \int_{\Omega} u(I - c_1)^2 + \lambda \int_{\Omega} (1 - u)(I - c_2)^2 \right\} \quad (3.66)$$

Applied to (3.66), Proposition 1 gives the same result that was already shown in [130]. Nonetheless, although closely related by

$$F_c(u, c_1, c_2) = F_{[130]}(u, c_1, c_2) + \lambda \int_{\Omega} (I - c_2)^2, \quad (3.67)$$

the two involved functionals lead to a slightly different perspective. $F_{[130]}$ is not to be considered as a minimization on the triplet (u, c_1, c_2) but as a convex alternative to obtain a minimizer of the original problem [40], when c_1 and c_2 are fixed. Indeed, no optimization of c_1 and c_2 is involved in [130]. In practice, this implies the choice of an arbitrary level set of u (e.g. $t = 0.5$) in step **(A)** of the alternate minimization scheme.

This may at first seem a minor issue since any level t should eventually produce a minimizer at convergence. However, full convergence of u is not obtained at each step **(B)** since the two steps are periodically interlaced. In particular in the first iterations, all levels of u are not equivalent. Hence the arbitrary choice of a level t for the computation of c_1 and c_2 may introduce a bias and slow down the optimization process. On the contrary, in the proposed approach, the derivatives of F_c with respect to scalars c_1 and c_2 give directly new

optimality conditions that naturally involve all levels of the fuzzy membership function and yield the weighted averages:¹ u :

$$c_1^* = \frac{\int_{\Omega} uI}{\int_{\Omega} u}, \quad c_2^* = \frac{\int_{\Omega} (1-u)I}{\int_{\Omega} (1-u)} \quad (3.68)$$

Fuzzy Region Competition with a piecewise-constant model follows the generic Algorithm 2, alternating on:

- (A) u being fixed, compute the weighted averages c_1 and c_2 using (3.68).
- (B) c_1 and c_2 perform a few inner iterations on v (3.59), u (3.61) and \mathbf{p} (3.62).

At convergence, the final segmentation is obtained by thresholding u at any level in $[0, 1]$, as justified by Proposition 1.

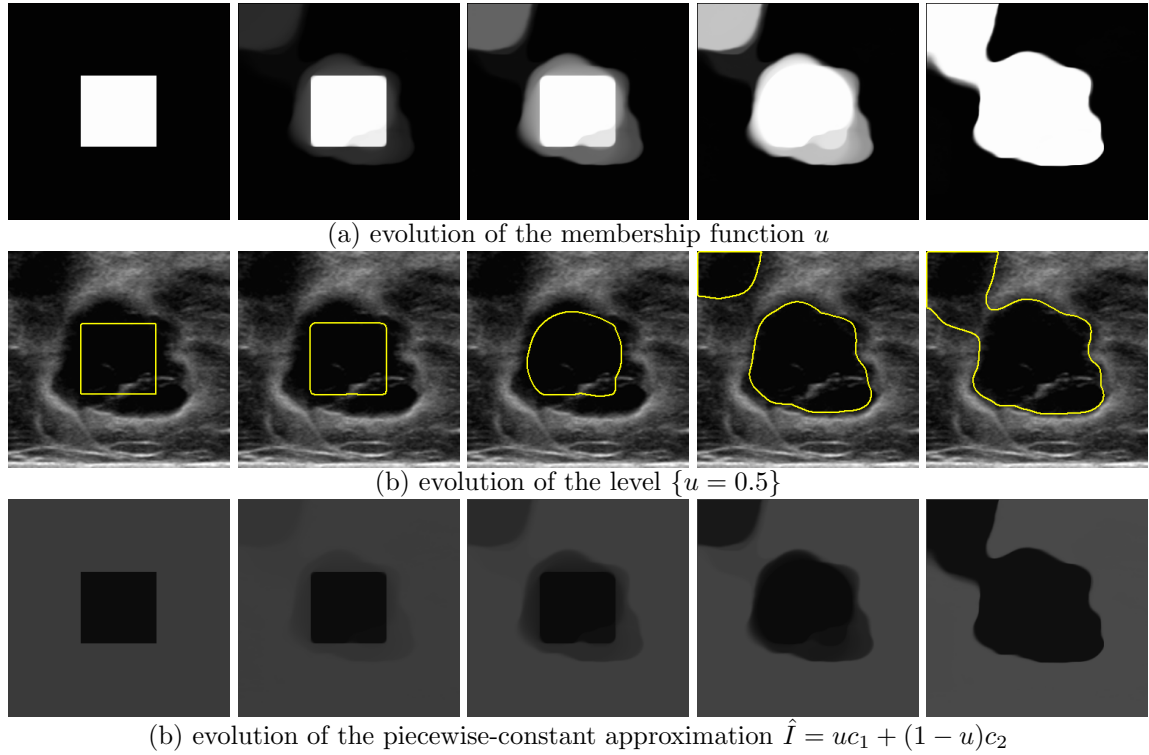


Figure 3.4 — Fuzzy Region Competition with a piecewise-constant model on the ultrasound breast lesion image. (a) evolution of the membership function, (b) segmentation boundary at level 0.5, (c) piecewise-constant approximation $\hat{I} = uc_1 + (1-u)c_2$. Initialization and all parameters are the same than in Fig. 3.3 for visual comparison with the flux-maximizing model.

¹If u is 0 almost everywhere (or 1 almost everywhere), $c_1^* = c_2^* = \frac{1}{|\Omega|} \int_{\Omega} I$.

In Figure 3.4, we show the results of the piecewise-constant model on the breast lesion ultrasound image. Observe that the lesion is fused with a surrounding tissue of similar intensity because the intensity of the wall separating them is closer to c_1 than to c_2 .

In Figure 3.5, this unsupervised segmentation algorithm is illustrated on a X-Ray image of a brain aneurysm phantom. As in the supervised case, the steady state is always a binary function. The final boundary does not depend on the initial conditions, randomly set in this example. However, as we will discuss in more details in the next chapter, symmetric foreground/background solutions can be obtained since they exactly have the same functional value $F_c(u, c_1, c_2) = F_c(1 - u, c_2, c_1)$.

This method is a tool for segmenting two-phase images corrupted by a Gaussian noise of constant variance, which is the underlying assumption. Unfortunately, as already discussed, this is hardly realistic for medical images in clinical applications.

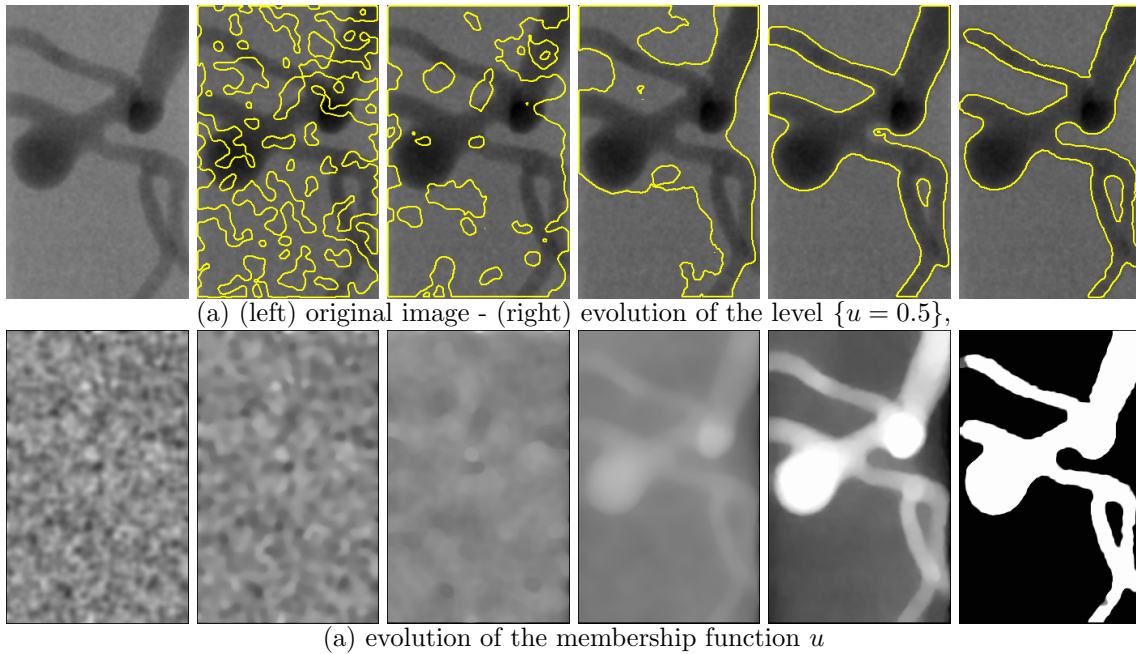


Figure 3.5 — Fuzzy Region Competition with a piecewise-constant model. The original image (a) on the left is an X-ray acquisition of a brain aneurysm phantom. The evolution of the level $\{u = 0.5\}$ together with the evolution of the membership function u , starting from a random initialization

3.4 Unsupervised Fuzzy Region Competition

In this section, we apply the convex extension and the Fuzzy Region Competition algorithm to show with examples the complementarity and versatility of the region intensity models defined in the beginning of this chapter for unsupervised segmentation, in 2D and 3D. As in the piecewise-constant case, region parameters are now estimated in a fuzzy way during the minimization process.

3.4.1 Non-Parametric Distributions

For a better characterization of region intensities, a possible way to relax the piecewise-constant and Gaussian assumptions is to minimize a negative log-likelihood error with a non-parametric probability distribution, and choose $r_i(\mathbf{x}, p_i) = -\log p_i(I(\mathbf{x}))$.

In order to illustrate the algorithm on natural color photographs, we consider a natural extension to multi-channel images. If $\mathbf{I} : \Omega \rightarrow \mathbb{R}^d$ is a vector-valued image with d components, $p_i : \mathcal{A} \subset \mathbb{R}^d \rightarrow \mathbb{R}$ becomes a d -dimensional joint probability distribution on the feature space \mathcal{A} . With a fuzzy membership function $u \in BV_{[0,1]}$, the classification error associated to the foreground becomes:

$$E_1(u, p_1) = - \int_{\Omega} u(\mathbf{x}) \log p_1(\mathbf{I}(\mathbf{x})) d\mathbf{x} \quad (3.69)$$

Using the same strategy than in section 3.2.2 and studying the optimality conditions of E_i with respect to the unknown feature distribution p_i under the additional constraint $\int_{\mathcal{A}} p_i(\mathbf{a}) d\mathbf{a} = 1$, it can be shown that for a fixed membership u , the optimal p_i^* are:

$$p_1^*(\mathbf{a}) = \frac{\int_{\Omega} u(\mathbf{x}) K_{\epsilon}(\mathbf{I}(\mathbf{x}) - \mathbf{a}) d\mathbf{x}}{\int_{\Omega} u(\mathbf{x}) d\mathbf{x}} \quad p_2^*(\mathbf{a}) = \frac{\int_{\Omega} (1 - u(\mathbf{x})) K_{\epsilon}(\mathbf{I}(\mathbf{x}) - \mathbf{a}) d\mathbf{x}}{\int_{\Omega} (1 - u(\mathbf{x})) d\mathbf{x}} \quad (3.70)$$

These optimal functions now correspond to continuous versions of *weighted* kernel density estimates. The contribution of each pixel \mathbf{x} to the estimation of the foreground distribution is weighted by its membership $u(\mathbf{x})$. During minimization, each pixel may contribute to both regions according to the *certainty* of its current classification.

A d -dimensional isotropic Gaussian can be used for the estimation kernel K_{ϵ} . In this case, the algorithmic complexity of discretizing $p_i(\mathbf{a})$ on N sampling bins is $O(MN)$ where M is the number of pixels. Among other methods to approximate a discrete sum of Gaussian kernels, the *Fast Gauss Transform*, proposed by Greengard and Strain [78], reduces the complexity to $O(M + N)$ with a controlled error bound. Histogram smoothing by Gaussian convolution, which we rely upon in our current implementation, is a cruder approximation that works reasonably well in practice if the scale ϵ is sufficiently larger to the bin size. In all experiments, we use 64^d bins and ϵ is set to 5% of the intensity range.

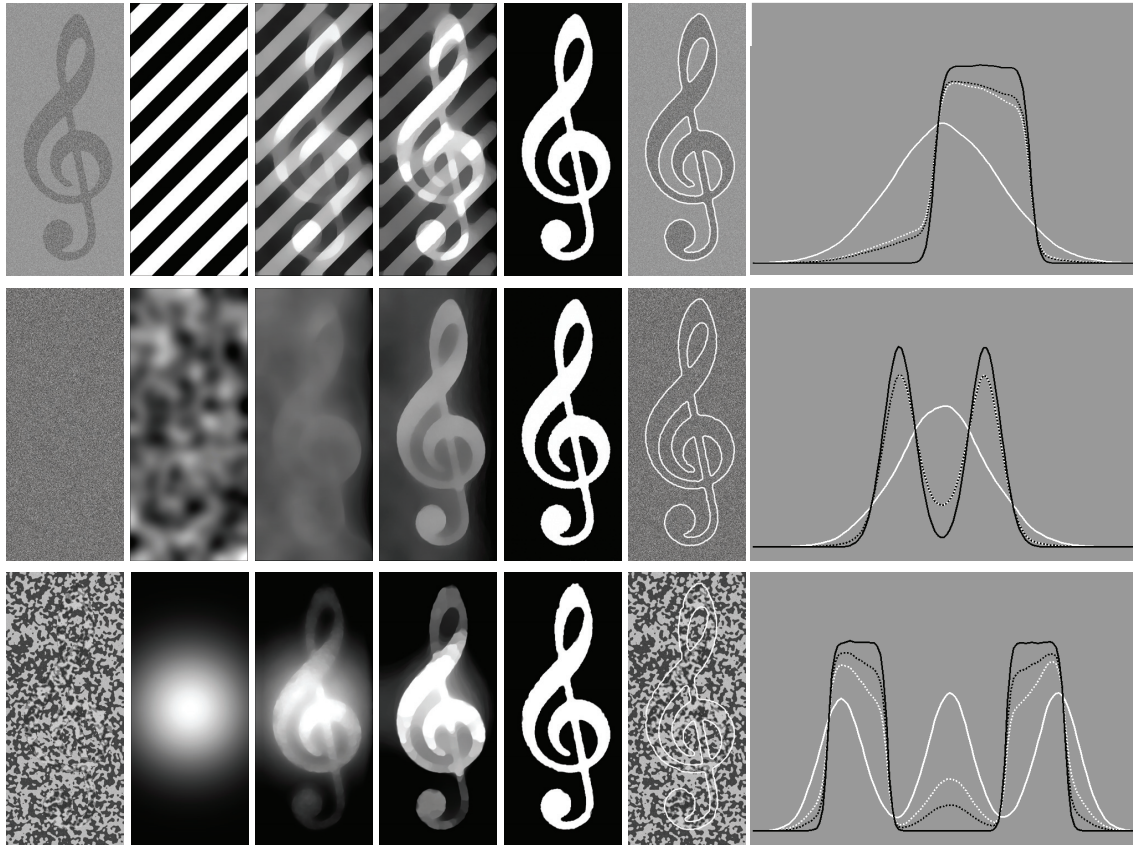


Figure 3.6 — Synthetic image segmentation with non-parametric distributions: In rows, we present 3 synthetic 2D experiments where foreground and background have been artificially generated by a global intensity probability density. In each row, from left to right: original image; initial membership function u ; two intermediate states of u ; result at convergence; corresponding boundary overlaid on the image; the initial (dashed) and final (solid) distributions of the foreground (white) and background (black). First row shows uni-modal densities of distinct mean and variance, a Gaussian foreground over a uniform background. Second row shows a uni-modal Gaussian foreground over a bi-modal Gaussian background, both distributions having the exact same mean and variance. Last row shows a tri-modal Gaussian foreground on a bi-modal uniform background, of equal mean and equal variance, with artificially-generated spatial correlations.

In Figure 3.6, the Fuzzy Region Competition algorithm with non-parametric distributions is shown on a set of synthetic gray-level images, using (3.70) to periodically re-evaluate the distributions. The method is able to cope with non-Gaussian, multi-modal, overlapping probability density functions. In the last two examples, both distributions have identical mean and variance, making the foreground virtually invisible.

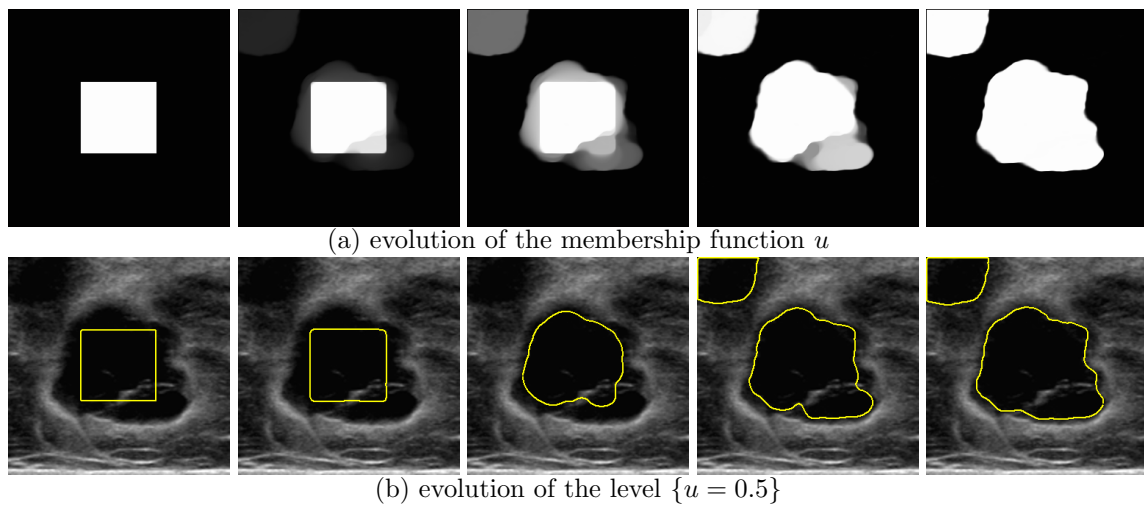


Figure 3.7 — Fuzzy Region Competition with a non-parametric probability distribution on the ultrasound breast lesion image. (a) evolution of the membership function, (b) segmentation boundary at level 0.5, Initialization and all parameters are the same than in Fig. 3.4 for visual comparison with the piecewise-constant model.

In Figure 3.7, the ultrasound breast lesion image is segmented with a non-parametric probability distribution to underline the difference with the piecewise-constant model. Contrary to Figure 3.4, the lesion is now well separated from the surrounding inhomogeneous tissue.

In Figure 3.8 and 3.9, foreground/background separation is realized on a set of photographic images to illustrate the multivariate case with $d = 3$. We have chosen as feature space $\mathcal{A} \in \mathbb{R}^3$ the CIEL*a*b* color space for its ability to mimic the logarithmic response of the eye and linearize the perception of color differences. The algorithm takes advantage of all channels simultaneously to discriminate regions that have a compact joint distribution composed of an arbitrary number of modes.

Contrary to the *supervised* case, the dependence on initial conditions of this *unsupervised* model is underlined on the two last rows of Figure 3.8. With different initial guesses for the membership function, the method extracts either the bear in the foreground or pieces of the background. Recall that the Fuzzy Region Competition functional (3.54), in this case $F(u, p_1, p_2)$, is only convex in u , and not *globally* convex, with respect to the triplet (u, p_1, p_2) . Consequently, it is not surprising that initial p_1 and p_2 select the most prominent feature modes for each region and influence the final result.

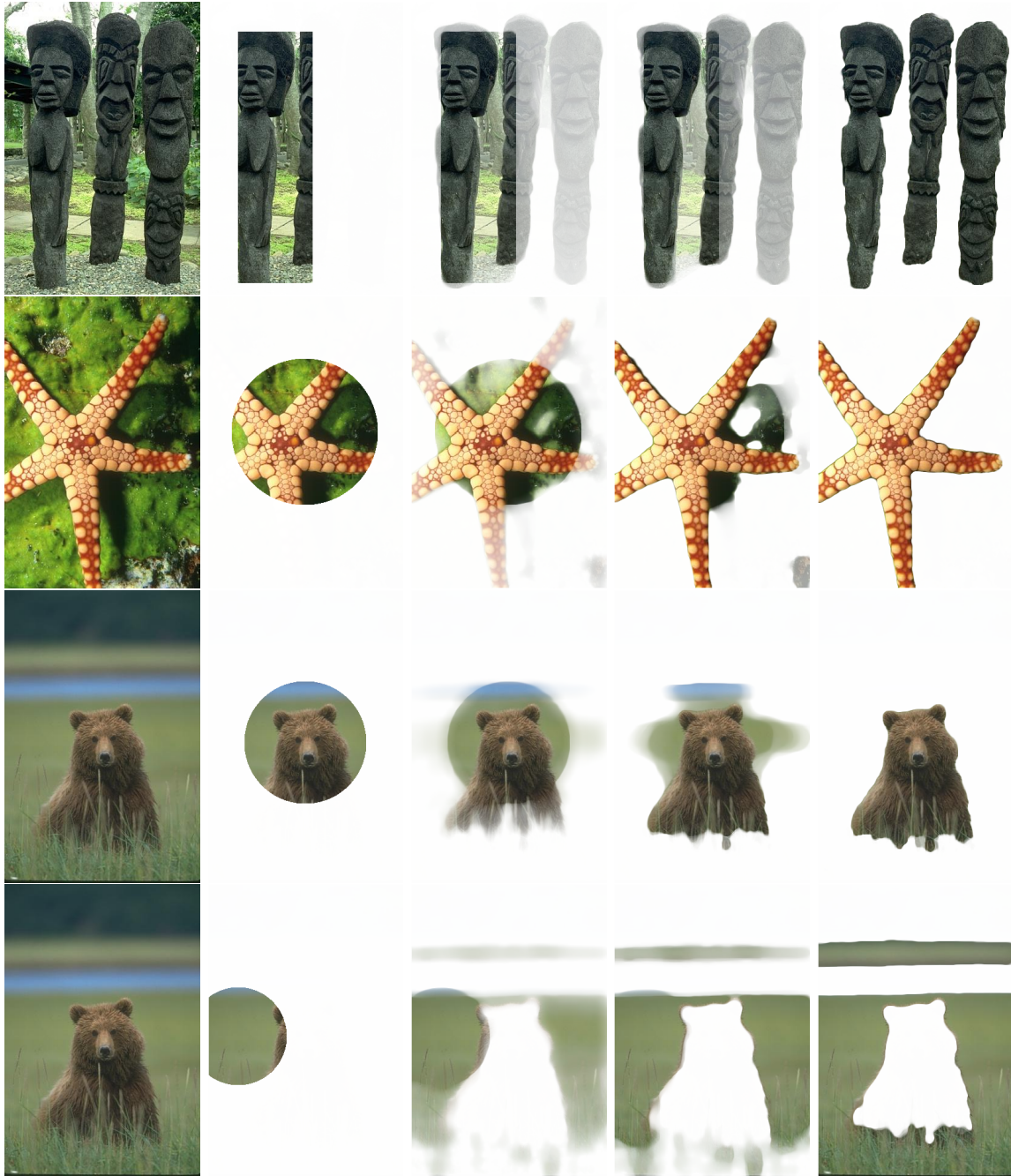


Figure 3.8 — Color images: the global non-parametric model in the multivariate case. The images are samples from the Berkeley segmentation database [118]. Feature space \mathcal{A} is CIE $L^*a^*b^*$, chosen for its ability to mimic the logarithmic response of the eye and linearize the perception of color differences. Simple euclidean distance can be used in \mathcal{A} , hence the covariance M for the kernel K can be set diagonal. In each row: (left) original image, evolution of the segmentation throughout the minimization process at iteration $k = 0$, $k = 50$, $k = 100$ and final $k = 250$. The membership function u is used as an alpha transparency map to visualize both the color image and the segmentation: the foreground object appears while its background becomes fully transparent (white). Last row: an example of initialization dependence; problem is only convex with respect to the membership function, hence initial density functions influence the result by selecting the most prominent feature modes in each region.



Figure 3.9 — Color images: the global non-parametric model in the multivariate case. Other examples from Berkely segmentation database. In each column: (left) original image, evolution of the segmentation throughout the minimization process at iteration $k = 0$, $k = 50$, $k = 100$ and final $k = 250$. The membership function u is used as an alpha transparency map to visualize both the color image and the segmentation: the foreground object appears while its background becomes fully transparent (white). The algorithm takes advantage of all channels and discriminates between regions that have a compact and multi-modal distribution in the 3D feature space (L^*, a^*, b^*).

3.4.2 The Piecewise-Smooth Case

As in section (3.2.3), we assume that the piecewise-constant hypothesis holds locally, i.e. at a certain *scale*, to account for slowly varying intensities. In order to keep the advantages of the convex framework, we introduce a symmetric window function $W : \Omega \mapsto \mathbb{R}^+$ and build a continuous sum of locally piecewise-constant models. This is achieved by choosing the region terms from Eq. (3.31) in each phase:

$$\begin{cases} \alpha_i = \{s_i\} \\ r_i(\mathbf{x}, s_i) = \int_{\Omega} W(\mathbf{x} - \mathbf{y}) (I(\mathbf{x}) - s_i(\mathbf{y}))^2 d\mathbf{y} \end{cases} \quad (3.71)$$

where the previously constant approximation c_1 becomes a function $s_1(\mathbf{y})$. The foreground classification error becomes:

$$E_1(u, s_1) = - \int_{\Omega} u(\mathbf{x}) \int_{\Omega} W(\mathbf{x} - \mathbf{y}) (I(\mathbf{x}) - s_1(\mathbf{y}))^2 d\mathbf{y} d\mathbf{x} \quad (3.72)$$

(3.72) corresponds to the specific settings $\alpha = (s_1, s_2) \in L^1(\Omega)^2$ and $r_i(\mathbf{x}, s_i)$ in the general Fuzzy Region Competition framework (3.54). The convexity in u , the *binarization* expected from Proposition 1 and the minimization scheme with Chambolle's projection algorithm are still valid. Therefore, we only need to specify how to minimize with respect to each unknown approximation. As in section 3.2.3, we can show that the update formula for s_1 and s_2 is:

$$s_1^* = \frac{W * [uI]}{W * u} \quad \text{and} \quad s_2^* = \frac{W * [(1-u)I]}{W * (1-u)} \quad (3.73)$$

The smooth case is analogous to the constant case: weighted averages c_1 and c_2 have been replaced by fuzzy normalized convolutions s_1 and s_2 . They can be interpreted either as local averages or as smooth approximations of the image within each region. Normalized convolutions naturally depend on the fuzzy membership u and $(1-u)$ as certainty measures throughout the alternate scheme:

- (A) Fixing u , compute normalized convolutions s_1 and s_2 using (3.73)
- (B) Fixing s_1 and s_2 , perform a few iterations of the projection algorithm to update the membership u with the competition function r given by:

$$r = r_1(s_1) - r_2(s_2) = W * (s_1^2 - s_2^2) - 2I.W * (s_1 - s_2) \quad (3.74)$$

At convergence, final segmentation is obtained by thresholding u^* at any level in $[0, 1]$.

Figure 3.10 shows the segmentation of the ultrasound lesion with this piecewise-smooth algorithm. The lesion boundary is better delineated than with piecewise-constant (Fig.3.4) and non-parametric (Fig.3.7) models, in the same parameter setting and initial conditions. W is chosen to be a Gaussian window so that its scale σ relates to the spatial extent of expected intensity variations. The scale could optionally take different values in foreground and background.

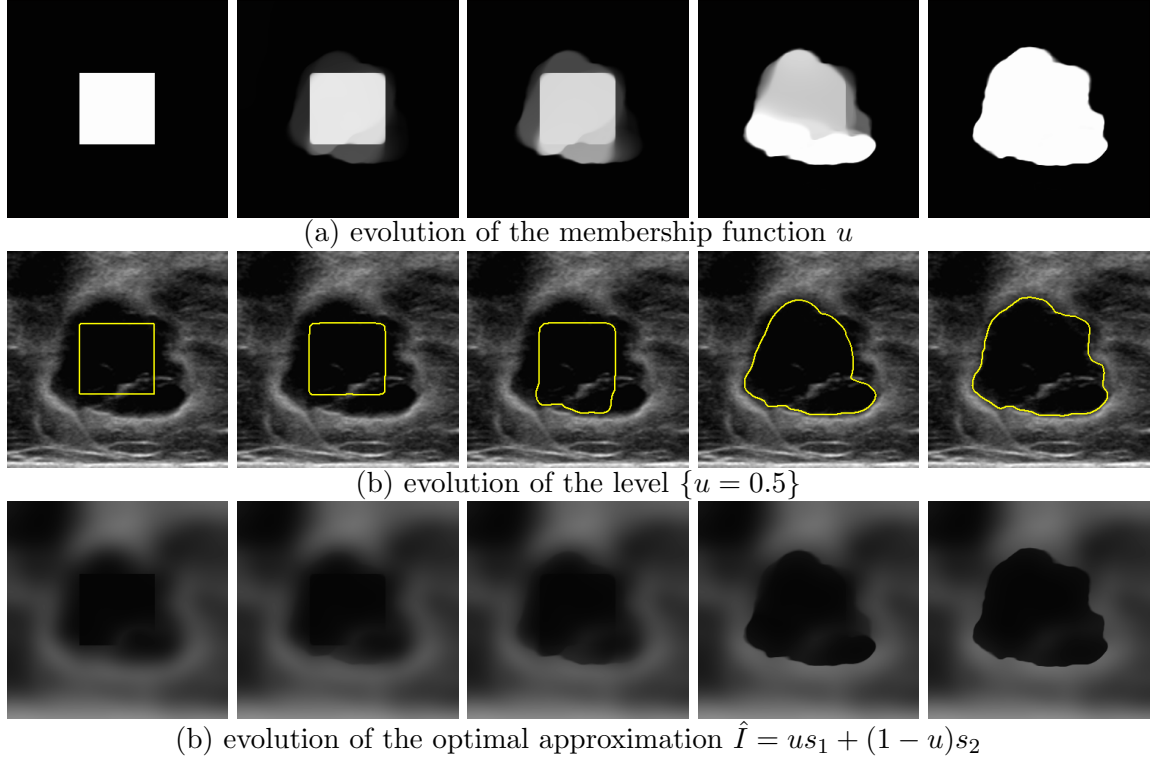


Figure 3.10 — Fuzzy Region Competition with a piecewise-smooth model on the lesion image of size 300^2 , with a scale $\sigma = 8$ pixels for the Gaussian window W . Parameter setting is identical to previous models ($\lambda = 0.1$ and $\theta = 0.01$) to show that the localized model provides more accurate boundaries and a single connected component in this case.

As shown on the gray-level photograph in Figure 3.11 in which the algorithm isolates a pandanus tree from its background, the final function $\hat{I} = u^*s_1 + (1 - u^*)s_2$ yields a piecewise-smooth approximation of the original image I at convergence. Indeed, binarization of u prevents smoothing across the boundary. In this respect, our approach relates to geometric methods derived from the *Mumford-Shah* functional [126] and a piecewise-smooth image model, with two significant advantages: the approximations are obtained by convolution and the functional is convex with respect to the membership function.

These computational advantages are particularly beneficial in 3D. Interestingly, the piecewise-smooth assumption is capable of modeling intensity variations due to the presence of contrast agent in angiography and its diffusion in irrigated tissues. In Figure 3.12, the algorithm is applied to extract a liver vascular tree from a Computerized Tomography image. In this experiment, a mask of the liver parenchyma was previously available. Within this liver mask, two-phase hypothesis (veins + tissue) is approximately valid, and the algorithm is able to capture the main branches of the vascular tree. However, besides the modeling of intensity variations, this algorithm is not specifically designed for vessel segmentation. In Chapter 4, dedicated constraints for vascular structures are developed in the Fuzzy Region Competition framework.

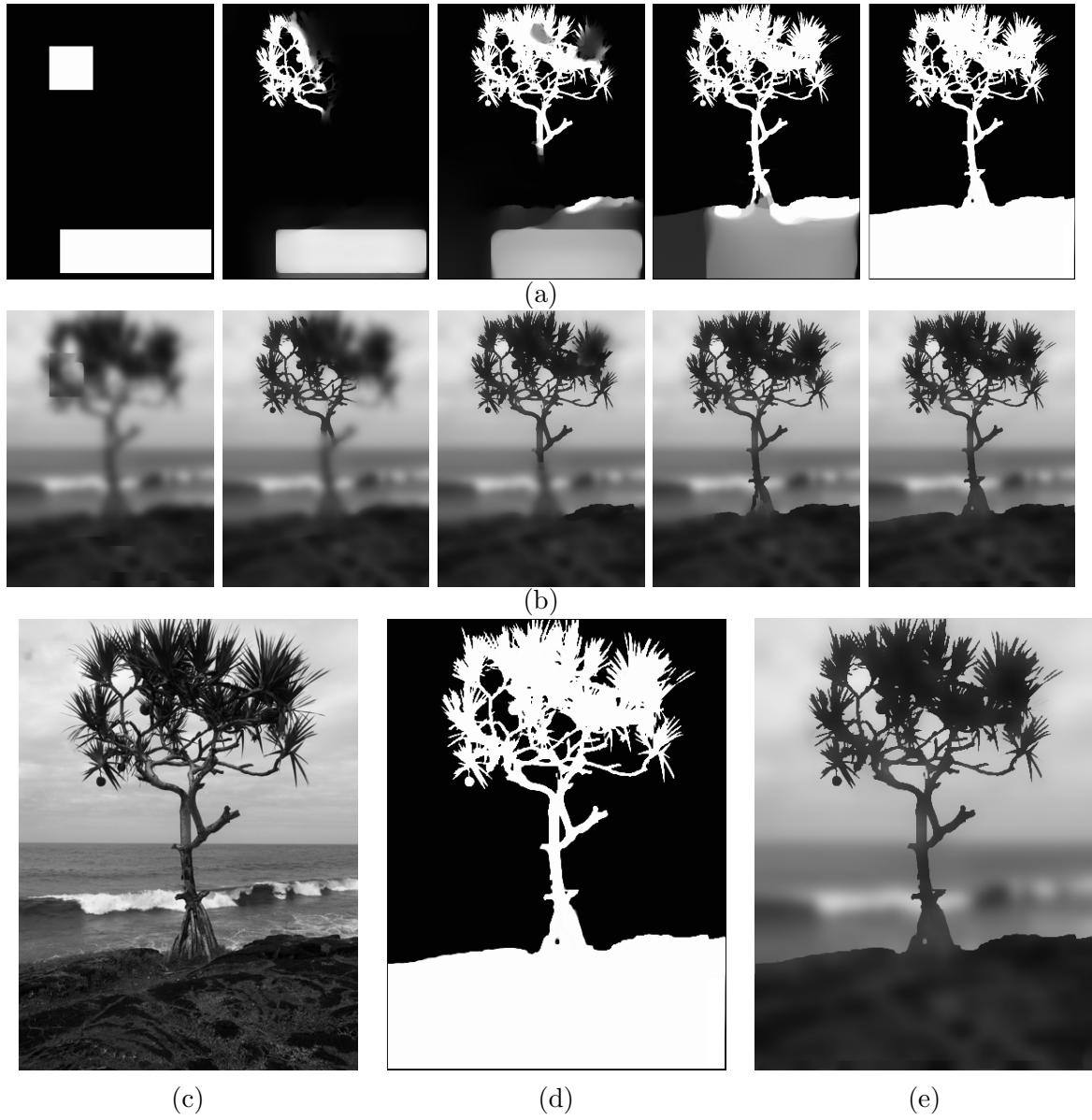
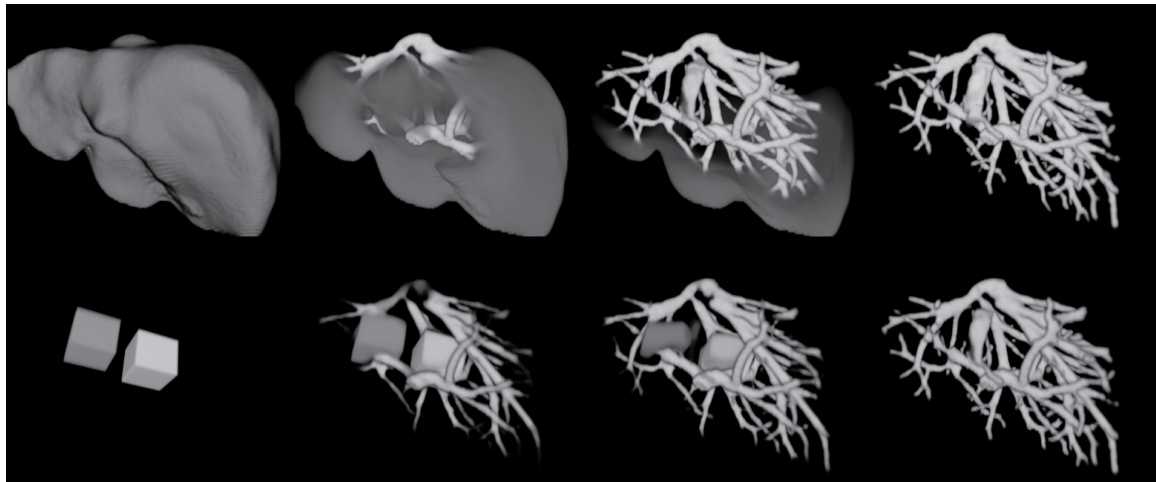
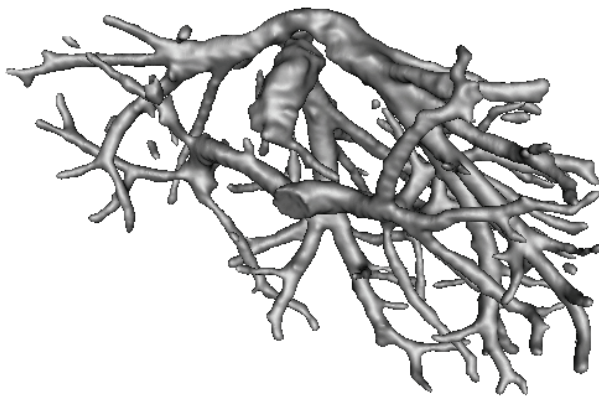


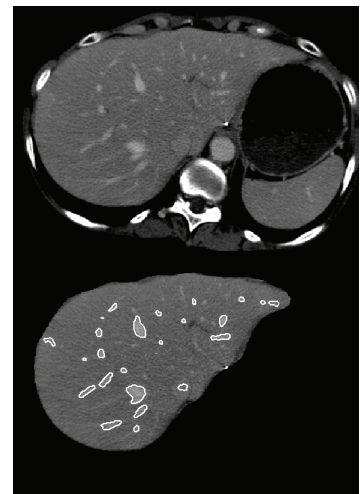
Figure 3.11 — An example of piecewise-smooth segmentation on a photograph of a pandanus tree: (a) evolution of the membership function u , (b) evolution of the piecewise-smooth approximation obtained with normalized convolutions: $\hat{I} = us_1 + (1 - u)s_2$, (c) original gray-level image I , (d) final segmentation, (e) final approximation. Parameter setting is $\lambda = 0.2$, $\theta = 0.01$, $\sigma = 8$



(a)



(b)



(c)

Figure 3.12 — Piecewise-smooth segmentation of a 3D medical image. The algorithm is applied to extract a liver vascular tree from a 294x215x101 CT angiography [156]. In this experiment, a mask of the liver parenchyma was available (c). Within this mask, two-phase hypothesis (veins + tissue) is approximately valid. In (a) two parallel evolutions of the membership function u for 100 iterations are shown using volume rendering. For two different initializations, the result is almost binary at convergence and independent of the initial conditions. Computation time is in the order of 15 sec. (b) shows the vessel mesh by rendering the surface $\{u = 0.5\}$. (c) shows an axial slice of the volume and the contours of the final segmentation overlaid on the masked liver. Parameters are, $\lambda = 0.5$, $\sigma = 16$ mm. A slightly larger value of the decoupling $\theta = 0.05$ is used to accelerate convergence.

3.4.3 Local Non-Parametric Distributions

To conclude the list of region classification errors from the catalog given in Table 3.2.5, we now address the most general case of local non-parametric distributions, from which all previously-described models can be derived. Following section 3.2.4, local non-parametric distributions are again obtained with a sliding window W , choosing:

$$\begin{cases} \alpha_i = \{p_i \in \Omega \times \mathbb{R}\} \\ r_i(\mathbf{x}, p_i) = - \int_{\Omega} W(\mathbf{x} - \mathbf{y}) \log p_i(\mathbf{y}, I(\mathbf{x})) d\mathbf{y} \end{cases} \quad (3.75)$$

which corresponds to a total classification error for the foreground of:

$$E_1(u, p_1) = \int_{\Omega} u(\mathbf{x}) \int_{\Omega} W(\mathbf{x} - \mathbf{y}) \log p_1(\mathbf{y}, I(\mathbf{x})) d\mathbf{y} d\mathbf{x} \quad (3.76)$$

With the additional constraint that $\forall \mathbf{y}, \int_{\mathbb{R}} p_1(\mathbf{y}, a) da = 1$, the optimality conditions of $E_1(u, p_1)$ yield the update formula for p_1 as:

$$p_1^*(\mathbf{y}, a) = \frac{\int_{\Omega} W(\mathbf{x} - \mathbf{y}) u(\mathbf{x}) K_{\epsilon}(I(\mathbf{x}) - a) d\mathbf{x}}{\int_{\Omega} W(\mathbf{x} - \mathbf{y}) u(\mathbf{x}) d\mathbf{x}} \quad (3.77)$$

and a similar expression for p_2 , replacing u by $1 - u$. These correspond to local, weighted, kernel density estimates. In the following, we show that they can be approximated using a Gaussian convolution in a $n + 1$ dimensional space. Assuming the estimation kernel K_{ϵ} is of the form:

$$K_{\epsilon}(t) = [K * \delta_{\epsilon}](t) = \int_{\mathbb{R}} K(b) \delta_{\epsilon}(t - b) db, \quad (3.78)$$

The numerator of (3.77) becomes:

$$N(\mathbf{y}, a) = \int_{\Omega} W(\mathbf{x} - \mathbf{y}) u(\mathbf{x}) \left(\int_{\mathbb{R}} K(b) \delta_{\epsilon}(I(\mathbf{x}) - a - b) db \right) d\mathbf{x} \quad (3.79)$$

After a simple change of variable and using the symmetry of K and W ,

$$\begin{aligned} N(\mathbf{y}, a) &= \int_{\Omega} W(\mathbf{x} - \mathbf{y}) u(\mathbf{x}) \left(\int_{\mathbb{R}} K(b - a) \delta_{\epsilon}(I(\mathbf{x}) - b) db \right) d\mathbf{x} \\ &= \int_{\Omega} \int_{\mathbb{R}} \underbrace{W(\mathbf{y} - \mathbf{x}) K(a - b)}_{\mathcal{K}} \underbrace{u(\mathbf{x}) \delta_{\epsilon}(I(\mathbf{x}) - b)}_{h_u(\mathbf{x}, b)} db d\mathbf{x} \end{aligned} \quad (3.80)$$

where $h_u : \Omega \times \mathbb{R} \rightarrow \mathbb{R}$ is essentially a sparse counting function that can be discretized by assigning the value $u(\mathbf{x})$ at each grid point $(\mathbf{x}, I(\mathbf{x}))$ in a $(n + 1)$ -dimensional lattice. Now, if we choose window W and kernel K as Gaussian functions so that their external product $\mathcal{K} = W \times K$ is still a Gaussian of dimension $n + 1$, (3.77) reduces to convolutions:

$$p_1^*(\mathbf{y}, a) = \frac{[\mathcal{K} * h_u](\mathbf{y}, a)}{[W * u](\mathbf{y})} \quad \text{and} \quad p_2^*(\mathbf{y}, a) = \frac{[\mathcal{K} * h_{1-u}](\mathbf{y}, a)}{[W * (1 - u)](\mathbf{y})} \quad (3.81)$$

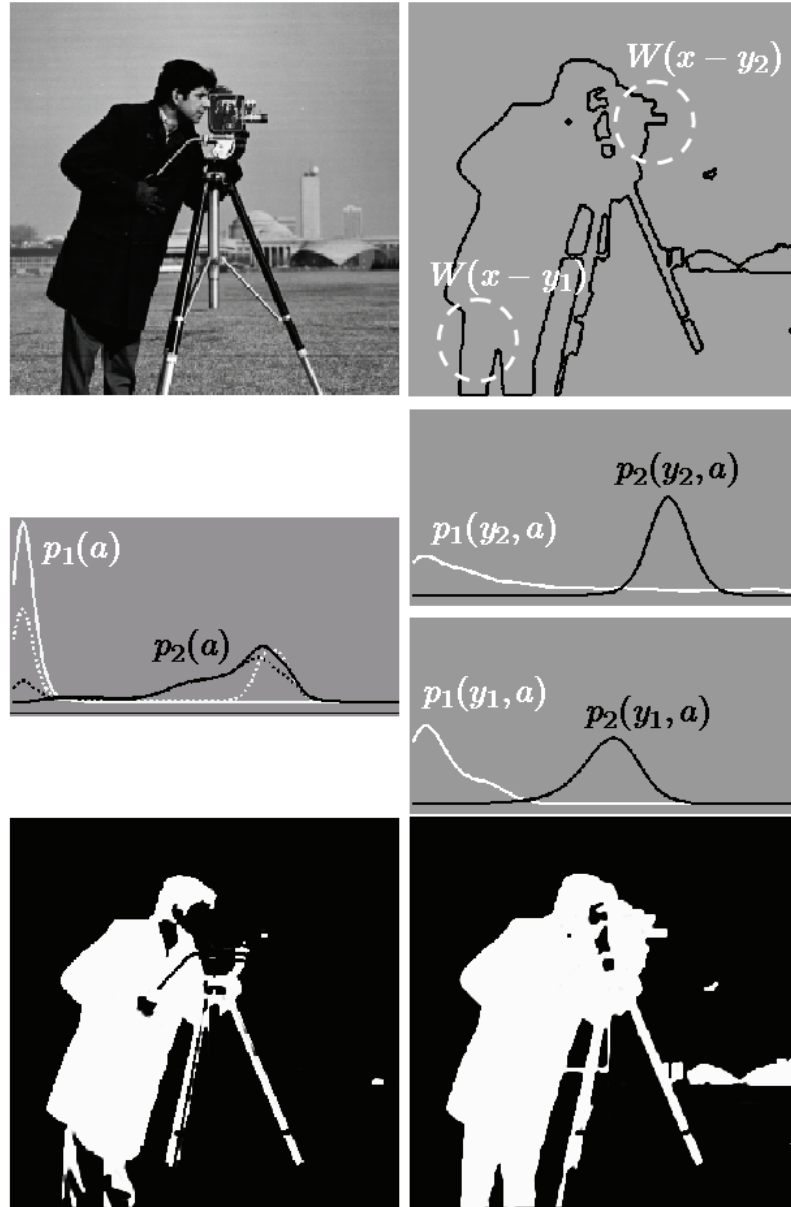


Figure 3.13 — Local non-parametric distributions on the cameraman image. Left column, results of the global model, original image (top), global distributions p_i (center) and final membership function u (bottom). Right column, results of the local model, solid final contours with a dashed representation of the window W at two pixel locations (top), local distributions p_i (center) and final u (bottom).

Figure 3.13 illustrates on the *cameraman* image the advantages of using local probability densities. The overall intensity distribution is mainly composed of 3 modes of increasing intensity, corresponding to the cameraman, the grass and the sky, respectively. On the bottom left, the global model easily extracts the first mode, but the boundary lacks precision. On the right, the result serves as initial guess for a subsequent refinement step by re-running the algorithm with local non-parametric distributions, which allows to recover more accurately the legs and the camera. The competition between foreground and background distributions implicitly selects optimal spatially-adaptive thresholds, which is visible on the plots of p_1 and p_2 on the right. Although the background seems to *locally* follow a Gaussian distribution, the model does not make that assumption explicitly.

Among all proposed models in this chapter, local probability distributions offer the most accurate, piecewise-smooth representation of statistical intensity properties. However, it is also the one that is by far the most sensitive to initial conditions. Based on our experience, we recommend to use it only as a final refinement step in a hierarchical strategy in which first stages rely on more robust models such as the piecewise-constant or the global non-parametric model. In Figure 3.4.3, we show an example of such a hierarchical algorithm in 3D to extract the lungs and their vascular structures from a CT image, in a recursive fashion. To satisfy the two-phase assumption, lungs are first separated from the rest of the body using Fuzzy Region Competition with global non-parametric distributions in the foreground and background. Then, the same algorithm is re-launched inside the mask of the lungs to coarsely separate the vessels from the lung tissue. Finally, local non-parametric distributions are used in a refinement step to improve precision and capture smaller distal branches of the vascular tree.

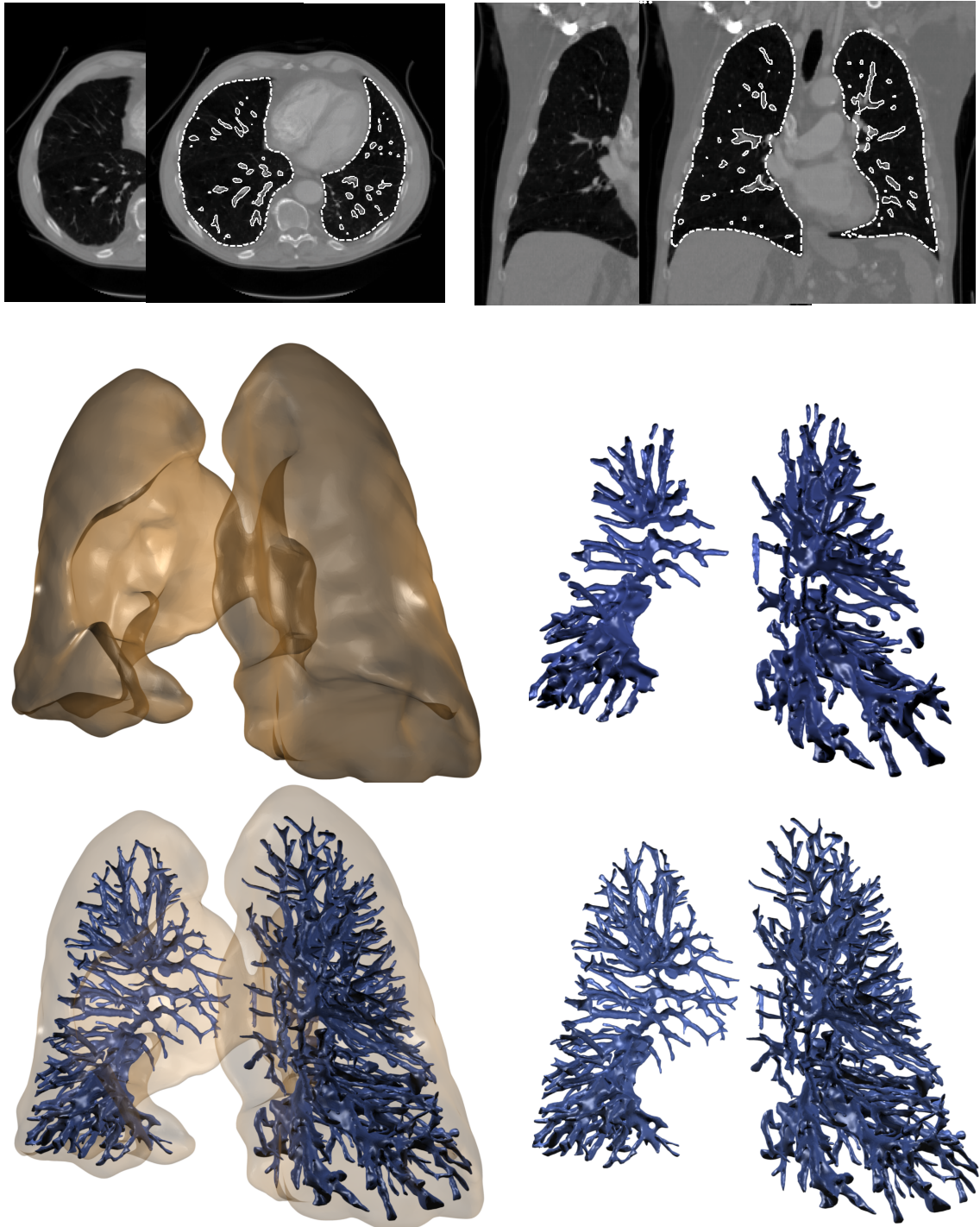


Figure 3.14 — Hierarchical segmentation of a 3D Computerized Tomography volume of the lungs. The global non-parametric model is used to extract the lung from the background, composed of all surrounding organs. Initial u is set to a small cube inside the lungs. At convergence, the exact same process with global distributions is recursively applied inside the lungs in order to separate pulmonary vessels from the lung tissue. Since the vascular tree exhibits a spatially-varying intensity distribution, the local model provides more precise boundaries if used as a final refinement step. On the left, coronal and axial views of the volume, with overlaid lung and vessel contours. Corresponding triangular meshes are rendered on the right: in the first column, the outer surface, alone (top) and mixed with the final vessels (bottom); in the second column, the vessels before (top) and after (bottom) local refinement for sake of comparison.

3.5 Conclusion

In this chapter, we introduced a general variational framework and methodology for two-phase image segmentation on which many existing approaches are derived. In this thesis, we follow this common methodology for the design of new algorithms and numerical schemes. Choosing a unified formulation is key for software re-usability, rapid prototyping and interoperability of the algorithms that often need to be combined to meet the diversity of clinical application requirements.

From this general formulation, specific segmentation algorithms essentially differ by their mathematical representation for the foreground region and by the chosen objective measure to assess the quality of the segmentation. Using Bayesian principles, the latter can be interpreted as a statistical classification error or equivalently as a region homogeneity criterion. We enumerated a number of valid choices and proposed new localized piecewise-smooth approximations. Since special care is devoted to computational complexity, we rely exclusively on normalized convolutions so that 3D applications are readily possible. In the following chapters, we will refer to this list of global or local region descriptions when concrete examples are shown.

As for the choice of an appropriate representation of the foreground region, we explore in this work a number of possibilities with the objective to cover a large spectrum of application requirements. As a first example, we have shown that a *fuzzy membership function* is particularly adapted if a geometric constraint on the region perimeter is imposed, like in most active contours and level-set algorithms. This induces a minimization problem in the space of functions of bounded variations that can be interpreted as a convex relaxation of the original formulation and guarantees to obtain, in the supervised case, a globally-optimal binary solution with a fast and stable numerical scheme. In the unsupervised case, we used this so-called *Fuzzy Region Competition* approach to illustrate on a variety of photographic and clinical images the versatility and potential applications of the new localized region intensity models.

While convexity effectively reduces sensitivity to initial conditions, it should nonetheless be slightly mitigated in the unsupervised setting. Indeed, the problem is only convex with respect to the membership function, for fixed region parameters, not globally convex with respect to all unknown variables. Therefore, the proposed model does not completely relieve the algorithmic chain of a careful initialization, in particular when local region-based criteria are involved.

In addition, convexity also relates to *topological flexibility*, a property that is often advocated as a major advantage of implicit representations over explicit curve/surface evolution schemes. The use of a membership function enables to go beyond standard merging/splitting changes of topology of level-sets in order to reach a global minimum. Spontaneous creation of holes or new regions may occur all over the image domain during minimization of the convex problem, resulting in a final segmentation that is free of any topological constraint. Depending on the application, this may or may not be an desirable feature. As guideline, we would recommend to use this convex formulation as a spatially-

constrained alternative to clustering methods. Indeed, Fuzzy Region Competition can be interpreted as a geometric, total-variation based regularized version of a locally-adaptive Expectation-Maximization (EM) algorithm.

More importantly, convexity and global minimization of a variational segmentation problem also has to be comprehended together with the complex notion of robustness and reproducibility in the clinical context. By definition, a globally-optimal solution is robust to initial conditions and reproducible, which unfortunately in most cases does not imply that it is a clinically-relevant one. For the automatic delineation of anatomical structures that often requires some knowledge that goes far beyond the image itself, the convex optimization framework induces a considerable requirement on the criterion to ensure that its minimum is indeed a reliable answer. Consequently, the convex framework remains limited to the applications in which this requirement can be met. Among others, one of these applications is the extraction of entire vascular structures from an already-segmented organ such as the lungs or the liver. In this case, the piecewise-smooth classification error is particularly adapted to model spatial variations of intensity due to the contrast product. This is the motivation behind the next chapter that describes our attempt to complement the convex formulation with vessel-specific constraints on the membership function as well as a new implicit representation for tubular shapes using convolution surfaces.

Tubular Constraints and Implicit Convolution Surfaces

4

In this chapter, we propose two novel and complementary approaches for segmentation of tubular shapes in 3D, with applications in angiography.

In the past, level-set representations have proved useful to separate vascular structures from their surrounding tissue in 3D, for their ability to capture an arbitrary and unknown topology [85, 86, 112, 116, 175]. Consequently, the first approach consists in applying the convex variational formulation of Chapter 3, with local regional information to model the spatial intensity variations that appear in angiography. We propose the incorporation of dedicated constraints to take into account the contrasted nature of vascular structures as well as their geometry, with very limited complexity overhead. As a result, the algorithm keeps advantages over level-set representations in terms of numerical stability and efficiency. Even though the new constrained problem is not convex anymore, sensitivity to initial conditions is still minimal. Illustrative experiments are shown on liver veins in Computerized Tomography.

We also consider a second, model-based approach to vessel segmentation, expected to be more robust when the topology is known in advance. The idea is to model each vessel branch as a generalized cylinder, implicitly represented with a convolution surface around its centerline. To our knowledge, this representation was successfully used for the purpose of rendering complex vascular structures [132], but not in the variational context of image segmentation. Within the unsupervised region-based formulation, we develop all the necessary components to perform a joint optimization of the vessel centerline curve and the corresponding scales, defined along the curve. We only address the case of a single branch, but the principle readily extends to vascular trees, as soon as knowledge on the configuration of the branches is available.

4.1 Introduction

Over the last two decades, technological improvements have led to the generalized use of 3D imaging tools for vascular studies. Clinicians are nowadays confronted with the task of analyzing considerable amounts of 3D data in a rather limited time. The topological complexity of vascular structures further increases the difficulty. The segmentation of the vascular system of an organ with manual or standard semi-automatic tools is a tedious, time-consuming and non-reproducible task. Fully automatic tools are thus strongly demanded for most frequent studies.

Vascular image processing is a very active field of research. We refer the reader to the recent review by Lesage et al [105] on 3D vessel segmentation, with a comprehensive survey of the published techniques in terms of models, features and extraction schemes. In particular, scale-space theory [110], medial representations [142] and front propagation methods [133] have helped the development of now well-established algorithms for vessel enhancement [68, 98] and robust centerline extraction [10, 58, 100, 108]. Most often relying on a multi-scale analysis of ridge-like curvilinear structures, they may however not suffice to obtain an accurate delineation of vessel boundaries. To fulfill this need, mathematically sound variational segmentation methods have been proposed as a complement to former approaches. For their ability to capture complex topologies in 3D, implicit surface evolution schemes with level-sets, minimizing boundary-based [112, 116, 146, 176] or robust and reliable region-based [85, 86, 116, 121, 175] criteria, are of particular relevance. In this chapter, we also propose means of segmenting vessels in 3D by optimizing a region-based objective functional, but without relying on a boundary evolution scheme.

We consider vessel segmentation as an optimal two-phase separation problem, where the two phases correspond to the vessel lumen and its background, respectively. Due to both spatial variations of the contrast agent density in blood and its diffusion into surrounding tissues, the usual assumption of approximately constant intensities in each phase is too restrictive. It is more valid to expect the observed intensity variations to be slowly-varying and smooth. Under this assumption, existing so-called *piecewise-smooth* segmentation models [126, 170, 177] are natural candidates for the vessel extraction task. However, those boundary evolution schemes require solving diffusion equations with new boundary conditions at each step, hence are seldom used in 3D due to their complexity. In the previous chapter, we described a much faster alternative for piecewise-smooth image segmentation, having not only very similar properties but also a weaker dependence on initial conditions. Within the region-based general formulation,

$$\min_{\Omega_1, \alpha_1, \alpha_2} \left\{ F(\Omega_1, \alpha_1, \alpha_2) = \mathcal{R}(\Omega_1) + \lambda \int_{\Omega_1} r_1(\mathbf{x}, \alpha_1) d\mathbf{x} + \lambda \int_{\Omega \setminus \Omega_1} r_2(\mathbf{x}, \alpha_2) d\mathbf{x} \right\} \quad (4.1)$$

the localized classification error is designed to describe piecewise-smooth structures corresponds, as in section 3.2.3, to the choice :

$$\begin{cases} \alpha_i = \{s_i\} \\ r_i(\mathbf{x}, s_i) = \int_{\Omega} W_a(\mathbf{x} - \mathbf{y}) (I(\mathbf{x}) - s_i(\mathbf{y}))^2 d\mathbf{y} \end{cases} \quad (4.2)$$

where W_a is for instance a Gaussian window of scale a controls the expected spatial intensity variations. We propose in this chapter two different, complementary specializations of (4.1) for vascular structures, in which the difference stems from the chosen representation for the foreground region Ω_1 . The first one is a *membership function* $u(\mathbf{x})$, as in the previous chapter, with dedicated constraints to favor tubular shapes. The second one is a totally different representation, with a convolution surface $\Phi_{\{\mathbf{m}, \sigma\}}$ built around a parameterized medial curve $\mathbf{m}(s)$, with varying scales $\sigma(s)$ defined along the curve.

This chapter is divided into two parts. In section 4.2, we provide the Fuzzy Region Competition algorithm and the convex framework with proper contrast and volume constraints and derive an algorithm for extracting vascular tress in 3D volumes. Even though the additional constraints break the convexity of problem, sensitivity to initial conditions is still minimal. Illustrative experiments are shown on liver veins in Computerized Tomography. In section 4.3, we propose a second representation with implicit generalized cylinders and perform the calculus of variations to jointly optimize a centerline and varying scales. The method is applied to model-based segmentation of the Inferior Vena Cava. In conclusion, we discuss the advantages and limitations of each representation.

4.2 Piecewise-Smooth Fuzzy Region Competition

Recall that the *Fuzzy Region Competition* algorithm, presented in chapter 3, realizes a minimization of 4.1 through a convex relaxation given by:

$$u, \min_{\alpha_1, \alpha_2} \left\{ \underbrace{\int_{\Omega} |Du| + \lambda \int_{\Omega} u(\mathbf{x}) r_1(\mathbf{x}, \alpha_1) d\mathbf{x} + \lambda \int_{\Omega} (1 - u(\mathbf{x})) r_2(\mathbf{x}, \alpha_2) d\mathbf{x}}_{F_1(u, \alpha_1, \alpha_2)} \right\} \quad (4.3)$$

where $u(\mathbf{x}) \in [0, 1]$ is the membership function to the foreground region. Combined with the intensity model with local averages (4.2), this algorithms has several attractive properties for segmentation of vessels in 3D angiography. First, it has the ability to capture the varying intensities induced by contrast agent diffusion. The scale parameter of W_a in (4.2) directly controls those variations. Moreover, the convexity in u significantly alleviates the model sensitivity to initial conditions. In practice, the segmentation of complex structures such as branching, stenoses and multiple disconnected trees can be properly handled, while these would constitute typical local minima in many non-convex variational approaches. As any implicit method, it readily extends to 3D, but also benefits from the computational advantages of the minimization scheme described in section 3.3.3.

Nevertheless, the method is not *specific to vessels*. Other positively or negatively contrasted non-vascular structures such as diffusion in tissues, lesions or movement artifacts, often satisfy the underlying piecewise-smooth assumption. Additional constraints need to be added in order to impose the expected *contrast sign* and better control the *foreground geometry*.

4.2.1 Contrast constraint

In most two-phase region competition models, foreground and background play symmetric roles. In the piecewise-constant case, with $r_i(\mathbf{x}, c_i) = (I(\mathbf{x}) - c_i)^2$, the functional F_1 satisfies:

$$\begin{aligned} F_1(u, c_1, c_2) &= \int_{\Omega} |Du| + \lambda \int_{\Omega} u r_2(c_1) + \lambda \int_{\Omega} (1-u) r_2(c_2) \\ &= F_1(1-u, c_2, c_1). \end{aligned} \quad (4.4)$$

The final choice between symmetric solutions is driven by the initial conditions. While this property does not influence the final boundary in the piecewise-constant case, its consequences can be critical in the smooth case, since symmetry also holds *locally*. Depending on initial conditions, the model may take inconsistent background/foreground decisions for distant areas of the same object (see Fig. 4.2.b). Note that this drawback, found in other piecewise-smooth approaches and seldom studied, can sometimes be overcome by putting more efforts in the initialization strategy to ensure that the spatial inconsistencies illustrated in Figure 4.2.1 do not occur.

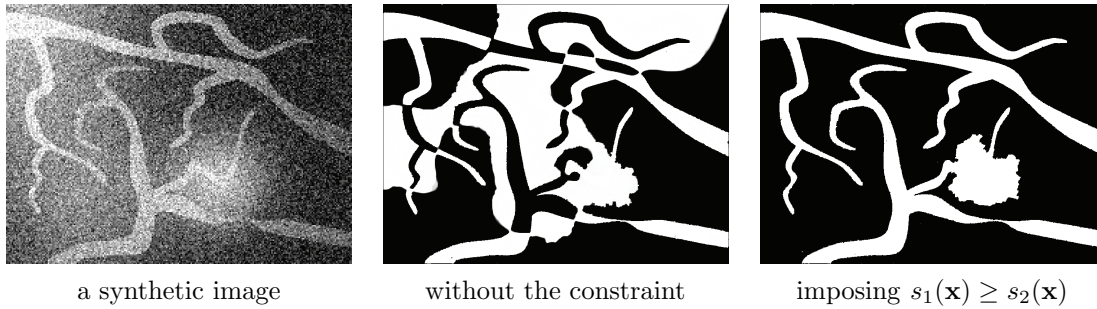


Figure 4.1 — Piecewise-smooth foreground/background segmentation results on a synthetic image with spatial inconsistencies due to local symmetry of the functional with respect to s_1 and s_2 .

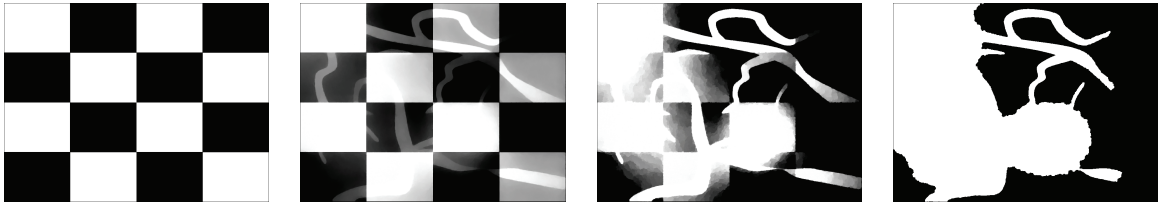
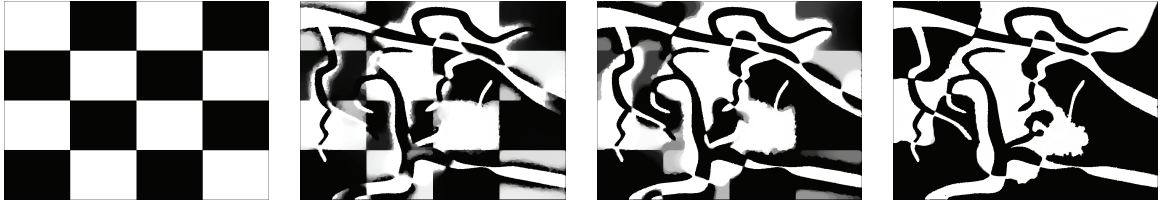
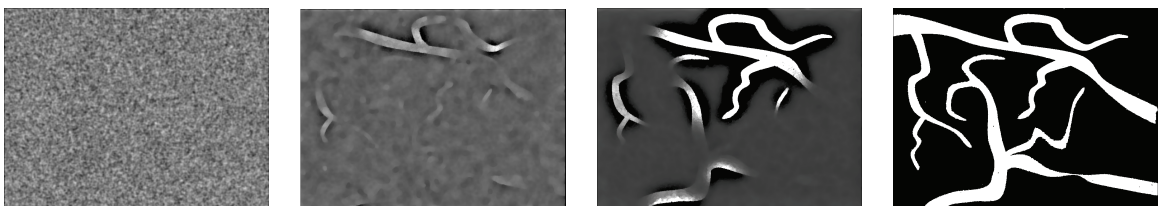
In the case of vessels, foreground is expected to be the lumen. Assuming that it is locally brighter than surrounding tissues due to contrast agent injection, the symmetry can be broken so that the ambiguities of the membership function u are removed. Indeed, as already mentioned, smooth approximation functions s_1 (foreground) and s_2 (background) are defined everywhere in the image domain contrary to classical piecewise-smooth approaches [170, 177]. Thus adding the inequality constraint

$$s_1(\mathbf{x}) \geq s_2(\mathbf{x}) \quad \forall \mathbf{x} \in \Omega \quad (4.5)$$

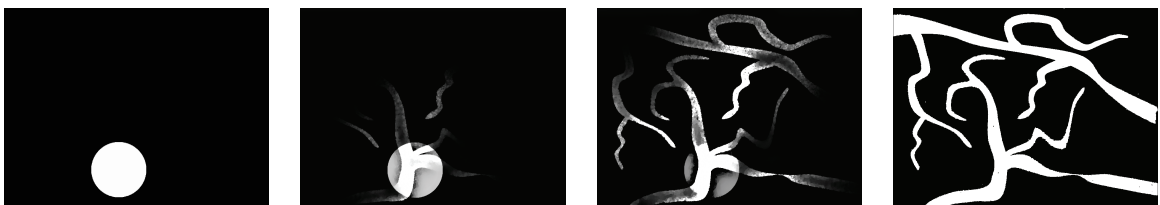
will automatically impose the foreground ($u = 1$) to be the vessel lumen.

4.2.2 Local Volume constraint

The foreground being unambiguously determined, geometrical constraints penalizing undesirable shapes can be now introduced in the membership function u .

(a) Evolution of the membership u using the piecewise-constant model (scale $a = +\infty$)(b) Unconstrained, piecewise-smooth, (scale $a = 16$). Inconsistent foreground decisions may occur.(c) Piecewise-smooth with contrast constraint $s_1 > s_2$, but without volume penalization ($\beta = 0$)(d) Piecewise-smooth with both contrast constraint $s_1 > s_2$ and volume penalization ($\beta = 0.5$)

(e) Piecewise-smooth (same parameters), initialized with a random membership function



(f) Piecewise-smooth (same parameters), initialized with a circle

Figure 4.2 — Evolution for various constraint settings and initial conditions.

The total variation of u is already a geometric constraint on the perimeter, but it only influences the smoothness of the foreground boundary, not its shape. The idea is to use an additional constraint on the *volume*. It is reasonable to assume that 3D vascular structures occupy a small fraction of the volume of the corresponding organ. Hence a global penalization of the foreground volume could be a way to limit possible leakages in surrounding tissues. Unfortunately, this is known to produce a global shrinking effect that indubitably also removes the smallest vessels.

A more suitable approach is to *locally* penalize the foreground volume beyond a given scale in order to limit leakages in the background while keeping the smallest structures. In [128], *Nain et al.* proposed such an algorithm imposing a spherical volume constraint within a classical level-set boundary evolution framework. In the following, we present a generalization where the constraint is expressed directly on the fuzzy membership function u and the local volume measure is computed using any given window function. An advantage of this generalization is then shown by deriving a fast minimization scheme based on linear filtering.

A local measure of the fuzzy foreground volume at any point $\mathbf{x} \in \Omega$ is:

$$V_\rho(u, \mathbf{x}) = \int_{\Omega} u(\mathbf{y}) B_\rho(\mathbf{x} - \mathbf{y}) d\mathbf{y} = [B_\rho * u](\mathbf{x}), \quad (4.6)$$

where B_ρ is an isotropic and symmetric window function of scale parameter ρ , such as a ball of radius ρ or a Gaussian of standard deviation ρ . Hence, ρ acts as a geometrical scale parameter. The penalization term to add to the functional in order to limit the appearance of large-scale structures is obtained by integrating V_ρ on the fuzzy foreground:

$$V(u) = \beta \int_{\Omega} u(\mathbf{x}) V_\rho(u, \mathbf{x}) d\mathbf{x} = \beta \int_{\Omega} u(\mathbf{x}) \int_{\Omega} u(\mathbf{y}) B_\rho(\mathbf{x} - \mathbf{y}) d\mathbf{x} d\mathbf{y} \quad (4.7)$$

where β controls the degree of volume penalization.

The sum of the total variation regularization, the local minimal variance error functions (3.31) and the local volume penalization (4.7) gives the complete expression of the functional to minimize. Adding the contrast inequality constraint, the vessel segmentation problem becomes:

$$\begin{aligned} & \text{minimize} && F_2(u, s_1, s_2) \\ & \text{subject to} && \forall \mathbf{x} \in \Omega, \begin{cases} u(\mathbf{x}) \in [0, 1] \\ s_1(\mathbf{x}) \geq s_2(\mathbf{x}) \end{cases} \end{aligned} \quad (4.8)$$

with

$$\begin{aligned} F_2(u, s_1, s_2) = & \int_{\Omega} |Du| + \lambda \int_{\Omega} u(\mathbf{x}) \left(\int_{\Omega} W_a(\mathbf{x} - \mathbf{y}) (I(\mathbf{x}) - s_1(\mathbf{y}))^2 d\mathbf{y} \right) d\mathbf{x} \\ & + \lambda \int_{\Omega} (1 - u(\mathbf{x})) \left(\int_{\Omega} W_a(\mathbf{x} - \mathbf{y}) (I(\mathbf{x}) - s_2(\mathbf{y}))^2 d\mathbf{y} \right) d\mathbf{x} \\ & + \beta \int_{\Omega} u(\mathbf{x}) \left(\int_{\Omega} u(\mathbf{y}) B_\rho(\mathbf{x} - \mathbf{y}) d\mathbf{y} \right) d\mathbf{x} \end{aligned} \quad (4.9)$$

4.2.3 Minimization Scheme

We shall now describe a strategy to carry out the minimization of Problem 4.8. To avoid relying on curvature computations, we follow, as in Chapter 3, the auxiliary variable strategy proposed by *Bresson et al.* [26]. In the following, we only insist on the specific adaptations that are needed to take into account the two new volume and contrast constraints. Introducing an auxiliary variable v and a relaxation parameter θ , we consider the following approximation of F_2 :

$$\int_{\Omega} |Du| + \frac{1}{2\theta} \int_{\Omega} |u - v|^2 + \lambda \int_{\Omega} v r(s_1) + \lambda \int_{\Omega} (1 - v) r(s_2) + V(v) \quad (4.10)$$

where $r(s_i)$ are given by (3.31), V by (4.7), and θ is chosen to be small enough so that the two components of any minimizing couple (u^*, v^*) are almost identical. Chambolle's projection algorithm [36] can be used to minimize w.r.t. u while the other variables are kept fixed (the first two terms). Considering each variable successively, we now only need to find optimal solutions for s_1 , s_2 and v taken independently. It turns out that these solutions can be computed without resorting to additional iterative schemes.

Optimal s_1 and s_2 should be updated by the normalized convolutions given in Eq. (3.73), replacing u by v . Although the inequality constraint $s_1 \geq s_2$ should be imposed through constrained optimization technique such as the Augmented Lagrangian used in Chapter 6, it is in practice sufficient to choose point-wise $s_1(\mathbf{x}) = \max\{s_1(\mathbf{x}), s_2(\mathbf{x})\}$ after computing the normalized convolutions.

As for the optimization of the auxiliary variable v , the corresponding Euler-Lagrange equation can be efficiently solved by inverse filtering. Indeed, the optimality conditions obtained by calculus of variations are:

$$v + 2\theta\beta[v * B_{\rho}] = u - \theta r \quad (4.11)$$

with $r = \lambda(r(s_1) - r(s_2))$. Taking the Fourier transform of (4.11) yields the inverse filter to obtain v as a function of u (\hat{f} denotes the Fourier transform of f):

$$\hat{v} = \frac{\hat{u} - \theta \hat{r}}{1 + 2\beta\theta \hat{B}_{\rho}} \quad (4.12)$$

In our implementation, we further take advantage of the assumption that θ must be small in order to find an even faster and simpler approximation. Assuming $2\beta\theta \hat{B}_{\rho} \ll 1$, (4.12) reads:

$$\hat{v} = \frac{\hat{u} - \theta \hat{r}}{1 + 2\beta\theta \hat{B}_{\rho}} \approx (\hat{u} - \theta \hat{r}) (1 - 2\beta\theta \hat{B}_{\rho}) \quad (4.13)$$

After an inverse Fourier transform, we finally use the following update formula for v , taking the saturation constraint into account:

$$v = \min(\max(w - 2\beta\theta [B_{\rho} * w], 0), 1) \text{ with } w = u - \theta r \quad (4.14)$$

This minimization algorithm is first applied in 2D in Figure 4.2 in which we illustrate the effect of both the contrast constraint and the volume constraint and the low sensitivity to initial conditions (chessboard/random/circle). In Figure 4.3, we show the piecewise-smooth reconstruction obtained at the end of the convergence. In particular, the background function s_2 , defined on the whole domain, is reconstructed by extrapolation with normalized convolution behind the foreground vessel.

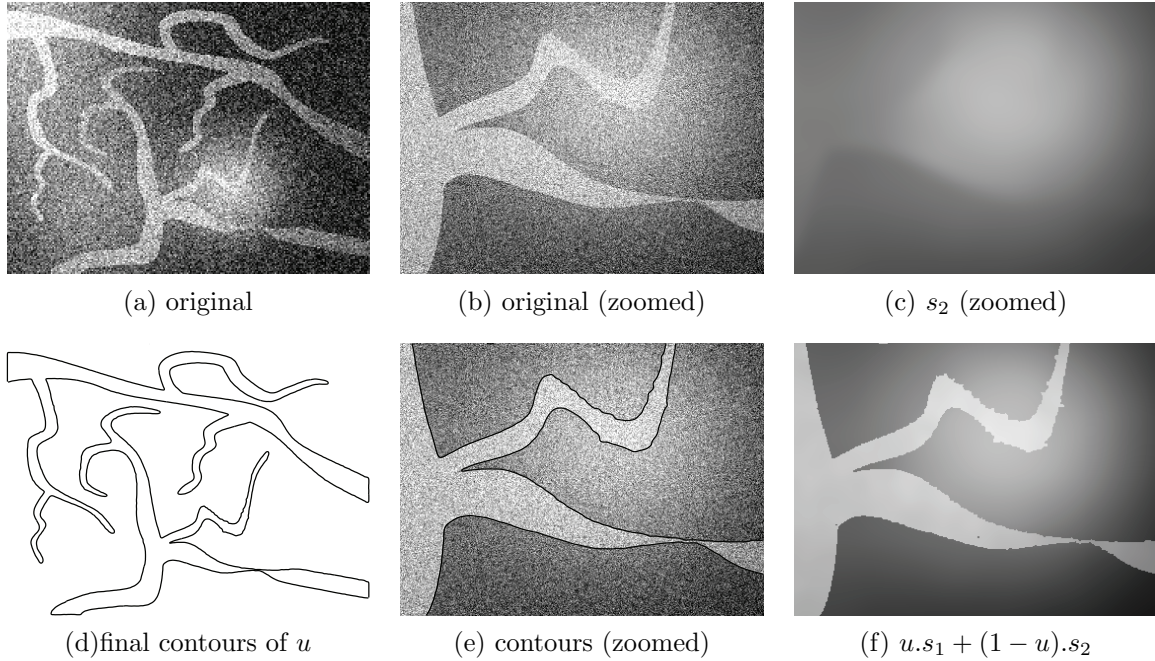


Figure 4.3 — Piecewise-Smooth vessels on a 2D synthetic image. On the right, a piecewise-smooth reconstruction at convergence is shown. In particular, the background function s_2 , defined on the whole domain, is reconstructed by extrapolation with normalized convolution behind the foreground

4.2.4 Extraction of liver veins in CTA

Computerized tomography angiography (CTA) of the liver is a routine examination in which the visualization of vessels is crucial. Imaging is performed using a radio-opaque contrast material injected intravenously. Acquisitions at different time intervals produce various volumetric images due to the diffusion and the transport of the contrast agent by blood. Adequate timings allow to image arteries and veins whose segmentation is very relevant for a tumor's nature assessment, intervention planning and follow-up [156].

In this clinical context, we use the Fuzzy Region Competition algorithm with the new constraints to segment the hepatic and portal veins in the liver. Typical results are shown in Figure 4.4, after performing the minimization scheme given in section 4.2.3 inside a previously-available mask of the liver.

The new constraints help to reduce the sensitivity to inconsistent initial conditions ($s_1 \geq s_2$), limit the appearance of possible leakages with the term $V(u)$ and do not add any significant complexity overhead (only 1 more convolution in (4.14)). However, besides these

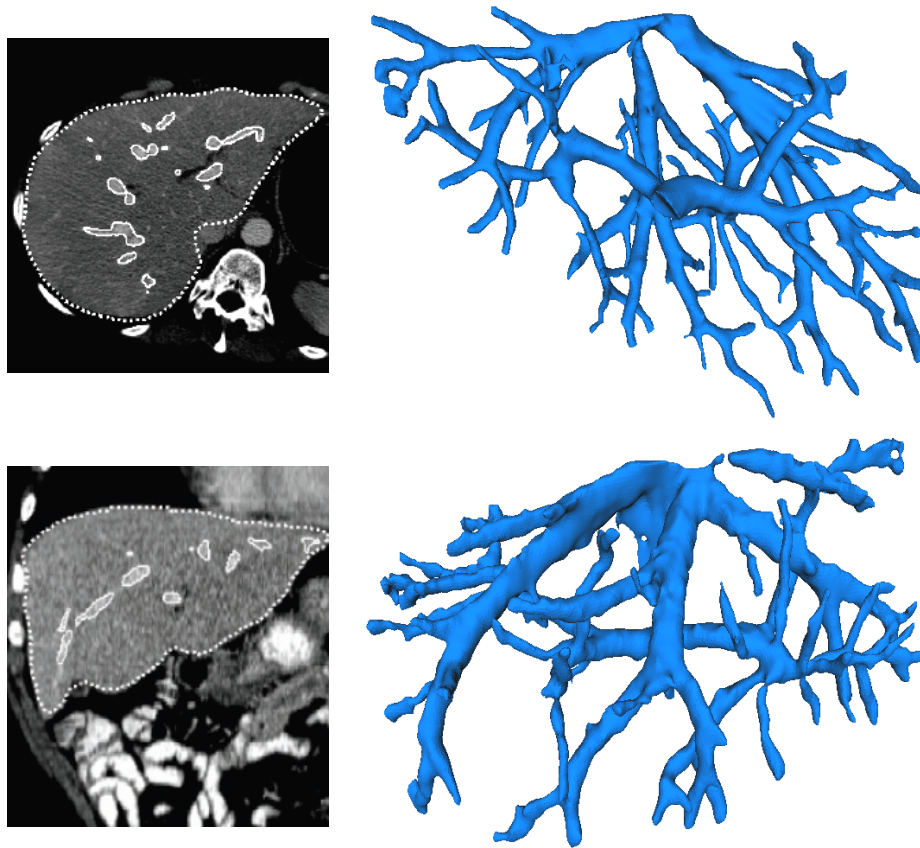


Figure 4.4 — Fuzzy Region Competition with vascular constraints in 3D liver CTA. First row shows on the left a portion of an axial slice of a 512x512x256 CT volume. Image domain has been restricted to a previously available segmentation of the liver, shown in dashed. Superimposed in solid are the contours of the segmentation obtained by the proposed algorithm, also represented as a surface rendering on the right. Second row shows a more difficult case, sagittal view with superimposed contours on the left and corresponding segmentation on the right. Third row shows additional examples for two other cases.

additional constraints, applicability of Fuzzy region Competition for vessel segmentation remains limited to the cases where only the vessels satisfy the piecewise-smooth image-based assumption. Due to the simplicity of the local volume constraint, the method would not be able to discriminate vessels from other structures based solely on their geometry. In the following section, we rely on a tubular model that is much more specific to vascular branches, with an implicit representation of generalized cylinders.

4.3 Implicit Convolution Surfaces

Convolution surfaces refer to a special type of implicit surfaces introduced by Bloomenthal [21] and mainly used in computer graphics for object modeling. They correspond to a generalization of popular models such as blobs, metaballs [20] and soft objects [182] to other skeletal primitives such as line segments, polygons and planes.

In this section, we introduce a possible use of this modeling technique in the context of variational image segmentation. We consider as an example the case of a single vessel branch and compute the derivatives of the region-based functional with respect to the free parameters of the representation. Yet, the modeling capabilities can be extended to more complex cases such as branching vascular structures.

4.3.1 Generalized Cylinder Implicit Representation

Assuming a circular cross-section, a vessel branch is often modeled by an open parameterized medial curve $\mathbf{m}(s) : [0, 1] \rightarrow \mathbb{R}^3$, with a set of corresponding point-wise radii. For recent examples of the use of generalized cylinders for vessel segmentation, we refer the reader to [105, 121] as well as the work on 4D minimal paths of Li and Yezzi [108]. Compared to previous works, the original feature of the model described in the following is the definition an *implicit* analytical representation of such a generalized cylinder.

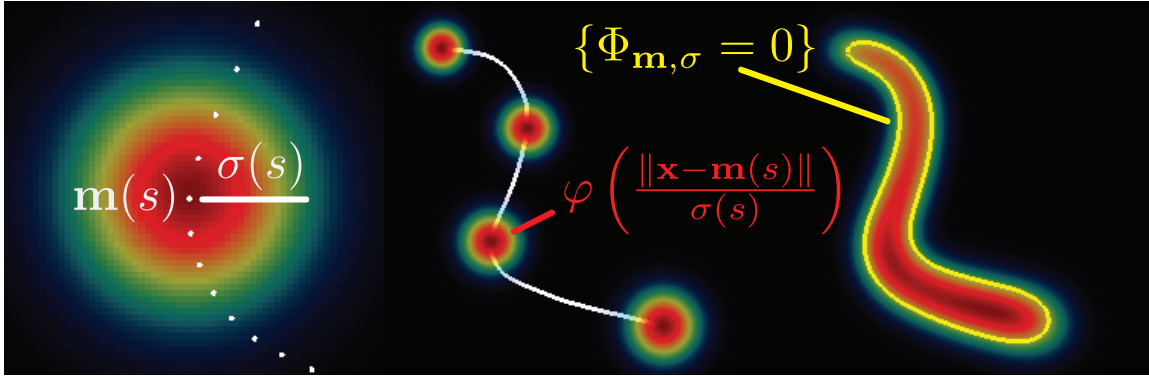


Figure 4.5 — Analytical implicit representation of a 2D vessel. $\Phi_{\mathbf{m},\sigma}$ is obtained by integrating a smooth radial function ω centered all over the curve $\mathbf{m}(s)$, with continuously-varying scales $\sigma(s)$

The scalar field is obtained by integrating a smooth decreasing radial function φ centered all over the medial curve $\mathbf{m}(s)$, with continuously-varying scales $\sigma(s)$, as shown in Fig. 4.5. This yields the following expression for $\Phi_{\mathbf{m},\sigma}$,

$$\Phi_{\mathbf{m},\sigma}(\mathbf{x}) = \int_0^1 \varphi\left(\frac{\|\mathbf{x} - \mathbf{m}(s)\|}{\sigma(s)}\right) \|\mathbf{m}'(s)\| ds - C \quad (4.15)$$

where \mathbf{x} is any point in the domain Ω , C an arbitrary positive constant and φ is typically a Gaussian function. Note that the above expression is valid in any dimension, which enables

the same approach to be applied in 2D and 3D. The term $\|\mathbf{m}'(s)\|$ ensures invariance with respect to parameterization.

In [132], Oeltze et al. used a similar representation for visualization and rendering of complex vascular structures, in particular in the liver, for their nice blending properties. However, the parameterized centerline $\mathbf{m}(s)$ and scales $\sigma(s)$ in (4.15) were assumed to be known and provided by other means, such as extraction of the skeleton of a binary segmentation. This surface reconstruction process with convolution surfaces is illustrated in Fig. 4.6. In contrast, we propose to use directly this model to perform segmentation, treating \mathbf{m} and σ as the unknown variables and integrate the representation in the region-based functional.

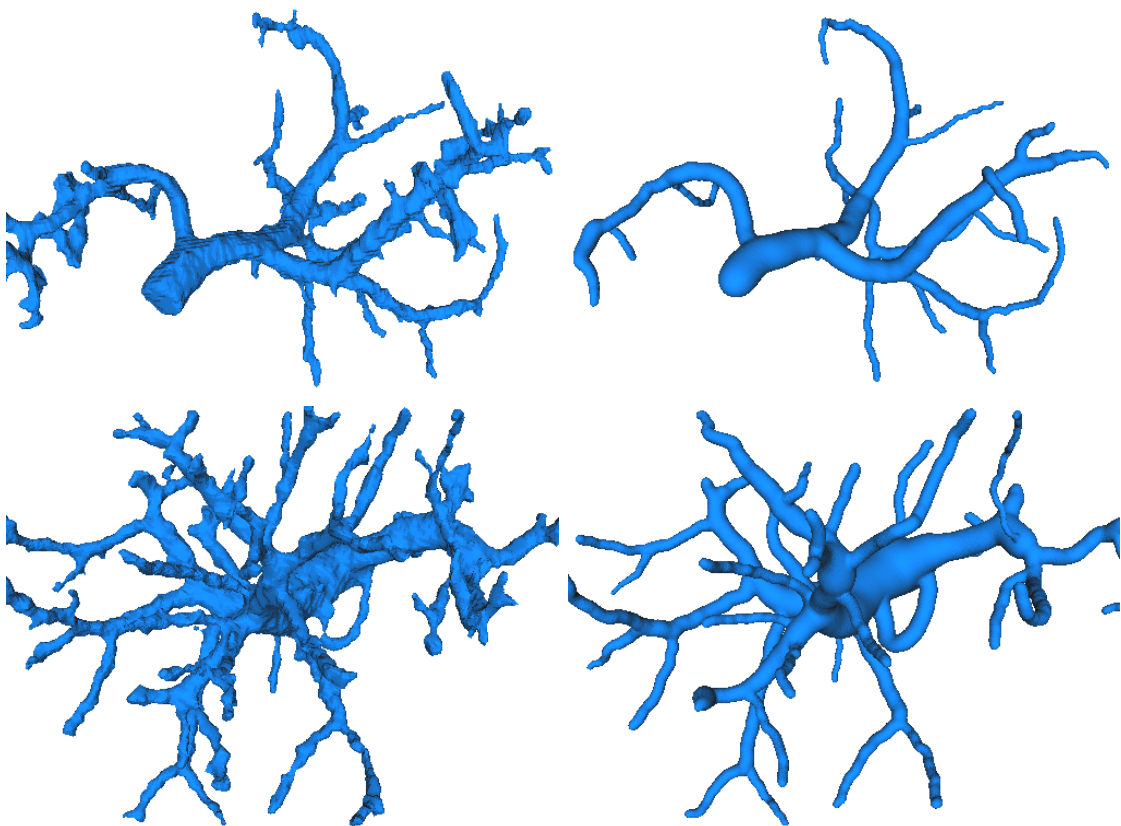


Figure 4.6 — Using convolution surfaces for visualizing complex vascular structures. The method proposed in [132] is used to clean a segmentation of the portal venous tree in the liver. On the left, two examples of raw result obtained with the algorithm in section 4.2. On the right, after skeletonization of the binary segmentation, we have reconstructed the vessel tree with implicit medial convolution surfaces, in which each vessel branch is modeled by (4.15)

4.3.2 Problem Formulation

Under the general framework presented in section 3.2, we consider the optimal partition of the image in two phases as the best trade-off between the foreground shape regularity and

the homogeneity of some features within each region:

$$\min_{\Omega_1, \alpha_1, \alpha_2} \left\{ \mathcal{R}(\Omega_1) + \int_{\Omega_1} r_1(\mathbf{x}, \alpha_1) d\mathbf{x} + \int_{\Omega \setminus \Omega_1} r_2(\mathbf{x}, \alpha_2) d\mathbf{x} \right\} \quad (4.16)$$

Recall that an implicit representation of Ω_1 can be used, defining a real function Φ , positive in the foreground. Using the Heaviside function H , $H(\Phi)$ is the characteristic function of the foreground region Ω_1 , and (4.16) is equivalent to

$$\begin{aligned} \min_{\Phi} \left\{ \mathcal{R}(\Phi) + \int_{\Omega} H(\Phi(\mathbf{x})) r(\mathbf{x}) d\mathbf{x} \right\} \\ \text{with } r(\mathbf{x}) = r_1(\mathbf{x}, \alpha_1) - r_2(\mathbf{x}, \alpha_2) \end{aligned} \quad (4.17)$$

Substituting the vessel representation (4.15) into the objective criterion (4.17) and associating specific regularization terms to the unknown centerline $\mathbf{m}(s)$ and scales $\sigma(s)$ yields:

$$\min_{\mathbf{m}, \sigma} \left\{ \mathcal{R}(\mathbf{m}, \sigma) + \int_{\Omega} H(\Phi_{\mathbf{m}, \sigma}(\mathbf{x})) r(\mathbf{x}) d\mathbf{x} \right\}, \quad (4.18)$$

where $\mathcal{R}(\mathbf{m}, \sigma)$ is designed to penalize both the *length* of the centerline and the *variations of scale* along it, controlled by the positive scalar parameters λ and μ respectively:

$$\mathcal{R}(\mathbf{m}, \sigma) = \lambda \int_0^1 \|\mathbf{m}'(s)\| ds + \mu \int_0^1 |\sigma'(s)|^2 ds \quad (4.19)$$

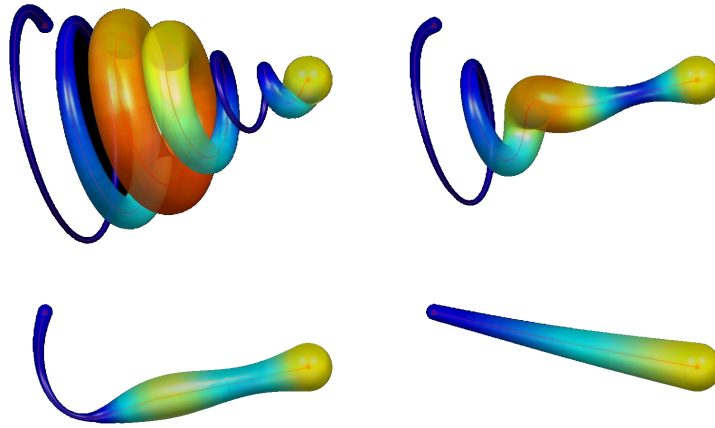


Figure 4.7 — Joint regularization of both the length of the centerline \mathbf{m} (curvature flow) and the variations of scales $\sigma(s)$ (1D heat equation) along the centerline, in the effect of minimizing the term $\mathcal{R}(\mathbf{m}, \sigma)$ (4.19), for fixed end-points. The scales $\sigma(s)$ are color-coded on the surface to better visualize the diffusion process.

4.3.3 Minimization Scheme

The Euler-Lagrange equations of the functional in (4.18) can be found by calculus of variations, taking advantage of the analytical expression of the implicit representation. The details of these calculations can be found in Annex C . They result in gradient-descent evolution equations for both the centerline and the scales, of the form:

$$\begin{aligned}
\forall s \in]0, 1[\quad \frac{\partial \mathbf{m}}{\partial t}(s) &= \kappa(s) \left(\lambda + \int_{\{\Phi=0\}} \frac{r(\mathbf{x})}{\|\nabla \Phi(\mathbf{x})\|} C(\mathbf{x}, s) d\mathbf{x} \right) \mathcal{N}(s) \\
&\quad - \|\mathbf{m}'(s)\| \int_{\{\Phi=0\}} \frac{r(\mathbf{x})}{\|\nabla \Phi(\mathbf{x})\|} \mathbf{N}(\mathbf{x}, s) d\mathbf{x} \\
\frac{\partial \mathbf{m}}{\partial t}(1) &= - \left(\lambda + \int_{\{\Phi=0\}} \frac{r(\mathbf{x})}{\|\nabla \Phi(\mathbf{x})\|} C(\mathbf{x}, 1) d\mathbf{x} \right) \mathcal{T}(1) \\
\frac{\partial \mathbf{m}}{\partial t}(0) &= \left(\lambda + \int_{\{\Phi=0\}} \frac{r(\mathbf{x})}{\|\nabla \Phi(\mathbf{x})\|} C(\mathbf{x}, 0) d\mathbf{x} \right) \mathcal{T}(0) \\
\forall s \in]0, 1[\quad \frac{\partial \sigma}{\partial t}(s) &= \mu \sigma'' - \|\mathbf{m}'(s)\| \int_{\{\Phi=0\}} \frac{r(\mathbf{x})}{\|\nabla \Phi(\mathbf{x})\|} B(\mathbf{x}, s) d\mathbf{x} \\
\frac{\partial \sigma}{\partial t}(1) &= -\mu \sigma'(1) \\
\frac{\partial \sigma}{\partial t}(0) &= \mu \sigma'(0)
\end{aligned} \tag{4.20}$$

where κ is the curvature of the centerline, \mathcal{T} its tangent, \mathcal{N} its normal, $\Phi = \Phi_{\mathbf{m}, \sigma}$ and functions, $C(\mathbf{x}, s)$, $\mathbf{N}(\mathbf{x}, s)$ and $B(\mathbf{x}, s)$ are given by

$$C(\mathbf{x}, s) = \frac{\sigma(s)}{2 \|\mathbf{x} - \mathbf{m}(s)\|} \varphi' \left(\frac{\|\mathbf{x} - \mathbf{m}(s)\|}{\sigma(s)} \right)$$

$$\mathbf{N}(\mathbf{x}, s) = C(\mathbf{x}, s) \frac{\mathbf{x} - \mathbf{m}(s)}{\sigma^2(s)}$$

$$B(\mathbf{x}, s) = - \left\langle \mathbf{N}(\mathbf{x}, s), \frac{\mathbf{x} - \mathbf{m}}{\sigma} \right\rangle$$

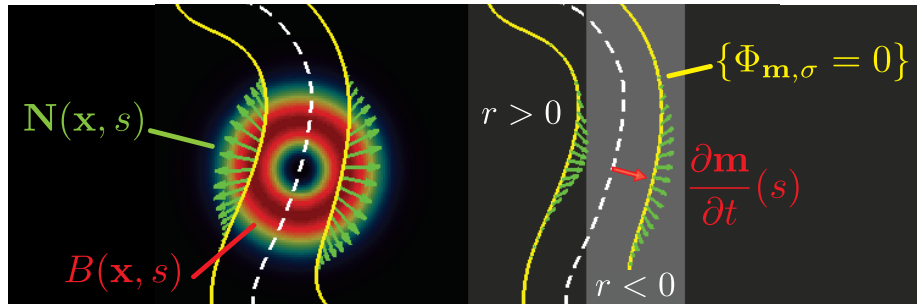


Figure 4.8 — Left: vector field $\mathbf{N}(\mathbf{x}, s)$ plotted only on the boundary $\{\Phi_{\mathbf{m},\sigma} = 0\}$, and $B(\mathbf{x}, s)$, color-coded. Right: Evolution of a centerline point with Eq.(4.20) as the sum of all forces $-r.\mathbf{N}$ computed on the boundary, for a simple image term $r(\mathbf{x})$ shown in gray.

The advantages of these coupled evolution equations for \mathbf{m} and σ are as follows:

- the centerline (skeleton) is *jointly estimated* with the boundary of the vessel, instead of considering one after the other.
- the model can be used with *free extremities*, with specific terms that naturally appear to handle the motion of $\mathbf{m}(0)$ and $\mathbf{m}(1)$, and similarly for σ .
- it is the *exact same formulation in 2D and 3D*, contrary to other approaches based on generalized cylinders.

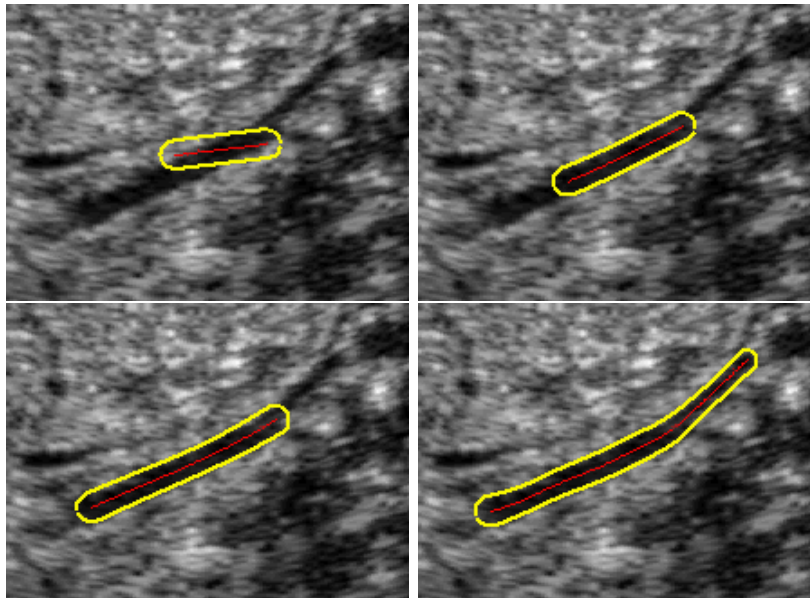


Figure 4.9 — 2D joint centerline and vessel boundary extraction on a ultrasound image of a vessel in the liver. Top left: initialization, Top right: final result. Joint the centerline curve \mathbf{m} , shown in red, as well as the scales $\sigma(s)$ along the curve. Observe that the model naturally *extends* in the structure and stops due to the longitudinal contrast found at the extremities. The region intensity model is the piecewise-smooth error term given in (4.2).

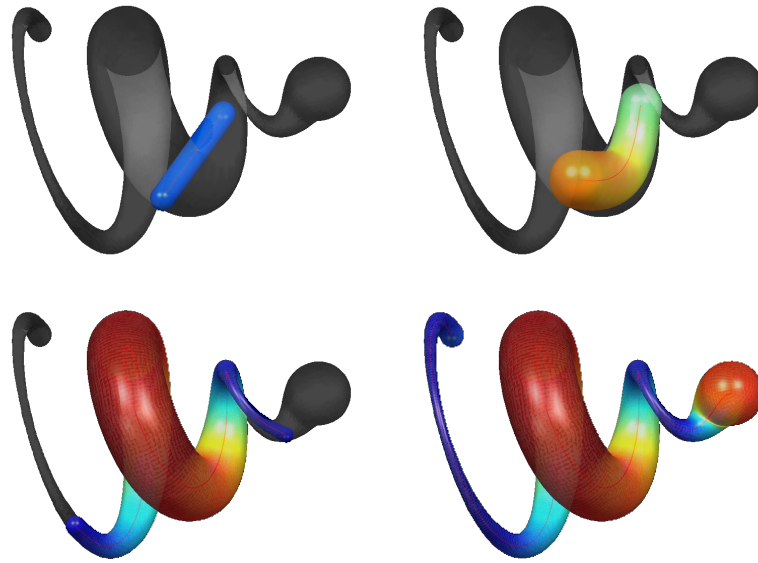


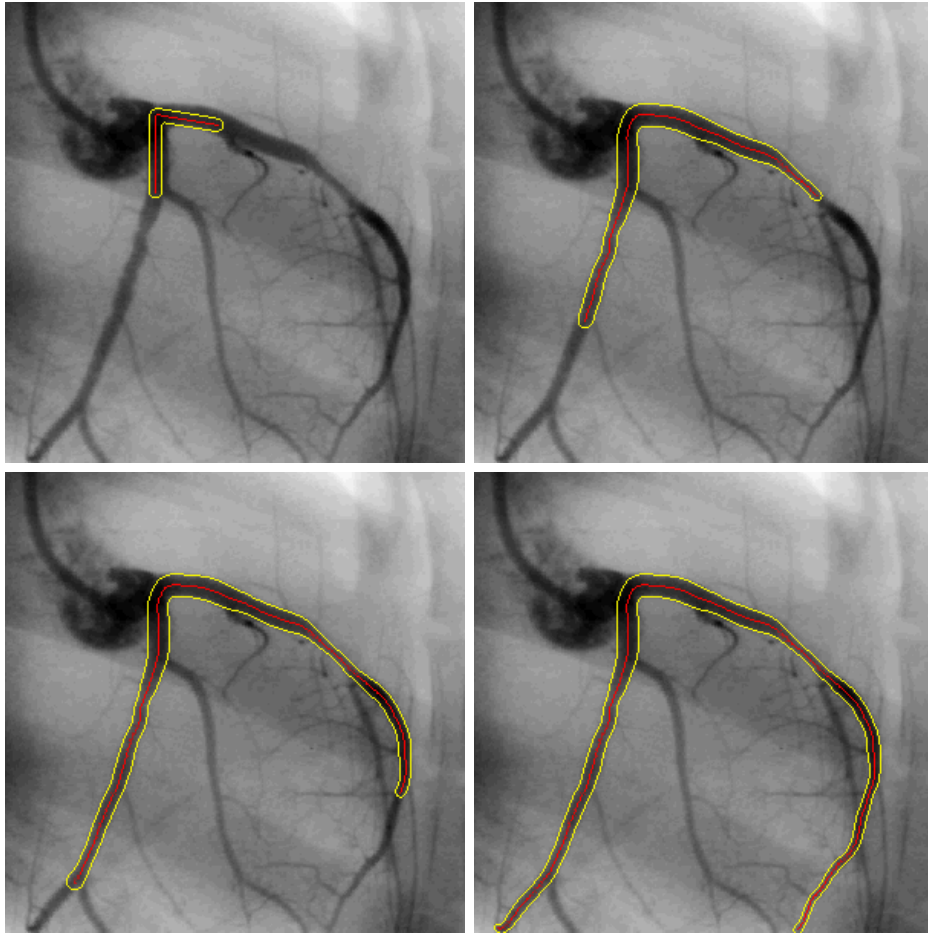
Figure 4.10 — 3D Evolution of a medial convolution surface on synthetic data - In gray, a rendering of the surface of a binary synthetic object. In color, the implicit convolution surface with a centerline and continuous scales is extending inside the object.

These properties are illustrated in Figures 4.11, 4.9 and 4.10. Figure 4.11 shows an evolution of an implicit convolution surface in the Left Anterior Descending (LAD) and Circumflex coronary arteries of a cardiac X-Ray angiography image. Robustness to branching vessels and to the aorta back-flow is observed, thanks to the long-range diffusion of $\sigma(s)$ along the centerline. With free extremities, the model is also capable of naturally *extending* in the arteries and stops, in this case, when the border of the image is attained. In Figure 4.9 and 4.10, image contrast at the end of the structure enables a natural equilibrium of the extremities.

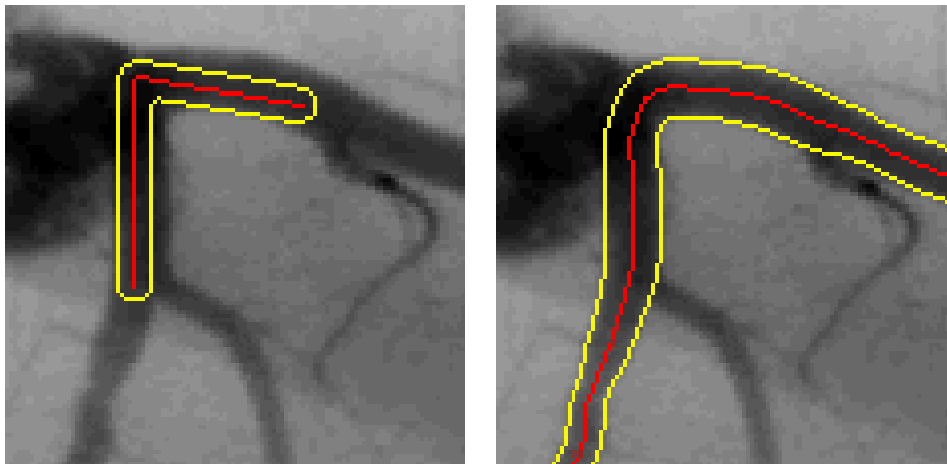
4.3.4 Inferior Vena Cava Segmentation

The Inferior Vena Cava (IVC) is the large vein that carries de-oxygenated blood from the lower half of the body into the right atrium of the heart. Before reaching the heart, the IVC passes through the liver without irrigating it. In the context of liver clinical diagnosis, pre-operative planning and therapy, IVC segmentation from CT scans plays a crucial role. This role is twofold. First, the accuracy of liver volumetry is critical for liver donor transplantation, and considering the IVC as part of the liver significantly overestimates the volume of its parenchyma. Second, the IVC is an essential landmark for the segmentation of the hepatic and portal vascular trees (brightest vessels in Fig.4.12) which are the base for the definition of liver segments, following a Couinaud anatomical model [5].

In clinical practice, manual segmentation by radiology experts is time-consuming, subjective and difficult. Recently, several fully automatic algorithms for liver segmentation have



evolution of the centerline (red) and boundary (yellow) following (4.20)



(e) initialization (zoomed)

(f) final result (zoomed)

Figure 4.11 — 2D joint centerline and vessel boundary extraction on a X-Ray coronary angiography. The model is initialized as in (e) the centerline curve \mathbf{m} , shown in red, as well as the scales $\sigma(s)$ along the curve are jointly optimized. Observe the robustness to branching and to the aorta back-flow due to the long-range diffusion of $\sigma(s)$ along the centerline. The model is also capable of naturally *extending* in the main vessel branch, thanks to free extremities. Similarly as in the previous section, the region intensity model is the piecewise-smooth error term given in (4.2).

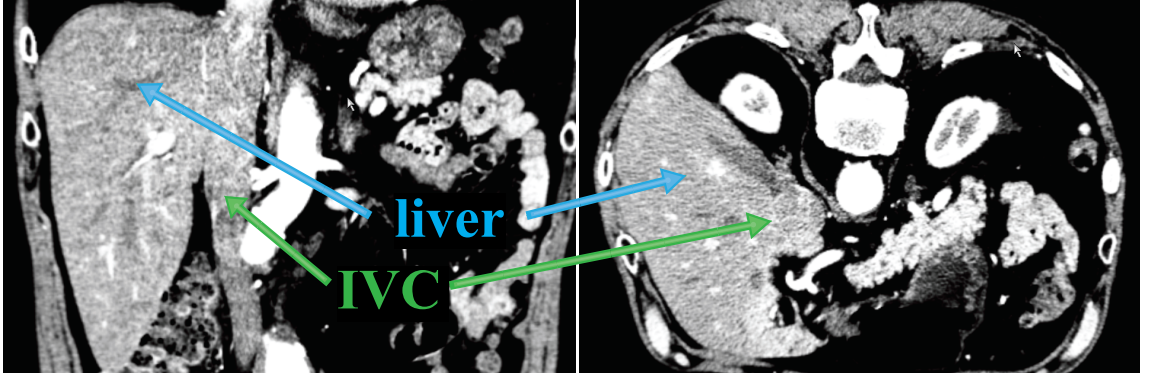


Figure 4.12 — Sagittal/axial views of a contrast-enhanced liver CT scan, showing lack of clear boundaries between the Inferior Vena Cava (IVC) and liver parenchyma.

been proposed and validated against manual segmentation references [5, 82]. However, only few attempts to automatically exclude the IVC from the liver segmentation have been carried out [41, 150]. Automatic IVC segmentation remains difficult given the anatomical inter-patient variability, the lack of well-defined boundaries with the liver parenchyma, the possible presence of nearby tumors and the effect of non-uniform distribution of the contrast agent. Consequently, existing approaches weakly perform under non-ideal scenarios, and the problem remains unresolved up to now. To cope with the aforementioned difficulties, our contribution is twofold: (1) a model of the IVC as an implicit representation of a generalized cylinder, as a direct application of the previous section and (2) a vessel-specific local region-based criterion along the centerline.

Local Statistics along the Centerline

These general evolution equations can be adapted to vessel segmentation by designing homogeneity measures r_1 and r_2 that capture the local variations due to the complex space-varying statistics of the outside tissues.

In this case of the IVC, the piecewise-smooth assumption does not suffice for the background, because the IVC is surrounded by too many structures of very distinct intensities. Neither do global non-parametric probability distributions apply due to the important contrast variations from the higher part (close to the heart) and the lower one (see Fig. 4.12). We already described a method to estimate local-non-parametric distributions in a way that is consistent with the variational formulation, in section 3.2.4.

In the following, we further specify their expression for vessels to avoid computing the distributions everywhere in space. The idea is to define a local probability density $p_i(I(\mathbf{x}), s)$ at each point $\mathbf{m}(s)$ of the curve, instead of at each point $\mathbf{y} \in \Omega$. The classification error at a given point $\mathbf{x} \in \Omega$ is obtained by a weighted integration of the contributions of each local probability densities $p_i(I(\mathbf{x}), s)$ along the centerline,

$$r_i(\mathbf{x}, p_i) = - \int_0^1 W_a(\mathbf{x} - \mathbf{m}(s)) \log p_i(I(\mathbf{x}), s) \|\mathbf{m}'(s)\| ds \quad (4.21)$$

where the blending scale a of W is related to the intensity variations along the vessel. Consistently with chapter 3, we define the total classification error $E_i(p_i)$ of region Ω_i as:

$$E_i(p_i) = \int_{\Omega_i} r_i(\mathbf{x}, p_i) d\mathbf{x} = - \int_{\Omega} \int_0^1 W_a(\mathbf{x} - \mathbf{m}(s)) \log p_i(I(\mathbf{x}), s) \|\mathbf{m}'(s)\| ds d\mathbf{x} \quad (4.22)$$

With very similar calculations to section 3.2.4, the optimality conditions of $E_i(p_i)$ subject to the constraint $\forall s \in [0, 1], \int_{\mathbb{R}} p_i(a, s) da = 1$ reveal that probability densities p_i should be updated periodically during optimization using:

$$p_i^*(a, s) = \frac{\int_{\Omega_i} W_a(\mathbf{x} - \mathbf{m}(s)) K_{\epsilon}(I(\mathbf{x}) - a) d\mathbf{x}}{\int_{\Omega_i} W_a(\mathbf{x} - \mathbf{m}(s)) d\mathbf{x}}, \quad (4.23)$$

Combined with this local region-based criterion that accurately represents the intensity statistics along the centerline, the implicit generalized cylinder has the required ability to follow image evidence where it is available (upper and lower parts) and *extrapolate* the tubular surface where it is missing (parts touching the liver). For the sake of robustness and control, we use the model with *fixed extremities*, setting the derivatives at the end-points to 0, in order to automatically segment the Inferior Vena Cava in contrasted CT images. The initialization strategy, based on an analysis of the surrounding anatomy to locate the extremities, is described in [104], and some typical results are shown in Figure 4.13 and Figure 4.14.

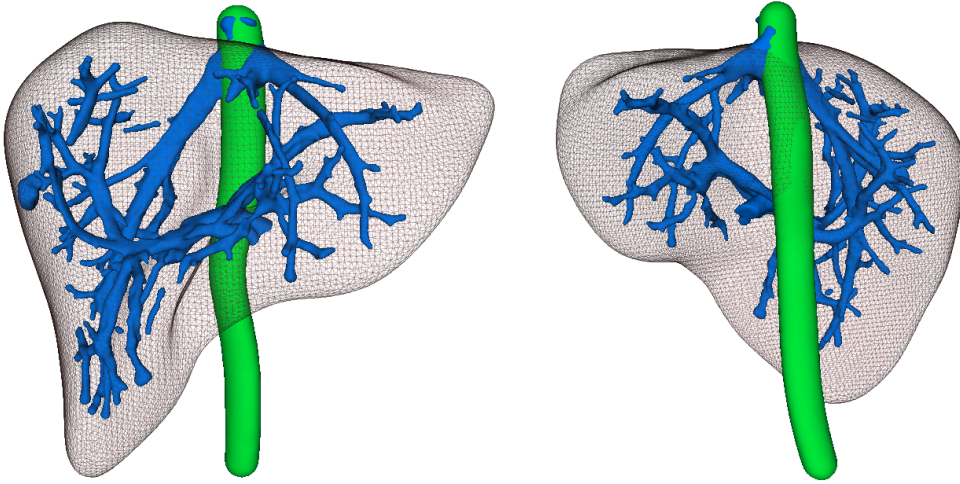


Figure 4.13 — Front and side views of IVC + liver veins segmentation, from the CT image shown in the introduction chapter. The Inferior vena Cava, segmented with a convolution surface $\Phi_{\mathbf{m},\sigma}$, is shown in green. The liver veins, represented with a membership function u as in section 4.2, is shown in blue. The mask of the liver in which the segmentation of the veins is performed is transparent.

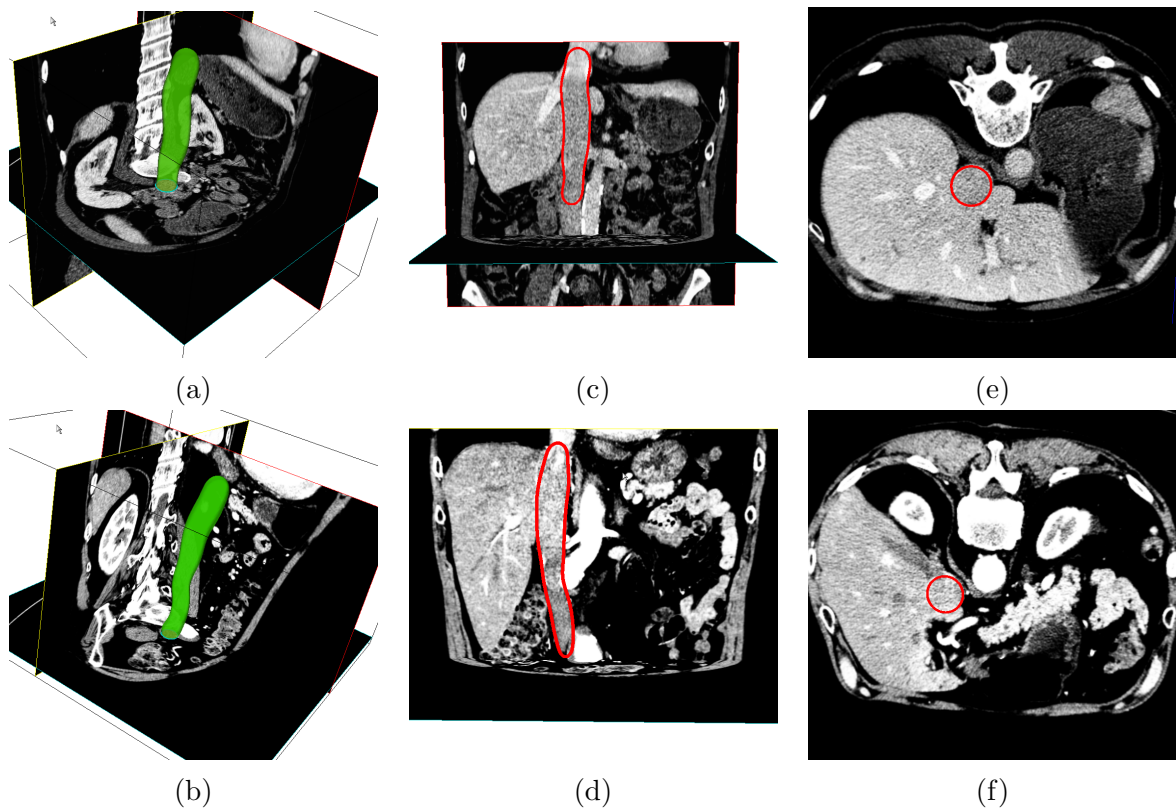


Figure 4.14 — Segmentation of the IVC in two different CT volumes, in each row. (a)-(b) show a 3D surface rendering, (c)-(d) sagittal views and (e)/(f) axial views, showing the algorithm performance in the absence of clear boundaries with the liver parenchyma.

4.4 Conclusion

In this chapter, we considered in the same region-based variational framework two completely different representations to extract vessels in 3D angiography. The common hypothesis is that vessel segmentation is viewed as a two-phase optimal separation problem where each phase (vessels/tissues) is assumed to show smoothly-varying intensities.

The first method uses the convex formulation of chapter 3 with a membership function, aimed at partitioning a volume into two non-overlapping smooth components subject to a perimeter constraint. We proposed additional constraints in order to control both the contrast of the vessel lumen and its geometry. The new constraints reduce the sensitivity to inconsistent initial conditions and limit the appearance of possible leakages, without any significant complexity overhead. We illustrated these advantages on 3D CT images of the hepatic vascular system. The advantage is that the topology of the target structures can be arbitrarily complex. However, besides the additional constraints, applicability remains limited either to the cases where there are mostly well-contrasted vessels in the image, or to a controlled spatial domain (here the pre-segmented liver).

The second representation is an implicit surface that is specifically adapted to tubular shapes and borrowed from computer graphics and modeling. It is a smooth approximation of a generalized cylinder, with a parameterized curve as skeleton primitive and varying-scale Gaussian elements blended along the curve. The smooth implicit representation enables to compute the derivatives of the region-based criterion with respect to the curve and the scales, which are expressed as boundary integrals over the surface with specific terms for the end-points. Consequently, extremities can either be free to move or fixed a priori, depending on the application. It would be interesting to extend the same principles to hierarchical tree structures, in particular to handle the case of evolution equations for the bifurcation points.

Since this second technique is based on a tubular model, it is more robust to missing contrast and imaging artifacts than the first one. However, robustness comes at the price of a fixed topology, here considered to be a single branch. Another consequence is that the result of the segmentation is not allowed to derive from a generalized tube with a circular cross-section, while vessels can have in reality more flattened shapes.

Recently, Pizaine et al. proposed an extension of the method presented in section 4.3.1 in [141]. The authors represent vessels with an implicit function built from the convolution of a centerline function with localized kernels of continuously-varying scales. Rather than modeling centerlines with *explicit* parameterized curves $\mathbf{m}(s)$, the authors use a second implicit function, which gives the topological flexibility to create new branches.

Interactive Segmentation with Non-Euclidean Radial Basis Functions

5

In this chapter, we propose a new implicit surface representation that is specifically designed to add *interactive* capabilities to 3D segmentation algorithms.

The main idea is to span a finite-dimensional subset of implicit functions with linear combinations of a small number of spatially-localized kernels that follow image features. This is achieved by replacing the *Euclidean* distance in conventional Radial Basis Functions, recently proposed in the context of image segmentation by Gelas et al. in [73], with *non-Euclidean, image-dependent distances*. For the minimization of a region-based criterion, this representation yields more accurate results with much fewer control points than its Euclidean counterpart, leading to a very small number of variables is to optimize.

If the user positions the control points, the non-Euclidean distance enables to further specify the local kernels for a target object in the image. Moreover, taking advantage of implicit representations in which the sign determines the membership to the object, interactive control over the segmentation result is obtained by casting inside/outside labels as inequality constraints. We use a variant of the Active Sets algorithm to solve the constrained optimization problem, since the constraints turn out to be linear with respect to the optimization variables.

Finally, we discuss several algorithmic aspects to achieve a responsive interactive workflow with instant feedback in 3D. Using this technique, the delineation of whole anatomical structures of moderately complex shape can be obtained in a few intuitive interactions.

5.1 Introduction

In the hope of reproducing human skills to localize and identify specific objects in images, many research efforts have been focused on the development of fully automatic segmentation algorithms. This goal can sometimes be reached, for instance when the shape of the object is known and modeled, by exploiting far more information than the image alone provides. Unfortunately, in many cases, such prior information is not available and the user has to be involved in the segmentation process. In medical imaging for instance, the knowledge of an expert practitioner is often irreplaceable. To be accepted in daily medical practice, in particular with volumetric data, general-purpose segmentation tools should not only be interactive but also provide intuitive, robust and responsive control.

In the past few years, fast interactive segmentation algorithms have been proposed [11, 53, 91, 127, 148, 186]. User interactions are typically handled in 2D by drawing so-called "scribbles", associating inside/outside labels to parts of the image. In this work, we present an interactive segmentation framework based on the selection of only a few points, inside or outside the object of interest. Our technique relies on the minimization of an objective criterion over a sensible, low-dimensional subset of possible implicit functions. This subset is spanned by a novel class of non-Euclidean *Radial Basis Functions*, built from image-dependent metrics using local image features such as intensity distributions or edge information. To the best of our knowledge, this is the first introduction of image-dependent non-Euclidean distances into Radial Basis Functions.

For segmentation with implicit surfaces, spatially-localized image-adaptive kernels achieve better accuracy with far fewer basis elements, as soon as they are properly positioned. Consequently, we propose an interactive scenario in which the dimension of the basis, hence the complexity of the optimization problem, increases progressively as the user introduces control points, depending on the difficulty of the segmentation task.

Moreover, the association of inside/outside labels to control points is formulated through additional linear inequality constraints. Finally, as the objective criterion may have local minima, we introduce an auxiliary quadratic programming problem that, solved in linear time, allows the user to guide the process toward a local minimum of his or her choice. Minimizing over a restricted low-dimensional space bears some similarities with the *GeoS* algorithm [53], in which optimization is performed over a two-dimensional space built from two *geodesic* morphological operators.

In section 5.2, we recall the implicit representation framework and the variational principles involved in the optimization of a region-based criterion. Recent formulations using Radial Basis Functions are also discussed. In section 5.3.1, we introduce an extension with non-Euclidean distances in order to build an image-adaptive basis of implicit functions. In section 5.3.2, we cast user interactions into linear inequality constraints. Finally, we describe in section 5.4 the complete sequential workflow of a real-time 3D interactive tool.

5.2 Segmentation with Radial Basis Functions

Recall from Chapter 3 that a variational formulation for partitioning a n -dimensional image $I : \Omega \subset \mathbb{R}^n \mapsto \mathbb{R}$ into two disjoint homogeneous regions $\Omega_1 \subset \Omega$ and $\Omega_2 = \Omega \setminus \Omega_1$ typically involves the choice of two application-specific components: a pixel-wise classification error for each region (r_1, r_2) and a representation for the foreground region with an associated regularity constraint \mathcal{R} . Formally, the minimization problem reads:

$$\min_{\Omega_1, \alpha_1, \alpha_2} \left\{ \mathcal{R}(\Omega_1) + \lambda \int_{\Omega_1} r_1(\mathbf{x}, \alpha_1) d\mathbf{x} + \lambda \int_{\Omega \setminus \Omega_1} r_2(\mathbf{x}, \alpha_2) d\mathbf{x} \right\} \quad (5.1)$$

In this chapter, we concentrate our efforts on the design of a representation for the foreground region that is particularly adapted to interactive segmentation. As an example, we use as region descriptors for all illustrations the global non-parametric classification error from section 3.2.2:

$$\begin{cases} \alpha_i = \{p_i\} \\ r_i(\mathbf{x}, p_i) = -\log p_i(I(\mathbf{x})) \end{cases} \quad (5.2)$$

With an implicit representation, the foreground Ω_1 is defined as the zero super-level set of a scalar function Φ , $\Omega_1 = \{\mathbf{x} \in \Omega, \Phi(\mathbf{x}) \geq 0\}$. Focusing on the supervised case where α_1 and α_2 are fixed, without loss of generality, and setting $r(\mathbf{x}) = \lambda r_1(\mathbf{x}, \alpha_1), -\lambda r_2(\mathbf{x}, \alpha_2)$ the criterion (5.1) can be re-formulated as a minimization over a functional set \mathcal{F} :

$$\min_{\Phi \in \mathcal{F}} \left\{ \mathcal{R}(\Phi) + \int_{\Omega} H(\Phi(\mathbf{x})) r(\mathbf{x}) d\mathbf{x} \right\} \quad (5.3)$$

where H is the Heaviside step function. \mathcal{F} is generally defined as an infinite-dimensional space such as Lipschitz functions. But relatively early in the history of implicit models, the idea of building \mathcal{F} as a space spanned by a finite basis was proposed [166], using for instance hyper-quadratics [42, 80]. Recently, this approach has regained interest and authors have proposed to generate \mathcal{F} with B-Splines [14, 15] or Radial Basis Functions [73, 124, 160].

Widely used for scattered data interpolation and surface reconstruction [22, 67, 101, 164, 180], Radial Basis Functions offer intrinsic smoothness and do not require a regular sampling of the image domain. The implicit function Φ is built up as a linear combination of translated and scaled versions of a radially-symmetric non-negative kernel φ centered around N points \mathbf{x}_i (see Fig.5.1):

$$\Phi_{\rho}(\mathbf{x}) = \sum_{i=1}^N \lambda_i \varphi \left(\frac{\|\mathbf{x} - \mathbf{x}_i\|}{\sigma_i} \right) = \sum_{i=1}^N \lambda_i \varphi_i(\mathbf{x}) \quad (5.4)$$

The scalar weights λ_i , positions \mathbf{x}_i and scales σ_i constitute the *discrete* set of parameters $\rho = \{\lambda_i, \mathbf{x}_i, \sigma_i\}$. The *functional* in (5.3) becomes a *function* of ρ :

$$\min_{\rho} \left\{ F(\rho) = \int_{\Omega} H(\Phi_{\rho}) r(\mathbf{x}) d\mathbf{x} \right\} \quad (5.5)$$

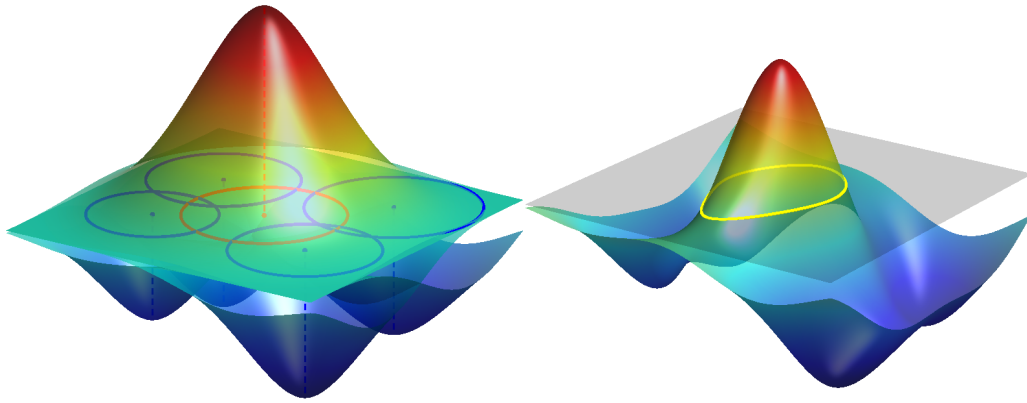


Figure 5.1 — An implicit contour with Euclidean RBFs. On the left, few basis functions with positive (red) and negative (blue) weights. On the right, an implicit function obtained by linear blending.

The regularization term \mathcal{R} is usually omitted since the basis functions are intrinsically smooth. Obviating regularization and minimizing F over a finite set are the key advantages of this parametric formulation. Compared to infinite-dimensional level-set techniques, this low-dimensional representation yields more efficient optimization algorithms while keeping topological flexibility in 2D and 3D.

Along these lines, Gelas et.al [73] have successfully used compactly-supported radial functions for segmentation, optimizing the weights λ_i for given positions \mathbf{x}_i and scales σ_i . However, as pointed out in the context of surface reconstruction [60], radially-symmetric kernels fail to model the asymmetric nature of sharp features such as straight edges. For image segmentation applications, this tends to compromise the low-dimensionality advantage, as the number of basis functions rapidly grows to accurately recover high curvature objects. To overcome this limitation, Slabaugh et.al [160] have proposed to use *anisotropic* Gaussian kernels and optimize their orientation as well as their weight, position and scales. Their 2D experiments show a better capture of image details at the price of increasing the dimensionality of the optimization space ($6N$ parameters).

5.3 Proposed Algorithm

5.3.1 Switching to Non-Euclidean Distances

In order to obtain more accurate segmentation results without increasing the number of parameters, we believe that the basis functions should be designed according to the actual image content. This is a key difference with previous works in which the kernels were purely geometric (spherical or elliptical). The basic idea is to span the space of implicit functions Φ by a richer basis in which each element φ_i is localized in space and also incorporates meaningful image information for segmentation. This can be obtained in the RBF framework by a modification inspired by front propagation theory [114]. By construction, Radial

Basis Functions only depend on the *distance* to their center. Their spherical shape is only a consequence of the choice of the *Euclidean* distance. Instead, we propose to switch to an image-dependent *non-Euclidean* distance to build the kernels. This extension opens up the design of basis functions with iso-levels that are no longer spherical and naturally follow the image features (see Fig.5.3). Each φ_i becomes:

$$\varphi_i(\mathbf{x}) = \varphi\left(\frac{\|\mathbf{x} - \mathbf{x}_i\|_{g_i}}{\sigma_i}\right). \quad (5.6)$$

To each control point \mathbf{x}_i can correspond a different metric function $g_i : \Omega \mapsto \mathbb{R}$, required to be strictly positive and smooth. A physically meaningful definition of the associated non-Euclidean distance is:

$$\|\mathbf{x} - \mathbf{x}_i\|_{g_i} = \inf_{\mathcal{C} \in \Gamma(\mathbf{x}_i, \mathbf{x})} \int_0^1 g_i(\mathcal{C}(s)) \|\mathcal{C}'(s)\| ds \quad (5.7)$$

where the infimum extends over the set Γ of all differentiable curves \mathcal{C} beginning at \mathbf{x}_i and ending at \mathbf{x} . This definition allows a rather intuitive design of g_i so that the level-sets of $\|\mathbf{x} - \mathbf{x}_i\|_{g_i}$ tend to fit the image features. Indeed, as shown in [45], they have a physical interpretation of fronts propagating from \mathbf{x}_i with the image-dependent speed function $1/g_i$, the Euclidean case being re-obtained by setting $g_i = 1$. A popular choice [45] that would snap level-sets to salient contours of the image is $g_i(\mathbf{x}) = 1 + \|\nabla I\|^2$, but an essential property arises from the fact that each metric g_i can also be adapted to the local image content around each control point \mathbf{x}_i . Prior assumptions on the targeted class of images should drive the choice of adapted metrics, such as $g_i(\mathbf{x}) = 1 + (I(\mathbf{x}) - I(\mathbf{x}_i))^2$ in the simple case of piecewise-constant images. In more general situations, we use the local image intensity distribution $P_{\mathbf{x}_i}$ estimated in the neighborhood of \mathbf{x}_i to define

$$g_i(\mathbf{x}) = 1 - \beta \log P_{\mathbf{x}_i}(I(\mathbf{x})) \quad (5.8)$$

where $\beta > 0$ controls the non-Euclidean part of the metric: the smaller β is the more spherical the basis function will be. This is illustrated in Fig.5.2 where we show various basis functions obtained with increasing values of β . The numerical computation of geodesic distances is very efficient, using fast marching [133] or sweeping methods [169, 179]

By construction, such non-Euclidean distances are meaningful only in a local neighborhood of the control point \mathbf{x}_i . As a consequence, the function φ must not only be non-negative as in the Euclidean case but also *monotonically-decreasing*, to discard meaningless high distance values. The localization of each basis function φ_i in (5.6) can then be controlled by its scale parameter σ_i . A Gaussian kernel would be a valid choice, but we use for complexity reasons the \mathcal{C}^2 compactly-supported Wendland function [73, 180]:

$$\forall a \in \mathbb{R}, \quad \varphi(a) = \begin{cases} (a-1)^4(4a+1) & \text{if } a \leq 1 \\ 0 & \text{otherwise} \end{cases} \quad (5.9)$$

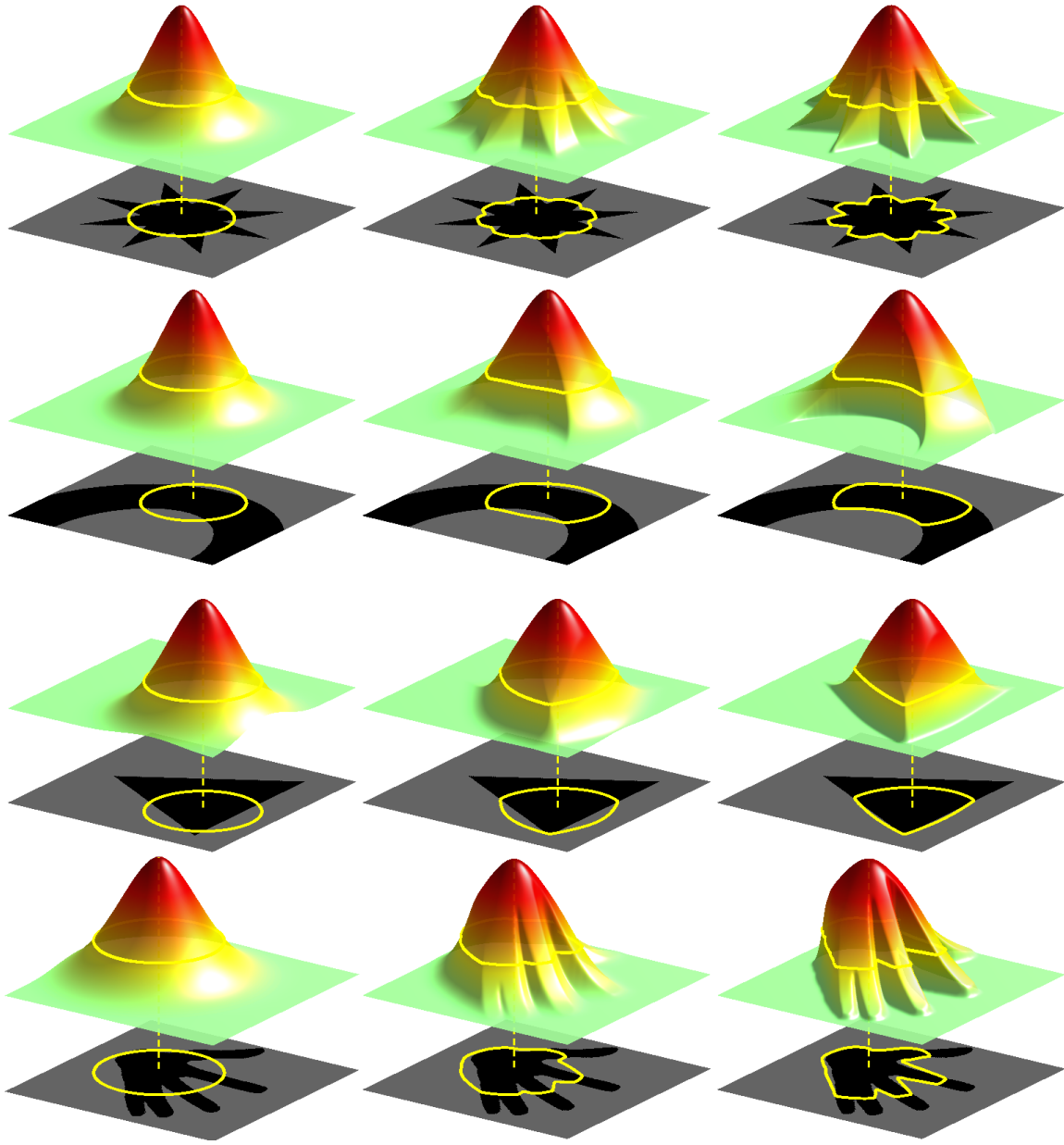


Figure 5.2 — Switching to non-Euclidean distances: From left to right, increasing the image adaptation of the non-Euclidean metric g_i turns each basis element φ_i from a spherical-shaped RBF ($\beta = 0$, left) into feature-aligned kernels ($\beta > 0$, middle/right).

Non-Euclidean distances have a long history in image segmentation, but not for the purpose of generalizing radial basis functions to build and represent implicit surfaces. In 1998, Malladi and Sethian had already used Non-Euclidean distances for Medical Shape Recovery [115] in 3D. In their algorithm, a front was propagated from a set of seed points with the Fast Marching algorithm [133] inside the structure of interest, further refined with a level-set algorithm. More recently, Bai et al. have used competing geodesic fronts from

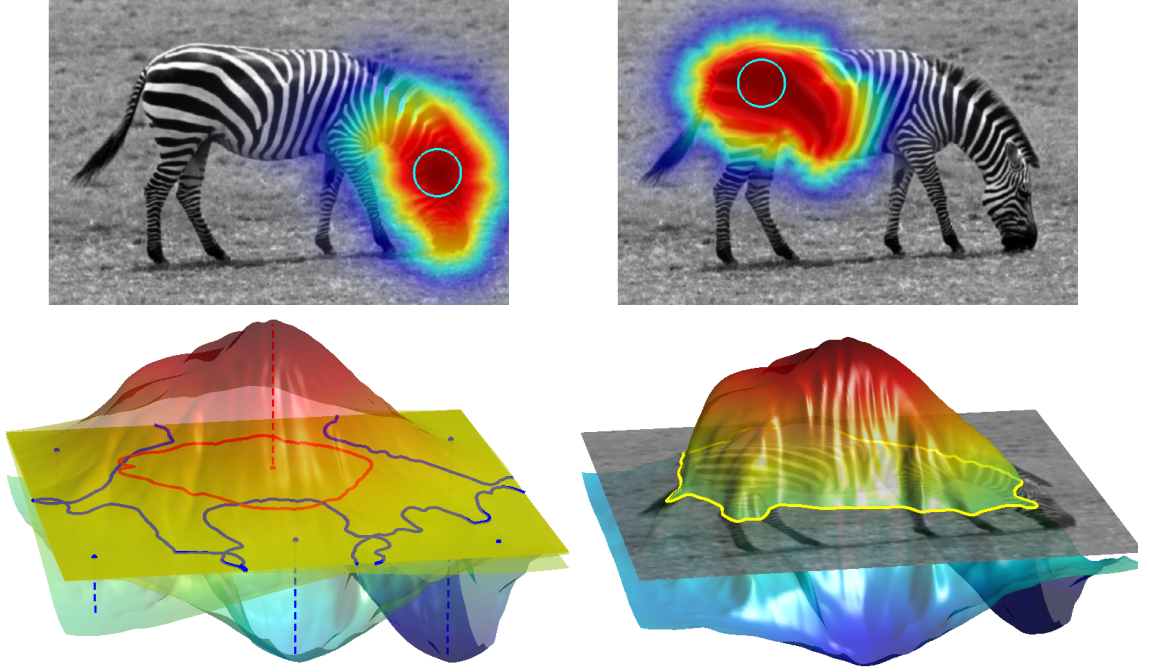


Figure 5.3 — Implicit contour based on non-Euclidean RBFs. Top: Two different basis functions on the *zebra* image, localized fronts propagated using local intensity distributions (5.8) estimated in the small circles. Bottom: on the left, several basis functions with positive (red) or negative (blue) weights λ_i ; on the right, the implicit function Φ_{λ} obtained by a linear blending of the basis functions.

scribbles inside and outside the target object for interactive segmentation of natural images and in temporal sequences [11]. Criminisi et al. defined geodesic morphological operators to reconstruct object boundaries from user-drawn scribbles in 2D and 3D [53].

A notable difference of the proposed technique is that segmentation is not directly obtained from a front propagation. Instead, multiple propagations serve to span a restricted set of admissible solutions for an independent, region-based, optimization problem. Any function Φ_{λ} of this finite-dimensional set is obtained by blending multiple localized fronts propagated at possibly different speeds:

$$\Phi_{\lambda}(\mathbf{x}) = \lambda_0 + \sum_{i=1}^N \lambda_i \varphi \left(\frac{\|\mathbf{x} - \mathbf{x}_i\|_{g_i}}{\sigma_i} \right) \quad (5.10)$$

where \mathbf{x}_i, σ_i are given control points and scales (see Fig.5.3). The weights λ_i are the only unknown parameters, with an additional negative scalar $\lambda_0 < 0$ introduced as boundary condition. Indeed, we can assume that away from all control points, every pixel should eventually be included in the background region $\{\Phi_{\lambda} < 0\}$. Since, as already mentioned, the function φ is required to vanish, then $\Phi_{\lambda}(\mathbf{x}) \rightarrow \lambda_0$ as $\|\mathbf{x} - \mathbf{x}_i\|_{g_i} \rightarrow +\infty$, which imposes the sign of λ_0 . With the above definition of the implicit function Φ_{λ} , we can now formulate

the segmentation criterion (5.5) as

$$F(\boldsymbol{\lambda}) = \int_{\Omega} H \left(\lambda_0 + \sum_{i=1}^N \lambda_i \varphi \left(\frac{\|\mathbf{x} - \mathbf{x}_i\|_{g_i}}{\sigma_i} \right) \right) r(\mathbf{x}) d\mathbf{x} \quad (5.11)$$

where $r(\mathbf{x})$ is the competition function, a pixel-wise likelihood test. The framework can be applied with any of the suitable homogeneity models presented in Chapter 3. Finally, since multiplication by a positive scalar does not change the sign of the implicit function, $\forall \alpha > 0$, $F(\alpha \boldsymbol{\lambda}) = F(\boldsymbol{\lambda})$, minimizing F is an ill-posed problem. This can be fixed as in [73] by an arbitrary normalization of the vector $\boldsymbol{\lambda}$, such as $\|\boldsymbol{\lambda}\| = 1$.

Fig.5.4 illustrates that switching to non-Euclidean kernels significantly increases segmentation accuracy, with the exact same control points.

5.3.2 Interactions as Linear Inequality Constraints

As in the case of Euclidean RBFs, a good positioning of the scattered points is essential to reach a correct segmentation with a minimal number of basis functions. Deriving an automatic scheme to optimally position the control points is a challenging research topic. However, in many cases, in particular in medical applications, the subjectivity of the segmentation task is such that this challenge is unreachable without additional prior knowledge. Within the framework introduced in the previous section, giving the user the possibility to position each control point, a dedicated shape space can be built that is not only adapted to the current image but also to the specific target object. Moreover, additional control and robustness can be offered if the user indicates whether control points lie inside or outside the object of interest. The low-dimensionality of our representation with few basis functions is a key feature to keep this interactive selection and labeling process easy and simple, in particular in 3D. With an implicit representation, the inside/outside labeling can be formalized as constraints on the sign of $\Phi_{\boldsymbol{\lambda}}$ at the precise location of the control points:

$$\forall k \in 1..N \quad C_k(\boldsymbol{\lambda}) \triangleq \gamma_k \Phi_{\boldsymbol{\lambda}}(\mathbf{x}_k) \geq 0 \quad (5.12)$$

with $\gamma_k = 1$ (resp. -1) for inside (resp. outside) points. Note that in contrast to scattered data interpolation methods, only the sign of $\Phi_{\boldsymbol{\lambda}}$ at control points is important, not its value. Developing $\Phi_{\boldsymbol{\lambda}}$ yields N linear inequality constraints for the vector $\boldsymbol{\lambda} = \{\lambda_i\}_{i=0..N}$

$$\forall k \in 1..N \quad \gamma_k \left(\lambda_0 + \sum_{i=1}^N \lambda_i \varphi \left(\frac{\|\mathbf{x}_k - \mathbf{x}_i\|_{g_i}}{\sigma_i} \right) \right) \geq 0 \quad (5.13)$$

Adding the background constraint at infinity $\lambda_0 \leq -\epsilon$, where ϵ is an arbitrary small positive constant, the $N + 1$ constraints can be rewritten in matrix form:

$$\mathbf{A}\boldsymbol{\lambda} + \mathbf{b} \geq 0 \quad (5.14)$$

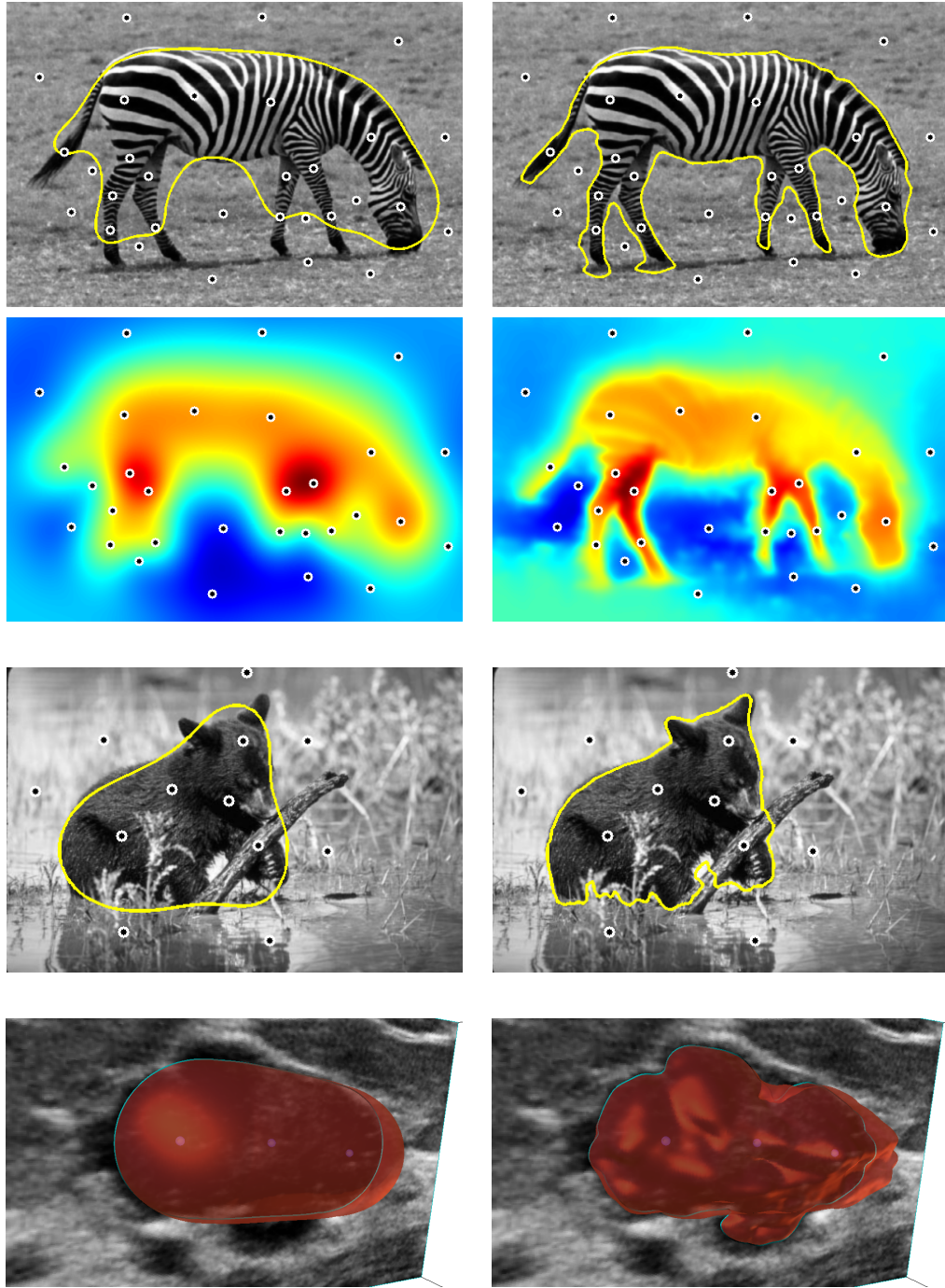


Figure 5.4 — Non-Euclidean kernels increase segmentation accuracy. Control points \mathbf{x}_i are shown as black dots. From top to bottom: Maximum-likelihood segmentation of the *zebra* image with $N = 30$ control points, using Euclidean RBFs (left) and non-Euclidean RBFs (right) built as in Fig.5.3; Corresponding optimal implicit functions, with Euclidean (left) and non-Euclidean (right) RBFs; segmentation of the *baby bear* image with $N = 12$ control points, with Euclidean (left) and non-Euclidean (right) RBFs; segmentation of a lesion in 3D Ultrasound with only $N = 3$ control points, with Euclidean (left) and non-Euclidean (right) RBFs.

$$\text{with } \mathbf{A} = \begin{bmatrix} -1 & & & \\ & \gamma_1 & & (0) \\ & & \ddots & \\ (0) & & & \gamma_N \end{bmatrix} \begin{bmatrix} 1 & 0 & \cdots & 0 \\ \vdots & & & \mathbf{M} \\ 1 & & & \end{bmatrix}$$

$$\text{and } \mathbf{M} = \left[\varphi \left(\frac{\|\mathbf{x}_i - \mathbf{x}_j\|_{g_j}}{\sigma_j} \right) \right]_{1 \leq i, j \leq N}, \quad \mathbf{b} = \begin{bmatrix} -\epsilon \\ 0 \\ \vdots \\ 0 \end{bmatrix}$$

Putting together the objective criterion (5.11) and the constraints (5.14) yields the minimization problem:

$$\begin{aligned} \min_{\boldsymbol{\lambda} \in \mathbb{R}^{N+1}} \quad & F(\boldsymbol{\lambda}) = \int_{\Omega} H \left(\sum_{i=0}^N \lambda_i \varphi_i(\mathbf{x}) \right) r(\mathbf{x}) d\mathbf{x} \\ \text{subject to} \quad & \mathbf{A}\boldsymbol{\lambda} + \mathbf{b} \geq 0 \end{aligned} \quad (5.15)$$

where the function φ_0 is constant with value 1.

5.3.3 Minimization Scheme with Active Sets

The general formulation (5.15) is a non-linear optimization problem with $N+1$ variables and the same number of linear inequality constraints. In numerical textbooks, this corresponds to a particular case of *linearly constrained programming* [131]. Its feasible set, the set of $\boldsymbol{\lambda}$ satisfying the constraints, is a cone (as many constraints as variables) with hyperplane boundaries. As soon as the matrix \mathbf{M} is invertible, this cone is non-empty and contains the summit $-\mathbf{A}^{-1}\mathbf{b}$. From a user perspective, this ensures that a segmentation can be found that satisfies the labeling constraints.

To solve (5.15) numerically, we use a variant of the *Active Set* method (see Algorithm 3), which generalizes unconstrained non-linear gradient-descent to handle inequality constraints.

Algorithm 3 relies on the computation of the gradient ∇E . Since the Heaviside function is not differentiable in the usual sense, the most popular technique consists in introducing a smooth approximation H_ϵ [40] satisfying $\lim_{\epsilon \rightarrow 0} H_\epsilon = H$. Noting δ_ϵ the derivative of H_ϵ , an approximated gradient $\nabla_\epsilon E$ would be:

$$\nabla_\epsilon F(\boldsymbol{\lambda}) = \left[\frac{\partial E}{\partial \lambda_i} \right]_i = \left[\int_{\mathbf{x} \in \Omega} \delta_\epsilon(\Phi_{\boldsymbol{\lambda}}) \varphi_i r d\mathbf{x} \right]_i \quad (5.16)$$

In classical level-set implementations, Φ is usually a signed distance function and $\delta_\epsilon(\Phi)$ defines around the zero level set a *narrow band* of constant width controlled by ϵ . In contrast, parametric implicit functions built over RBFs are *not* distance functions and $\|\nabla \Phi_{\boldsymbol{\lambda}}\|$ may undergo strong variations around the zero level-set. As shown in Fig. 5.6, the width of the band $\delta_\epsilon(\Phi_{\boldsymbol{\lambda}})$ is no longer uniform. The numerical precision of the integral

Algorithm 3: Principles of the Active Set Algorithm

A constraint $C_k \geq 0$ (5.12) is *active* at λ if $C_k(\lambda) = 0$.

Let $\mathbf{n}_k = [\varphi_k(\mathbf{x}_i)]_i$ be the normal to the hyperplane $\{C_k(\lambda) = 0\}$.

The *Active Set* $AS(\lambda)$ is the set of indices of all the active constraints at λ : $\{k | C_k(\lambda) = 0\}$.

Given a starting feasible λ^0 and its $AS(\lambda^0)$,

repeat

 Compute the function gradient $-\nabla F(\lambda^n)$

 Compute its orthogonal projection on the space spanned by $[n_k]_{k \in AS(\lambda^n)}$:

$$P^\perp(-\nabla F(\lambda^n)) = \sum_{k \in AS(\lambda^n)} e_k \mathbf{n}_k$$

 Compute a feasible direction by subtracting blocking components of the active set ($e_k < 0$)

$$\mathbf{d}^n = -\nabla F(\lambda^n) - \sum_{\{k \in AS(\lambda^n) | e_k < 0\}} e_k \mathbf{n}_k$$

 Find optimal step $\alpha^* \geq 0$ by a bounded line search

$$\lambda^{n+1} = \lambda^n + \alpha^* \mathbf{d}^n$$

 Update the *Active Set* at λ^{n+1} : $AS(\lambda^{n+1})$

until $\|\lambda^{n+1} - \lambda^n\| < \epsilon$

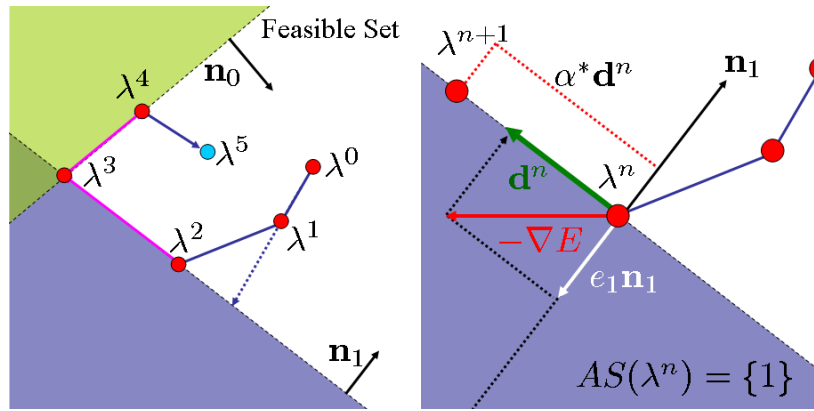


Figure 5.5 — Principles of Active Sets Algorithm

computation (5.16) is strongly affected by the choice of ϵ and might lead to unexpected results such as unwanted topology changes. To find a better approximation and avoid this arbitrary choice, one can study the limit of $\nabla_\epsilon E$ as ϵ goes to 0. Each component of this limit gradient consists of a domain integral of the form $\lim_{\epsilon \rightarrow 0} \int_\Omega \delta_\epsilon(\Phi(\mathbf{x})) f(\mathbf{x}) d\mathbf{x}$. This limit, developed in the Appendix, reveals the generalized scaling property of the δ function:

$$\lim_{\epsilon \rightarrow 0} \int_\Omega \delta_\epsilon(\Phi(\mathbf{x})) f(\mathbf{x}) d\mathbf{x} = \int_{\{\Phi=0\}} \frac{f(\mathbf{s})}{\|\nabla \Phi(\mathbf{s})\|} ds \quad (5.17)$$

This yields the exact expression of the gradient:

$$\nabla F(\boldsymbol{\lambda}) = \left[\int_{\{\Phi_{\boldsymbol{\lambda}}=0\}} \frac{\varphi_i(\mathbf{s})r(\mathbf{s})}{\|\nabla\Phi_{\boldsymbol{\lambda}}(\mathbf{s})\|} d\mathbf{s} \right]_i \quad (5.18)$$

where the domain integral (5.16) reduces to a boundary integral. This suggests a fast computation that does not involve any approximation of δ nor arbitrary choice of ϵ : extract the zero-level of $\Phi_{\boldsymbol{\lambda}}$ by any standard algorithm and numerically integrate (5.18) over this boundary using interpolated values of φ_i , r and $\|\nabla\Phi_{\boldsymbol{\lambda}}\|$. Note that omitting the denominator in (5.18) would be justified for a distance function ($\|\nabla\Phi_{\boldsymbol{\lambda}}\| = 1$) but leads to a wrong approximation in the general case.



Figure 5.6 — Approximation $\delta_{\epsilon}(\Phi_{\boldsymbol{\lambda}})$ for $\epsilon = 0.01, 0.05$ and 0.15

5.4 3D Interactive Application Workflow

Our goal is to provide as much control of the 3D segmentation process as possible with minimal and intuitive interactions in real-time. A direct application of the previously-described framework would consist in first collecting user given labeled (inside/outside) points, then launching the constrained optimization algorithm. However, this workflow would not be optimal.

In this section, we describe a more responsive sequential workflow in which dimensionality increases progressively as the user introduces corrections. At each step, a non-convex multidimensional minimization problem (5.15) should be solved, potentially facing many local minima. Unlike fully automatic segmentation algorithms for which the non-convexity is generally considered problematic, interactive methods can turn local minima into an advantage. The rationale behind the proposed workflow is to let the user drive seamlessly the optimization algorithm toward a minimum of his or her choice by deducing sound initial conditions from previous stages.

This iterative workflow is described in Algorithm 4. The user has to give the first control point required to be set inside the object of interest. The first step will propose an initial segmentation on which the user will interact to introduce corrections. It corresponds to solving problem (5.15) for two unknowns $\boldsymbol{\lambda} = [\lambda_0, \lambda_1]$ under constraints $\lambda_0 + \lambda_1\varphi_1(\mathbf{x}_1) > 0$ and $\lambda_0 < 0$. Since $\varphi_1 \in [0, 1]$ (5.9), a non-empty segmentation requires $\lambda_1 > 0$. Thus,

Algorithm 4: Sequential WorkFlow

From single *inside* point \mathbf{x}_1 compute g_1 and φ_1 ($N=1$)

Perform 1D optimization (5.19) $\longrightarrow \tilde{\lambda}^{(1)} = [\tilde{\lambda}_0^{(1)}, \tilde{\lambda}_1^{(1)}]$

repeat

 New control point \mathbf{x}_{N+1} and constraint C_{N+1}

 Compute g_{N+1} and φ_{N+1}

 Solve Constrained Quadratic Programming (5.20)

$$[\tilde{\lambda}^N, 0] \longrightarrow \lambda^{N+1}$$

 Run non-linear Active Set, Algorithm 3

$$\lambda^{N+1} \longrightarrow \tilde{\lambda}^{N+1}$$

$N \longrightarrow N + 1$

until *User is satisfied*

as already mentioned, $F(\lambda) = F(\lambda/\lambda_1)$ and (5.15) is equivalent to the following one-dimensional thresholding problem

$$\min_{\theta \in \mathbb{R}^+} F(\theta) = \int_{\Omega} H \left(\varphi \left(\frac{\|\mathbf{x} - \mathbf{x}_1\|_{g_1}}{\sigma_1} \right) - \theta \right) r(\mathbf{x}) d\mathbf{x} \quad (5.19)$$

Since φ is monotonous, selecting a threshold θ corresponds to a choice of the front propagated from the seed point \mathbf{x}_1 at the image-dependent speed $1/g_1$. This is related to methods based on the choice of propagated front [114], with a fundamental difference: the chosen front is not arbitrary and minimizes an objective region-based criterion $F(\Omega_1)$ over the one-dimensional embedding defined by the levels of the propagation.

This "one-click" step often provides already a good initial guess in case the metric g_1 can be designed to capture most of the image features, for instance with objects of homogeneous intensity distribution if a log-likelihood metric as (5.8) is used (see Figure 5.7).

Subsequently, until the user is satisfied with the result, corrections can be made by introducing a new labeled point \mathbf{x}_{N+1} and hence a new constraint. Typically, the user can drop a new *outside* point where a leakage occurred, or an *inside* point where under-segmentation is observed (see Fig.5.8 and Fig.5.9). In both cases, the new constraint is violated by the current segmentation. Since Algorithm 4 has to be initialized from a *feasible* position, the difficulty now lays on finding a suitable initialization λ^{N+1} that satisfies not only the new constraint but also the previous ones. This choice is critical, because Algorithm 4 will find the closest local minimum of the non-convex function F (5.15). To go further, we assume that an intuitive and stable correction should not only satisfy the constraints but also stay close to the current segmentation. Therefore, a sensible strategy is to find a *feasible* λ^{N+1} so that $\Phi_{\lambda^{N+1}}$ is *as close as possible* to the previous optimal implicit function $\Phi_{\tilde{\lambda}^N}$, in the L_2 sense. Formally, this corresponds to solving after each interaction:

$$\lambda^{N+1} = \underset{A\lambda^{N+1} + \mathbf{b} \geq 0}{\operatorname{argmin}} \left\| \Phi_{\lambda^{N+1}} - \Phi_{\tilde{\lambda}^N} \right\|_2^2 \quad (5.20)$$

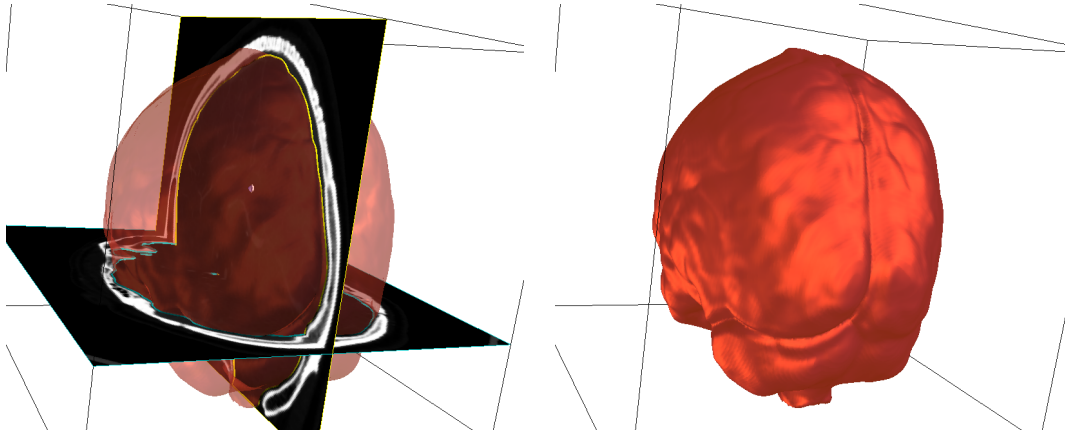


Figure 5.7 — "One-Click" initialization, segmentation of a brain volume in CT to extract the region enclosed by the skull. Optimizing over a one-dimensional embedding of shapes (5.19) can be enough if the metric g_1 captures most of the image features.

Expanding functions over the basis (φ_i) we have:

$$\begin{aligned}
 \left\| \Phi_{\lambda^{N+1}} - \Phi_{\tilde{\lambda}^N} \right\|_2^2 &= \int_{\Omega} \left(\sum_{i=0}^{N+1} (\tilde{\lambda}_i^N - \lambda_i^{N+1}) \varphi_i \right)^2 \\
 &= (\tilde{\lambda}^N - \lambda^{N+1})^T \mathcal{G} (\tilde{\lambda}^N - \lambda^{N+1}) \tag{5.21}
 \end{aligned}$$

with $\mathcal{G} = \left[\int_{\Omega} \varphi_i(\mathbf{x}) \varphi_j(\mathbf{x}) \right]_{(i,j) \in [0, \dots, N+1]}$

(5.20) is a low-dimensional constrained quadratic programming problem, if \mathcal{G} is not singular its unique solution can be found in linear time [131]. Solving this problem is extremely fast, since it only depends on the scalar products between the basis functions, not on the image. The next optimal segmentation of the image that satisfies all the constraints is presented to the user after applying the non-linear Active Set method from this sound initial condition.

5.5 Conclusion

In this chapter, we described a flexible framework for interactive image segmentation based on the selection of a few points inside and outside the object of interest. Our variational formulation is based on the minimization of a broad class of two-phase segmentation functionals, which includes the well-known maximum-likelihood criterion, taken here as an example.

The crux of the technique stems from performing the minimization over a low-dimensional, image-adaptive subset of implicit functions. This subset is spanned by localized kernels, constructed with a novel extension of Radial Basis Functions with image-dependent non-Euclidean distances, using local image information around each control point.

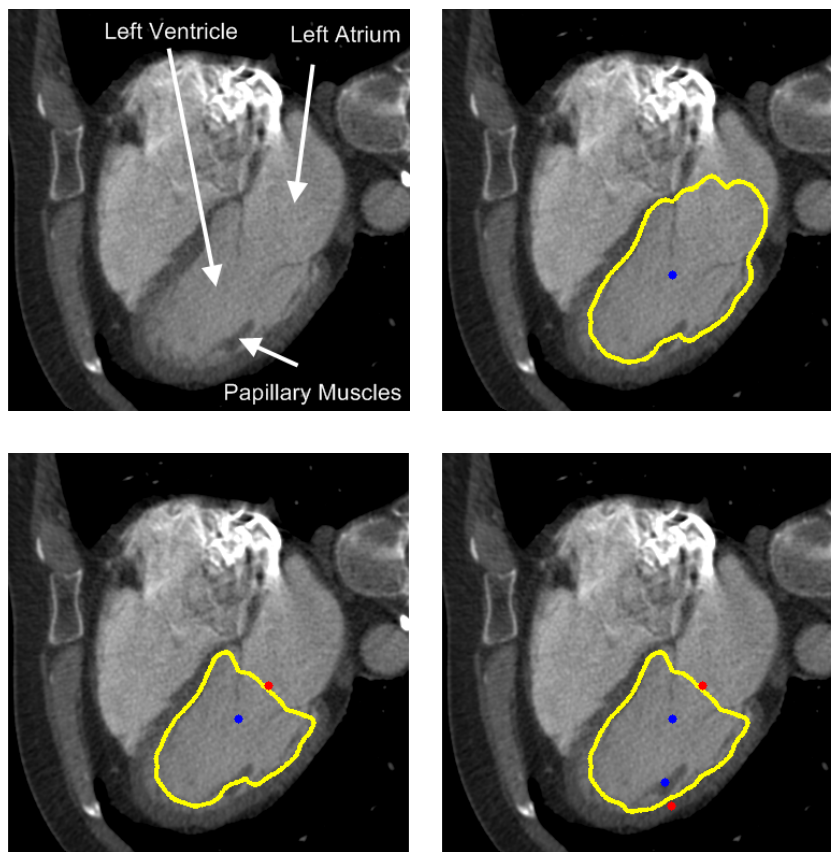


Figure 5.8 — 2D interactive segmentation of the Left Ventricle in a Cardiac CT slice. Top-left: original image. Top-right: one single click *inside* (blue) the ventricle captures most of its shape but also the atrium, which has a very similar intensity distribution. Bottom-left: one single *outside* (red) click on the mitral valve removes the atrium. Bottom-right: Two final control points allow as fine corrections to include the papillary muscles of different intensity.

This extension opens up the design of non-spherical, feature-aligned basis functions with the immediate consequence that far fewer control points are needed to accurately recover sharp details such as straight edges or corners. Fully automatic segmentation algorithms can already benefit from this representation, but if a user provides the control points, the basis functions can be made even more specific to the targeted object. In such an interactive scenario, the inside/outside labeling can be expressed through simple linear inequality constraints in the parameter space.

We applied this constrained formulation to build a general-purpose 3D segmentation tool based on a sequential workflow in which the dimension of the optimization problem increases progressively as the user interacts.

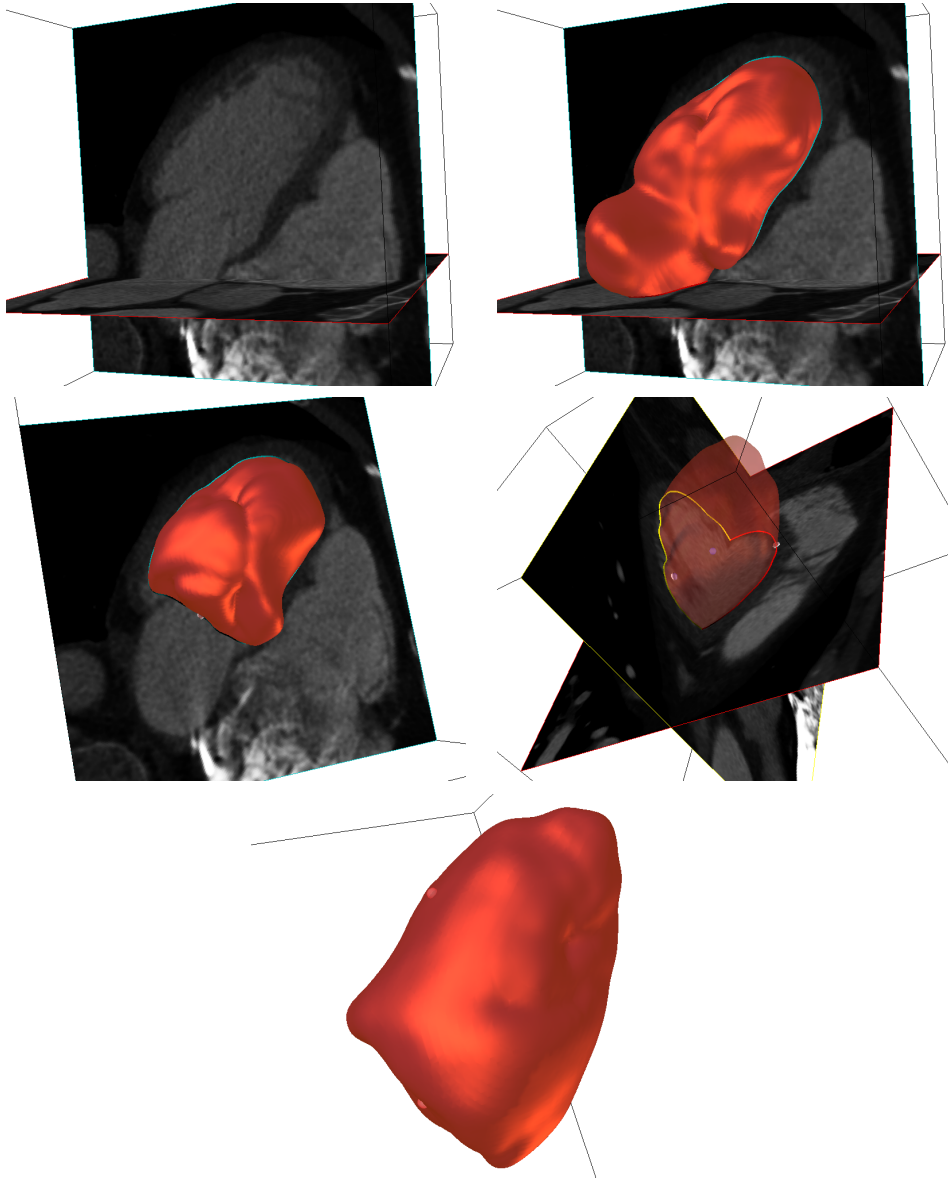


Figure 5.9 — General-purpose 3D interactive segmentation tool, tested on a 2 GHz processor on images of typical size 256^3 . Response time after each user interaction is about one second. Left column: Segmentation of the left ventricle in a cardiac CT volume. As in Fig.5.8, a single click in the ventricle extracts most of the 3D shape but also the atrium. The atrium is first removed with an *outside* click on the valve. 4 subsequent clicks increase the accuracy and include the papillary muscles in the ventricle ($N = 6$).

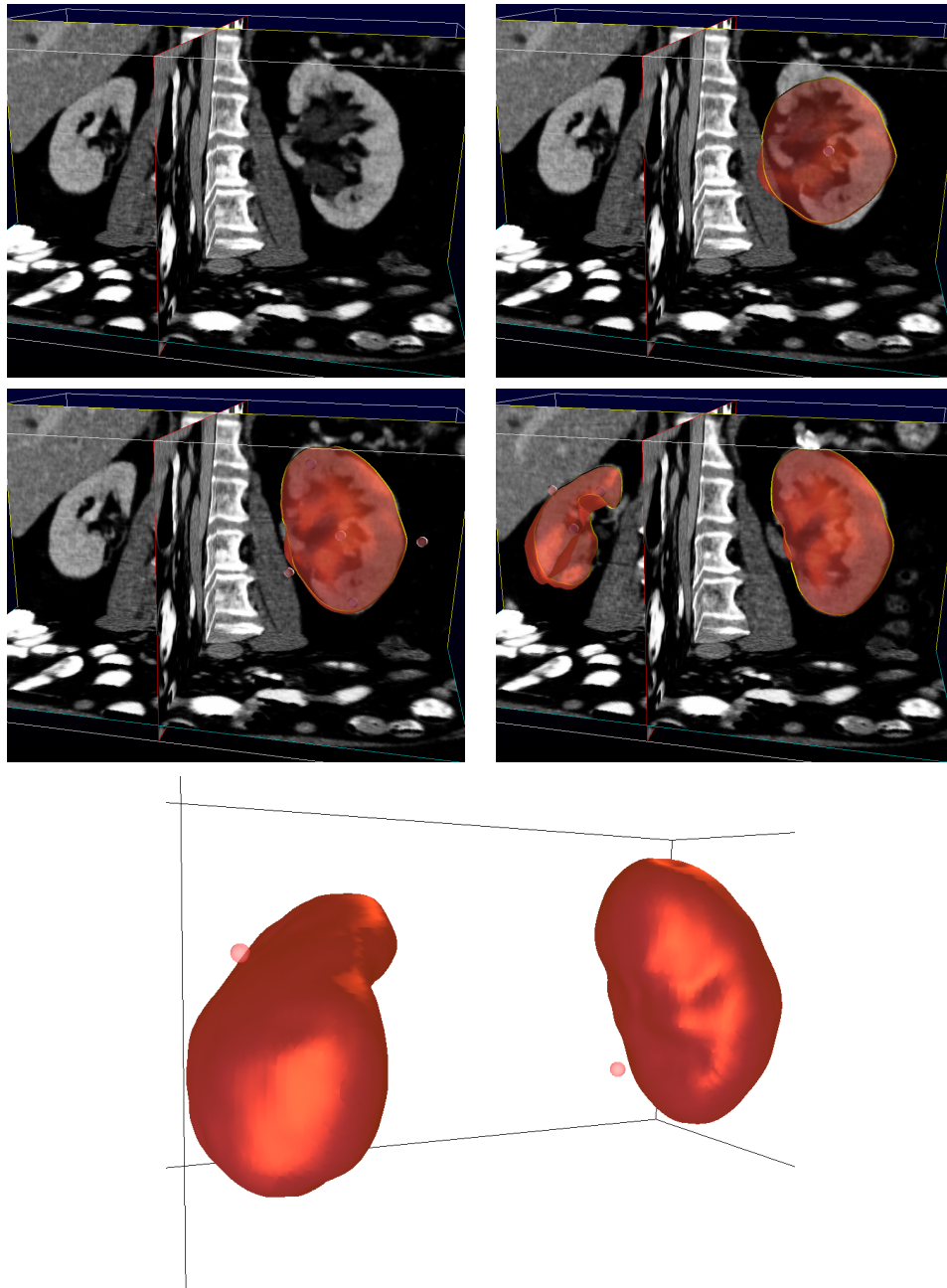


Figure 5.10 — General-purpose 3D interactive segmentation tool. Segmentation of the kidneys in a CT volume with $N = 10$ control points. Note that the second kidney, with similar intensity distribution, can easily be obtained after the first one, thanks to the topological flexibility of the implicit representation.

Non-Rigid Implicit Template Deformation with User Constraints

6

In this chapter, we develop an algorithm for 3D interactive segmentation by non-rigid deformation of an implicit template towards the image, with three main features.

First, we formulate region-based template-to-image registration in a way that is consistent with the notion of *shape*. This enables a natural decoupling of *global* and *local* components of the unknown geometric transformation as well as a joint estimation of both contributions. Moreover, regularization of the non-rigid component is intrinsic to the shape and invariant with respect to the *pose*. The pose can for instance correspond to a similarity transformation that encodes the object position, scale and orientation.

User input is incorporated through inside/outside labeled points, as in chapter 5, to drive the deformation and improve clinical reliability. Contrary to the previous chapter, the resulting inequality constraints are here *non-linear*. The overall problem of recovering jointly the optimal pose and the non-rigid deformation field, subject to a set of non-linear inequality constraints, is solved using an Augmented Lagrangian approach.

Finally, we use a fast version of non-rigid deformation by considering smoothness as a built-in feature of the displacement field, directly expressed as a Gaussian convolution in the functional to minimize. This relates to Thirion's well-known *Demons* image registration algorithm [168], here applied in the context of shape deformation and template-to-image registration. Mainly motivated by efficiency reasons, this choice allows to impose arbitrary long-range smoothness in real-time, which enables easy interactions in 3D with a live visual feedback of the deformation.

Results are shown on 3D medical images of various anatomical structures acquired from several modalities, with execution times of the order of a few seconds, including surface deformation rendering and user interactions.

6.1 Introduction

Segmentation of images subjected to noise, occlusions and low-contrasted regions can be significantly facilitated by the incorporation of some prior knowledge. This approach has been extensively studied in terms of shape prior by constraining the solution to remain close to a given pre-defined shape. For instance, statistical methods have been proposed to model shapes, such as the *Active Shape Models* [48]. Such models require careful preliminary training to capture the variability of the shape. In the level-set framework, shape priors have also been introduced by penalizing the dissimilarity between the implicit object representation and the one embedding the prior shape, *via* an additive shape constraint [38, 50, 136, 144]. The model of Leventon *et al.* [106] and further works along the same line [27, 171] combine the two approaches by embedding a PCA of training shapes in distance functions and defining a linear statistical model for the shape term. Non-linear versions have been explored as well [51]. In some cases, in particular for objects composed of multiple components, these methods may however suffer from the uncontrollable topology changes allowed by the implicit representation.

A possible alternative to control the topology is to apply a geometric deformation to the prior shape, using the principle of variational *template-to-image* registration [7, 151, 162]. In this approach, two-phase segmentation is performed by deforming a binary template towards the image. The prior is the template itself, and the shape constraint consists in a regularization of the deformation. The optimization is guided by the likelihood maximization of user-defined intensity models, given the pixel values observed in both the foreground and the background. This approach, sometimes referred to as non-rigid *template matching* has been recently applied by Saddi et al. in [152] for liver segmentation in CT.

In pathological cases presenting extreme variabilities of image features and organ shapes, shape priors may be helpful but insufficient; expert input is then essential to guide the segmentation. Designing intuitive and reliable interactive tools remain a key challenge, particularly in 3D. Few attempts to combine shape priors and interactivity have been made [69]. Along the same line, we propose to incorporate user input in the form of inside/outside label constraints that must be strictly satisfied. A fast implementation results in an application that provides instant visual feedback of the current non-rigid deformation and intuitive live interactions.

In section 6.2, we recall the principles of region-based segmentation with template non-rigid deformation. In the general framework, this corresponds to a specific choice of representation for the implicit function Φ as a geometrically-transformed version of a template shape Φ_0 . In section 6.3, we propose a new approach to add interactive capabilities with additional inequality constraints and choose a transformation model that enables the joint recovery of a global shape alignment and a non-rigid deformation field. Finally, in section 6.4, we illustrate the versatility of this template deformation framework by segmenting many anatomical structures with a known expected shape, in various imaging modalities. An experimental validation of the effectiveness of user interactions is performed for the segmentation of kidneys in Contrast-Enhanced 3D ultrasound images.

6.2 Region-Based Implicit Template Deformation

Let us start with a brief reminder on the region-based segmentation variational formulation followed throughout this thesis. With an implicit representation Φ , positive in the foreground, the minimization problem involves a regularization $\mathcal{R}(\Phi)$ and a volume integral measuring the classification error, of the form:

$$\begin{aligned} \min_{\Phi} \left\{ \mathcal{R}(\Phi) + \int_{\Omega} H(\Phi(\mathbf{x})) r(\mathbf{x}) d\mathbf{x} \right\} \\ \text{with } r(\mathbf{x}) = r_1(\mathbf{x}, \alpha_1) - r_2(\mathbf{x}, \alpha_2) \end{aligned} \quad (6.1)$$

For sake of simplicity, the optimization with respect to the region parameters α_i is omitted, but we would like to emphasize that the template deformation framework developed in the following sections can be used both in a supervised and unsupervised setting, with any for the region quality measures r_i that were developed in Chapter 3, such as the piecewise-smooth model with normalized convolutions from section 3.2.3, or the non-parametric maximum-likelihood term:

$$r(\mathbf{x}) = -\log \frac{p_1(I(\mathbf{x}))}{p_2(I(\mathbf{x}))} \quad (6.2)$$

In the literature on image segmentation with shape prior in the level-set framework, the regularization $\mathcal{R}(\Phi)$ in (6.1) is often complemented with an additional shape term that enforces the solution to remain close to a predefined implicit representation. For instance, Paragios et al. in [136] constrain Φ to be a distance function in order to penalize its L_2 -distance to a globally transformed template. Nevertheless, this technique does not guarantee that the zero level-set of the solution preserves the topology of the shape prior. Moreover, $\mathcal{R}(\Phi)$ is classically chosen to penalize the perimeter of the region boundary, which is counter-productive since it inevitably smooths out possible important details of the prior shape.

To cope with these problems, an alternative approach is to rather deform a template shape, assumed here to be defined in its own referential Ω_0 , with a geometric transformation $\psi : \Omega_0 \rightarrow \Omega$. The template is implicitly represented by a function $\Phi_0 : \Omega_0 \rightarrow \mathbb{R}$, while the segmentation boundary is given by the zero-level of:

$$\Phi = \Phi_0 \circ \psi \quad (6.3)$$

The unknown becomes the transformation ψ and the penalization $\mathcal{R}(\Phi)$ in (6.1) is replaced by a shape term $\mathcal{S}(\psi)$, consisting in a regularization constraint acting on ψ . This is illustrated in Fig. 6.2 where we show a star-shaped template in 2D, deformed with a regular transformation ψ . Note how the deformed template keeps its sharp details after transformation, which can be a desirable feature in some applications.

Thus, going back to the optimization problem (6.1), the problem of region-based image segmentation by implicit template deformation can be formalized as follows:

$$\min_{\psi} \left\{ \mathcal{S}(\psi) + \int_{\Omega} H(\Phi_0 \circ \psi(\mathbf{x})) r(\mathbf{x}) d\mathbf{x} \right\} \quad (6.4)$$

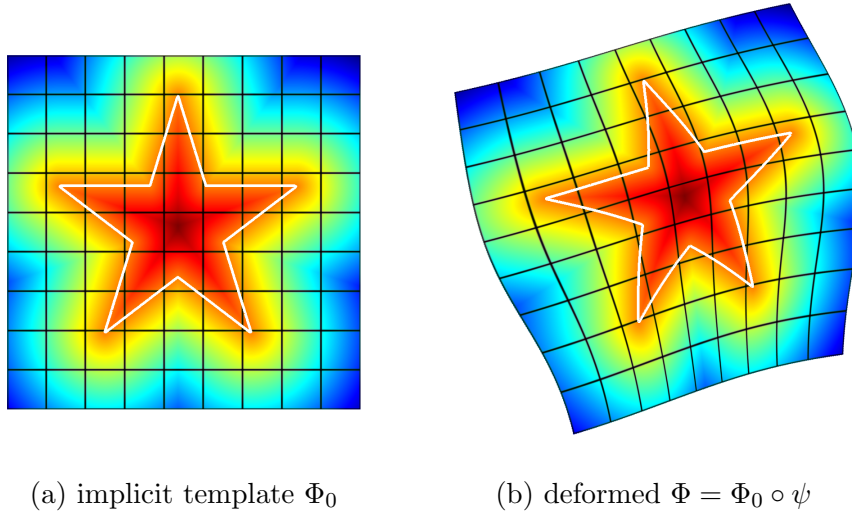


Figure 6.1 — Implicit template deformation

Compliance with the shape prior is determined by both the deformation model ψ and its associated constraint $\mathcal{S}(\psi)$, which must therefore be chosen carefully. In a related context, a similarity transformation was used by An and Chen [7], excluding more local deformations. In the non-rigid case, Saddi *et al.* [151] regularized the deformation with a diffeomorphic fluid model with no specific shape constraint, thus enabling the result to strongly deviate from the prior shape. Somphone *et al.* proposed deformations based on finite elements with partition of unity as a compromise between global and local models [162]. Huang and Metaxas have proposed to use Free Form Deformations, with B-Splines, in the *Metamorphs* algorithm [88].

6.3 Proposed Algorithm

We would like to address the two following limitations that are common to all above approaches:

1. There is no way to easily integrate user interactions in any of the existing template deformation schemes. In section 6.3.1, we cast user interactions as additional non-linear inequality constraints, turning the method into a semi-automatic technique in which both the user input and the shape constraints drive the template deformation towards image features, in real-time. The principle is exposed in section 6.3.1, and further developed in section 6.3.4 with an Augmented Lagrangian approach to minimize the constrained formulation.
2. The shape constraint $\mathcal{S}(\psi)$ is not *intrinsic* to the shape, in particular it is not invariant with respect to the pose of the object. Consider the scaling factor for instance, a transformation ψ changing only the shape size should not induce a change in the value of $\mathcal{S}(\psi)$, otherwise the relative balance with the image term in (6.4) would

also change. Intuitively, global transformations should be differently handled than actual shape *deformations*. In practice, pose-invariance is required to enable a single shape model to be used for segmenting objects of the same *class* in a variety of image acquisition conditions, with the same parameter settings. A general framework based on group theory is presented in section 6.3.2 to ensure pose-invariance of the shape term $\mathcal{S}(\psi)$, consistently with the notion of shape.

6.3.1 Interactions as Non-Linear Inequalities

Additional control and robustness can be obtained by offering to the user the possibility to indicate whether some specific points shall lie inside or outside the surface to extract.

Denoting $\{\mathbf{x}_k \in \Omega\}_{k \in \{0, \dots, N-1\}}$ these labeled points, user input can be translated into N constraints on the sign of the transformed template $\Phi = \Phi_0 \circ \psi$, at $\{\mathbf{x}_k\}$:

$$\forall k \in \{0, \dots, N-1\} \quad \gamma_k \Phi_0 \circ \psi(\mathbf{x}_k) \geq 0 \quad (6.5)$$

where $\gamma_k = 1$ (resp. -1) for inside (resp. outside) points. Fig. 6.2 illustrates the constraint induced by an inside point (in blue) and an outside point (in red) on the deformation of the star-shaped object of Fig. 6.2.

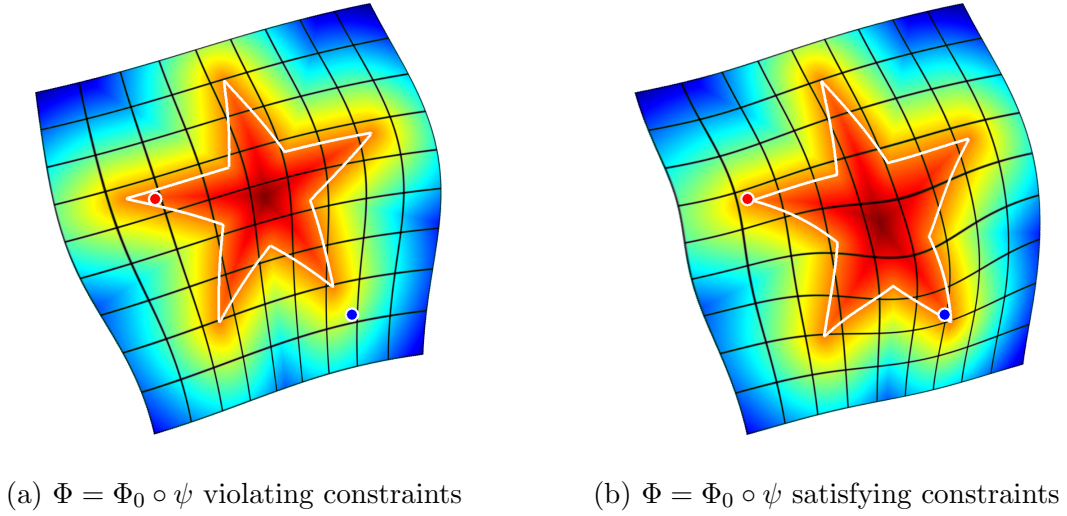


Figure 6.2 — User constraints as inside/outside labeled points

Putting together the criterion (6.4) and the constraints (6.5) yields a general formulation of implicit template deformation with user interactions, as the minimization problem:

$$\begin{aligned} \min_{\psi} \quad & \left\{ E(\psi) = \mathcal{S}(\psi) + \int_{\Omega} H(\Phi_0 \circ \psi(\mathbf{x})) r(\mathbf{x}) d\mathbf{x} \right\} \\ \text{subject to} \quad & \gamma_k \Phi_0 \circ \psi(\mathbf{x}_k) \geq 0, \quad \forall k \in \{0, \dots, N-1\} \end{aligned} \quad (6.6)$$

Note that forcing the resulting surface $\Phi^{-1}(0)$ to pass through a specific point \mathbf{x} can be obtained by adding at this same point both inside/outside constraints.

6.3.2 Algebraic Definition Of Shapes

In this section, we present a transformation model that is specifically designed for non-rigid shape deformation and ensures pose-invariance of the shape term \mathcal{S} . One may intuitively comprehend a *shape* as a set of objects that share the same visual aspect. In particular, a shape shall be invariant to some simple geometric transforms such as translation, rotation, scaling or shearing, depending on the application. For instance, 3D rigid objects projected onto a 2D image plane from a pinhole camera are known to be subject to perspective transformations, which was exploited for 2D segmentation with a 3D shape prior by Raviv et al. in [144]. When dealing with organs and other structures in 3D medical images, transformations preserving the aspect ratio, such as similarities, should often be preferred. In the following, such a global transformation will be referred to as the *pose*.

To set up a clear distinction between shape pose and subsequent shape *deformation*, it is natural to design the template transformation model ψ as a combination of global and non-rigid local components, that we denote G and L respectively. As we will see, the mathematically correct way of combining both components is through a *functional composition*, such that:

$$\psi(\mathbf{x}) = L \circ G(\mathbf{x}) \quad (6.7)$$

Considering a point \mathbf{x} in the image domain, this composition can be interpreted as successive realizations of a change of referential $\mathbf{x} \mapsto \mathbf{y} = G(\mathbf{x})$, reflecting the shape pose (top diagram in Fig. 6.3), followed by the actual template deformation $\mathbf{y} \mapsto L(\mathbf{y})$. Note that if Φ is an implicit representation of a surface Γ , then $G^{-1}(\Gamma)$ is the zero-level of $\Phi \circ G$.

We shall now briefly present a formal justification of this transformation model with an algebraic definition of shapes, as well as describe some of its advantages regarding pose-invariant template deformation.

Let \mathcal{C} be the set of all closed surfaces in \mathbb{R}^d and (\mathcal{G}, \circ) a group generated from a set \mathcal{G} of given geometric transforms of \mathbb{R}^d , associated with the composition operation. Considering the *group action* of \mathcal{G} on \mathcal{C} , we define a shape as an *orbit* with respect to this action, *i.e.* a class of the equivalence relation $R_{\mathcal{G}}$ defined on \mathcal{C} by:

$$\Gamma_1 R_{\mathcal{G}} \Gamma_2 \iff \exists G \in \mathcal{G}, \Gamma_2 = G(\Gamma_1) \quad (6.8)$$

for any Γ_1, Γ_2 in \mathcal{C} . Thus, the orbits form a partition of \mathcal{C} , meaning that any closed surface belongs to one and only one shape; this partition – and hence the shape space – depends on the choice of \mathcal{G} . We consider groups of global, parametric transforms, typically the similarity or affine transforms.

In practice, the prior shape is provided as a particular surface Γ_0 of the orbit, together with an associated *shape domain* Ω_0 , defined as a subdomain of \mathbb{R}^d containing Γ_0 . In formulation (6.4), Γ_0 is represented by an implicit function Φ_0 defined on Ω_0 . At this point, it is important to distinguish between the *image referential* Ω , that embeds the image to segment as well as all the elements of \mathcal{C} , and the *shape referential* Ω_0 , centered on Γ_0 and serving as the referential for deformations. This distinction is illustrated on Fig. 6.3 in the 2D case.

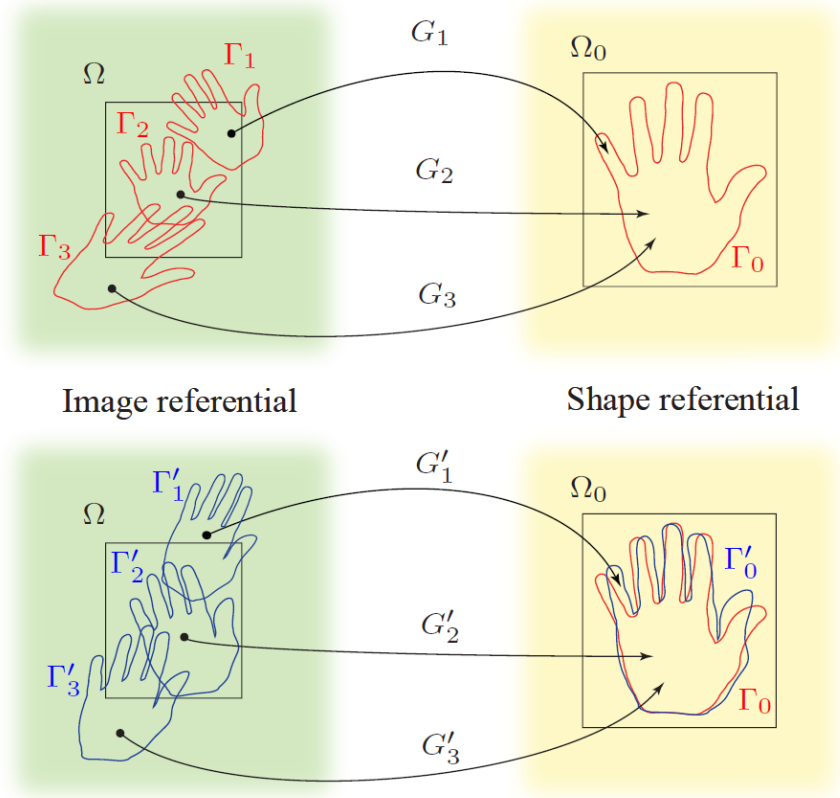


Figure 6.3 — Image and shape referentials in \mathbb{R}^2 . The shape prior is provided as a particular contour Γ_0 . (Top) Contours from the orbit of the shape prior: Γ_1 , Γ_2 and Γ_3 can be exactly matched to Γ_0 with global transforms from \mathcal{G} . (Bottom) Contours from another orbit. A deformation of the optimal pose is necessary to exactly match Γ_0 .

On the top diagram, several contours of an orbit are represented in the image referential. Since Γ_1 , Γ_2 , Γ_3 can be exactly matched to Γ_0 with transforms G_1 , G_2 and G_3 belonging to \mathcal{G} , no further deformation in the shape referential is needed. On the bottom diagram, contours Γ'_1 , Γ'_2 and Γ'_3 belonging to another orbit are shown. Since they cannot be exactly matched to Γ_0 with transforms from \mathcal{G} , a deformation L in the shape referential is necessary to complete the matching so that $L(\Gamma'_0) = \Gamma_0$.

A similar definition of shapes was previously introduced by Soatto and Yezzi in the context of shape averaging [161, 184]. For segmentation with template deformation, decomposing the unknown transform as $\psi = L \circ G$ proves essential since it allows to define the shape term in a unique referential (namely the shape referential Ω_0). All surfaces $(\Gamma'_1, \Gamma'_2, \Gamma'_3, \dots)$ of a same orbit, once globally aligned, result in a same optimal surface (Γ'_0) . The cost to reach the exact match is then equal to $\mathcal{S}(L)$ and is intrinsic to the shape. A pose will be qualified as optimal when the associated deformation is minimal with respect to \mathcal{S} . Designing \mathcal{S} such that it penalizes L only yields a constraint which is independent of the pose. Moreover, \mathcal{S} is also independent of the image referential, domain and discretization.

6.3.3 Transformation Model

In accordance with the previous section, we set up a clear distinction between the pose and the subsequent shape *deformation* by designing the template transformation model as:

$$\psi = L \circ G \quad (6.9)$$

Fig. 6.4 illustrates this composition on an implicit sphere in 3D. The template surface, a sphere (in green in Fig. 6.4.a), is transformed to reach a target shape, undergoing first a global transformation (scaling and translation, in yellow in Fig. 6.4.b), followed by a non-rigid deformation (in red in Fig. 6.4.b).

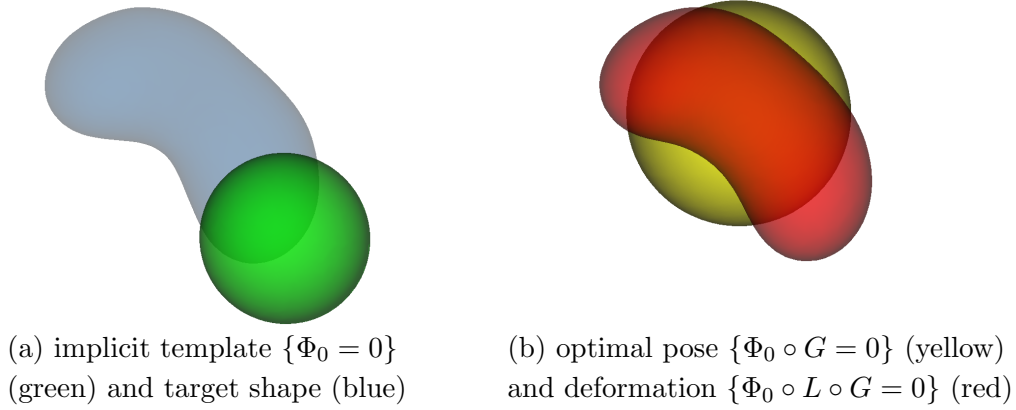


Figure 6.4 — Transformation decomposition into pose and deformation

Pose

$G : \Omega \rightarrow \Omega_0$ is chosen as a parametric transform that coarsely aligns the template with the target object in the image. For anatomical structures in 3D medical images, similarities (which preserve the aspect ratio) are particularly adapted. G is thus represented by a matrix in homogeneous coordinates defined by 7 parameters $\mathbf{p} = \{p_i\}_{i=1\dots 7}$ and noted $G_{\mathbf{p}}$.

Deformation

$L : \Omega_0 \rightarrow \Omega_0$ is expressed using a displacement field \mathbf{u} in the template referential Ω_0 :

$$L = \mathbf{Id} + \mathbf{u} \quad (6.10)$$

Similarly to image registration and optical flow algorithms [155], \mathbf{u} should be smoothly-varying in space. While adding penalizations on differential terms on \mathbf{u} to $\mathcal{S}(\psi)$ is a valid approach, fast implementations are often difficult to derive. Taking advantage of efficient linear filtering, smoothness of the displacement \mathbf{u} is set as a built-in property: \mathbf{u} is defined as a filtered version of an integrable unknown displacement field \mathbf{v} ,

$$\mathbf{u}(\mathbf{x}) = [W_\sigma * \mathbf{v}](\mathbf{x}) = \int_{\Omega_0} W_\sigma(\mathbf{x} - \mathbf{y}) \mathbf{v}(\mathbf{y}) d\mathbf{y} \quad (6.11)$$

where W_σ is a Gaussian kernel of scale σ and the free variable of the representation becomes the field \mathbf{v} , *before* smoothing. By construction, \mathbf{u} is regular. The scale σ in (6.11) is the only critical parameter and corresponds to the spatial extent of the smoothness. Fortunately, since the displacement is expressed in the template referential, regardless of the pose, the scale selection will be naturally linked to the shape.

This deformation model relates to the *Demons* image registration algorithm [168], here applied in the context of shape deformation and template-to-image registration. Mainly motivated by efficiency reasons, this choice allows to impose arbitrarily long-range regularity in real-time, using a recursive implementation of the Gaussian filter with a computational complexity that is independent of σ . As shown in section 6.3.4, the computation of the functional derivatives with respect to the unknown displacement field \mathbf{v} is also expressed as a convolution.

Shape Term

Decomposing $\psi = L \circ G$ allows to define the shape prior term independently from the pose: $\mathcal{S}(\psi) = \mathcal{S}(L)$. \mathcal{S} thus quantifies how much the segmentation Φ deviates from the prior *shape* Φ_0 . Using the L_2 norm, we choose to compel L towards the identity \mathbf{Id} :

$$\mathcal{S}(L) = \frac{\lambda}{2} \|L - \mathbf{Id}\|_2^2 = \frac{\lambda}{2} \int_{\Omega_0} \|\mathbf{u}(\mathbf{x})\|^2 d\mathbf{x} \quad (6.12)$$

where λ is a positive scalar parameter controlling the strength of the shape prior. In the absence of features in certain areas of the image, $r(\mathbf{x}) \approx 0$ in (6.4), this shape constraint dominates and tends to locally extrapolate the transformation with the global transformation that is optimal with respect to the other areas. In the limiting case $\lambda \rightarrow +\infty$, the technique reduces to a global template alignment algorithm.

6.3.4 Augmented Lagrangian Minimization Scheme

The constrained optimization problem to solve finally reads:

$$\begin{aligned} \min_{\mathbf{p}, \mathbf{v}} \quad & \left\{ E(\psi_{\mathbf{p}, \mathbf{v}}) = \frac{\lambda}{2} \int_{\Omega_0} \|W_\sigma * \mathbf{v}(\mathbf{x})\|^2 d\mathbf{x} + \int_{\Omega} H(\Phi_0 \circ \psi_{\mathbf{p}, \mathbf{v}}(\mathbf{x})) r(\mathbf{x}) d\mathbf{x} \right\} \\ \text{subject to} \quad & \gamma_k \Phi_0 \circ \psi_{\mathbf{p}, \mathbf{v}}(\mathbf{x}_k) \geq 0, \quad \forall k \in 0..N-1 \\ \text{with} \quad & \psi_{\mathbf{p}, \mathbf{v}} = G_{\mathbf{p}} + (W_\sigma * \mathbf{v}) \circ G_{\mathbf{p}} \end{aligned} \quad (6.13)$$

Minimizing under constraints

Since $E(\psi_{\mathbf{p},\mathbf{v}})$ is a non-convex functional to be minimized under a set of non-linear constraints, no specifically tailored algorithms are available. For this matter, we follow a general Augmented Lagrangian methodology and define an equivalent unconstrained problem that can be locally minimized by gradient descent [131]. Although we adopted $\psi = \psi_{\mathbf{p},\mathbf{v}}$ as specified in (6.13), the following strategy generalizes to any transformation model.

The constrained problem (6.13) can equivalently be written as an unconstrained minimization problem of the form

$$\min_{\psi_{\mathbf{p},\mathbf{v}}} \left\{ \tilde{E}(\psi_{\mathbf{p},\mathbf{v}}) = \max_{\alpha \geq 0} \left\{ E(\psi_{\mathbf{p},\mathbf{v}}) - \sum_{k=0}^{N-1} \alpha_k c_k(\psi_{\mathbf{p},\mathbf{v}}) \right\} \right\} \text{ with } c_k(\psi_{\mathbf{p},\mathbf{v}}) = \gamma_k \Phi_0 \circ \psi_{\mathbf{p},\mathbf{v}}(\mathbf{x}_k) \quad (6.14)$$

where α_k is the Lagrange multiplier associated to the k^{th} constraint. (6.14) has the same set of solutions as the original problem (6.13): if $\psi_{\mathbf{p},\mathbf{v}}$ satisfies all the constraints c_k ($\psi_{\mathbf{p},\mathbf{v}}$ is feasible), then $\tilde{E}(\psi_{\mathbf{p},\mathbf{v}}) = E(\psi_{\mathbf{p},\mathbf{v}})$, otherwise $\tilde{E}(\psi_{\mathbf{p},\mathbf{v}})$ is infinite. Since \tilde{E} jumps from finite to infinite values at the boundary of the feasible set, a more practical minimization requires to introduce a smooth approximation \hat{E} . Within an iterative process, in order to constrain the maximizers $\alpha = \{\alpha_k\}_{k=0,\dots,N-1}$ to finite values, one can explicitly introduce at each iteration a quadratic penalty parameter μ and a set of Lagrange multipliers α^j (at the j^{th} iteration) to define

$$\hat{E}_\mu(\psi_{\mathbf{p},\mathbf{v}}, \alpha^j) = \max_{\alpha \geq 0} \left\{ E(\psi_{\mathbf{p},\mathbf{v}}) - \sum_{k=0}^{N-1} \alpha_k c_k(\psi_{\mathbf{p},\mathbf{v}}) - \frac{1}{2\mu} \sum_{k=0}^{N-1} (\alpha_k - \alpha_k^j)^2 \right\} \quad (6.15)$$

The maximizing Lagrange multipliers associated to each constraint $c_k(\psi_{\mathbf{p},\mathbf{v}})$ can then be found as functions of previously estimated values:

$$\alpha_k^{j+1} = \begin{cases} 0 & \text{if } \alpha_k^j - \mu c_k(\psi_{\mathbf{p},\mathbf{v}}) \leq 0 \\ \alpha_k^j - \mu c_k(\psi_{\mathbf{p},\mathbf{v}}) & \text{otherwise.} \end{cases} \quad (6.16)$$

Substituting (6.16) in (6.15) yields the expression of the smooth approximation \hat{E} :

$$\hat{E}_\mu(\psi_{\mathbf{p},\mathbf{v}}, \alpha^j) = E(\psi_{\mathbf{p},\mathbf{v}}) + \sum_{k=0}^{N-1} \Psi_\mu(c_k(\psi_{\mathbf{p},\mathbf{v}}), \alpha_k^j) \quad (6.17)$$

$$\text{with } \Psi_\mu(a, b) = \begin{cases} -ab + \frac{\mu}{2}a^2 & \text{if } \mu a \leq b \\ -\frac{1}{2\mu}b^2 & \text{otherwise.} \end{cases} \quad (6.18)$$

The alternate scheme described in Algorithm 3, in which the penalty parameter μ is gradually increased, will provide a local minimizer of (6.13) that eventually satisfies the user constraints.

Algorithm 5: Augmented Lagrangian Scheme For Inequality Constraints

given starting penalty parameter μ^0 , and $\alpha^0 = 0$,

repeat

 choose $\mu^t > \mu^{t-1}$,

repeat

 (1) $\psi_{\mathbf{p}, \mathbf{v}}$ being fixed, update the Lagrange multipliers α^{j+1} (6.16)

 (2) α^j being fixed, update $\psi_{\mathbf{p}, \mathbf{v}}$ by minimizing $\hat{E}_{\mu^t}(\psi_{\mathbf{p}, \mathbf{v}}, \alpha^j)$ (6.17)

until convergence;

until a local minimum of $E(\psi_{\mathbf{p}, \mathbf{v}})$ satisfying $\forall k, c_k(\psi_{\mathbf{p}, \mathbf{v}}) \geq 0$ is found;

Gradient-Descent

An important feature of the proposed technique is its interactivity. Therefore, iterations of the gradient descent chosen to minimize the smooth approximation $\hat{E}_{\mu}(\psi_{\mathbf{p}, \mathbf{v}}) = \hat{E}(\mathbf{p}, \mathbf{v})$ in (6.17) should be fast enough to provide a real-time display of the surface evolution.

The gradient descent evolution equations are obtained by applying standard calculus of variations; recall that

$$\hat{E}(\mathbf{p}, \mathbf{v}) = E(\mathbf{p}, \mathbf{v}) + \sum_{k=0}^{N-1} \Psi_{\mu}(c_k(p_i, \mathbf{v}), \alpha_k^j) \Rightarrow \begin{cases} \frac{\partial p_i}{\partial t} = -\frac{\partial \hat{E}}{\partial p_i} \\ \frac{\partial \mathbf{v}}{\partial t} = -\frac{\partial \hat{E}}{\partial \mathbf{v}} \end{cases} \quad (6.19)$$

By setting

$$\mathcal{A}_i(\mathbf{x}) = \left\langle \nabla \Phi_0 \circ L(\mathbf{x}), (\mathbf{I} + \mathbf{J}_{\mathbf{u}} \circ G) \frac{\partial G}{\partial p_i} \circ G^{-1}(\mathbf{x}) \right\rangle \quad (6.20)$$

$$\text{and} \quad b_k = \gamma_k \frac{\partial \Psi_{\mu}}{\partial a}(c_k, \alpha_k^j)$$

where \mathbf{I} is the Identity matrix, $\mathbf{J}_{\mathbf{u}}$ is the Jacobian matrix of \mathbf{u} , the final expression of the evolution equations for p_i and \mathbf{v} reads

$$\begin{cases} \frac{\partial p_i}{\partial t} = & - \int_{\Omega_0} \delta(\Phi_0 \circ L) r \circ G^{-1} \mathcal{A}_i & - \sum_{k=0}^{N-1} b_k \mathcal{A}_i \circ G(\mathbf{x}_k) \\ \frac{\partial \mathbf{v}}{\partial t} = & -W_{\sigma} * \left[\underbrace{\lambda \mathbf{u}}_{\text{shape}} + \underbrace{\left(\delta(\Phi_0 \circ L) r \circ G^{-1} \right)}_{\text{image force}} + \underbrace{\left(\sum_{k=0}^{N-1} b_k \delta_{G(\mathbf{x}_k)} \right)}_{\text{constraints}} \right] \nabla \Phi_0 \circ L \end{cases} \quad (6.21)$$

A quick analysis of (6.21) reveals several key aspects for an efficient implementation. Interpolating $\Phi_0 \circ L$ and $\nabla \Phi_0 \circ L$ over the whole domain Ω_0 would be extremely time-consuming. Nevertheless, since it is multiplied either by $\delta(\Phi_0 \circ L)$ or $\delta_{G(\mathbf{x}_k)}$, the warped gradient field $\nabla \Phi_0 \circ L$ is only needed on the set $\{\Phi_0 \circ L = 0\}$ and at a limited number of points $\{\mathbf{x}_k\}$ (Fig. 6.5.a) which highly reduces computational burden.

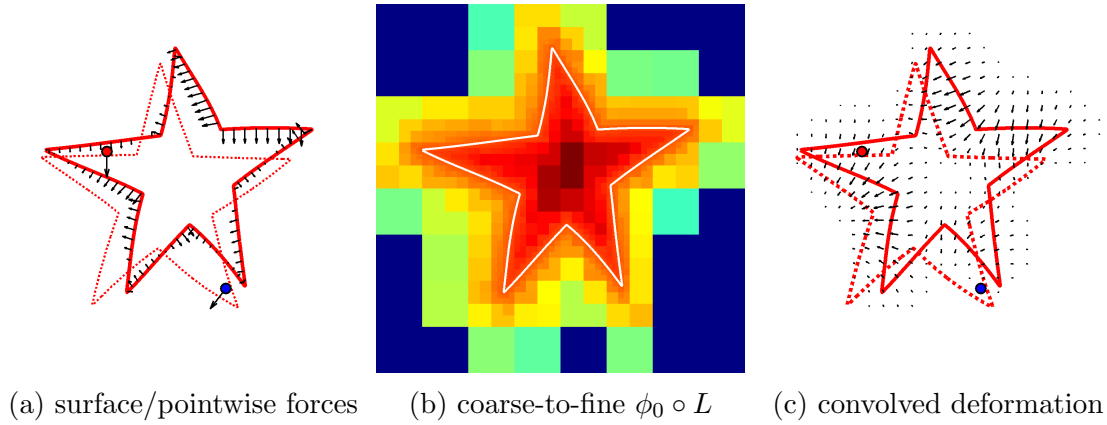


Figure 6.5 — Fast gradient computation with coarse-to-fine distance function warping and convolutions

Moreover, precise knowledge of the warped template $\Phi_0 \circ L$ is only necessary near its zero level set. Setting Φ_0 to a distance function to the template surface Γ_0 allows a coarse-to-fine approach using octrees. At each level a decision is made to further refine the cell depending on the distance measure (Fig. 6.5.b), drastically dropping complexity. Finally, stemming from the displacement model (6.11), the extrapolation of image and point-wise forces to the whole space boils down to a convolution with W_σ (Fig. 6.5.c).

In practice, our current 3D implementation supports up to 100 time steps per second when discretizing Ω_0 with a lattice containing 48^3 points. This execution speed allows a visual feedback of the deforming surface with a live response to constraints.

6.4 Experiments and Validation

In this section, the versatility of this template deformation framework is illustrated with the segmentation of anatomical structures with a known expected shape, in various imaging modalities. In addition to the template shape, a source of prior information relates to the image data itself, in the form of application-specific region quality measures. We discussed some relevant choices for $r(\mathbf{x}) = r_1(\mathbf{x}) - r_2(\mathbf{x})$ in Chapter 3, relying on global or spatially-varying statistical models depending on the imaging modality.

A strength of the region-based paradigm stems from the possibility to combine different intensity models, according to some image or physical evidence, with the option of setting up different models for foreground and background. Similarly, the choice of the parametric transform for the pose and the scale of the local deformations also participate to the flexibility. Although the best models and parameters for a given target object within a specific modality can be learned from statistical training, they can also be subject to heuristic tuning and experience when large annotated datasets are not available.

For pathological cases, the shape prior only might be insufficient, due to possible organ defects inducing a change in shape that cannot be recovered by a moderate deformation of the template; in that case, the user interactions are very helpful, as shown in section 6.4.2.

6.4.1 Applications Without User Interactions

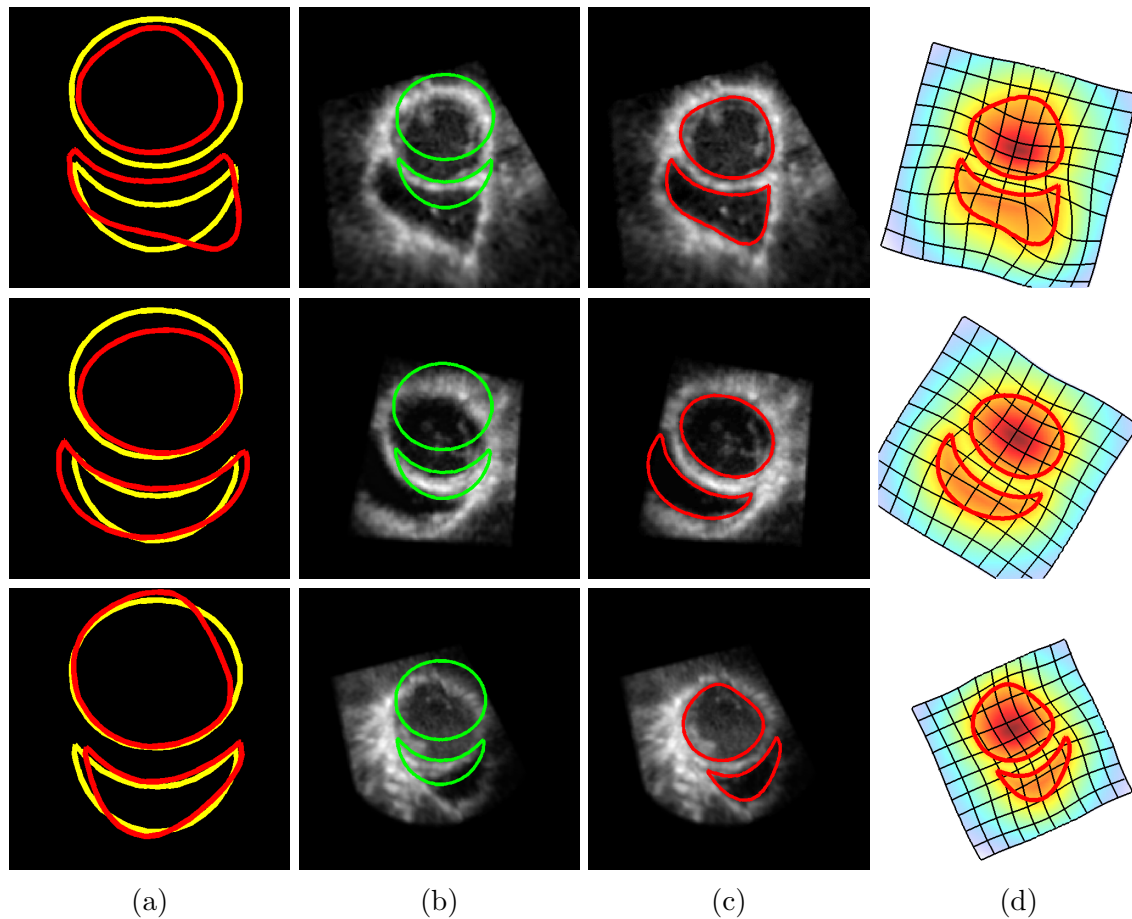


Figure 6.6 — Segmentation of cardiac ultrasound images in short axis view. The same prior template, shown in yellow in (a), is used for the three cases. (a) template referential, in yellow Φ_0 , in red $\Phi_0 \circ$. (b) initialization (green). (c) segmentation result (red). (d) visualization of the warped template in the image referential - the deformed grid represents the transform $\psi = L \circ G$.

Incorporating shape information into segmentation algorithms is essential in cardiac ultrasound images to cope with poor quality images obtained on difficult conditions or with loss of contrast due to shadows, the dark regions created by air or bones that may attenuate the ultrasound beam almost totally. On Fig. 6.6, some results are shown on 2D short-axis images, using a single template with two components for the left and right ventricles. A piecewise-smooth intensity region model is used (3.31) to take into account the varying echogenicity. The implicit template deformation approach is particularly adapted to such cases of objects with multiple components for its topology-preserving feature.

We also conducted various 3D experiments on Ultrasound (US) and Computerized Tomography (CT) volumes to test the ability of the approach to extract whole organs with predictable shapes. In all cases, the two patients are different and the same template was used in both modalities (CT and US). The algorithm runs in a few seconds, depending on initial model placement, left here to the user, and the chosen intensity models. In particular, the piecewise-smooth model induces a slightly increased, though reasonable, complexity.

Three anatomical structures were considered in these simulations. The kidney (Fig. 6.7), the left ventricle myocardium (Fig. 6.8) and the four chambers of the heart (Fig. 6.9). The ability to preserve the topology is again essential to dissociate the cardiac chambers (Fig. 6.9.b) or to prevent the endocardium and epicardium from collapsing in the absence of contrast (Fig. 6.8.b).

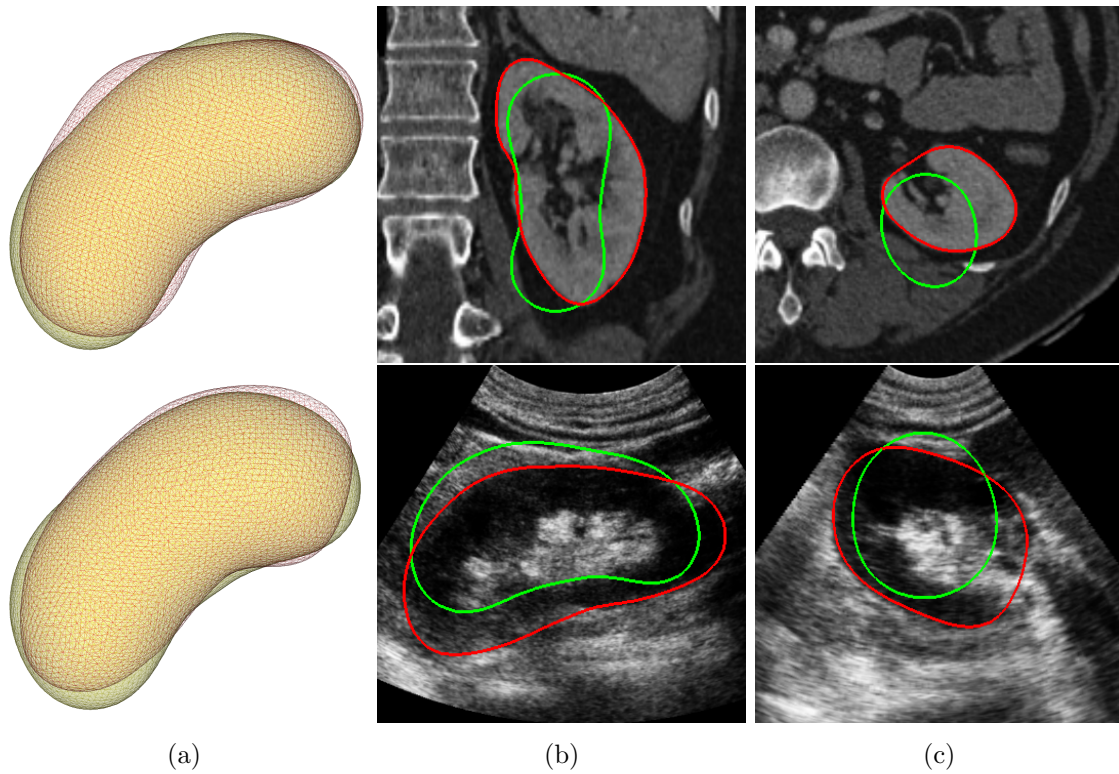


Figure 6.7 — 3D kidney segmentation for two different patients in CT (first row) and Ultrasound (second row). (a) Wireframe renderings, with optimal pose template in transparent yellow $\{\Phi_0 \circ G = 0\}$, as well as optimal deformation, $\{\Phi_0 \circ \psi = 0\}$, in red. (b)/(c) coronal/axial slices, overlaid segmentation results.

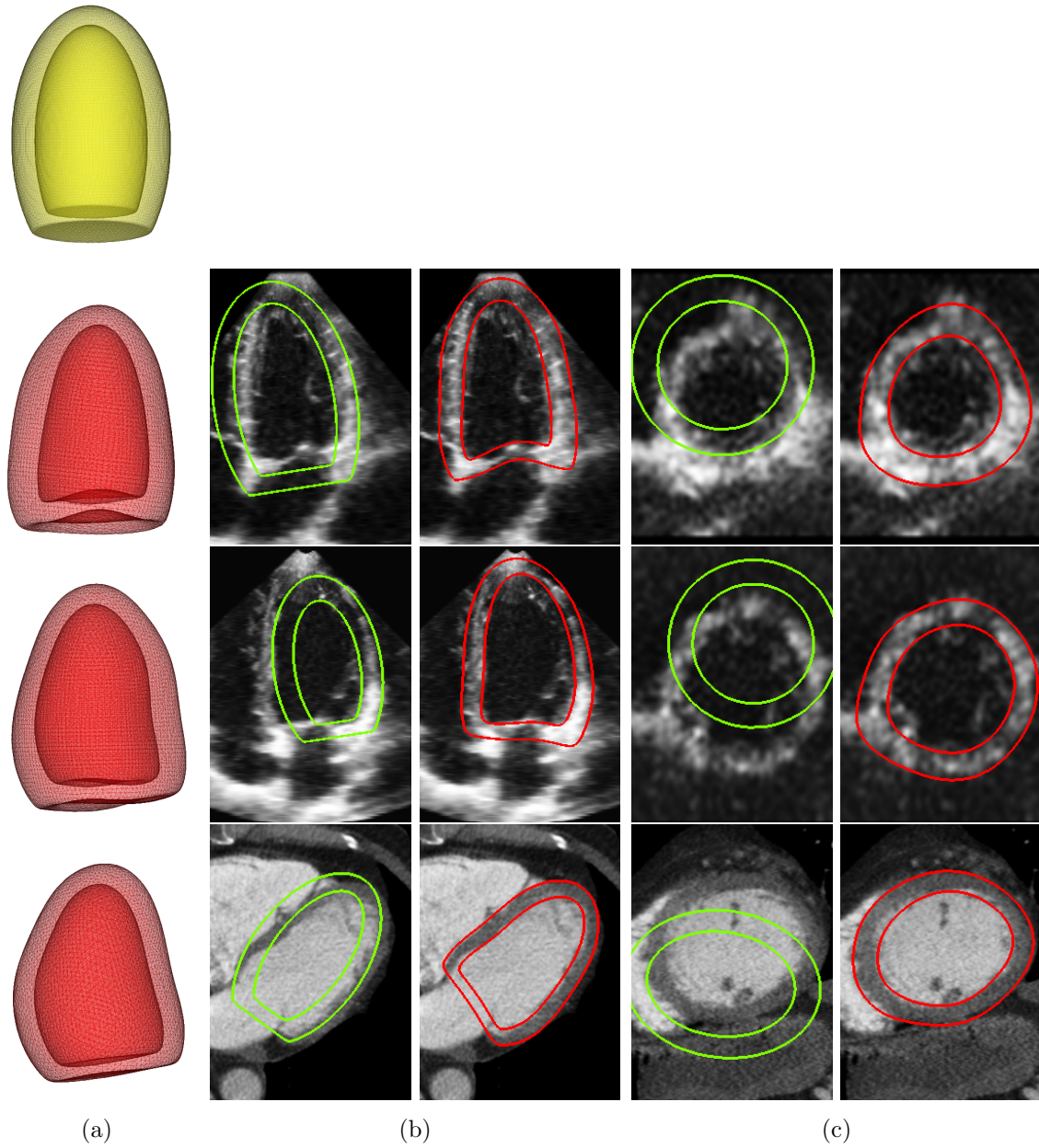


Figure 6.8 — Myocardium segmentation for 3 different patients in 3D echocardiography (first & second row) and cardiac CT (last row). Top left: synthetic truncated ellipsoid annular template, used for all experiments (yellow). (a) Optimal deformation $\{\Phi_0 \circ L = 0\}$ in red, in the template referential Ω_0 . (b)/(c) long/short axis, overlaid segmentation.

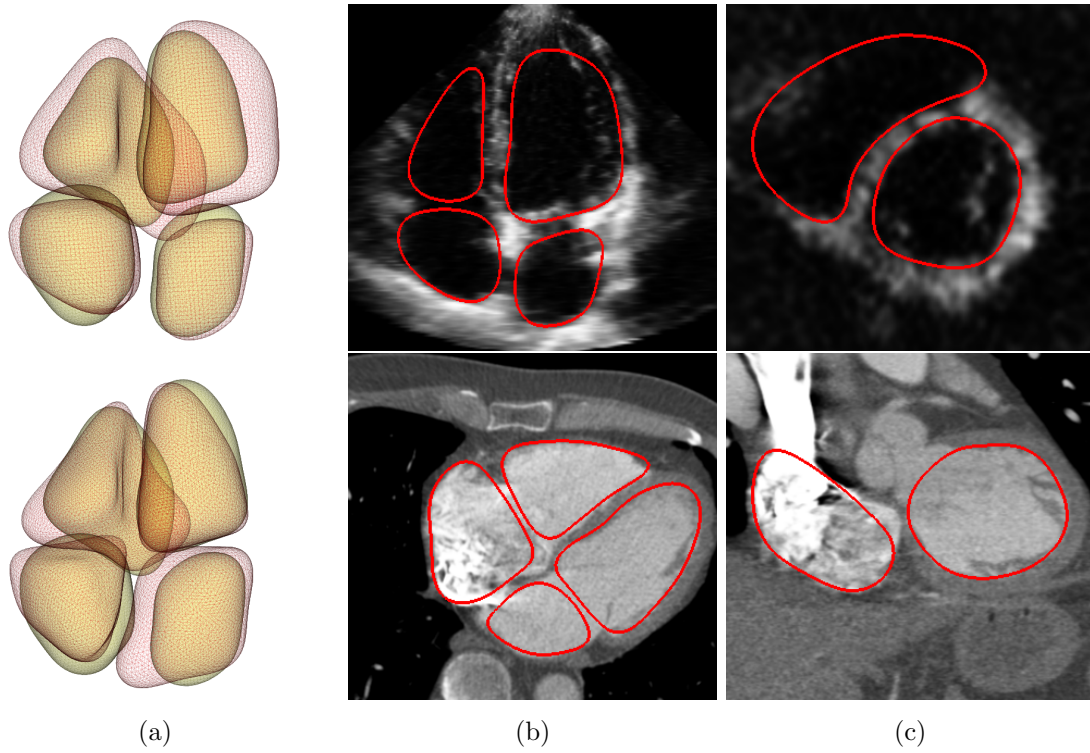


Figure 6.9 — Cardiac segmentation of the 4 chambers (left/right ventricle and left/right atrium), for 2 different patients in 3D echocardiography (first row) and cardiac CT (second row) with the same template with 4 disconnected components. (a) Optimal pose in yellow and deformation in red, in the template referential Ω_0 . (b)/(c) long/short axis, overlaid segmentation in red.

6.4.2 Applications With User Interactions

Workflow description & Liver Magnetic Resonance Imaging

The interactive workflow is illustrated through an example in pre-operative planning of liver cancer treatment, in which the liver volume is measured in Magnetic Resonance Imaging. Variability in liver shape as well as the presence of large lesions contribute to the difficulty of the segmentation.

As illustrated in Figure 6.10, the user first manually places the model Φ_0 , which initializes pose G (6.10.a). From this point and further on, the optimization algorithm is launched as a background task. Thanks to real-time feedback, the user observes the surface evolution based on image descriptors (6.10.b). At any time, constraints can be added by simple clicks on 2D slices and integrated into the optimization algorithm. Live update of the effect of each interaction enables the user to drive the segmentation process (6.10.c).

In this application, the surface model Φ_0 is generated from an average mesh built from segmentations on good quality CT images, while the image-based terms r_1 and r_2 are set to a convex combination of negative log-likelihoods as in (4.17) and gradient flux maximization, as in (3.46). Note that even though image quality is fair, user interactions are necessary for a correct surface extraction given the severe and protuberant lesion.

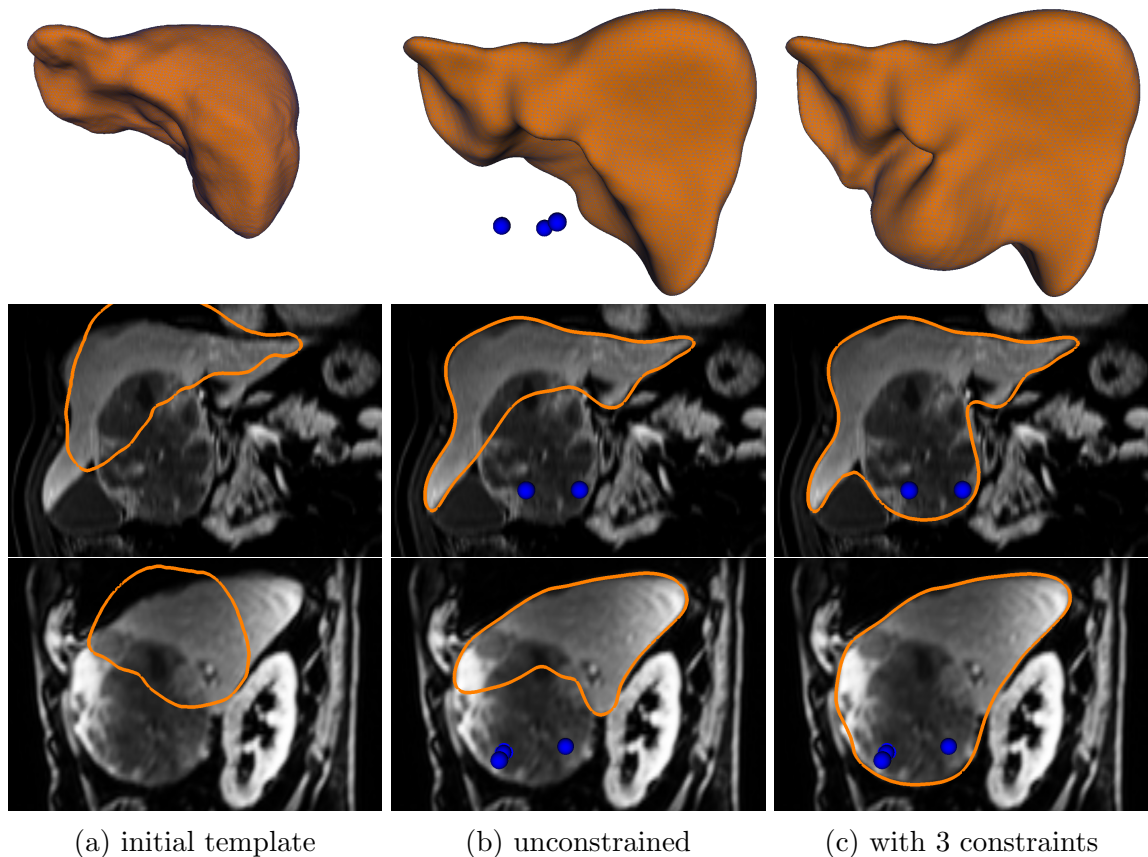


Figure 6.10 — MRI of the liver for preoperative resection planning. A 3D template of the liver (a) is deformed to extract most of the liver tissue (b). In this case, 3 inside user constraints are required to include a severe and unpredictable protuberant lesion (c).

Carotid in Conventional Ultrasound

In the context of plaque measurements in ultrasound images of carotids, semi-automatic segmentation of the carotid wall would generate significant time gains in daily practice.

For this application, the foreground term r_1 assumes a Gaussian distribution while the background term r_2 is updated at each iteration with a non-parametric estimation of the intensity distribution. The template Φ_0 is set to a cylinder. User interactions are necessary when significant plaque clogs up a large portion of vessel lumen (see Figure 6.11).

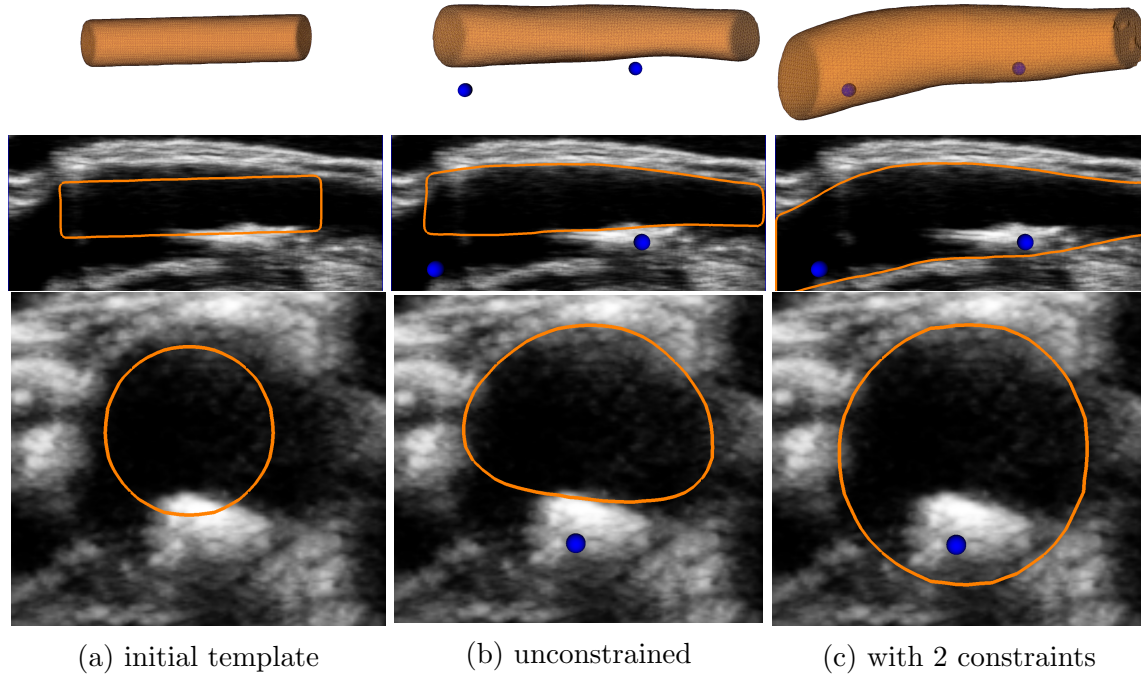


Figure 6.11 — Illustration on a 3D Ultrasound image of the carotid for atherosclerosis assessment. A synthetic tubular template deforms towards the image to segment the artery wall. Two user inputs allow to correct for under-segmentation due to a sclerotic plaque.



Figure 6.12 — 3D CEUS image of a kidney, here shown three orthogonal cross-sections (courtesy of Prof. J.M. Correia, Hospital Necker - Paris, France)

Validation on Contrast-Enhanced Ultrasounds (CEUS) of kidneys

After the promising, though only illustrative, experiment results, we have also started to perform a clinical validation of the method presented in this chapter. Contrast-Enhanced Ultrasound (CEUS) images is a recent imaging modality for which automatic segmentation algorithms are very challenging. CEUS is an imaging technique that has proven essential for both its relatively low toxicity and cost, in particular during radio-frequency (RF) ablation planning of kidney tumors. Comparing kidney and tumor volumes (before the operation) with kidney and resection volumes (after the operation) is necessary to evaluate the success of the intervention. However, segmenting the kidney in CEUS images is a particularly difficult task: the presence gas-filled micro-bubbles as contrast agent generates noisy data, the limited field of view of probes often prevents the acquisition of the whole kidney and

the presence of lesions induces variations in the usual shape (see Figure 6.12).

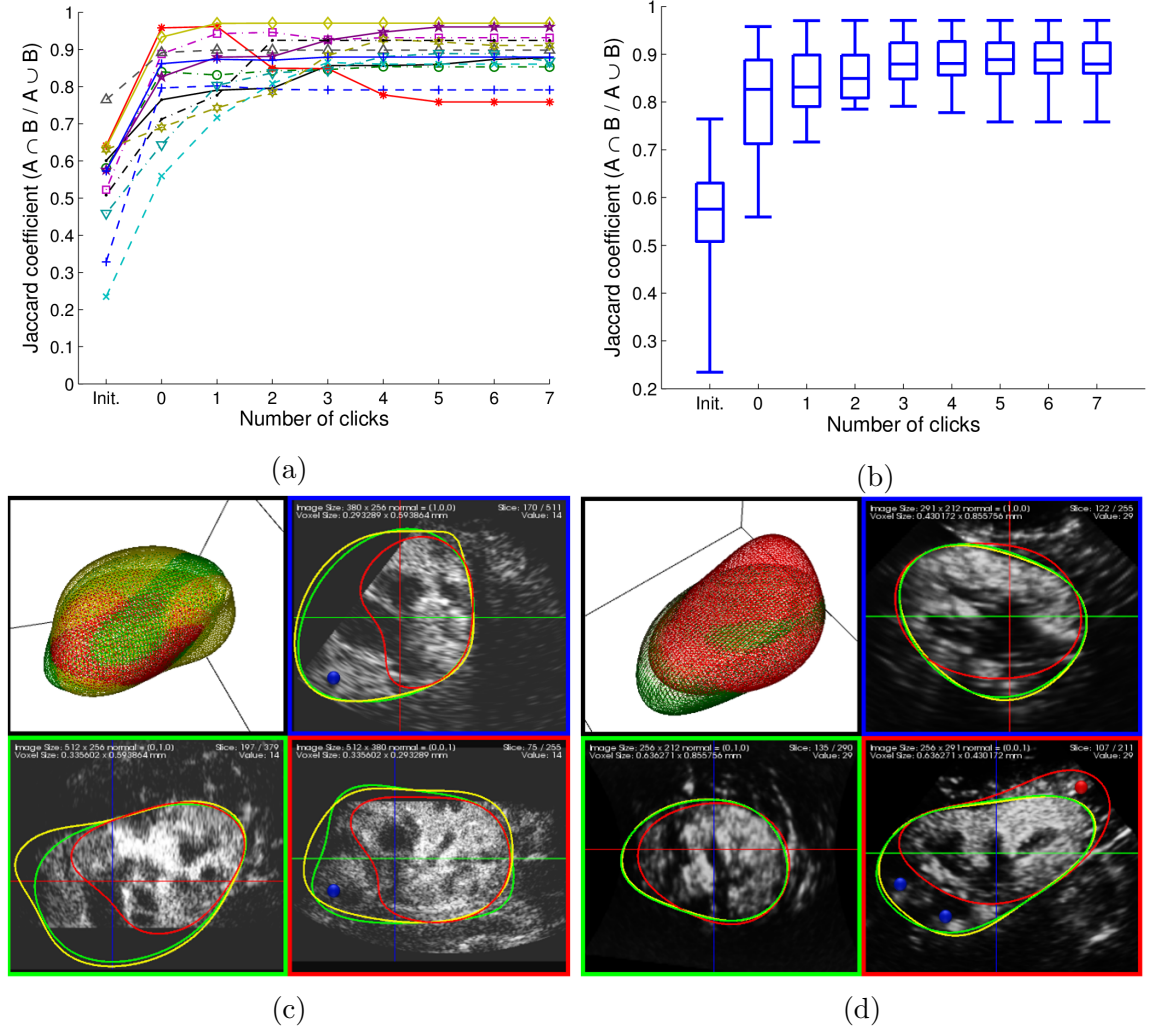


Figure 6.13 — (a) and (b): Similarity between segmentation and the ground truth defined by $J(A, B) = |A \cap B| / |A \cup B|$, as a function of the number of interactions. Left: each curve correspond to a single image. Right: box plot summarizing curves.

(c) and (d): Example of two different images, with different segmentations superimposed: ground truth (yellow), deformation result with no constraint (red) and final result (green) with interactions. Blue/red dots indicate points marked as inside/outside.

In collaboration with the radiology department of Hospital Necker (Paris, France) - the main medical center for renal RF ablation in Europe - we have quantified the benefits of our method. For thirteen patients, a specialist was asked to produce a ground truth segmentation to measure the quality of our algorithm as a function of the number of interactions. The model surface Φ_0 was set to an ellipsoid and r_i to $-\log(p_i(I))$, $i = 1, 2$. G was initialized by the user and deformation L to identity ($\mathbf{u} = \mathbf{0}$). The graphs in Figures 6.13.a and 6.13.b show that without interactions, the minimization of E (see Eq (6.4)) already considerably reduces the segmentation error. As the user interacts the closer the segmentation gets to the ground truth, often less than three clicks are needed for a satisfactory

result (in an average of 15 seconds). The ground truth is never exactly matched due to high intra-operator variability. Figures 6.13.c and 6.13.d show two examples where image features, shape prior and user interactions are all essential to the correctness of the final segmentation.

6.5 Conclusion

Although proven a solid approach for medical image segmentation, template deformation is still unable to cope with the wide spectrum of shapes that pathologies can generate. Providing users with reliable interactions is essential for the general acceptance of these segmentation tools. In this context, we introduced 3D interactions in a template deformation framework as points inside or outside the target anatomical structure. The formulation inherits from the region-based variational principles of Chapter 3 the supervised and unsupervised settings, with any global/local/flux classification error.

Our approach enforces compliance with a prior template through a pose-invariant shape term, consisting in a constraint on the deformation that is intrinsic to the shape referential. Moreover, this formulation results in a fast joint optimization scheme for both pose and deformation. Experiments were presented for several anatomical structures in various imaging modalities to illustrate the advantages of pose-invariance and the robustness with respect to the preservation of the template, with execution times of the order of a few seconds. A special care has been devoted to algorithmic efficiency to provide an even more intuitive control of the segmentation process with a real-time visualization of the evolution under constraints.

Since the Active Shape Models [48], shape priors through learning have been an extensive topic of research in image segmentation, in terms of statistical linear or non-linear shape models [27, 38, 50, 51, 106, 136, 144, 171]. In this work, we focused our attention on a consistent pose-invariant formulation for variational template-to-image registration, without relying on any learning nor training phase. However, the two approaches are not mutually-exclusive, but rather very complementary; in particular, since our pose-invariant transformation model relies on an intrinsic shape referential, it seems particularly-adapted to a subsequent learning of the deformation fields. The tedious process of constituting ground-truth segmentation datasets in order to learn these deformations can be made easier by the real-time interactive capabilities offered by this approach.

Conclusion

To cope with a considerable variety of clinical needs in terms of application requirements, practical approaches to image segmentation in medical imaging would benefit from both *unification* and *diversity*. While general paradigms are important for software re-usability as well as rapid prototyping and interoperability of the algorithms, only a diversity of object representations that fit together in a unified formulation can be broadly useful. Throughout this manuscript, we followed a methodology that derives from the mathematical framework of *variational image segmentation with implicit surfaces*. In this conclusion, we summarize our contributions and discuss some possible future extensions.

7.1 Unified Variational Formulation

In this thesis, we revisited a classical variational formulation for image segmentation based on region-wise features. Denoting by a function $u(\mathbf{x}) \in [0, 1]$ the membership of pixel \mathbf{x} to the target anatomical structure, the involved minimization problem reads:

$$\min_{u, \boldsymbol{\alpha}_1, \boldsymbol{\alpha}_2} \left\{ \mathcal{R}(u) + \lambda \int_{\Omega} u(\mathbf{x}) r_1(\mathbf{x}, \boldsymbol{\alpha}_1) d\mathbf{x} + \lambda \int_{\Omega} (1 - u(\mathbf{x})) r_2(\mathbf{x}, \boldsymbol{\alpha}_2) d\mathbf{x} \right\} \quad (7.1)$$

where both the function u and the parameters describing each region, $\boldsymbol{\alpha}_1$ and $\boldsymbol{\alpha}_2$, are unknown.

Within this unified unsupervised formulation, our first contribution was to *generalize statistical criteria derived from Bayesian principles to localized and non-parametric classification errors*, efficiently computed using Gaussian convolutions. We provided a large number of illustrative examples to help the reader choose the most suitable classification error $r_i(\mathbf{x}, \boldsymbol{\alpha}_i)$ for specific applications.

If a standard geometric constraint on the perimeter of the region is chosen for the regularization term $\mathcal{R}(u)$, problem can be solved with convex relaxation, which gives a globally-optimal solution to the supervised segmentation process, when the region parameters are known in advance. This approach has significant advantages in terms of robustness to initial conditions and numerical stability over the alternative level-set implementations of surface evolution equations.

7.2 Diversity of Representations

Nevertheless, we have also shown that implicit representations of 3D surfaces can also be very powerful for interactive image segmentation. We considered more constrained settings by restricting the solution space to take specific forms according to some prior knowledge on the object shape.

With a scalar field $\Phi(\mathbf{x})$ describing the surface $\{\Phi = 0\}$, the membership function in (7.1) becomes $u(\mathbf{x}) = H(\Phi(\mathbf{x}))$, where H denotes the Heaviside step function. The minimization problem becomes non-convex due to the presence of H and the optimization scheme depends on how the function Φ is represented.

Interactions as Inequality Constraints

Our contribution to the field of interactive image segmentation with implicit surfaces was to *formalize user interactions as additional inequality constraints*. Giving an expert the opportunity to locate inside ($\gamma_k = 1$) or outside ($\gamma_k = -1$) points \mathbf{x}_k , for instance by clicking on the image, user interactions mathematically translate as:

$$[\gamma_k \Phi(\mathbf{x}_k) \geq 0]_{k \in \{0 \dots M\}} \quad (7.2)$$

These additional constraints are either linear or non-linear depending on the chosen representation for Φ . In general, dedicated constrained optimization algorithms from numerical textbooks can be used to ensure that user interactions are satisfied.

From chapter 4 to chapter 6, we proposed 3 examples of implicit representations in order to address a large spectrum of typical anatomical structures of interest in medical imaging.

Implicit Generalized Cylinders

The first representation specifically targets the modeling and segmentation of vessels, a fundamental problem in vascular imaging for visualization and measurements of stenoses and aneurysms. Our contribution to this field was the *first introduction of convolution surfaces in a variational segmentation framework*, although they were already proposed as a visualization tool for complex vascular structures.

From a curve $\mathbf{m}(s)$ and continuously-varying scales $\sigma(s)$, a scalar field that approximates an implicit generalized cylinder is expressed as:

$$\Phi(\mathbf{x}) = \int_0^1 \varphi \left(\frac{\|\mathbf{x} - \mathbf{m}(s)\|}{\sigma(s)} \right) \|\mathbf{m}'(s)\| ds - C \quad (7.3)$$

We calculated the derivatives of the region-based criterion 7.1 with respect to $\mathbf{m}(s)$ and $\sigma(s)$ in order to perform a joint optimization of the centerline and the vessel boundaries. This smooth representation is the same in 2D and 3D and provides evolution equations for the end-points, allowing expansion and shrinking consistently with the variational formulation.

As future work, we would like to consider the extension to hierarchical structures of implicit tubular branches. The blending properties of convolution surfaces enable to smoothly model the surface of entire vascular tree structures such as liver veins or arteries. The simultaneous optimization of all branches would in particular involve the calculation of derivatives at bifurcation points, with additional dedicated constraints.

Non-Euclidean Radial Basis Functions

The second representation specifically targets the interactive segmentation of approximately spherical shapes such as lesions, even though we showed a number of other examples where it is also applicable. It generalizes the notion of radial distance in the Radial Basis Functions framework and constitutes the *first introduction of non-Euclidean, image-dependent distances in Radial Basis Functions for image segmentation*. The scalar field is a discrete sum of translated and scaled versions of a radially-symmetric kernel φ and is expressed as:

$$\Phi(\mathbf{x}) = \sum_{i=1}^N \lambda_i \varphi \left(\frac{\|\mathbf{x} - \mathbf{x}_i\|_{g_i}}{\sigma_i} \right) - C \quad (7.4)$$

where the new image-dependent geodesic distance g_i extends the notion of radial symmetry and enables the design of basis functions that naturally align with the salient image features. An intuitive interpretation of this representation in terms of shape space is that the set of admissible shapes is directly learned from the image.

For user-provided points \mathbf{x}_i and scales σ_i , the weights λ_i are the only free parameters. The optimization problem is low-dimensional hence it can be solved with fast algorithms. In this case, the constraints (7.2) are *linear* with respect to the variables λ_i . We used a variant of the Active Sets algorithm to solve the non-convex optimization problem (7.1) under a set of linear constraints.

In Chapter 5, the control points \mathbf{x}_i are provided by an expert, in an interactive fashion. In the future, it would be worth trying to automatically position the control points as well as optimize the scale of each basis function. Although it is a relatively easy task in the Euclidean case, the non-Euclidean Radial Basis Function framework poses the additional difficulty that the geodesic distance $\|\mathbf{x} - \mathbf{x}_i\|_{g_i}$ is not differentiable with respect to \mathbf{x}_i .

Implicit Template Deformation

The last representation considered in this manuscript casts image segmentation into a template-to-image registration problem. As such, it specifically targets anatomical structures that have a predictable shape as well as the applications in which the object of interest has a topology that shall be preserved. The unknown scalar field Φ is obtained by a geometric transformation ψ of a prior implicit template Φ_0 , expressed as:

$$\Phi(\mathbf{x}) = \Phi_0 \circ \psi(\mathbf{x}) \quad \text{with} \quad \psi = L \circ G \quad (7.5)$$

where the unknown variables become the global alignment G and the non-rigid deformation field L , jointly optimized. The regularization term \mathcal{R} in (7.1) is chosen to penalize L only, so that the shape constraint is invariant with respect to the pose G .

In this case, the inequality constraints (7.2) stemming from inside/outside labeled points are *non-linear* with respect to L and G . We adopted an Augmented Lagrangian approach to minimize the region-based criterion under the non-linear constraints.

Furthermore, we implemented a fast version of non-rigid deformation by considering smoothness as a built-in feature of the displacement field, expressed as a Gaussian convolution. At tens of iterations per second, the method yields *a real-time, interactive and model-based 3D segmentation tool*, providing experts with a live visual feedback in order to drive the template deformation towards a solution that is more clinically-relevant.

Interestingly, the template Φ_0 is itself an implicit function, hence it can be represented with non-Euclidean Radial Basis Functions or implicit generalized cylinders. In the latter case, the combination of non-rigid template deformation with the generalized cylinder model would allow to deviate from the strict tubular constraint and thus provide a closer fit to real vessels.

Proof of Proposition 1



Let F_0 and F_1 be defined by:

$$\begin{aligned}
 F_0(\Omega_1, \alpha_1, \alpha_2) &= \text{Per}(\partial\Omega_1) + \lambda \int_{\Omega_1} r_1(\mathbf{x}, \alpha_1) d\mathbf{x} + \lambda \int_{\Omega \setminus \Omega_1} r_2(\mathbf{x}, \alpha_2) d\mathbf{x} \\
 F_1(u, \alpha_1, \alpha_2) &= \int_{\Omega} \|\nabla u\| + \lambda \int_{\Omega} u(\mathbf{x}) r_1(\mathbf{x}, \alpha_1) d\mathbf{x} + \lambda \int_{\Omega} (1 - u(\mathbf{x})) r_2(\mathbf{x}, \alpha_2) d\mathbf{x}
 \end{aligned} \tag{A.1}$$

Proposition 1 *Fixing α_1 and α_2 , if $u^* \in BV_{[0,1]}(\Omega)$ is a global minimizer of F_1 then for almost every $t \in [0, 1]$, the characteristic function $\chi_u^*(\mathbf{x}, t)$ defined in $\Omega \times [0, 1]$ by*

$$\chi_u^*(\mathbf{x}, t) = \begin{cases} 1 & \text{if } u^*(\mathbf{x}) > t \\ 0 & \text{otherwise} \end{cases} \tag{A.2}$$

is also a global minimizer of F_1 . In addition, the set $\Omega_t = \{\mathbf{x} \in \Omega, u^(\mathbf{x}) > t\}$ is a global minimizer of F_0 .*

Proof:

For sake of simplicity, we omit the fixed variables α_1 and α_2 in the following. For any functions $u \in BV_{[0,1]}(\Omega)$ and $r \in L^1(\Omega)$, both the *co-area* formula (A.3) and the *layer-cake* formula (A.4) hold [65]:

$$\int_{\Omega} \|\nabla u\| = \int_0^1 \int_{\Omega} \|\nabla \chi_u(\mathbf{x}, t)\| d\mathbf{x} dt \tag{A.3}$$

$$\int_{\Omega} ur = \int_{\Omega} \left(\int_0^{u(\mathbf{x})} dt \right) r(\mathbf{x}) d\mathbf{x} = \int_{\Omega} \left(\int_0^1 \chi_u(\mathbf{x}, t) dt \right) r(\mathbf{x}) d\mathbf{x} = \int_0^1 \int_{\Omega} \chi_u(\mathbf{x}, t) r(\mathbf{x}) d\mathbf{x} dt \tag{A.4}$$

With $r = r_1(\cdot, \alpha_1) - r_2(\cdot, \alpha_2)$, applying (A.3) and (A.4) to the minimizer u^* yields:

$$F_1(u^*) = \int_0^1 F_1(\chi_{u^*}(\cdot, t)) dt, \quad (\text{A.5})$$

or, equivalently:

$$\int_0^1 \{F_1(\chi_{u^*}(\cdot, t)) - F_1(u^*)\} dt = 0. \quad (\text{A.6})$$

Since u^* minimizes F_1 ,

$$\forall t \in [0, 1], \quad F_1(u^*) \leq F_1(\chi_{u^*}(\cdot, t)),$$

Then, the *thresholded* characteristic function χ_{u^*} has the same functional value than the *fuzzy* minimizer u^* :

$$F_1(\chi_{u^*}(\cdot, t)) = F_1(u^*) \text{ for a.e. } t \in [0, 1]$$

This proves the first part of Proposition 1: $\chi_{u^*}(\cdot, t)$ is also a minimizer of F_1 for almost every $t \in [0, 1]$.

In addition, assuming there exists a region $\mathcal{A} \subset \Omega$ such that

$$F_0(\mathcal{A}) < F_1(u^*)$$

then its characteristic function also satisfies:

$$F_0(\mathcal{A}) = F_1(\chi^{\mathcal{A}}) < F_1(u^*)$$

which is a contradiction with respect to the hypothesis that u^* is a minimizer of F_1 . Since for almost every $t \in [0, 1]$ $F_0(\Omega_t) = F_1(\chi_{u^*}(\cdot, t)) = F_1(u^*)$, we finally have:

$$\forall \mathcal{A} \subset \Omega, \quad F_0(\Omega_t) \leq F_0(\mathcal{A})$$

□

Generalized Scaling Property of δ

B

Let Ω be a subdomain of \mathbb{R}^d , $f : \Omega \rightarrow \mathbb{R}$ a continuous function and $\Phi : \Omega \rightarrow \mathbb{R}$ a Lipschitz-continuous function such that almost every of its level-sets is a smooth hypersurface. The generalized scaling property of δ reads:

$$\int_{\Omega} \delta(\Phi) f = \int_{\Phi=0} \frac{f}{\|\nabla \Phi\|} \quad (\text{B.1})$$

Proof. Let δ_{ϵ} be a compactly-supported approximation of the Dirac distribution, having its support in $[-c, c]$. Suppose $\|\nabla \Phi\| \neq 0$ in any measurable subset of $\Phi^{-1}([-c, c])$. Using the coarea formula [65]:

$$\int_{\Omega} F \|\nabla \Phi\| = \int_{-\infty}^{+\infty} \left(\int_{\{\Phi=a\}} F(\mathbf{s}) d\mathbf{s} \right) da$$

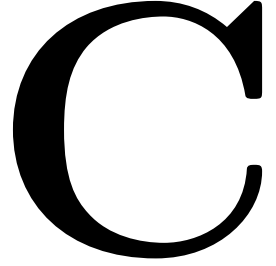
with $F = \delta_{\epsilon}(\Phi) \frac{f}{\|\nabla \Phi\|}$, where f is continuous, we have:

$$\begin{aligned} \int_{\Omega} \delta_{\epsilon}(\Phi) f &= \int_{-c}^c \left(\int_{\{\Phi=a\}} \delta_{\epsilon}(\Phi(\mathbf{s})) \frac{f(\mathbf{s})}{\|\nabla \Phi(\mathbf{s})\|} d\mathbf{s} \right) da \\ &= \int_{-c}^c \delta_{\epsilon}(a) \left(\int_{\{\Phi=a\}} \frac{f(\mathbf{s})}{\|\nabla \Phi(\mathbf{s})\|} d\mathbf{s} \right) da \end{aligned} \quad (\text{B.2})$$

Since by definition $\lim_{\epsilon \rightarrow 0} \int_{-c}^c \delta_{\epsilon}(a) G(a) da = G(0)$, for any continuous function G , we finally obtain:

$$\lim_{\epsilon \rightarrow 0} \int_{\Omega} \delta_{\epsilon}(\Phi(\mathbf{x})) f(\mathbf{x}) d\mathbf{x} = \int_{\{\Phi=0\}} \frac{f(\mathbf{s})}{\|\nabla \Phi(\mathbf{s})\|} d\mathbf{s}. \quad (\text{B.3})$$

Centerline and Scales Derivatives



In this annex, we give the technical details to obtain the gradient direction in order to locally minimize the following problem:

$$\min_{\mathbf{m}, \sigma} \left\{ F(\mathbf{m}, \sigma) = \mathcal{R}(\mathbf{m}, \sigma) + \int_{\Omega} H(\Phi_{\mathbf{m}, \sigma}(\mathbf{x})) r(\mathbf{x}) d\mathbf{x} \right\}, \quad (\text{C.1})$$

with

$$\Phi_{\mathbf{m}, \sigma}(\mathbf{x}) = \int_0^1 K \left(\frac{\|\mathbf{x} - \mathbf{m}(s)\|^2}{\sigma(s)^2} \right) \|\mathbf{m}'(s)\| ds - C \quad (\text{C.2})$$

and where $\mathcal{R}(\mathbf{m}, \sigma)$ is designed to penalize both the *length* of the centerline and the *variations of scale* along it, controlled by the positive scalar parameters λ and μ respectively:

$$\mathcal{R}(\mathbf{m}, \sigma) = \lambda \int_0^1 \|\mathbf{m}'(s)\| + \mu \int_0^1 |\sigma'(s)|^2 \quad (\text{C.3})$$

Kernel K is here of the form $K = A \cdot \exp$, which is coherent with the choice of a Gaussian kernel φ used in chapter 4. In order to simplify notation we set:

$$\frac{\|\mathbf{x} - \mathbf{m}(s)\|^2}{\sigma(s)^2} = d_{\mathbf{m}, \sigma}^2$$

Moreover, we take the usual definitions for the Frenet referential $\mathcal{T}, \mathcal{N}, \mathcal{B}$ defined on curve \mathbf{m} . That is, if curve \mathbf{m} is parameterized with respect to its arc length a (which is not the case in our computations): $\mathcal{T} = \frac{d\mathbf{m}}{da}$, $\mathcal{N} = \kappa \frac{d\mathcal{T}}{da}$ and $\mathcal{B} = \mathcal{T} \wedge \mathcal{N}$, scalar κ being the curvature of \mathbf{m} . Note that if \mathbf{m} is not parameterized with respect to its arc length, we have $\mathcal{T} = \frac{\mathbf{m}'}{\|\mathbf{m}'\|}$ and one can prove that second derivative \mathbf{m}'' belongs to the plane generated by the couple $(\mathcal{T}, \mathcal{N})$.

Calculus of Variations with respect to \mathbf{m}

Let us consider an arbitrary perturbation $\boldsymbol{\eta}$ of the curve \mathbf{m} , parameterized on $[0, 1]$ and infinitely differentiable. If \mathbf{m} is a local minimizer of F , it should satisfy:

$$\left. \frac{dF(\mathbf{m} + t\boldsymbol{\eta})}{dt} \right|_{t=0} = 0$$

Let us compute this derivative:

$$\left. \frac{dF(\mathbf{m} + t\boldsymbol{\eta})}{dt} \right|_{t=0} = \underbrace{\left. \frac{d\mathcal{R}(\mathbf{m} + t\boldsymbol{\eta})}{dt} \right|_{t=0}}_{\mathcal{R}_\eta} + \underbrace{\int_{\Omega} \delta(\Phi_{\mathbf{m},\sigma}(\mathbf{x})) \left. \frac{d\Phi_{\mathbf{m}+t\boldsymbol{\eta},\sigma}}{dt} \right|_{t=0} r(\mathbf{x}) d\mathbf{x}}_{\mathcal{A}_\eta}$$

For the computation of the Attachment term (\mathcal{A}_η) we have:

$$\begin{aligned} \left. \frac{d\Phi_{\mathbf{m}+t\boldsymbol{\eta},\sigma}}{dt} \right|_{t=0} &= \int_0^1 \left. \frac{dK(d_{\mathbf{m}+t\boldsymbol{\eta},\sigma}^2)}{dt} \right|_{t=0} \|\mathbf{m}'(s)\| ds \\ &+ \int_0^1 K(d_{\mathbf{m},\sigma}^2) \left. \frac{d\|\mathbf{m}'(s) + t\boldsymbol{\eta}'(s)\|}{dt} \right|_{t=0} ds \end{aligned}$$

Derivative of the first term is relatively straightforward, noticing that $K' = K$

$$\begin{aligned} \left. \frac{dK(d_{\mathbf{m}+t\boldsymbol{\eta},\sigma}^2)}{dt} \right|_{t=0} \|\mathbf{m}'(s)\| &= \int_0^1 K(d_{\mathbf{m},\sigma}^2) \left\langle \frac{\mathbf{x} - \mathbf{m}}{\sigma^2}, \boldsymbol{\eta} \right\rangle \|\mathbf{m}'(s)\| ds \\ &= \int_0^1 \left\langle K(d_{\mathbf{m},\sigma}^2) \|\mathbf{m}'(s)\| \frac{\mathbf{x} - \mathbf{m}}{\sigma^2}, \boldsymbol{\eta} \right\rangle ds \end{aligned}$$

Computing the derivative of the second term involves integration by parts to expose $\boldsymbol{\eta}$:

$$\begin{aligned} \int_0^1 K(d_{\mathbf{m},\sigma}^2) \left. \frac{d\|\mathbf{m}'(s) + t\boldsymbol{\eta}'(s)\|}{dt} \right|_{t=0} ds &= \int_0^1 \left\langle K(d_{\mathbf{m},\sigma}^2) \frac{\mathbf{m}'}{\|\mathbf{m}'\|}, \boldsymbol{\eta}' \right\rangle ds \\ &= \left[\left\langle K(d_{\mathbf{m},\sigma}^2) \frac{\mathbf{m}'}{\|\mathbf{m}'\|}, \boldsymbol{\eta} \right\rangle \right]_0^1 - \int_0^1 \left\langle \frac{d}{ds} \left\{ K(d_{\mathbf{m},\sigma}^2) \frac{\mathbf{m}'}{\|\mathbf{m}'\|} \right\}, \boldsymbol{\eta} \right\rangle ds \end{aligned}$$

and

$$\begin{aligned} \int_0^1 \left\langle \frac{d}{ds} \left\{ K(d_{\mathbf{m},\sigma}^2) \frac{\mathbf{m}'}{\|\mathbf{m}'\|} \right\}, \boldsymbol{\eta} \right\rangle ds &= \\ \int_0^1 \left\langle \frac{d}{ds} \left\{ K(d_{\mathbf{m},\sigma}^2) \right\} \boldsymbol{\tau} + K(d_{\mathbf{m},\sigma}^2) \kappa \boldsymbol{\mathcal{N}}, \boldsymbol{\eta} \right\rangle ds \end{aligned}$$

Combining these computations, we have:

$$\begin{aligned} \left. \frac{d\Phi_{\mathbf{m}+t\boldsymbol{\eta},\sigma}}{dt} \right|_{t=0} = & \\ \int_0^1 \left\langle K(d_{\mathbf{m},\sigma}^2) \|\mathbf{m}'(s)\| \frac{\mathbf{x}-\mathbf{m}}{\sigma^2} - \frac{d}{ds} \{K(d_{\mathbf{m},\sigma}^2)\} \mathcal{T} - K(d_{\mathbf{m},\sigma}^2) \kappa \mathcal{N}, \boldsymbol{\eta} \right\rangle & \\ + [\langle K(d_{\mathbf{m},\sigma}^2) \mathcal{T}, \boldsymbol{\eta} \rangle]_0^1 & \end{aligned}$$

This yields:

$$\begin{aligned} \mathcal{A}_{\boldsymbol{\eta}} = & \\ \int_0^1 \left\langle \int_{\Omega} \delta(\Phi_{\mathbf{m},\sigma}(\mathbf{x})) r(\mathbf{x}) \left(K(d_{\mathbf{m},\sigma}^2) \|\mathbf{m}'(s)\| \frac{\mathbf{x}-\mathbf{m}}{\sigma^2} \right. \right. & \\ \left. \left. - K(d_{\mathbf{m},\sigma}^2) \kappa \mathcal{N} - \frac{d}{ds} \{K(d_{\mathbf{m},\sigma}^2)\} \mathcal{T} \right) d\mathbf{x} \right. & \\ \left. , \boldsymbol{\eta} \right\rangle ds & \\ + \left\langle \left(\int_{\Omega} \delta(\Phi_{\mathbf{m},\sigma}(\mathbf{x})) r(\mathbf{x}) K(d_{\mathbf{m}(1),\sigma(1)}^2) d\mathbf{x} \right) \mathcal{T}(1), \boldsymbol{\eta}(1) \right\rangle & \\ - \left\langle \left(\int_{\Omega} \delta(\Phi_{\mathbf{m},\sigma}(\mathbf{x})) r(\mathbf{x}) K(d_{\mathbf{m}(0),\sigma(0)}^2) d\mathbf{x} \right) \mathcal{T}(0), \boldsymbol{\eta}(0) \right\rangle & \end{aligned}$$

Very similarly, the computation of the regularization part $\mathcal{R}_{\boldsymbol{\eta}}$ gives

$$\mathcal{R}_{\boldsymbol{\eta}} = - \int_0^1 \langle \kappa \mathcal{N}, \boldsymbol{\eta} \rangle + \langle \mathcal{T}(1), \boldsymbol{\eta}(1) \rangle - \langle \mathcal{T}(0), \boldsymbol{\eta}(0) \rangle$$

Bringing all together and using the general scaling property of δ (see appendix B)

$$\begin{aligned}
& \left. \frac{dF(\mathbf{m} + t\boldsymbol{\eta})}{dt} \right|_{t=0} = \\
& \int_0^1 \left\langle \left\| \mathbf{m}'(s) \right\| \int_{\{\Phi_{\mathbf{m},\sigma}=0\}} r(\mathbf{x}) \frac{K(d_{\mathbf{m},\sigma}^2)}{\|\nabla \Phi_{\mathbf{m},\sigma}(\mathbf{x})\|} \frac{\mathbf{x} - \mathbf{m}}{\sigma^2} - \left(\lambda + \int_{\{\Phi_{\mathbf{m},\sigma}=0\}} r(\mathbf{x}) \frac{K(d_{\mathbf{m},\sigma}^2)}{\|\nabla \Phi_{\mathbf{m},\sigma}(\mathbf{x})\|} \right) \kappa \mathcal{N}, \boldsymbol{\eta} \right\rangle \\
& + \int_0^1 \left\langle \frac{d}{ds} \{K(d_{\mathbf{m},\sigma}^2)\} \mathcal{T}, \boldsymbol{\eta} \right\rangle \\
& + \left\langle \left(\lambda + \int_{\{\Phi_{\mathbf{m},\sigma}=0\}} r(\mathbf{x}) \frac{K(d_{\mathbf{m}(1),\sigma(1)}^2)}{\|\nabla \Phi_{\mathbf{m},\sigma}(\mathbf{x})\|} \right) \mathcal{T}(1), \boldsymbol{\eta}(1) \right\rangle - \left\langle \left(\lambda + \int_{\{\Phi_{\mathbf{m},\sigma}=0\}} r(\mathbf{x}) \frac{K(d_{\mathbf{m}(0),\sigma(0)}^2)}{\|\nabla \Phi_{\mathbf{m},\sigma}(\mathbf{x})\|} \right) \mathcal{T}(0), \boldsymbol{\eta}(0) \right\rangle
\end{aligned}$$

where the tangential part (second line) can be ignored since it only changes the parameterization of the curve, not its geometry.

Gradient descent equation for \mathbf{m}

This yields the following gradient-descent equation for \mathbf{m} , setting $\Phi = \Phi_{\mathbf{m},\sigma}$:

$$\begin{aligned} \forall s \in]0, 1[\quad \frac{\partial \mathbf{m}}{\partial t}(s) &= \kappa(s) \left(\lambda + \int_{\{\Phi=0\}} \frac{r(\mathbf{x})}{\|\nabla \Phi(\mathbf{x})\|} C(\mathbf{x}, s) \right) \mathcal{N}(s) \\ &\quad - \|\mathbf{m}'(s)\| \int_{\{\Phi=0\}} \frac{r(\mathbf{x})}{\|\nabla \Phi(\mathbf{x})\|} \mathbf{N}(\mathbf{x}, s) d\mathbf{x} \end{aligned}$$

$$\frac{\partial \mathbf{m}}{\partial t}(1) = - \left(\lambda + \int_{\{\Phi=0\}} \frac{r(\mathbf{x})}{\|\nabla \Phi(\mathbf{x})\|} C(\mathbf{x}, 1) \right) \mathcal{T}(1)$$

$$\frac{\partial \mathbf{m}}{\partial t}(0) = \left(\lambda + \int_{\{\Phi=0\}} \frac{r(\mathbf{x})}{\|\nabla \Phi(\mathbf{x})\|} C(\mathbf{x}, 0) \right) \mathcal{T}(0)$$

$$C(\mathbf{x}, s) = K(d_{\mathbf{m},\sigma}^2) = \frac{\sigma(s) \varphi' \left(\frac{\|\mathbf{x} - \mathbf{m}(s)\|}{\sigma(s)} \right)}{2 \|\mathbf{x} - \mathbf{m}(s)\|}$$

$$\mathbf{N}(\mathbf{x}, s) = C(\mathbf{x}, s) \frac{\mathbf{x} - \mathbf{m}(s)}{\sigma^2(s)} = \frac{\varphi' \left(\frac{\|\mathbf{x} - \mathbf{m}(s)\|}{\sigma(s)} \right)}{2\sigma(s)} \frac{\mathbf{x} - \mathbf{m}(s)}{\|\mathbf{x} - \mathbf{m}(s)\|}$$

Calculus of Variations with respect to σ

Similarly to computations made for \mathbf{m} , we consider now a infinitely differentiable scalar function η . If σ is a local minimizer of F we must have

$$\left. \frac{dF(\sigma + t\eta)}{dt} \right|_{t=0} = 0$$

And we have:

$$\left. \frac{dF(\sigma + t\eta)}{dt} \right|_{t=0} = \underbrace{\left. \frac{d\mathcal{R}(\sigma + t\eta)}{dt} \right|_{t=0}}_{\mathcal{R}_\eta} + \underbrace{\int_{\Omega} \delta(\Phi_{\mathbf{m},\sigma}(\mathbf{x})) \left. \frac{d\Phi_{\mathbf{m},\sigma+t\eta}}{dt} \right|_{t=0} r(\mathbf{x}) d\mathbf{x}}_{\mathcal{A}_\eta}$$

Moreover,

$$\begin{aligned} \left. \frac{d\Phi_{\mathbf{m},\sigma+t\eta}}{dt} \right|_{t=0} &= \int_0^1 \left. \frac{dK(d_{\mathbf{m},\sigma+t\eta}^2)}{dt} \right|_{t=0} \|\mathbf{m}'(s)\| ds \\ &= - \int_0^1 K(d_{\mathbf{m},\sigma}^2) \frac{2\|\mathbf{x} - \mathbf{m}\|^2}{\sigma^3} \|\mathbf{m}'(s)\| \eta ds \end{aligned}$$

So that

$$A_\eta = -2 \int_0^1 \left(\|\mathbf{m}'(s)\| \int_{\Omega} \delta(\Phi_{\mathbf{m},\sigma}(\mathbf{x})) K(d_{\mathbf{m},\sigma}^2) r(\mathbf{x}) \frac{\|\mathbf{x} - \mathbf{m}\|^2}{\sigma^3} \right) \eta ds$$

Along the same line, we have

$$\mathcal{R}_\eta = 2 \left(- \int_0^1 \sigma'' \eta ds + \sigma'(1)\eta(1) - \sigma'(0)\eta(0) \right)$$

Putting everything together and using the general scaling property of δ

$$\begin{aligned} \left. \frac{dF(\sigma + t\eta)}{dt} \right|_{t=0} &= -2 \int_0^1 \left(\mu \sigma'' + \|\mathbf{m}'(s)\| \int_{\{\Phi_{\mathbf{m},\sigma}=0\}} r(\mathbf{x}) \frac{K(d_{\mathbf{m},\sigma}^2)}{\|\nabla \Phi_{\mathbf{m},\sigma}(\mathbf{x})\|} \frac{\|\mathbf{x} - \mathbf{m}\|^2}{\sigma^3} \right) \eta ds \\ &+ 2\mu \left(\sigma'(1)\eta(1) - \sigma'(0)\eta(0) \right) \end{aligned}$$

Gradient descent equation for σ

The previous computations provide the following gradient descent equation for σ

$$\forall s \in]0, 1[\quad \frac{\partial \sigma}{\partial t}(s) = \mu \sigma'' - \|\mathbf{m}'(s)\| \int_{\{\Phi=0\}} \frac{r(\mathbf{x})}{\|\nabla \Phi(\mathbf{x})\|} B(\mathbf{x}, s)$$

$$\frac{\partial \sigma}{\partial t}(1) = -\mu \sigma'(1)$$

$$\frac{\partial \sigma}{\partial t}(0) = \mu \sigma'(0)$$

with

$$B(\mathbf{x}, s) = - \left\langle \mathbf{N}(\mathbf{x}, s), \frac{\mathbf{x} - \mathbf{m}}{\sigma} \right\rangle = - \frac{\varphi' \left(\frac{\|\mathbf{x} - \mathbf{m}(s)\|}{\sigma(s)} \right)}{2\sigma^2(s)} \|\mathbf{x} - \mathbf{m}(s)\|$$

Curriculum Vitae

Benoit MORY

French, born on January, 6, 1976

28, rue Lacépède
75005 Paris. France.

Tel. (work): +33147283593

Education

- | | |
|-----------|---|
| 2007–2011 | Ecole Polytechnique Fédérale de Lausanne (EPFL) . Switzerland.
Signal Processing Laboratory 5 (LTS5).
PhD student under the supervision of Prof. Jean-Philippe Thiran. |
| 1995–1998 | Ecole Supérieure d'Electricité (SUPELEC) . Gif-sur-Yvette, France.
Specialization in Image Processing and Pattern Recognition. |
| 1993–1995 | Université Paris-Sud (Paris XI) . Orsay, France.
Two-year University Degree (DEUG) in Mathematics and Physics. |

Work Experience

- | | |
|-----------|---|
| 2007–2011 | Medisys Research Lab, Philips Healthcare . Suresnes, France.
Senior Scientist. Research on 3D interactive image segmentation algorithms with implicit surfaces. |
| 2003–2007 | Philips Medical Systems Research France . Suresnes, France.
Senior Scientist. Projects on image restoration, registration, segmentation and tracking in X-Ray, Ultrasound, CT, MRI. |
| 1998–2002 | Philips Research France . Limeil-Brevannes, France.
Research Scientist. Projects on motion estimation for video stitching and content-based retrieval (MPEG-7). |

Skills

Image processing, medical imaging, computer vision, computer science (C, C++, Matlab).

Publications

Conference Proceedings

- B. Mory, O. Somphone, R. Prevost and R. Ardon. Template Deformation with User Constraints for Live 3D Interactive Surface Extraction. *Mesh Processing in Medical Imaging (MeshMed), Workshop of Medical Image Computing and Computer-Assisted Interventions (MICCAI)*. 2011.
- K. Elagouni, C. Ciofolio-Veit and B. Mory. Automatic Segmentation of Pathological Tissues in Cardiac MRI. *International Symposium on Biomedical Imaging (ISBI)*, 472-475, 2010.
- T. Lefevre, B. Mory, R. Ardon, J. Sanchez-Castro and A. Yezzi. Automatic Inferior Vena Cava Segmentation in Contrast-Enhanced CT Volumes. *International Symposium on Biomedical Imaging (ISBI)*, 420-423, 2010.
- B. Mory, R. Ardon, A. Yezzi and J.P. Thiran. Non-Euclidean Image-Adaptive Radial Basis Functions for 3D Interactive Segmentation. *International Conference On Computer Vision (ICCV)*. 787-794, 2009.
- O. Somphone, B. Mory, S. Makram-Ebeid and L. Cohen. Prior-Based Piecewise-Smooth Segmentation by Template Competitive Deformation Using Partitions of Unity. *European Conference On Computer Vision (ECCV)*. 628-641, 2008.
- C. Ciofolio, M. Fradkin, B. Mory, G. Hautvast and M. Breeuwer. Automatic Myocardium Segmentation of Cine Cardiac MR Images. *International Symposium on Biomedical Imaging (ISBI)*. 225-228. 2008.
- M. Fradkin, C. Ciofolio, B. Mory, G. Hautvast and M. Breeuwer. Comprehensive Segmentation of Cine Cardiac MR Images *Medical Image Computing and Computer-Assisted Interventions (MICCAI)*. 178-185. 2008.
- B. Mory, R. Ardon and J.P. Thiran. Variational Segmentation using Fuzzy Region Competition and Local Non-Parametric Probability Density Functions. *International Conference On Computer Vision (ICCV)*. 14-20. 2007.
- B. Mory and R. Ardon. Fuzzy Region Competition: A Convex Two-Phase Segmentation Framework. *International Conference On Scale-Space and Variational Methods (SSVM)*. 214-226. 2007.

Journal Papers

S. Makram-Ebeid and B. Mory. Scale-Space Image Analysis based on Hermite Polynomials Theory. *International Journal of Computer Vision*. 64(2-3). 125-241. 2005

S. Jeannin and B. Mory. Video Motion Representation for Improved Content Access. *IEEE Transactions on Consumer Electronics*. 46. 645-655, 2000.

S. Jeannin, R. Jasinski, A. She, T. Naveen, B. Mory and A.Tabatabai. Motion Descriptors for Content-Based Video Representation. *Signal Processing: Image Communication Journal*. 16(1-2). 59-85. 2000.

Book Chapters

B.S. Manjunath, P. Salembier and T. Sikora (Eds) Introduction to MPEG-7: Multimedia Content Description Description Interface. Chap: Motion Descriptors by S. Jeannin, A. Divakaran and B. Mory. J. Wiley & Sons, ISBN:978-0-471-48678-7. 2002.

Bibliography

- [1] D. Adalsteinsson and J.A. Sethian. A fast level set method for propagating interfaces. *Journal of Computational Physics*, 112:269–277, 1995.
- [2] R. Adams and L. Bischof. Seeded region growing. *IEEE Transactions on Pattern Analysis And Machine Intelligence*, 16:641–646, 1994.
- [3] L. Ambrosio and V. Tortorelli. Approximation of functionals depending on jumps by elliptic functionals via γ -convergence. *Communications on Pure and Applied Mathematics*, 43:999–1036, 1990.
- [4] Luigi Ambrosio, Vicent Caselles, Simon Masnou, and Jean-Michel Morel. Connected components of sets of finite perimeter and applications to image processing. *JOURNAL OF THE EUROPEAN MATHEMATICAL SOCIETY*, 3:39–92, 1999.
- [5] A.Mihalcea. A new pc based software for semi automatic liver segmentation. clinical study for preoperative tumor localization. *InfoRAD 2003, Radiological Society of North America RSNA*, 2003.
- [6] Amir A. Amini, Terry E. Weymouth, and Ramesh Jain. Using dynamic programming for solving variational problems in vision. *IEEE Trans. Pattern Anal. Mach. Intell.*, 12(9):855–867, 1990.
- [7] J. H. An and Y. Chen. Region based image segmentation using a modified mumford-shah algorithm. In *SSVM*, pages 733–742, 2007.
- [8] Ben Appleton and Hugues Talbot. Globally minimal surfaces by continuous maximal flows. *IEEE Transactions on Pattern Analysis And Machine Intelligence*, 2006.
- [9] S. P. Awate, T. Tasdizen, and R. T. Whitaker. Unsupervised texture segmentation with nonparametric neighborhood statistics. *European Conference on Computer Vision, Proceedings*, pages 494–507, 2006.
- [10] S. Aylward and E. Bullitt. Initialization, noise, singularities, and scale in height ridge traversal for tubular object centerline extraction. *IEEE Trans. On Medical Imaging*, 21(2):61–75, 2002.

- [11] Xue Bai and Guillermo Sapiro. A geodesic framework for fast interactive image and video segmentation and matting. In *IEEE International Conference On Computer Vision*, pages 1–8, 2007.
- [12] E. Bardinet, L.D. Cohen, and N. Ayache. A parametric deformable model to fit unstructured 3d data. *Computer Vision and Image Understanding*, 71:39–54, 1998.
- [13] Eric Bardinet, Laurent D. Cohen, and Nicholas Ayache. Superquadrics and free-form deformations : a global model to fit and track 3d medical data. *Proc. of International conference on Computer Vision, Virtual reality and robotics in Medicine*, pages 319–326, 1995.
- [14] O. Bernard, D. Friboulet, P. Thevenaz, and M. Unser. Variational b-spline level-set method for fast image segmentation. In *International Symposium on Biomedical Imaging*, pages 177–180, May 2008.
- [15] O. Bernard, D. Friboulet, P. Thévenaz, and M. Unser. Variational B-spline level-set: A linear filtering approach for fast deformable model evolution. *IEEE Transactions on Image Processing*, 18(6):1179–1191, June 2009.
- [16] Olivier Bernard, Basma Touil, Arnaud Gelas, Rémy Prost, and Denis Friboulet. Segmentation of myocardial regions in echocardiography using the statistics of the radio-frequency signal. In *Functional Imaging and Modeling of the Heart, Proceedings*, 2007.
- [17] Andrew Blake, Carsten Rother, M. Brown, P. Perez, and P. Torr. Interactive image segmentation using an adaptive gmmrf model. *European Conference on Computer Vision, Proceedings*, 1:428–441, 2004.
- [18] Andrew Blake and Alan Yuille. *Active Vision*. MIT Press, Cambridge, MA, 1992.
- [19] Andrew Blake and Andrew Zisserman. *Visual reconstruction*. MIT Press, Cambridge, MA, USA, 1987.
- [20] J. Blinn. A generalization of algebraic surface drawing. *ACM Transactions on Graphics*, 1:235–256, 1982.
- [21] Jules Bloomenthal. *Introduction to Implicit Surfaces*. Morgan Kaufmann Publishers, Inc., San Francisco, California, 1997.
- [22] F. Bookstein. Principal warps: Thin-plate splines and the decomposition of deformations. *IEEE Transactions on Pattern Analysis And Machine Intelligence*, 11(6):567–585, 1989.
- [23] Y. Boykov and M. P. Jolly. Interactive graph cuts for optimal boundary and region segmentation of objects in n-d images. *Proc. of IEEE International Conference on Computer Vision (ICCV)*, 1:105–112, 2001.

- [24] Yuri Boykov and Vladimir Kolmogorov. Computing geodesics and minimal surfaces via graph cuts. In *IEEE International Conference on Computer Vision*, volume 1, pages 26–33, October 2003.
- [25] Yuri Boykov and Vladimir Kolmogorov. An experimental comparison of min-cut/max-flow algorithms for energy minimization in vision. *IEEE Transactions on Pattern Analysis and Machine Intelligence*, 26:1124–1137, 2004.
- [26] Xavier Bresson, Selim Esedoğlu, Pierre Vandergheynst, Jean-Philippe Thiran, and Stanley Osher. Fast global minimization of the active contour/snake model. *Journal of Mathematical Imaging and Vision*, 28(2):151–167, 2007.
- [27] Xavier Bresson, Pierre Vandergheynst, and Jean-Philippe Thiran. A variational model for object segmentation using boundary information and shape prior driven by the mumford-shah functional. *International Journal On Computer Vision*, 68(2):145–162, 2006.
- [28] C.R. Brice and C.L. Fennema. Scene analysis using regions. *Artificial Intelligence*, 1:205–226, 1970.
- [29] T. Brox and D. Cremers. On the statistical interpretation of the piecewise smooth mumford-shah functional. In *SSVM*, pages 203–213, 2007.
- [30] T. Brox, M. Rousson, R. Deriche, and J. Weickert. Unsupervised segmentation incorporating colour, texture, and motion. *Computer Analysis of Images and Patterns. Lecture Notes in Computer Science*, 2756:353–360, 2003.
- [31] Thomas Brox, Mikael Rousson, Rachid Deriche, and Joachim Weickert. Colour, texture, and motion in level set based segmentation and tracking. *Image and Vision Computing*, 2009.
- [32] J.W. Bruce and P.J. Giblin. *Curves and singularities: A geometrical introduction to singularity theory*. Cambridge University Press, 1992.
- [33] V. Caselles, F. Catte, T. Coll, and F. Dibos. A geometric model for active contours in image processing. Technical Report 9210, CEREMADE, Université Paris Dauphine, 1992.
- [34] Vicent Caselles, Ron Kimmel, and Guillermo Sapiro. Geodesic active contours. *International Journal On Computer Vision*, 22(1):61–79, 1997.
- [35] A. Chakraborty, L. H. Staib, and J. S. Duncan. Deformable boundary finding in medical images by integrating gradient and region information. *IEEE Transactions on Medical Imaging*, 15(6):859–870, 1996.
- [36] Antonin Chambolle. An algorithm for total variation minimization and applications. *Journal of Mathematical Imaging and Vision*, 20(1):89–97, 2004.

- [37] T Chan, S. Esedoglu, and Kangyu Ni. Histogram based segmentation using wasserstein distances. *Scale Space and Variational Methods in Computer Vision, Proceedings*, pages 697–708, 2007.
- [38] T. F. Chan and W. Zhu. Level set based shape prior segmentation. In *IEEE CVPR*, pages II: 1164–1170, 2005.
- [39] TF Chan and LA Vese. Active contours without edges. *IEEE Trans on Image Processing*, 10(2):266–277, 2001.
- [40] Tony F. Chan and Luminita A. Vese. A level set algorithm for minimizing the mumford-shah functional in image processing. In *VLSM '01: Proceedings of the IEEE Workshop on Variational and Level Set Methods (VLSM'01)*, page 161, Washington, DC, USA, 2001. IEEE Computer Society.
- [41] Ying Chi, O. Peter M. M. Cashman, and Bello, and Richard I. Kitney. A discussion on the evaluation of a new automatic liver volume segmentation method for specified CT image datasets. *MICCAI*, pages 167–175, 2007.
- [42] I. Cohen and L.D. Cohen. A hybrid hyperquadric model for 2-D and 3-D data fitting. *ICPR*, pages 403–405, 1994.
- [43] I. Cohen, L.D. Cohen, and N. Ayache. Using deformable surfaces to segment 3d images and infer differential structure. *CVGIP: Image Understanding*, 56:242–263, 1992.
- [44] L. Cohen, E. Bardinet, and N. Ayache. Reconstruction of digital terrain model with a lake. In *Proceedings of SPIE'93, Geometric Methods in Computer Vision*, 1993.
- [45] Laurent D. Cohen and Ron Kimmel. Fast marching the global minimum of active contours. In *IEEE International Conference on Image Processing*, pages 473–476, 1996.
- [46] Laurent D. Cohen and Ron Kimmel. Global minimum for active contour models: A minimal path approach. *International Journal On Computer Vision*, 24(1):57–78, 1997.
- [47] Dorin Comaniciu and Peter Meer. Mean shift: A robust approach toward feature space analysis. *IEEE Transactions on Pattern Analysis and Machine Intelligence*, 24(5):603–619, 2002.
- [48] T. F. Cootes, C. J. Taylor, D. H. Cooper, and J. Graham. Active shape models: Their training and application. *Computer Vision and Image Understanding*, 61(1):38–59, January 1995.
- [49] C. Couprie, L. Grady, L. Naiman, and H. Talbot. Power watersheds: A new image segmentation framework extending graph cuts, random walker and optimal spanning forest. *International Conference on Pattern Recognition*, 2009.

- [50] D. Cremers, N. A. Sochen, and C. Schnorr. Towards recognition-based variational segmentation using shape priors and dynamic labeling. In *Scale Space*, pages 388–400, 2003.
- [51] Daniel Cremers, Timo Kohlberger, and Christoph Schnörr. Shape statistics in kernel space for variational image segmentation. *Pattern Recognition*, 36(9):1929–1943, 2003.
- [52] Daniel Cremers, Mikael Rousson, and Rachid Deriche. A review of statistical approaches to level set segmentation: Integrating color, texture, motion and shape. *International Journal On Computer Vision*, 72(2):195–215, 2007.
- [53] Antonio Criminisi, Toby Sharp, and Andrew Blake. Geos: Geodesic image segmentation. In *IEEE European Conference On Computer Vision (1)*, pages 99–112, 2008.
- [54] Debreuve, M Gastaud, M Barlaud, and G Aubert. Using the shape gradient for active contour segmentation: from the continuous to the discrete formulation. *Journal of Mathematical Imaging and Vision*, 28(1):47–66, 2007.
- [55] Michel C. Delfour and Jean-Paul Zolésio. Shapes and geometries: Analysis, differential calculus, and optimization. *Advances in Design and Control, SIAM*, 2001.
- [56] H. Delingette. General object reconstruction based on simplex meshes. *International Journal On Computer Vision*, 32(2):1–36, September 1999.
- [57] R. Deriche. Recursively implementing the Gaussian and its derivatives. Technical Report 1893, INRIA, May 1993.
- [58] T. Deschamps and L. Cohen. Fast extraction of tubular and tree 3d surfaces with front propagation methods. *International Conference on Pattern Recognition*, pages 731–734, 2002.
- [59] Maxime Descoteaux and Rachid Deriche. High angular resolution diffusion mri segmentation using region-based statistical surface evolution. *Journal of Mathematical Imaging and Vision*, 2008.
- [60] Q. Dinh, G. Turk, and G. Slabaugh. Reconstructing surfaces using anisotropic basis functions. In *IEEE International Conference On Computer Vision*, pages 606–613, 2001.
- [61] J.C. Dunn. A fuzzy relative of the isodata process and its use in detecting compact well separated clusters. *Journal of Cybernetics*, 3:32–57, 1974.
- [62] Ivar Ekeland and Roger Témam. *Convex Analysis and Variational Problems*. Classics. SIAM, 1999.
- [63] Khaoula Elagouni, Cybèle Ciofolo-Veit, and Benoit Mory. Automatic segmentation of pathological tissues in cardiac mri. In *International Symposium on Biomedical Imaging, Proceedings*, pages 472–475, 2010.

- [64] P. Felzenszwalb and D. Huttenlocher. Efficient graph-based image segmentation. *International Journal On Computer Vision*, 59(2), 2004.
- [65] W. Fleming and R. Rishel. An integral formula for total gradient variation. *Archiv Der Mathematik*, 11:218–222, 1960.
- [66] L.R. Ford and Fulkerson. Maximal flow through a network. *Canadian Journal of Mathematics*, 8:399–404, 1956.
- [67] J.M. Fornefett, K. Rohr, and H.S. Stiehl. Elastic registration of medical images using radial basis functions with compact support. In *CVPR*, pages 402–409, June 1999.
- [68] A. Frangi, W. Niessen, R. Hoogeveen, T. van Walsum, and M. Viergever. Model-based quantification of 3d magnetic resonance angiographic images. *IEEE Transactions on Medical Imaging*, 18(10):946–956, 1999.
- [69] D. Freedman and Tao Zhang. Interactive graph cut based segmentation with shape priors. In *Computer Vision and Pattern Recognition, 2005. CVPR 2005. IEEE Computer Society Conference on*, volume 1, pages 755–762 vol. 1, June 2005.
- [70] Yoav Freund and Robert E. Schapir. A decision-theoretic generalization of on-line learning and an application to boosting. *Journal of Computer and System Sciences*, 55, 1997.
- [71] Pascal Fua and Yvan G. Leclerc. Model driven edge detection. *Machine Vision Applications*, 3(1):45–56, 1990.
- [72] M. Gage and R.S. Hamilton. The heat equation shrinking convex plane curves. *Journal of Differential Geometry*, 23:69–96, 1986.
- [73] A. Gelas, O. Bernard, D. Friboulet, and R. Prost. Compactly supported radial basis functions based collocation method for level-set evolution in image segmentation. *IEEE Transactions on Image Processing*, 16(7):1873–1887, 2007.
- [74] S. Geman and D. Geman. Stochastic relaxation, gibbs distributions, and the bayesian restoration of images. *IEEE Transactions on Pattern Analysis And Machine Intelligence*, 1984.
- [75] R Goldenberg, R Kimmel, E Rivlin, and M Rudzsky. Fast geodesic active contours. *IEEE Trans on Image Processing*, 10(10):1467–1475, 2001.
- [76] L Grady. Random walks for image segmentation. *IEEE Transactions on Pattern Analysis and Machine Intelligence*, 28(11):1768–1783, 2006.
- [77] Leo Grady and Eric L. Schwartz. Isoperimetric graph partitioning for image segmentation. *IEEE Transactions on Pattern Analysis And Machine Intelligence*, 3:469–475, 2006.

- [78] L. Greengard and J. Strain. The fast gauss transform. *SIAM journal of scientific and statistical computing*, 12(7):79–84, 1991.
- [79] V. Guillemin and A. Pollack. *Differential Topology*. Prentice Hall, 1974.
- [80] A.J. Hanson. Hyperquadrics: Smoothly deformable shapes with convex polyhedral bounds. *Computer Vision, Graphics, and Image Processing*, 44:191–210, 1994.
- [81] R. Haralick and L. Shapiro. Image segmentation techniques. *Computer Vision, Graphics, and Image Processing*, 29:100–132, 1985.
- [82] T. Heimann, B. van Ginneken, and Eds. M. Styner. 3D segmentation in the clinic: A grand challenge. *MICCAI*, 2007.
- [83] A. Herbulot, S. Jehan-Besson, M. Barlaud, and G. Aubert. Shape gradient for multi-modal image segmentation using mutual information. *Proc. of IEEE Int. Conference on Image Processing (ICIP)*, 10(8):2729–2732, October 2004.
- [84] Ariane Herbulot, Stéphanie Jehan-Besson, Stefan Duffner, Michel Barlaud, and Gilles Aubert. Segmentation of vectorial image features using shape gradients and information measures. *Journal of Mathematical Imaging and Vision*, 25(3):365–386, 2006.
- [85] M. Hernandez and A. Frangi. Non-parametric geodesic active regions: Method and evaluation for cerebral aneurysms segmentation in 3dra and cta. *Medical Image Analysis*, 11(3):224–241, 2007.
- [86] M. Holtzman-Gazit, R. Kimmel, N. Peled, and D. Goldsher. Segmentation of thin structures in volumetric medical images. *IEEE Transactions on Image Processing*, 15(2):354–363, 2006.
- [87] Nawal Houhou, J.-P. Thiran, and X. Bresson. Fast texture segmentation model based on the shape operator and active contour. *Proc. of Computer Vision and Pattern Recognition*, 2008.
- [88] X.L. Huang and D.N. Metaxas. Metamorphs: Deformable shape and appearance models. *IEEE Trans. PAMI*, 30(8):1444–1459, August 2008.
- [89] Stéphanie Jehan-Besson, Michel Barlaud, and Gilles Aubert. Dream2s: Deformable regions driven by an eulerian accurate minimization method for image and video segmentation. In *ECCV '02: Proceedings of the 7th European Conference on Computer Vision-Part III*, pages 365–380, London, UK, 2002. Springer-Verlag.
- [90] T. Kadir and M. Brady. Unsupervised non-parametric region segmentation using level sets. *International Conference on Computer Vision, Proceedings*, 2(1267-1274), 2003.
- [91] Yan Kang, Klaus Engelke, and Willi Kalender. Interactive 3d editing tools for image segmentation. *Medical Image Analysis*, 8(1):35–46, 2004.

- [92] M. Kass, A.P. Witkin, and D. Terzopoulos. Snakes: Active contour models. *IEEE International Conference On Computer Vision*, 1(4):321–331, January 1988.
- [93] S. Kichenassamy, A. Kumar, P. Olver, A. Tannenbaum, and A.J. Yezzi. Gradient flows and geometric active contour models. *IEEE International Conference On Computer Vision*, pages 810–815, 1995.
- [94] S. Kichenassamy, A. Kumar, P. Olver, A. Tannenbaum, and A.J. Yezzi. Conformal curvature flows: From phase transitions to active vision. *Archive for Rational Mechanics and Analysis*, 134:275–301, 1996.
- [95] J. Kim, J.W. Fisher, A.Yezzi, M. Cetin, and A.S. Willsky. A nonparametric statistical method for image segmentation using information theory and curve evolution. *IEEE Trans. on Image Processing*, 14:1486–1502, 2005.
- [96] R. Kimmel and A. M. Bruckstein. Regularized laplacian zero crossings as optimal edge integrators. *International Journal On Computer Vision*, 53(3):225–243, 2003.
- [97] H. Knutsson and C.F. Westin. Normalized and differential convolution: Methods for interpolation and filtering of incomplete and uncertain data. *Proc. of Computer Vision and Pattern Recognition*, pages 515–523, 1993.
- [98] T. Koller, G. Gerig, G. Székely, and D. Dettwiler. Multiscale detection of curvilinear structures in 2d and 3d image data. *International Conference on Computer Vision, Proceedings*, pages 864–869, 1995.
- [99] V. Kolmogorov and R. Zabih. What energy functions can be minimized via graph cuts. *IEEE Transactions on Pattern Analysis And Machine Intelligence*, 26(2):147–159, 2004.
- [100] K. Krissian, G. Malandain, N. Ayache, R. Vaillant, and Y. Troussel. Model-based multiscale detection of 3d vessels. *Proc. of Computer Vision and Pattern Recognition*, pages 722–727, 1998.
- [101] J. Kybic and M. Unser. Multidimensional elastic registration of images using splines. In *International Conference on Image Processing*, pages 455–458, September 2000.
- [102] S. Lankton and A. Tannenbaum. Localizing region-based active contours. *Image Processing, IEEE Transactions on*, 17(11):2029–2039, nov. 2008.
- [103] Y. G. Leclerc. Constructing simple stable descriptions for image partitioning. *International Journal On Co*, 3:73–102, 1989.
- [104] T. Lefevre, B. Mory, R. Ardon, J. Sanchez-Castro, and A. Yezzi. Automatic inferior vena cava segmentation in contrast-enhanced ct volumes. In *Biomedical Imaging: From Nano to Macro, 2010 IEEE International Symposium on*, pages 420–423, april 2010.

-
- [105] David Lesage, Elsa D. Angelini, Isabelle Bloch, and Gareth Funka-Lea. A review of 3d vessel lumen segmentation techniques: Models, features and extraction schemes. *Medical Image Analysis*, 13:819–945, 2009.
 - [106] M. Leventon, E. Grimson, and O. Faugeras. Statistical shape influence in geodesic active contours. *Proceedings of IEEE International Conference on Computer Vision and Pattern Recognition*, 1:316–323, June 2000.
 - [107] C. M. Li, C. Y. Kao, J. C. Gore, and Z. H. Ding. Implicit active contours driven by local binary fitting energy. In *IEEE CVPR*, pages 1–7, 2007.
 - [108] Hua Li and A Yezzi. Vessels as 4-d curves: Global minimal 4-d paths to extract 3-d tubular surfaces and centerlines. *IEEE Transactions on Medical Imaging*, 26(9):1213–1223, 2007.
 - [109] Stan Z. Li. *Markov Random Field Modeling in Image Analysis*. Computer Science Workbench. Springer-Verlag, 2009.
 - [110] Tony Lindeberg. *Scale-Space Theory in Computer Vision*. Kluwer Academic Publishers, 1994.
 - [111] W. E. Lorensen and H. Cline. Marching cubes: A high resolution 3-d surface construction algorithm. *Proc. ACM Computer Graphics*, 21:163–169, 1987.
 - [112] L. Lorigo, O. Faugeras, W. Grimson, R. Keriven, R. Kikinis, A. Nabavi, and C. Westin. Curves: Curve evolution for vessel segmentation. *Medical Image Analysis*, 5(3):195–206, 2001.
 - [113] R. Malladi, J. Sethian, and B. Vemuri. Shape modeling with front propagation: a level-set approach. *IEEE Transactions on Pat*, 17:158–175, 1995.
 - [114] R. Malladi and J. A. Sethian. Level set and fast marching methods in image processing and computer vision. In *IEEE International Conference on Image Processing*, pages I: 489–492, 1996.
 - [115] R. Malladi and J. A. Sethian. A real-time algorithm for medical shape recovery. In *IEEE International Conference On Computer Vision*, pages 304–310, 1998.
 - [116] R. Manniesing, B. Velthuis, M. van Leeuwen, I. van der Schaaf, P. van Laar, and W. Niessen. Level set based cerebral vasculature segmentation and diameter quantification in ct angiography. *Medical Image Analysis*, 10:200–214, 2006.
 - [117] I.N. Manousakas, P.E. Undrill, G.G. Cameron, and T.W. Redpath. Split-and-merge segmentation of magnetic resonance medical images: performance evaluation and extension to three dimensions. *Computers and Biomedical Research*, 31:393–412, 1998.

- [118] D. R. Martin, C. Fowlkes, D. Tal, and J. Malik. A database of human segmented natural images and its application to evaluating segmentation algorithms and measuring ecological statistics. *International Conference on Computer Vision, Proceedings*, pages 416–425, 2001.
- [119] Tim McInerney and Demetri Terzopoulos. Deformable models in medical image analysis: A survey. *Medical Image Analysis*, 1:91–108, 1996.
- [120] O Michailovich, Y Rathi, and A Tannenbaum. Image segmentation using active contours driven by the bhattacharyya gradient flow. *IEEE Transactions on Image Processing*, 16(11):2787–2801, 2007.
- [121] Julien Mille. Narrow band region-based active contours and surfaces for 2d and 3d segmentation. *Computer Vision and Image Understanding*, 113(9):946–965, 2009.
- [122] J. Montagnat, H. Delingette, and N. Ayache. A review of deformable surfaces: Topology, geometry and deformation. *Image and Vision Computing*, 2001.
- [123] Jean Michel Morel and Sergio Solimini. *Variational methods in image segmentation*. Birkhauser Boston Inc., Cambridge, MA, USA, 1995.
- [124] B. S. Morse, W. M. Liu, T. S. Yoo, and K. Subramanian. Active contours using a constraint-based implicit representation. In *IEEE Conference on Computer Vision and Pattern Recognition*, pages 285–292, 2005.
- [125] Benoît Mory and Roberto Ardon. Fuzzy Region Competition: A Convex Two-Phase Segmentation Framework. In *Scale Space and Variational Methods in Computer Vision*, volume 4485/2008 of *Lecture Notes in Computer Science*, pages 214–226, Ischia, Italie, May 2007. Springer Berlin / Heidelberg. Acknowledgement: Copyright Springer 2007. Please download the publisher version of this paper by using <http://www.springerlink.com/content/ww29242w64453651/> or DOI 10.1007/978-3-540-72823-8_19.
- [126] D. Mumford and J. Shah. Optimal approximations by piecewise smooth functions and associated variational problems. *Comm. on Pure and Applied Mathematics*, 42(5):577–685, 1989.
- [127] Ken Museth, David E. Breen, Ross T. Whitaker, and Alan H. Barr. Level set surface editing operators. *ACM Transactions on Graphics*, 21(3):330–338, 2002.
- [128] D. Nain, A. Yezzi, , and G. Turk. Vessel segmentation using a shape driven flow. *Proc. of Medical Image Computing and Computer-Assisted Interventions*, 1:51–59, 2004.
- [129] Kangyu Ni, Xavier Bresson, Tony Chan, and Selim Esedoglu. Local histogram based segmentation using the wasserstein distance. *International Journal On Computer Vision*, 84:97–111, August 2009.

- [130] Mila Nikolova, Selim Esedoglu, and Tony Chan. Algorithms for finding global minimizers of image segmentation and denoising models. *SIAM Journal on Applied Mathematics*, 66(5):1632–1648, 2006.
- [131] Jorge Nocedal and Stephen J. Wright. *Numerical optimization*. Springer, 1999.
- [132] S. Oeltze and B. Preim. Visualization of vasculature with convolution surfaces: Method, validation and evaluation. *IEEE Transactions on Medical Imaging*, 24(4):540–548, April 2005.
- [133] Stanley Osher and James Sethian. Fronts propagating with curvature-dependent speed: Algorithms based on hamilton-Jacobi formulations. *Journal of Computational Physics*, 79:12–49, 1988.
- [134] N Paragios and R Deriche. Geodesic active contours and level sets for the detection and tracking of moving objects. *IEEE Transactions on Pattern Analysis and Machine Intelligence*, 22(3):266–280, 2000.
- [135] N Paragios and R Deriche. Geodesic active regions and level set methods for motion estimation and tracking. *Computer Vision and Image Understanding*, 97(3):259–282, 2005.
- [136] N. Paragios, M. Rousson, and V. Ramesh. Matching distance functions: A shape-to-area variational approach for global-to-local registration. In *ECCV*, page II: 775 ff., 2002.
- [137] Nikos Paragios and Rachid Deriche. Geodesic active regions and level set methods for supervised texture segmentation. *International Journal On Computer Vision*, 46(3):223–247, 2002.
- [138] E Parzen. On the estimation of a probability density function and mode. *Annals of Mathematical Statistics*, 33:1065–1076, 1962.
- [139] Theodosios Pavlidis. *Algorithms for graphics and image processing*. Rockville: Computer Science Press, 1982.
- [140] J. Piovano, M. Rousson, and T. Papadopoulos. Efficient segmentation of piecewise smooth images. In *Scale Space and Variational Methods in Computer Vision, Proceedings*, 2007.
- [141] G. Pizaine, E.D. Angelini, I. Bloch, and S. Makram-Ebeid. Vessel geometry modeling and segmentation using convolution surfaces and an implicit medial axis. In *Biomedical Imaging: From Nano to Macro, 2011. ISBI'11. IEEE International Symposium on*, pages 1421–1424, 2011.
- [142] Stephen Pizer, Christina Burbeck, James Coggins, Daniel Fritsch, and Bryan Morse. Object shape before boundary shape: Scale-space medial axes. *Journal of Mathematical Imaging and Vision*, 4(3):303–313, 1994.

- [143] Thomas Pock, Daniel Cremers, Horst Bischof, and Antonin Chambolle. An algorithm for minimizing the mumford-shah functional. In *IEEE International Conference on Computer Vision, Proceedings*, pages 1133–1140, 2009.
- [144] T. Riklin Raviv, N. Kiryati, and N. A. Sochen. Prior-based segmentation and shape registration in the presence of perspective distortion. *International Journal On Computer Vision*, 72(3):309–328, May 2007.
- [145] L.G. Roberts. *Machine Perception of thre-dimensional solids*. MIT Press, Cambridge, MA, 1965.
- [146] Marie Rochery, Ian H. Jermyn, and Josiane Zerubia. Higher order active contours. *International Journal On Computer Vision*, 69(1):27–42, 2006.
- [147] Rémi Ronfard. Region-based strategies for active contour models. *International Journal On Computer Vision*, 13(2):229–251, 1994.
- [148] Carsten Rother, Vladimir Kolmogorov, and Andrew Blake. Grabcut: interactive foreground extraction using iterated graph cuts. *ACM Transactions on Graphics*, 23(3):309–314, 2004.
- [149] L.I Rudin, S. Osher, and E. Fatemi. Nonlinear total variation based noise removal algorithms. *Physica D* 60, 60, 1992.
- [150] L. Rusko, G. Bekes, G. Nemeth, and M. Fidrich. Fully automatic liver segmentation for contrast-enhanced CT images. *MICCAI, 3D Segmentation in the Clinic: A Grand Challenge*, pages 143–150, 2007.
- [151] K. A. Saddi, C. Chefd’hotel, M. Rousson, and F. Cheriet. Region-based segmentation via non-rigid template matching. In *Workshop on Mathematical Methods in Biomedical Image Analysis*, October 2007.
- [152] K. A. Saddi, M. Rousson, C. Chefd’hotel, and F. Cheriet. Global-to-local shape matching for liver segmentation in ct imaging. In *MICCAI*, October 2007.
- [153] Christophe Samson, Laure Blanc-Féraud, Gilles Aubert, and Josiane Zerubia. A level set model for image classification. *International Journal On Computer Vision*, 40(3):187–197, 2000.
- [154] Guillermo Sapiro. *Geometric Partial Differential Equations and Image Analysis*. Cambridge University Press, New York, NY, USA, 2006.
- [155] B.G. Schunck and B.K.P. Horn. Determining optical flow. In *Image Understanding Workshop*, pages 144–156, 1981.
- [156] D Selle, B Preim, A Schenk, and HO Peitgen. Analysis of vasculature for liver surgical planning. *IEEE Trans. On Medical Imaging*, 21(11):1344–1357, 2002.

- [157] J. Shah. Recovery of shapes by evolution of zero- crossings. Technical report, Dept. of Mathematics, Northeastern University, Boston, MA, 1995.
- [158] Jianbo Shi and Jitendra Malik. Normalized cuts and image segmentation. *IEEE Transactions on Pattern Analysis and Machine Intelligence*, 22(8):888–905, 2000.
- [159] A.K. Sinop and L. Grady. A seeded image segmentation framework unifying graph cuts and random walker which yields a new algorithm. *International Conference on Computer Vision, Proceedings*, 2007.
- [160] G. G. Slabaugh, Q. Dinh, and G. Unal. A variational approach to the evolution of radial basis functions for image segmentation. In *IEEE Conference on Computer Vision and Pattern Recognition*, pages 1–8, 2007.
- [161] Stefano Soatto and Anthony J Yezzi. Deforming motion , shape average and the joint registration and segmentation of images. *Computer Vision Eccv 2002 Pt Iii*, 2352(3):32–47, 2002.
- [162] O. Somphone, B. Mory, S. Makram-Ebeid, and L. D. Cohen. Prior-based piecewise-smooth segmentation by template competitive deformation using partitions of unity. In *ECCV*, October 2008.
- [163] John Strain. Tree methods for moving interfaces. *Journal of Computational Physics*, 151:616–648, May 1999.
- [164] D. Suter. Motion estimation and vector splines. In *Conference on Computer Vision and Pattern Recognition*, pages 939–942. IEEE Computer Society Press, 1994.
- [165] Xue-Cheng Tai, Knut-Andreas Lie, Tony F. Chan, and Stanley Osher. *Image Processing Based on Partial Differential Equations: Proceedings of the International Conference on PDE-Based Image Processing and Related Inverse ... 8-12, 2005 (Mathematics and Visualization)*. Springer-Verlag New York, Inc., Secaucus, NJ, USA, 2007.
- [166] G. Taubin. An improved algorithm for algebraic curve and surface fitting. *IEEE International Conference On Computer Vision*, pages 658–665, June 1993.
- [167] D. Terzopoulos, A. Witkin, and M. Kass. Constraints on deformable models: Recovering 3d shape and nonrigid motion. *Artificial Intelligence*, 36:91–123, 1988.
- [168] J.P. Thirion. Image matching as a diffusion process: An analogy with maxwell’s demons. *Medical I*, 2:243–260, 1998.
- [169] Pekka J. Toivanen. New geodesic distance transforms for gray-scale images. *Pattern Recognition Letters*, 17(5):437–450, 1996.

- [170] A Tsai, A Yezzi, and AS Willsky. Curve evolution implementation of the mumford-shah functional for image segmentation, denoising, interpolation, and magnification. *IEEE Transactions on Image Processing*, 10(8):1169–1186, 2001.
- [171] A. Tsai, A. J. Yezzi, W. M. Wells, III, C. Tempany, D. Tucker, A. Fan, W. E. L. Grimson, and A. S. Willsky. A shape-based approach to the segmentation of medical imagery using level sets. *IEEE Transactions on Medical Imaging*, 22(2):137–154, February 2003.
- [172] A. Tsai, A. J. Yezzi, Jr., W. M. Wells, III, C. Tempany, D. Tucker, A. Fan, W. E. L. Grimson, and A. S. Willsky. Model-based curve evolution technique for image segmentation. In *IEEE CVPR*, pages I:463–468, 2001.
- [173] Shuowen Tu. Probabilistic boosting tree: Learning discriminative models for classification, recognition and clustering. *IEEE International Conference On Computer Vision*, 2, 2005.
- [174] R. Urquhart. Graph theoretical clustering based on limited neighborhood sets. *Pattern Recognition*, 15(3):173–187, 1982.
- [175] C. van Bommel, L. Spreeuwens, M. Viergever, and W. Niessen. Level-set-based artery-vein separation in blood pool agent ce-mr angiograms. *IEEE Transactions on Medical Imaging*, 22(10):1224–1234, 2003.
- [176] Alexander Vasilevskiy and Kaleem Siddiqi. Flux maximizing geometric flows. *IEEE Transactions on Pattern Analysis and Machine Intelligence*, 24(12):1565–1578, 2002.
- [177] Luminita Vese and Tony Chan. A multiphase level set framework for image segmentation using the mumford and shah model. *International Journal On Computer Vision*, 50(3):271–293, 2002.
- [178] S. Wang, W.Y. Zhu, and Z.P. Liang. Shape deformation: Svm regression and application to medical image segmentation. *IEEE International Conference On Computer Vision*, 2:209–216, 2001.
- [179] Guihua Wen, Lijun Jiang, and Jun Wen. Using locally estimated geodesic distance to optimize neighborhood graph for isometric data embedding. *Pattern Recognition*, 41(7):2226–2236, 2008.
- [180] H. Wendland. *Scattered Data Approximation*. Cambridge university press, 2005.
- [181] Z. Wu and R. Leahy. An optimal graph-theoretic approach to data clustering: Theory and its application to image segmentation. *IEEE Transactions on Pattern Analysis And Machine Intelligence*, 15(11):1101–1113, 1993.
- [182] G. Wyvill, C. McPheeters, and Wyvill B. Soft objects. In *Proceedings of Computer Graphics*, 1986.

- [183] Chenyang Xu and JL Prince. Snakes, shapes, and gradient vector flow. *IEEE Transactions on Image Processing*, 7(3):359–369, 1998.
- [184] A.J. Yezzi and S. Soatto. Deformation: Deforming motion, shape average and the joint registration and approximation of structures in images. *International Journal On Computer Vision*, 53(2):153–167, 2003.
- [185] Ian T. Young and Lucas J. van Vliet. Recursive implementation of the gaussian filter. *Signal Process.*, 44:139–151, June 1995.
- [186] Paul A. Yushkevich, Joseph Piven, Heather Cody Hazlett, Rachel Gimpel Smith, Sean Ho, James C. Gee, and Guido Gerig. User-guided 3D active contour segmentation of anatomical structures: Significantly improved efficiency and reliability. *Neuroimage*, 31(3):1116–1128, 2006.
- [187] C.T. Zahn. Graph-theoretic methods for detecting and describing gestalt clusters. *IEEE Transactions on Computing*, 20:68–86, 1971.
- [188] Hong-Kai Zhao, T Chan, B Merriman, and S Osher. A variational level set approach to multiphase motion. *Journal of Computational Physics*, 127(1):179–195, 1996.
- [189] Song Zhu and Alan Yuille. Region competition: Unifying snakes, region growing, and bayes/mdl for multiband image segmentation. *IEEE Transactions on Pattern Analysis and Machine Intelligence*, 18:884–900, 1996.